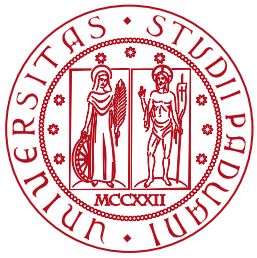

Department of Physics and Astronomy "G. Galilei"

Doctoral School in Astronomy

On the formation of bulges from their observed properties in nearby galaxies

Author:
Luca Costantin

Supervisor:
Prof. Enrico Maria Corsini

Co-Supervisor:
Dr. Jairo Méndez Abreu

Director of the Doctoral School:
Prof. Giampaolo Piotto

Ph.D. Cycle XXX

Examination date:

Part of the results of this thesis has been already published in the following papers:

L. Costantin J. Méndez-Abreu, E. M. Corsini, L. Morelli, J. A. L. Aguerri, E. Dalla Bontà, and A. Pizzella, 2017, A&A, 601, A84
No evidence for small disk-like bulges in a sample of late-type spirals

L. Costantin, J. Méndez-Abreu, E. M. Corsini, M. C. Eliche-Moral, T. Tapia, L. Morelli, E. Dalla Bontà, and A. Pizzella, 2018, A&A, in press (arXiv: 1710.05222)
The intrinsic shape of bulges in the nearby Universe

J. Méndez-Abreu, T. Ruiz-Lara, L. Sánchez-Menguiano, A. de Lorenzo-Cáceres, L. Costantin, et al. 2017, A&A, 598, A32
Two-dimensional multi-component photometric decomposition of CALIFA galaxies

A mamma e papà

- La scienza non è altro che conoscenza
immaginaria di una verità assoluta. -
L. N. Tolstoj

Abstract

The question whether the observed properties of galaxies are imprinted by the initial conditions of their formation or determined by different evolutionary processes is still open. In the local Universe, more than 60% of stars reside in elliptical galaxies and bulges of lenticular and spiral galaxies. Thus, unveiling the paths of bulge formation and evolution ensures a better understanding of galaxies themselves. The current paradigm separates galactic bulges into two broad categories, namely classical and disk-like bulges. In this scenario, we focus on the description of the bulge component in nearby galaxies from an observational point of view. We aim to properly interpret how observed properties of bulges provide evidences of different mechanisms responsible for their formation and evolution. Indeed, the separation of bulge types according to their observed properties has become a common task in extragalactic astronomy, even if there are no unambiguous ways of doing it yet.

We present the technical procedures followed to characterize the structural properties of the bulge component as well as to determine its three-dimensional shape. We elucidate how the photometric algorithm allows to describe the surface brightness distribution of galaxies. We also revise and fine-tune the procedures and methods adopted to constrain the three-dimensional shape of bulges, detailing both the geometrical and statistical analysis.

We describe the two-dimensional multi-component photometric decomposition of 404 galaxies from the Calar Alto Legacy Integral Field Area (CALIFA) data release 3. We provide the community with an accurate photometric characterization of the multiple stellar structures shaping the CALIFA galaxies, describing them with the suitable combination of a nuclear point source, a bulge, a single or double bar, and a pure exponential or double-exponential disk component. Moreover, we use a human-supervised approach to evaluate the optimal number of structures to be accounted for fitting the surface brightness distribution. We release the photometric parameters of the CALIFA galaxies, together with statistical errors and a visual analysis of the quality of each fit. The analysis of the photometric components reveals a clear segregation of the structural composition of galaxies with stellar mass. At high masses ($\log(M_\star/\mathrm{M}_\odot) > 11$), the galaxy population is dominated by galaxies modeled with a single Sérsic or a bulge+disk with a bulge-to-total luminosity ratio $B/T > 0.2$. At

intermediate masses ($9.5 < \log(M_\star/\mathrm{M}_\odot) < 11$), galaxies described with bulge+disk and $B/T < 0.2$ are preponderant, whereas, at the low mass end ($\log(M_\star/\mathrm{M}_\odot) < 9.5$), the prevailing population is constituted by galaxies modeled with either pure disks or nuclear point sources+disks (i.e., with no discernible bulge). We set the basis for new studies combining photometric information with the wealth of two-dimensional spatially resolved spectroscopic information provided by the CALIFA survey.

In an effort to push the limits of the scaling relations studied so far to the very low-σ regime we describe the small bulges at the end of the Hubble sequence. To this aim, we derive the photometric and kinematic properties of 9 nearby late-type spiral galaxies. We analyze the i-band images of the Sloan Digital Sky Survey (SDSS) of these galaxies to characterize the structural parameters of their bulges by means of a two-dimensional photometric decomposition. Moreover, we measure the line-of-sight stellar velocity distribution within the bulge effective radius from the long-slit spectra taken with high spectral resolution at the Telescopio Nazionale Galileo. Finally, we combine the photometric and kinematic information of the sample bulges to study their location in the fundamental plane, Kormendy, and Faber-Jackson relations defined for elliptical galaxies and large bulges. We find that each of our bulge follows the same scaling relations of elliptical galaxies, massive bulges, and compact early-type galaxies so they cannot be classified as disk-like systems. This analysis suggests that a single population of galaxy spheroids follows the same scaling relations, where the mass seems to lead to a smooth transition in the photometric and kinematic properties from less to more massive bulges and elliptical galaxies.

The thorough description of the bulge structural features in the CALIFA sample results in the characterization of the bulge three-dimensional shape. Constraining the intrinsic shape of bulges allows to provide new clues on the bulge formation mechanisms and set new limitations for future simulations. Firstly, we take advantage of `GalMer` numerical simulations to estimate the reliability of the procedure. Thus, we create a set of mock SDSS i-band images at different galaxy inclinations for a set of simulated galaxies, that closely resemble lenticular galaxies. We perform a two-dimensional photometric decomposition of all the mock images applying the same procedure as for real galaxies, in order to characterize the geometrical parameters of bulge and disk which we use to recover the bulge intrinsic shape. We conclude that for galaxies in the inclination range $25^\circ < \theta < 65^\circ$ we can safely derive the intrinsic shape of their bulges. Moreover, we also realize that a very accurate photometric decomposition is mandatory to retrieve the bulge intrinsic shape. Secondly, we obtain the intrinsic shape of 83 bulges from the CALIFA survey. We introduce the (B/A, C/A) diagram to analyze possible correlations between the intrinsic shape and properties of bulges. We find that our CALIFA bulges tend to be nearly oblate systems (66%), with a smaller fraction of prolate spheroids (19%) and triaxial ellipsoids (15%). The majority of triaxial bulges are in barred galaxies (75%). Moreover, we

find that bulges with low Sérsic indices or in galaxies with low bulge-to-total luminosity ratios form a heterogeneous class of objects; additionally, bulges in late-type galaxies or in less massive galaxies have no preference for being oblate, prolate, or triaxial. On the contrary, bulges with high Sérsic index, in early-type galaxies, or in more massive galaxies are mostly oblate systems. We conclude that various evolutionary pathways may coexist in galaxies, with merging events and dissipative collapse being the main mechanisms driving the formation of the most massive oblate bulges and bar evolution reshaping the less massive triaxial bulges.

Finally, we discuss the observational criteria usually applied to discriminate bulge types in classical and disk-like spheroids. We derive the photometric, kinematic, stellar population, and intrinsic shape properties of bulges in nine lenticular galaxies from the ATLAS^{3D} survey. Our analysis is based on all the observed diagnostics commonly adopted in recent works and tests their efficiency on our sample of meticulously selected systems. Indeed, the morphology of our sample galaxies is chosen to deal with the most simple examples of disk galaxies. We argue that the bulge Sérsic index is a poor tool to discriminate the different bulge types. Moreover, we find that the kinematic properties and line-strength indices of the sample bulges provide no clear identification of the bulge type; this remains true also when comparing the results obtained from the line-strength indices with those obtained from the photometric analysis. We conclude that the common practice of applying the observational criteria for distinguishing bulge types, based on *a priori* classification according to their morphology or Sérsic index, has to be carefully reconsidered. We remark that, even if the different observational characteristics look well motivated in terms of distinct formation paths, their interplay might result in contradictory outcomes. We propose to characterize the disk-like bulges in terms of their intrinsic shape and dynamical status as the most reliable way to separate them from the classical bulges.

Contents

List of Figures

List of Tables

1

INTRODUCTION

1.1 Definition of galactic bulges

The term *bulge* entered the vocabulary of extragalactic astrophysics in the early 1940s, when Edwin Hubble, debating about the direction of rotation of extragalactic nebulae with respect to their spiral pattern, denominated the observed central protuberances as *nuclear bulges* (Hubble 1943). It is undeniable that this word was referred to an observed component that seemed to stick out in the nebulae.

The word was marginally employed in the following years and applied to describe the Galaxy central region (Stebbins & Whitford 1947). However, in the early 1960s, the subject of bulges moved from the Galaxy again to extragalactic objects, when Allan Sandage illustrated and annotated 176 galaxies available in the Mount Wilson-Palomar plate collection and started a new era in extragalactic terminology (The Hubble Atlas of Galaxies, Sandage 1961). Indeed, the golden age of galaxy classification was a prolific time for employing a lot of synonyms describing the central region of galaxies. Sandage described lenticular galaxies such as NGC 1201 (panel 4[1]), NGC 4684 (panel 4), and NGC 524 (panel 5) as composed by *an intense nucleus, an intermediate zone of lower surface brightness, called the lens, and the characteristic faint outer envelope.* Moreover, he mentioned the *box-shaped nucleus* of NGC 128 (panel 7) or the *box-shaped central region* of NGC 7332 (panel 7), the *central envelope* of NGC 4457 (panel 9), and the *large amorphous center* of NGC 3898 (panel 10).

[1] All panels in this Section referred to The Hubble Atlas of Galaxies (Sandage 1961).

Sandage gave a detailed description of the galaxy NGC 2685 (panel 7), where he asked himself whether *the central feature* was *a spheroid (with two axes equal as in a plate or pancake), or* it was *an ellipsoid like a cigar*. The term *bulge* appears only in the description of nine out of 176 galaxies. In the Hubble atlas we found that a *notable feature of NGC 4594* (panel 24), the well-known Sombrero galaxy, is *the large nuclear bulge*. Additionally, he defined the presence or absence of a *nuclear central bulge* in NGC 4565, NGC 4244, NGC 4216, NGC 5907, NGC 891, NGC 4631 (all in panel 25), and NGC 3556 (panel 35). One possible influence in the terminology used to illustrate the Sombrero galaxy (panel 24) and the above mentioned galaxies (panel 25), could came from Lindblad (1951). Indeed, he described a photographic plate of NGC 4594 taken by Walter Baade in ultraviolet light, interpreting the wide and intense central system as the *central bulge*. Finally, explaining the differences from Sc to Sa spiral galaxies, Sandage stated that *the arms, starting tangent to the central amorphous bulge, become more tightly coiled, thinner, and more regular*.

After that, Wallerstein (1962) adopted the term again, studying the stellar content of the Galaxy nuclear bulge, while Burbidge & Burbidge (1962) called *nuclear bulge* the central region of spiral and irregular galaxies. With a lot of data available, the first description of the central region of extragalactic systems became an illustrative rather than a rigorous definition of the observed physics (Madore 2016). But, since science is not poetry, the community needed a common language to interpret the actual mechanisms acting in the Universe. It took only few years when Arp (1965) defined the first quantitative criterion to classify galaxies, extending the definition to our Milky Way. The bulge-to-disk luminosity ratio (B/D) established the role of bulge as a proxy for other galaxy properties.

The idea of a component sticking out the galaxy disk was well established, but only after a relatively long period the word *bulge* became widely used in the literature. John Kormendy, in his early works, defined these features as *spheroids* that *contribute significant light in regions dominated by the disk* (Kormendy 1977). Later, he stated that *disk-galaxy spheroids differ significantly from elliptical galaxies*, going toward the idea that the inner and brighter region of the galaxy could be compare to a self-consistent system (Kormendy & Bruzual 1978). It was only in 1979 when the term *bulge* was used to describe the triaxial central feature present in several galaxies, notably NGC 3945 (Kormendy 1979). After that, the idea of *bulge* appeared in all Kormendy's works (e.g., Kormendy & Illingworth 1982).

In the last twenty years, due to the technological progress, modern observing facilities, and better available data, the word *bulge* assumed different meanings. The general idea is to refer at *bulges* as a well-defined physical systems, even if a lot of open questions remain unresolved. Some authors defined the bulge as the inner region of disk galaxies, where the isophotes are apparently less flattened than those of the outer disk and assuming the two components to have elliptical isophotes of constant but different flattening (Kent 1986; Andredakis et al. 1995). Renzini (1999) adopted the standard interpretation of Hubble - Sandage - de Vaucouleurs, looking at the bulge as an elliptical galaxy surrounded by an outer prominent disk or, conversely, considering elliptical galaxies as bulges of lenticular or spiral galaxies that somehow were able to acquire and preserve a disk component. Carollo et al. (1999) gave an operative definition of bulge as the inner component of a galaxy which is photometrically superimposed onto an exponential extended disk; this definition has the advantage to deal with all disk galaxies regardless of their inclination. Regarding the bulge formation scenario, Kormendy & Kennicutt (2004) discriminated between *classical bulges* and *pseudobulges*. They asserted that classical bulges are shaped throughout hierarchical merging or clustering and resemble elliptical galaxies embedded into a disk component whereas pseudobulges undergo a slow and secular rearrangement of mass related to phenomena such as spiral structure, bars, and triaxial dark matter halos.

Therefore, what is a bulge? An unambiguous definition does not exist yet, since the endless evolution of interpretations and conjectures made the term suitable to different and sometimes misleading applications. In this work we tried to investigate if there is a particular property, such as the intrinsic three-dimensional shape, that would clarify the role of bulges in extragalactic astronomy. To do so, we applied the photometric definition of bulge, as the extra component dominating the galaxy light above the surface brightness profile of the disk extrapolated in the inner regions of the galaxy. In this context, the bulge surface brightness is usually fit with a Sérsic law spanning a large range of profile shapes, whereas the disk surface brightness is usually fit with an exponential law (Andredakis 1998; Prieto et al. 2001; Aguerri et al. 2005; Gadotti 2009; Méndez-Abreu et al. 2017).

This Chapter is organized as follows. The state of the art of galaxy formation processes and their implications for bulge evolution are described in Section 1.2. The bulges classification is given in Section 1.3. Finally, the aim of the thesis is presented in Section 1.4.

1.2 Formation and evolution of galactic bulges

Currently, the baryonic mass in the Universe accounts for more than 60% of stars that reside in elliptical galaxies and bulges of lenticular and spiral galaxies (Persic & Salucci 1992; Fukugita et al. 1998; Driver et al. 2017). Thus, unveiling the paths of bulge formation and evolution ensures a better understanding of galaxies themselves.

In the complexity of the formation and evolution scenarios of galaxies, some phenomena such as star formation, gas recycling, metal enrichment, and energy feedback via supernovae, are always present. Other phenomena are instead used to characterize different evolutionary paths and can be divided into internal or external ones (see Fig. 1.1). Among the internal processes we can find the protogalactic collapse and secular evolution driven by bar instabilities, dark matter halos, bars and oval distortions, spiral structures, supermassive black holes, and galactic winds. On the other hand, external process that build up galaxies are represented by galaxy major and minor mergers, ram-pressure stripping of gas, and the secular evolution driven by prolonged gas infall and galaxy harassment (see Kormendy & Kennicutt 2004, for a review).

Moreover, there is a reiterated change of the relative importance of each physical mechanism at work in galaxies as a consequence of the expansion of the Universe, with fast processes being replaced by slower ones (Conselice 2003). The consequence of the virialization of the density fluctuations of cold dark matter in the primordial Universe is the assembly of galaxies through dissipative collapse (Sandage 1990) or mergers (Toomre 1977). Interaction processes are really fast and their violence might have a remarkable impact in the actual observed properties of galaxies. However, the violent and rapid phenomena that characterized the early stages of galaxy formation are making their way to secular pathways of evolution (Kormendy & Kennicutt 2004). Secular processes have longer timescale and become relevant when spiral structures, bars, triaxial dark matter halos, and oval distortions are involved. But, it is important that the system experienced no disruptive events for a long time in order to see the effects of secular evolution.

Since the Universe experienced different transition epochs, both slow and fast, internal and external processes assume a relevant role in determining the actual morphology and observed properties of nearby galaxies. The direct consequence is that various kind of bulges

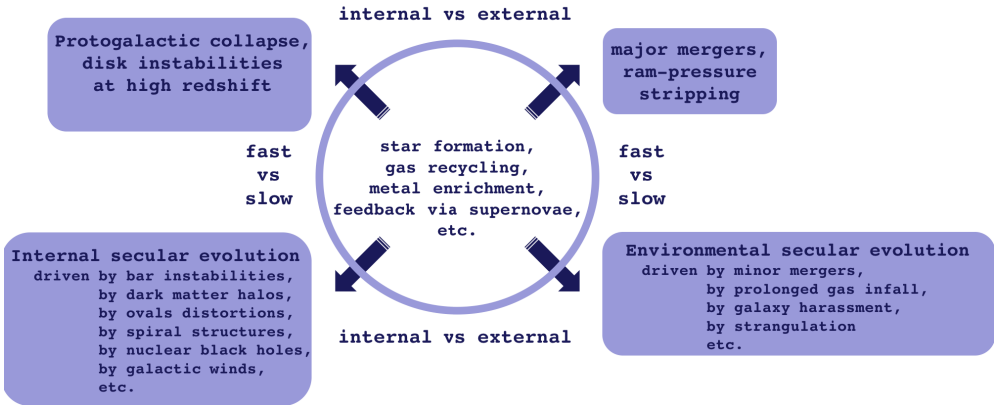

Figure 1.1: Morphological box (Zwicky 1957) of galaxy evolution processes revised from Kormendy & Kennicutt (2004). The central processes are common for all types of galaxy evolution. Fast processes (*top*) are vertically divided from and slow processes (*bottom*), while purely internally mechanisms (*left*) are horizontally separated from ones driven by external and environmental effects (*right*).

and different processes can coexist in the same galaxy (Athanassoula 2005). The implicit agreement is that the gas physics, star formation mechanisms, implementation of different sorts of feedback, and improvement of numerical resolution have to be fine tuned in order to match the actual properties observed in galactic bulges in local Universe.

1.2.1 Dissipative protogalactic rapid collapse

At early times, the evolution of galaxies was probably dominated by the violent and dissipative collapse of their protogalaxies. This scenario was firstly explored by Eggen et al. (1962), studying the correlation between the velocity perpendicular to the galactic plane and ultraviolet excess for 221 dwarf stars in the Galaxy (Eggen 1962). They interpreted this correlation as due to the collapse toward the fundamental plane of the protogalaxy, which shrinks in diameter and sets circular orbits once the equilibrium between the gravitational attraction and centrifugal acceleration is reached. Moreover, they also found a correlation between the chemical composition of those stars, eccentricity of their galactic orbits, their angular momenta, and their height above the galactic plane. They argued that the rapid collapse on a timescale of 100 Myr of a pre-existing protogalaxy with a diameter at least ten times greater than the actual one could explain those observed relations. This violent event built up the oldest stars with the lowest abundance of heavy elements.

In this scenario, a protogalaxy with initial non-zero angular momentum began to shrink

out of intergalactic material approximately 10 Gyr ago. Once the baryonic matter began to fall together, the first globular clusters started to form by condensation. The collapse continued undisturbed along the vertical direction, forming the thin disk, while the rotation was eventually able to arrest the collapse along the radial direction. At this stage there was an inevitable boost of star formation because of the increment of local density. This led to the formation of the second generation stars that exhibit a smaller ultraviolet excess, since the first generation stars enriched the gas with heavy elements during their evolution. Finally, the energy generated in the collapse was wiped out by the hot gas. After the initial coupling between the orbits of the stars and gas, the angular momentum forced the gas to settle into circular orbits, whereas the first-generation stars could not change the highly eccentric orbits shaped by the original collapse.

Decades later, Sandage (1990) clarified some controversial details about the rapid and dissipative collapse that formed the Galaxy according to the model proposed by Eggen et al. (1962). Firstly, various authors criticized that the model cannot be monolithic, because of the spread in age observed in globular clusters (Gratton & Ortolani 1988; Green & Norris 1990) or measured between the oldest disk and halo stars. Sandage agreed on this point, highlighting that the word *monolithic* was never used in Eggen et al. (1962): the density spread in the initial protogalactic gas cloud gave rise to the age spread among the halo clusters. Secondly, the controversial presence of a metallicity gradient was under debate. In this context, the model considers a phase of free-fall of the halo, where no metallicity gradient can occur. However, the absence of a gradient in the halo only means that there was no dissipation of energy during the free-fall phases, as expected. If a metallicity gradient existed within the thick disk as resulted in Sandage (1990), the first phases of the disk formation had started when the gas regions encountered dissipation with other gas near the galactic plane.

1.2.2 Major mergers

The hierarchical growth of extragalactic structures predicted by Λ cold dark matter (CDM) cosmology (White & Rees 1978) makes major mergers, and galaxy interactions in general, an inescapable channel for galaxy formation and evolution. It is worth noting that

the *bottom-up* hierarchical scenario may be fine tuned with several observational evidences pointing toward a *downsizing* of the mechanisms of galaxy formation (Cowie et al. 1996; Neistein et al. 2006; Thomas et al. 2010).

The pioneering numerical results from Toomre & Toomre (1972) are widely used to explain the morphologies of spheroids (i.e., elliptical galaxies and bulges in disk galaxies) at early times, as well as the observational properties of nearby galaxies as remnants of interactions found in the local Universe (Lake & Dressler 1986; Dasyra et al. 2007). In this scenario, low-mass dark matter halos firstly form and progressively merge to create massive and larger structures (Blumenthal et al. 1984). As a consequence, the dark potential wells capture baryons and allow the creation of first stars and rotationally supported galaxies (Fall & Efstathiou 1980). Finally, the on-going external accretion of intergalactic material triggers the star formation (Kauffmann et al. 1993; Baugh et al. 1998).

Major merger events are responsible for the dramatic reshaping of the galactic structures. During the mergers, the tidal torques support the gas inflow into the central regions of galaxies, which can fuel intense starbursts (Mihos & Hernquist 1994b) or rapid black hole growth (Di Matteo et al. 2005). When two galaxies of the same mass experience a wet major merger, there is an enhance of the star formation activity each time the galactic nuclei are sufficiently close, ending up in a burst of star formation at the final merger (Mihos & Hernquist 1996). This triggering mechanism is very efficient, converting up to 80% of the total original gas mass into stars. Both simulations (i.e., Cox et al. 2006b) and observations (Schweizer 1982) highlight that the violence of the major merger events is able to transform the stellar disks into spheroids. Thus, the direct consequence of starbursts events, supernova winds, and feedbacks from black hole growth is the stop of the star formation, making the galaxies remnant evolve from the blue cloud to the red sequence (Springel et al. 2005).

A major merger tends to destroy the disk component of the progenitor galaxies (Naab & Burkert 2003). In this context, the current understanding of bulges, and galaxies in general, lacks in explaining the formation of disk galaxies; indeed, since disks experienced a large number of merger events, they have somehow to survive in order to explain the abundance of disk-dominated galaxies observed so far. It is well known that, even without any stellar feedback, a remnant with an embedded disk can result from the major merger of two preexisting disks (Hernquist & Barnes 1991). Fully cosmological simulations have

demonstrated that the survival of disk galaxies is only possible in major mergers if a mixture of strong stellar feedbacks and large gas content are appropriately taken into account, as might be appropriate for systems at high redshifts (Springel & Hernquist 2005; Governato et al. 2007). The violent destruction of the disk can be followed by a transition phase where the disk rebuilds either from the gas reservoir infalling from the cosmic web or from the left-over of both gas and stripped stars after a wet merger on a timescale of 2–4 Gyr (Somerville & Primack 1999; Querejeta et al. 2015a). In the latter case, the angular momentum of the reconstituted stellar disk should be the same of the infalling gas.

Major mergers are supposed to be responsible for the different kinematic structure of fast and slow rotators early-types galaxies (ETGs; Emsellem et al. 2007; Naab et al. 2014). Slow rotators experienced up to three major encounters with the latter happening at redshift $z > 1.5$; on the contrary, fast rotators have on average less than one major merger in their past (Khochfar et al. 2011). Thus, since slow rotators are most subject to those violent events, they may most likely form peculiar structures such as the kinematically decoupled cores (KDCs; Krajnović et al. 2008).

However, the result of a major merger is not only a bulge-dominated galaxy, since the presence of a large gas fraction can be responsible to shape little bulges. In this scenario, the bulge and disk do not form separately but they together survive mergers. This addresses the well-known open problem of the systematic overprediction of the mass fraction of bulges from theoretical models, especially in low-mass galaxies (Hopkins et al. 2009).

1.2.3 Minor mergers

The role of minor mergers due to the accretion of low-mass satellites in disk galaxies have been extensively studied using numerical simulations (Mihos et al. 1995; Bournaud et al. 2004; Aceves et al. 2006). It seems reasonable that a galaxy can experience several encounters over a Hubble time. The merger rate of bright galaxies ($M_B \leq -20 - 1.1z$ mag) evolves as $(1 + z)^n$, with the power-law index $n = 2.7 \pm 0.5$ for blue galaxies and $n = 1.3 \pm 0.4$ for red galaxies; thus, integrating the merger rate over cosmic time, the average number of mergers per galaxy since $z = 1$ is $N_{\rm red} = 0.57 \pm 0.05$ for red galaxies and $N_{\rm blue} = 0.26 \pm 0.02$ for blue galaxies (López-Sanjuan et al. 2015).

While major mergers with massive companions might destroy the galaxy structure (Barnes & Hernquist 1991), minor mergers are supposed to do less damage to the disk. Additionally, the accreted small satellites can reach the center of the galaxy, and induce dynamical resonances and oval distortions in the disk component, driving the smooth growth of the central bulge.

The frequency of minor mergers can explain the different formation process of fast and slow rotators ETGs. The use of semi-analytic models analysis allowed Khochfar et al. (2011) to predict that slow rotators accreted up to 90% of their stellar mass from external satellites, whereas it is less than 50% in fast rotators. This allows fast rotators to retain most of their kinematic properties, while the high rate of minor mergers in slow rotators tends to lower their specific angular momentum, building peculiar features like KDC. Moreover, the smoother changes induced by minor mergers can explain low ellipticities presented rarely by slow rotators (Naab et al. 2014) and the existence of lenticular galaxies with kinematic properties that lie between fast and slow rotators (Tapia et al. 2014).

Unfortunately, early studies usually focused the attention on the consequences of minor mergers on the disks, such as thickening and warping, instead of analyzing the inner bulge component (Walker et al. 1996). The issue regarding the role of satellite accretion driving the formation and growth of bulges was addressed only in the last twenty years. Using collisionless N-body simulations, Aguerri et al. (2001) suggested that the mass of the central bulge and its Sérsic index grow proportional to the accreted mass of a dense spheroidal satellite (see also Eliche-Moral et al. 2006). They found that in a minor merger with a satellite as massive as the bulge, the outcome is a bulge closely following the $r^{1/4}$ profile. In this scenario, the center of the remnant acquires most of the mass, orbital energy, and angular momentum of the high-density massive satellite. Nevertheless, the majority of satellites of disk galaxies in the local Universe present a lower density; thus, once disrupted in the merger, satellites deposit their mass at intermediate radii.

1.2.4 Disk instabilities at high redshift

Resolved high redshift galaxies (out to $z \sim 5$) in the Hubble Space Telescope (HST) Ultra Deep Field (UDF) as well as intermediate redshift galaxies ($0 < z < 0.5$) in the COSMOS

field resemble disk-like systems dominated by giant clumps with high star formation activity (Elmegreen et al. 2007; Hinojosa-Goñi et al. 2016). Those galaxies are usually known as chain or clump cluster galaxies. The irregular and peculiar optical morphologies presented by those galaxies compared to nearby spiral galaxies of similar mass, already known from the Hubble Deep Field (HDF) survey and Medium Deep Survey (MDS) (Abraham et al. 1996; van den Bergh et al. 1996), resulted in an enigmatic view: those systems can be interpreted as irregulars seen in the rest-frame ultraviolet or very late-type spiral galaxies with high luminosity, merger remnants, or different systems with no counterpart in the local Universe.

Interferometric studies at millimeter wavelengths probe that the gas fraction in main sequence galaxies at redshift $z > 1$ reaches up to 50% of their baryonic mass, counting only the molecular content (Daddi et al. 2010; Tacconi et al. 2013). As a consequence, the fundamental mechanism that powers the star formation at high redshift is the so-called cold-flow accretion, that is the build-up of pristine gas from the cosmic web (Dekel et al. 2009; Aumer et al. 2010; L'Huillier et al. 2012). At the time that the dark matter halo is sufficiently diffuse, the cool gas in the cosmic web starts to stream toward either the inner halo or the disk, supplying new material for forming further stars. This accreting mechanism of metal-poor gas from the cosmic web is also able to switch on the star formation in the disk of nearby galaxies (Sánchez Almeida et al. 2014).

In distant galaxies, the star formation activity is mainly triggered in giant clumps, as recently confirmed both by observations and numerical simulations (see Bournaud 2016, and references therein). Those clumps have sizes in the 0.1–1 kpc range, masses from $\sim 10^9$ $M_\odot$ to $\sim 10^{10}$ $M_\odot$ each, and young stellar ages ($\sim$ 100 Myr) compared to the host galaxy. A possible explanation is that those clumps can form *ex-situ*, that is by accreting new mass through minor mergers of small companions or external gas clumps (Mandelker et al. 2014). However, this hypothesis might be ruled out by the young age observed in the majority of clumps compared to the older small external galaxies at the same redshift (Bournaud 2016; Förster Schreiber et al. 2011; Wuyts et al. 2012). The main mechanism of clumps formation is *in-situ*, that is by gravitational Jeans instabilities and fragmentation in turbulent disks (Noguchi 1999; Immeli et al. 2004a,b). According to Toomre (1964), the disk instability arises once there is either an increase of the surface density, responsible for the local self-gravity, or a decrease of the circular velocity and velocity dispersion, which tend to balance

local collapse against gravity.

The migration of the star forming clumps from the outer disk toward the galaxy center is a candidate scenario of bulge formation and growth in high redshift galaxies. There is still great uncertainty about the properties of bulges formed through this process. If the clumps are efficiently destroyed by stellar feedback in short timescale (50–100 Myr), the diffuse remnant of the clumps migrates toward the center (Genel et al. 2012; Hopkins et al. 2012). This path for bulge growth, even if with some caveats (see Bournaud 2016), in absence of other relaxation processes in the galaxy center leads to low-concentration disk-like bulges, with a stellar population older than in the disk clumps (Genzel et al. 2008), but younger than in regular spiral galaxies (Elmegreen et al. 2008). On the contrary, if clumps live on longer timescales (300–700 Myr), their recurring coalescence together with repeated and sudden supply of cold gas replenishing the disk as it is being drained (Elmegreen et al. 2008; Dekel et al. 2009), lead to bulges which are more concentrated and with low rotational support. Nevertheless, regardless of the lifetime of these clumps, they induce torques in the disk region and funnel the gas toward the center of the galaxy; thus, this mechanism might eventually form stars helping the build up of the bulge.

1.2.5 Internal secular evolution

The structure of galaxies is continuously and slowly rearranged through internal mechanisms that take place over time scales much longer than the galactic rotation period. Secular evolution processes, such as the formation and evolution of a bar component, instabilities due to spiral patterns, and general response of the stellar component to the radial rearrangement of stars and gas, are meant to gradually reshape the galaxies and their observed properties (Kormendy & Kennicutt 2004).

This process accounts for the growth of bulges due to internal dynamical instabilities of the disk material such as bars, which are present in about 70% of nearby disk galaxies (Eskridge et al. 2000; Aguerri et al. 2009). The bar properties change due to interaction with mass components in the galaxy, affecting the evolution of the whole galaxy. These processes result either in the vertical instability of the bar itself (Combes & Sanders 1981; Debattista et al. 2004), or in the bar dissolution caused by the growth of a central mass concentration

(Hasan et al. 1993; Norman et al. 1996).

Non-axisymmetric galaxy structures support the gas flow into the bulge region of the galaxy and the associated increase of the central mass density, being very efficient in re-organizing disk material (Pfenniger & Norman 1990; Friedli & Benz 1995). In particular, spiral patterns are responsible for redistributing angular momentum and causing an increase of the random motions of the stars; moreover, they provide a smoothing of the small-scale irregularities of the mass distribution and determine extensive radial mixing of both the gas and star components (Sellwood 2014). Finally, satellite accretion triggered by the environment rather than internally and resulting inward inflow of disk material to the bulge region are somehow considered to be secular process as well (Kormendy & Kennicutt 2004; Eliche-Moral et al. 2006).

Internal secular evolution processes are thought to be responsible of producing bulges with disk-like features (Kormendy 2016). Indeed, these bulges have to retain a memory of their disky origin, resembling flattened oblate spheroids. Moreover, they will present correspondingly large ratios of ordered to random velocities, being dominated by rotation (Kormendy & Kennicutt 2004).

■ 1.3 Observed properties of galactic bulges

The current paradigm separates galactic bulges into two broad categories, namely classical and disk-like bulges (Athanassoula 2005). Recently, Fisher & Drory (2016) reviewed the observed properties of bulges in nearby galaxies extending the criteria provided by Kormendy & Kennicutt (2004). In this Section we discuss the most probable formation scenarios for various bulge types; moreover, we describe in detail the photometric, kinematic, and stellar population properties that are usually adopted to discriminate them in modern literature.

1.3.1 Classical bulges

The term classical refers to the general historic belief that bulges were thought to resemble small elliptical galaxies in the center of disk galaxies (Wyse et al. 1997). For this reason, they were initially thought to be the result of destructive events in the history of galaxies such as a gravitational collapse (Toomre 1977, but see also Merlin & Chiosi 2006). Major and

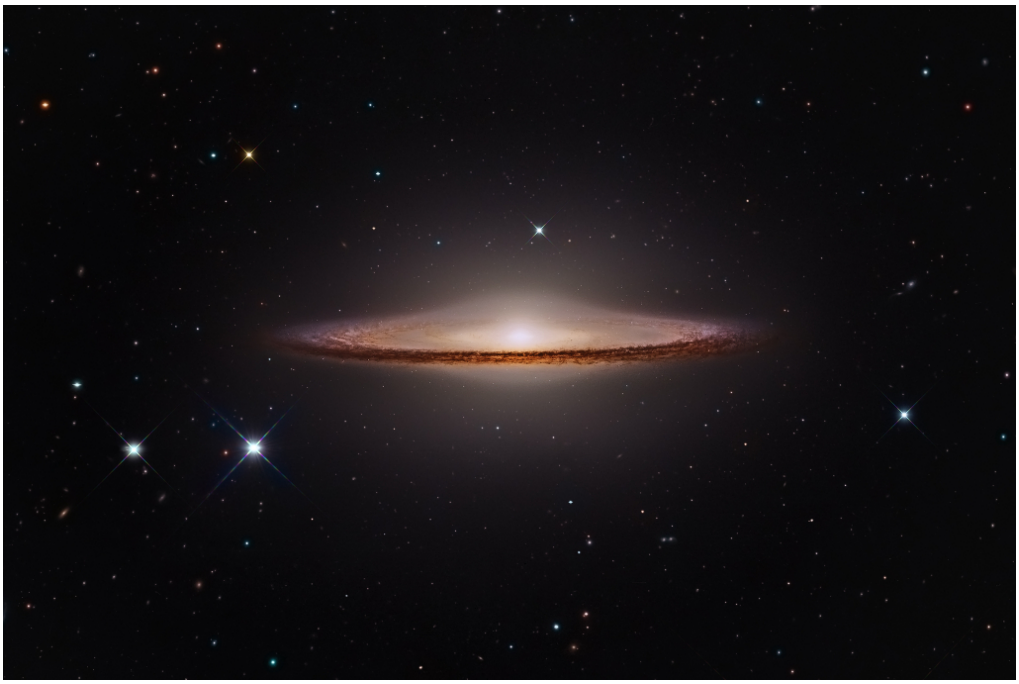

Figure 1.2: Classical bulge in NGC 4594 (Sombrero galaxy). Credits: NASA, ESO, NAOJ.

minor merger events (Cole et al. 2000; Aguerri et al. 2001; Hopkins et al. 2009) or recurring coalescence of long-lived giant star-forming clumps at high redshift was later proposed as a mechanism for the formation of classical bulges (Dekel et al. 2009; Ceverino et al. 2015). The rapid formation of classical bulges occurred in the early stage of galaxies evolution, before the build up of the disk component (Sommer-Larsen et al. 2003), even if it is possible that the disk was already formed at the time of the bulge growth (Noguchi 1999; Fu et al. 2003).

As a matter of fact, classical bulges share some properties with elliptical galaxies and are characterized by rounder shapes than their surrounding disks (see Fig. 1.2), although they present different mass-size relations (Gadotti 2009). The common understanding is that classical bulges show no evidence of disk-like structures such as spiral arms, nuclear rings, or bar components (see Fisher & Drory 2016, for a review).

The luminosity of classical bulges is correlated with their velocity dispersion (Kormendy & Cornell 2004) similarly as for the well-known Faber-Jackson relation (FJR; Faber & Jackson 1976) valid for elliptical galaxies; moreover, dust lanes can also be found in the central region of classical bulges (Lauer et al. 2005). The surface-brightness radial profile of classical bulges is usually fit with a Sérsic law (Sérsic 1968) with high Sérsic index (Scannapieco &

Tissera 2003; Tissera et al. 2006), mimicking the $r^{1/4}$ profile used for elliptical galaxies (Andredakis et al. 1995; Möllenhoff & Heidt 2001). Fisher & Drory (2008) found that bulges, which are morphologically classified *a priori* as classical, systematically show a Sérsic index $n > 2$ (but see Chapter 4, for different results).

Classical bulges present a strongly peaked velocity dispersion profile, having $d\log(\sigma)/d\log(r) < -0.1$ (Fabricius et al. 2012). Moreover, this class of objects is consistent with being isotropic oblate rotators (Kormendy & Illingworth 1982). They are consistent with the fundamental plane (FP; Djorgovski & Davis 1987), Kormendy (KR; Kormendy 1985), and FJ relations (Bender et al. 1992; Aguerri et al. 2005), as defined for elliptical galaxies.

Several simulations reproduce the red-sequence position in the color-magnitude diagram of classical bulges (Steinmetz & Muller 1995; Samland & Gerhard 2003), making them indiscernible from elliptical galaxies, with old and metal-rich stellar population (Thomas & Davies 2006; Drory & Fisher 2007). However, it is worth noting that, if a bulge is old and metal rich, this does not necessary mean that it is classical (Inoue & Saitoh 2012).

1.3.2 Disk-like bulges

As their name suggests, disk-like bulges are reminiscent of disks. Their formation is thought to be strongly correlated with galactic secular evolution mechanisms involving disk material. These processes of radial redistribution of gas and stars linked to the evolution of galactic substructures (e.g., bars, lenses, and ovals; see Kormendy 2016, for a review), or environmental phenomena, such as the accretion of low-density satellites (Eliche-Moral et al. 2011), can shape the central region of galaxies into disk-like bulges. Moreover, the fast disruption of short-lived giant clumps at high redshift can result in building up a central bulge with disk-like properties (Hopkins et al. 2012; Bournaud 2016).

Because of their similarity with disk structures, they are supposed to be highly flattened and axisymmetric objects (see Fig. 1.3). Their disk-like origin can result in substructures typical of disks, such as spiral arms, rings, intense star-forming regions, or dust lanes (Kormendy 1993; Kormendy & Kennicutt 2004). They are mainly found in low-density environments (Zhao 2012) and in gas-rich late-type galaxies (Carollo et al. 1998), even if they can

Figure 1.3: Disk-like bulge in NGC 3370. Credits: NASA, ESA, Hubble Heritage.

be also present in lenticular galaxies (Erwin et al. 2003; Laurikainen et al. 2007).

Disk-like bulges have nearly exponential surface brightness profiles, usually described with a Sérsic law with low value of Sérsic index ($n < 2$; Andredakis et al. 1995; Fisher & Drory 2008). Indeed, their limited contribution to the total luminosity of the galaxy is estimated to be always $B/T < 0.3$ (Fisher & Drory 2016).

Disk-like bulges present cold kinematics, mainly dominated by rotation and with a low degree of random motions (Kormendy et al. 2002); they are indeed rotationally supported oblate spheroids (Méndez-Abreu et al. 2010). Moreover, the shape of the velocity dispersion profile is considered one of the best way to identify a disk-like bulge, having $d\log(\sigma)/d\log(r) \geq -0.1$ and $\langle v^2\rangle/\langle\sigma^2\rangle \geq 0.35$ (Fabricius et al. 2012; Fisher & Drory 2016). Absorption lines can also be used to identify the bulge type, since disk-like bulges present a difference in the Mg line ($\Delta\mathrm{Mg\,b} < 0.7$ Å) compared either to the correlations of Mg b – σ_0 or Mg b – Fe valid for elliptical galaxies (Ganda et al. 2007).

Disk-like bulges tend to be low-σ outliers both in the KR (Gadotti 2009; Neumann et al. 2017) and in the FJR (Kormendy 2016). On the contrary, recent results by Costantin et al.

(2017) have revealed that the KR is a poor proxy of the bulge properties due to its large intrinsic scatter and magnitude bias (see Chapter 4, for all details). This mass bias was previously suggested by Nigoche-Netro et al. (2008, 2010).

Finally, disk-like bulges are, on average, composed by young stellar population, presenting similar colors to disks (Peletier & Balcells 1996), and occupy the so-called blue cloud in the color-magnitude diagram (Drory & Fisher 2007).

1.3.2.1 Pseudo-bulges

The term pseudobulge, widely spread in modern literature, is rather ambiguous at present. It was created having in mind the relaxed Universe where slow secular processes dominate the evolution of galaxies and galaxy mergers were not so relevant. Nowadays, numerous studies refer at pseudobulges describing either structures with morphological features such as dust lanes, spiral arms, rings, nuclear scale-bars, ovals, or boxy/peanut components (Kormendy & Kennicutt 2004; Fisher & Drory 2008); other authors describe pseudobulges as the central component with a Sérsic index $n < 2$ (Fisher & Drory 2016), or even any structure with $n < 4$ (Laurikainen et al. 2009); moreover, pseudobulges are also defined by means of a combination of their size and luminosity as the central galaxy component with a low value of surface brightness compared to the expected value for elliptical galaxies of the same size (Gadotti 2009).

The classification of galactic bulges based on their supposed formation mechanisms is probably still premature, though desirable. Given that, even if we consider that the observed properties of nearby bulges have to preserve the answer for their formation and evolution, the misuse of the term pseudobulge has lead to a chaotic picture for their characterization. Moreover, a combination of both photometric and kinematic properties, well represented in the FJR or in the FPR, is necessary to really understand the nature of different bulges. Finally, since we think that the result of secular evolution processes in galaxies is a central structure with flattening similar to that of the main galaxy disk and mainly dominated by ordered motions of its stars, the intrinsic shape of bulges can lead to an unbiased distinction of their formation scenario. Thus, we prefer to refer to such components in galaxies as disk-like bulges.

1.3.3 Boxy/peanut structures

There is large evidence in nearby galaxies of thick component swelling out of the disk plane which has a boxy, peanut, or a X shape (see Fig. 1.4; Burbidge & Burbidge 1959; Jarvis 1986). Indeed, more than 50% of edge-on galaxies, including our Galaxy (Dwek et al. 1995; Wegg & Gerhard 2013), show this boxy, peanut, or X-shape component in their central parts (Lütticke et al. 2000a,b). Although these structures are usually called boxy/peanut (B/P) bulges, this terminology could be misleading because they are just part of edge-on bars (Combes & Sanders 1981; Chung & Bureau 2004; Laurikainen & Salo 2016). In fact, the fraction of barred galaxies is consistent with that of edge-on galaxies with B/P structures (Eskridge et al. 2000). Moreover, numerical simulations of stellar orbits confirmed that B/P structures are connected to bars (Bureau & Athanassoula 2005; Athanassoula 2013) and photometric and kinematic observations showed that B/P structures share the same properties as bars (Méndez-Abreu et al. 2008b; Erwin & Debattista 2013).

B/P structures are the result of secular evolution processes of bars, in which vertical instabilities redistribute the stellar orbits in the characteristic boxy or peanut shape (Raha et al. 1991; Martinez-Valpuesta et al. 2006). In particular, numerical simulations state that a combination of buckling and resonant star scattering are responsible of heating the bar in the vertical direction (Shen et al. 2010).

Structural photometric decompositions allowed the interpretation of B/P components as bars; the surface brightness of B/P structures can be fit with a Sérsic law consistent with an exponential profile (Kormendy et al. 2010). The contribution of B/P components can represent an important fraction of their host galaxies mass (e.g., $B_{\rm BP}/T \sim 0.4$ in NGC 4565).

B/P structures show cylindrical velocity fields (Williams et al. 2011), with a low degree of velocity dispersion except for a central weak peak (Shaw 1993; Bureau et al. 2006). The analysis of the position-velocity diagram from emission and absorption lines reveals that edge-on B/P structures present a particular figure-of-eight structure in the line-of-sight velocity distribution (LOSVD), due to different values of velocities at the same radius (Kuijken & Merrifield 1995; Vega Beltrán et al. 1997), which is another confirmation of the bar nature of B/P structures.

The analysis of the bulge stellar population of barred and unbarred galaxies, considering

Figure 1.4: Boxy/peanut structure in NGC 4565. Credits: NOAO, AURA, NSF.

both face-on (Sánchez-Blázquez et al. 2014) and edge-on systems (Jablonka et al. 2007), shows no differences in metallicity or age gradients. B/P structures in early-type disk galaxies show an old stellar population similar to elliptical galaxies, even if they lack the correlation between the velocity dispersion and metallicity gradient, which is typical for elliptical galaxies (Williams et al. 2011).

1.3.4 Composite bulges

The whole picture of galactic bulges is further complicated by the coexistence of classical and disk-like bulges in the same galaxy (Gadotti 2009) and their combination with B/P structures in barred galaxies (Méndez-Abreu et al. 2014). Erwin et al. (2015) have recently demonstrated that a single galaxy can present a round and kinematically hot stellar system – the classical bulge – embedded into a more flattened object dominated by rotational motions – the disk-like bulge. Other examples of structural photometric decomposition of composite bulges were carried out by Kormendy & Barentine (2010) and Barentine & Kormendy (2012). They analyzed the surface brightness profile of the bulge component in NGC 4565 with

separate Sérsic functions for both a B/P component and a disk-like bulge. In NGC 4565, the B/P structure and disk-like bulge are not mutually exclusive, with the first one contributing 40% to the total light of the galaxy ($B_{\rm BP}/T \sim 0.4$) compared to the smaller contribution of the disk-like bulge ($B_{\rm disk}/T \sim 0.06$). Moreover, de Lorenzo-Cáceres et al. (2012) revealed the presence of a composite bulge in their detailed analysis of the double-barred galaxy NGC 357, which is characterized by a central decoupled structure that rotates faster than its surroundings. Finally, the presence of the bar component (interpreted as B/P structure) in galaxies with composite bulges (classical and disk-like; Erwin et al. 2015) makes possible the coexistence of the three types of bulges, as also suggested by Athanassoula (2005).

■ 1.4 Aim and content of the thesis

In this thesis we focus on the description of the bulge component in nearby galaxies from an observational point of view. We aim to properly interpret how observed properties of galactic bulges provide evidences of different mechanisms responsible for their formation and evolution. Indeed, the separation of bulge types according to their observed properties has become a common task in extragalactic astronomy, even if there are no unambiguous ways of doing it yet. A series of open questions still remain unanswered: *Do bulges share the same properties all along the Hubble sequence? Which is their three-dimensional shape? Is there any feature that uniquely characterizes them as classical or disk-like?* In order to answer these questions, we plan to describe how the observed properties of bulges in nearby galaxies allow to distinguish physical processes involved in their formation and evolution from the most accurate perspective.

Throughout this thesis, we analyze both the photometric and kinematic properties of bulges in nearby galaxies. We want to push the limits of the scaling relations studied so far to the very low-σ regime describing small bulges at the end of the Hubble sequence. Furthermore, the complete description of the bulge structural properties results in the characterization of the bulge three-dimensional shape. We propose the intrinsic shape of the bulge as the most solid marker of its evolutionary process, once combined with the dynamical information retrieved from its two-dimensional photometry and kinematics. The thesis is organized as follows.

Chapter 2. We present the technical procedures followed to characterize the structural properties of the bulge component as well as to determine its three-dimensional shape. We elucidate how the photometric algorithm allows to describe the surface brightness distribution of galaxies. Moreover, we revise and fine-tune the procedures and methods adopted to constrain the three-dimensional shape of bulges, detailing both the geometrical and statistical analysis.

Chapter 3. We describe the two-dimensional multi-component photometric decomposition of 404 galaxies from the Calar Alto Legacy Integral Field Area (CALIFA) data release 3 (DR3). We provide the community with an accurate photometric characterization of the multiple stellar structures shaping the CALIFA galaxies, describing them with the suitable combination of a nuclear point source, bulge, single or double bar, and pure exponential or double-exponential disk component. Indeed, we use a human-supervised approach to evaluate the optimal number of structures to be accounted for fitting the surface brightness distribution. We release the photometric parameters of the CALIFA galaxies, together with statistical errors and a visual analysis of the quality of each fit.

Chapter 4. We investigate whether small bulges of late-type spiral galaxies follow the same scaling relations traced by elliptical galaxies and large bulges. A global understanding of bulge properties all along the Hubble sequence might allow to understand the evolution of their different observed properties. To this aim, we derive the photometric and kinematic properties of 9 nearby late-type spiral galaxies. We analyze the i-band images of the Sloan Digital Sky Survey (SDSS) of these galaxies to characterize the structural parameters of their bulges by means of a two-dimensional photometric decomposition. We measure the line-of-sight stellar velocity distribution within the bulge effective radius from the long-slit spectra taken with high spectral resolution at the Telescopio Nazionale Galileo. Finally, we combine the photometric and kinematic information of the sample bulges to study their location in the fundamental plane, Kormendy, and Faber-Jackson relations defined for elliptical galaxies and large bulges.

Chapter 5. We want to derive accurate constraints to the intrinsic shape of bulges to provide new clues on their formation mechanisms and set new limitations for future simulations. Firstly, we take advantage of numerical simulations to estimate the reliability of the procedure. Thus, we create a set of mock SDSS i-band images at different galaxy inclinations for a set of simulated galaxies, that closely resembling lenticular galaxies. We perform a two-dimensional photometric decomposition of all the mock images applying the same procedure as for real galaxies, in order to characterize the geometrical parameters of bulge and disk which we use to recover the bulge intrinsic shape. Secondly, we obtain the intrinsic shape of 83 bulges from the CALIFA survey. We introduce the (B/A, C/A) diagram to analyze possible correlations between the intrinsic shape and properties of bulges.

Chapter 6. We discuss the observational criteria usually applied to discriminate bulge types in classical and disk-like spheroids. To this aim, we fully characterize the photometry, stellar kinematics, line-strength indices, and intrinsic shape of the bulge in nine lenticular galaxies from the ATLAS^{3D} survey. We apply all the observed diagnostics commonly adopted in recent works and test their efficiency in identifying classical and disk-like bulges in our sample of carefully selected galaxies.

Chapter 7. We summarize the conclusions obtained throughout this thesis, illustrating future research lines opened by this work.

2

INTRINSIC SHAPE OF GALACTIC BULGES

We provided an accurate review of the technical procedures used to obtain the results presented in this thesis. In this way we aimed to condense all the technical background in order to concentrate mainly on the science goal of our analysis in the following Chapters. The description of these methods result in crucial understanding of all the details and possible limitations of the data analysis as well as the potential value of such tools. Moreover, we revised and fine-tuned here procedures and methods already applied in previous studies (Méndez-Abreu et al. 2008a, 2010), in light of the increasing of our knowledge in dealing with photometric decomposition analyses and probabilistic considerations on the nature of bulge shape.

2.1 Two-dimensional photometric decomposition

A large number of two-dimensional photometric decomposition algorithms have been developed in the last two decades based on different minimization routines. We would like to highlight, among others: Galaxy IMage 2D (GIM2D; Simard 1998), GALFIT (Peng et al. 2002), Multi-Gaussian Expansion (MGE Cappellari 2002), BUlge/Disk Decomposition Analysis (BUDDA de Souza et al. 2004), Galaxy Automated Surface PHOTometry (GASPHOT; Pignatelli et al. 2006), GAlaxy Surface Photometry 2 Dimensional decomposition (GASP2D; Méndez-Abreu et al. 2008a, 2014), Galaxy IMage FITting (IMFIT; Erwin 2015), and bayesian Profile Fitting of galaxy images (ProFit; Robotham et al. 2017). These methods address the question of how the light is distributed in galaxies, and how their geometric parameters (e.g., ellipticity ϵ and position angle PA) change in a two-dimensional framework. Indeed, only a two-dimensional photometric analysis allows to fully characterize the geometry of each galactic component.

Throughout this work we made use of the two-dimensional photometric code GASP2D, written in IDL[1]. The algorithm works like GIM2D and GASPHOT in minimizing the interaction with the user. It adopts a set of analytical functions to model the light contribution of the galaxy components and it is efficient in dealing with a large sample of galaxies. Moreover, like GALFIT, the two-dimensional surface brightness of the galaxies is fit adopting a Levenberg-Marquardt algorithm (Moré et al. 1980) using the IDL task MPFIT (Markwardt 2009), optimized to reduce the computational time needed to obtain robust and reliable estimates of the galaxy structural parameters. The user interaction with the GASP2D code consists in a series of initial information about the galaxy model and galaxy image. In the first Section of this Chapter we will guide the reader through the fitting_file list that allows the user to interact with the source algorithm. As an example, we took into account the case of the spiral galaxy NGC 180 in g band, as studied in Chapter 3 (see also Méndez-Abreu et al. 2017, for details). The image of NGC 180 is taken from the SDSS DR7 (Abazajian et al. 2009).

[1]Interactive Data Language is distributed by ITT Visual Information Solutions. It is available from http://www.ittvis.com.

2.1.1 Multi-component analysis of galaxy surface brightness

The surface brightness distribution of a galaxy can be assumed to be the sum of a combination of a bulge, a disk, a primary and/or secondary bar, and a nuclear point source (NPS). Currently, we did not consider any other additional component, such as spiral arms, lenses, or ovals. Actually, whenever possible we masked their corresponding regions in the galaxy images in order to exclude them from the fitting process. The user defines which structural components are used to model the given galaxy using an external file (fitting_file) that can be modified before performing the decomposition (see the gray colorbox below, for an example). In particular, the galaxy NGC 180 is composed by three components, that is, a bulge, a disk and a primary bar:

```
Fit the bulge (0 → no, 1 → yes)
1
Fit the disk (0 → no, 1 → yes)
1
Fit a Type II/III exponential disk profile (0 → no, 1 → yes)
0
Fit the bar (0 → no, 1 → yes)
1
Fit a secondary bar (0 → no, 1 → yes)
0
Fit Nuclear Source (0 → no, 1 → yes)
0
```

The Sérsic profile (Sérsic 1968) is used to describe the surface brightness distribution of the bulge component

$$I_{\rm bulge}(x,y) = I_{\rm e} 10^{-b_n\left[\left(\frac{r_{\rm bulge}(x,\,y)}{r_{\rm e}}\right)^{1/n}-1\right]}, \tag{2.1}$$

where $r_{\rm e}$ is the effective radius, $I_{\rm e}$ is the surface brightness at $r_{\rm e}$, n is a shape parameter

describing the curvature of the surface brightness profile, and $b_n = 0.868n - 0.142$ (Caon et al. 1993). A profile with the Sérsic index $n = 4$ corresponds to the $r^{1/4}$ model (de Vaucouleurs 1948) traditionally used to describe bright elliptical galaxies, while a profile with $n = 1$ corresponds to a pure exponential model. In addition, the bulge isophotes are assumed to be elliptical and centered on the galaxy center (x_0, y_0) with constant position angle $PA_{\rm bulge}$ and constant axial ratio $q_{\rm bulge} = 1 - \epsilon_{\rm bulge}$. The radius $r_{\rm bulge}$ is given by

$$r_{\rm bulge}(x, y) = \Big[(-(x - x_0)\sin PA_{\rm bulge} + (y - y_0)\cos PA_{\rm bulge})^2 + ((x - x_0)\cos PA_{\rm bulge} + (y - y_0)\sin PA_{\rm bulge})^2 / q_{\rm bulge}^2 \Big]^{1/2} \tag{2.2}$$

and the total luminosity of the bulge is given by

$$L_{\rm bulge} = 2\pi q_{\rm bulge} \int_0^\infty I_{\rm bulge}(r) r dr = 2\pi I_{\rm e} r_{\rm e}^2 n e^{b_n} q_{\rm bulge} \frac{\Gamma(2n)}{b_n^{2n}}\,, \tag{2.3}$$

where $\Gamma(2n)$ is the complete gamma function (Abramowitz & Stengun 1964). This law is extensively used in the literature to model the surface brightness of elliptical galaxies (Capaccioli et al. 1987; Graham & Guzmán 2003), bulges of early- and late-type galaxies (Morelli et al. 2016; Méndez-Abreu et al. 2017; Costantin et al. 2017), low surface brightness of blue compact galaxies (Caon et al. 2005; Papaderos et al. 1996; Amorín et al. 2007), and dwarf elliptical galaxies (Binggeli & Jerjen 1998; Aguerri et al. 2005; Graham & Guzmán 2003).

GASP2D allows the user to keep each bulge parameter either free to vary or fixed at a given value:

Bulge effective intensity (0 → fixed, 1 → variable)

1

Bulge effective radius (0 → fixed, 1 → variable)

1

Bulge Sérsic parameter n (0 → fixed, 1 → variable)

1

Bulge ellipticity (0 → fixed, 1 → variable)

1

Bulge position angle (0 → fixed, 1 → variable)

1

The exponential law (Freeman 1970) is commonly used to describe the surface brightness distribution of the disk component. However, recent studies of the light distribution in the fainter part of the disk profile have highlighted three different behaviors (Erwin et al. 2005; Pohlen & Trujillo 2006): (i) the profiles of Type I disks remain unchanged along the whole optical extent of the galaxy; (ii) Type II profiles present a down-bending beyond the so-called break radius; (iii) Type III profiles exhibit an up-bending in the outer parts of the galaxy. Type I disks are described with a single exponential profile, while Type II and Type III profiles are parametrized with a double-exponential law.

The general description of the disk is given by

$$I_{\rm disk}(x,\,y) = I_0 \left[e^{-\frac{r_{\rm disk}(x,\,y)}{h}} \zeta + e^{-\frac{r_{\rm break}(h_{\rm out}-h)}{h_{\rm out}h}} e^{-\frac{r_{\rm disk}(x,\,y)}{h_{\rm out}}} (1-\zeta) \right], \tag{2.4}$$

where

$$\zeta = \begin{cases} 1 & \text{if } r_{\rm disk} < r_{\rm break} \\ 0 & \text{if } r_{\rm disk} > r_{\rm break} \end{cases}, \tag{2.5}$$

and I_0, h, $h_{\rm out}$, and $r_{\rm break}$ are the central surface brightness, the inner scale length, the outer scale length, and the break radius of the disk, respectively. This simple description of the break of exponential disks is adopted in order to minimize the number of free parameters involved in the fitting process, even if more elaborate functions have been proposed in the literature (e.g., Peng et al. 2010; Erwin 2015). The disk component is assumed to have elliptical isophotes centered on the galaxy center $(x_0,\,y_0)$, a constant position angle $PA_{\rm disk}$

and axial ratio $q_{\rm disk} = 1 - \epsilon_{\rm disk}$. The radius $r_{\rm disk}$ is given by

$$r_{\rm disk}(x,\, y) = \Big[(-\,(x - x_0)\sin PA_{\rm disk} + (y - y_0)\cos PA_{\rm disk})^2 + ((x - x_0)\cos PA_{\rm disk} + (y - y_0)\sin PA_{\rm disk})^2 / q_{\rm disk}^2 \Big]^{1/2} \tag{2.6}$$

and the total luminosity of the disk is given by

$$\begin{aligned} L_{\rm disk} &= 2\pi q_{\rm disk} \int_0^\infty I_{\rm disk}(r) r dr \\ &= 2\pi I_0 h^2 q_{\rm disk} \left(1 + e^{r_{\rm break}\left(\frac{1}{h_{\rm out}} - \frac{1}{h}\right)} \right) . \end{aligned} \tag{2.7}$$

GASP2D allows the user to keep each disk parameter either free to vary or fixed at a given value:

Disk central intensity (0 → fixed, 1 → variable)

1

Disk scale length (0 → fixed, 1 → variable)

1

Disk scale length outer (0 → fixed, 1 → variable)

0

Disk break radius (0 → fixed, 1 → variable)

0

Disk ellipticity (0 → fixed, 1 → variable)

1

Disk position angle (0 → fixed, 1 → variable)

1

The relative light fraction contributed by the bulge and disk is relevant to the study of galaxy structure. This can be expressed in terms of the bulge-to-disk luminosity ratio B/D, derived by integrating the bulge and disk luminosity profiles to infinity. The B/D is a very useful parameter widely used to characterize galaxies properties (i.e., morphological type,

mass, and size; Weinzirl et al. 2008; Graham & Worley 2008). It can be expressed as

$$\frac{B}{D} = \frac{I_{\rm e} n e^{b_n} \Gamma(2n)}{I_0 b_n^{2n} \left(1 + e^{r_{\rm break}\left(\frac{1}{h_{\rm out}} - \frac{1}{h}\right)} \right)} \left(\frac{q_{\rm bulge}}{q_{\rm disk}} \right) \left(\frac{r_{\rm e}}{h} \right)^2 , \tag{2.8}$$

using Eq. 2.3 and Eq. 2.7.

The surface brightness of the bar is described in three different ways, either using the projected surface density of a three-dimensional Ferrers ellipsoid (Ferrers 1877, see also Aguerri et al. 2009), or a flat profile (Prieto et al. 1997), or an elliptical profile (Freeman 1966):

Select the model for the bar (0 → Ferrers, 1 → Flat, 2 → Elliptical)

0

Select the model for the secondary bar (0 → Ferrers, 1 → Flat, 2 → Elliptical)

0

The Ferrers surface brightness profile is described as

$$I_{\rm bar}^{\rm Ferrers}(x,\, y) = \begin{cases} I_{0,\,\rm bar} \left[1 - \left(\dfrac{r_{\rm bar}(x,\, y)}{a_{\rm bar}} \right)^2 \right]^{n_{\rm bar}+0.5} & \text{if } r_{\rm bar} \leq a_{\rm bar} \\ 0 & \text{if } r_{\rm bar} > a_{\rm bar} \end{cases} , \tag{2.9}$$

where $I_{0,\,\rm bar}$ represents the central surface brightness, $a_{\rm bar}$ is the length, and $n_{\rm bar}$ is the shape parameter of the bar.

The flat surface brightness profile is described as

$$I_{\rm bar}^{\rm flat}(x,\, y) = I_{0,\,\rm bar} \left(\frac{1}{1 + e^{\dfrac{r_{\rm bar}(x,\, y) - a_{\rm bar}}{r_{\rm s}}}} \right) , \tag{2.10}$$

where $I_{0,\,\rm bar}$ and $a_{\rm bar}$ represent the central surface brightness and length of the bar, respectively; the surface brightness profile falls of with a scalelength $r_{\rm s}$ for radii larger than $r_{\rm bar}$ (Prieto et al. 1997).

Finally, the elliptical surface brightness profile is described as

$$I_{\rm bar}^{\rm Freeman}(x,\,y) = I_{0,\,\rm bar}\sqrt{1-\left(\frac{r_{\rm bar}(x,\,y)}{a_{\rm bar}}\right)^2}\,, \tag{2.11}$$

where $I_{0,\,\rm bar}$ and $a_{\rm bar}$ represent again the central surface brightness and length of the bar, respectively.

The isophotes of the bar are assumed to be generalized ellipses (Athanassoula et al. 1990) centered on the galaxy center $(x_0,\,y_0)$ with constant position angle $PA_{\rm bar}$ and constant axial ratio $q_{\rm bar} = 1 - \epsilon_{bar}$. The $r_{\rm bar}$ radius is defined as

$$\begin{aligned} r_{\rm bar}(x,\,y) = \Bigg[& \left|\,(y-y_0)\cos PA_{\rm bar} - (x-x_0)\sin PA_{\rm bar}\right|^c \\ & + \left|\,((x-x_0)\cos PA_{\rm bar} + (y-y_0)\sin PA_{\rm bar})\,/q_{\rm bar}\right|^c \Bigg]^{1/c}\,, \end{aligned} \tag{2.12}$$

where c controls the shape of the bar isophotes; $c = 2$ corresponds to a bar with pure elliptical isophotes, while $c < 2$ and $c > 2$ describe an ellipsoid with disky and boxy isophotes, respectively. This serves the same purpose as the $\cos 4\theta$ Fourier coefficient, which is usually adopted to describe the boxiness/diskyness of the isophotes (Jedrzejewski 1987; Bender & Moellenhoff 1987). The total luminosity of the Ferrers bar profile is given by

$$\begin{aligned} L_{\rm bar}^{\rm Ferrers} &= 2\pi q_{\rm bar}\int_0^\infty I_{\rm bar}(r) r dr \\ &= \pi I_{0,\,\rm bar}\frac{r_{\rm bar}^2 q_{\rm bar}}{R(c)}\frac{\Gamma(n_{\rm bar}+1.5)}{\Gamma(n_{\rm bar}+2.5)}\,, \end{aligned} \tag{2.13}$$

where

$$R(c) = \frac{\pi(c-2)}{4\,\beta\left(\dfrac{1}{c-2},\,1+\dfrac{1}{c-2}\right)} \tag{2.14}$$

accounts for the shape of the isophotes.

It is well known that in a multi-component representation of the galaxy it is crucial to include the bar in order to retrieve the correct bulge parameters. In fact, both the bulge-to-disk luminosity ratio and the Sérsic index can be overestimated if the bar is not properly accounted for (Aguerri et al. 2005; Gadotti 2009; Méndez-Abreu et al. 2014). Moreover, it is important to mention that the shape parameter of the bar $n_{\rm bar}$ introduces a high degree of

degeneracy in the parameters space. Thus, it is sometimes kept as a fixed parameter during the fitting process. The default value usually used is $n_{\rm bar} = 2$ (see also Laurikainen et al. 2005; Méndez-Abreu et al. 2017).

GASP2D allows the user to keep each bar parameter either free to vary or fixed at a given value:

Bar central intensity (0 → fixed, 1 → variable)
1
Bar length (0 → fixed, 1 → variable)
1
Bar scale length (0 → fixed, 1 → variable)
- only for the flat profile -
0
Bar shape parameter (0 → fixed, 1 → variable)
- only for the Ferrers profile -
0
Bar generalized ellipse shape parameter C (0 → fixed, 1 → variable)
0

Bar ellipticity (0 → fixed, 1 → variable)
1
Bar position angle (0 → fixed, 1 → variable)
1

The same conditions apply also if a secondary bar component is added to the model.

The NPS is modeled using a Moffat function mimicking the circular point spread function (PSF) of the galaxy image

$$I_{\rm nps}(x,y) = I_{0,\,\rm nps}\left(1+\left(\frac{r_{\rm nps}(x,\,y)}{\alpha}\right)^2\right)^{-\beta}, \tag{2.15}$$

where $I_{0,\,\rm nps}$ is the central surface brightness of the NPS; the parameters α and β define the profile shape and are related to the full width at half maximum (FHWM) such that

$FWHM = 2\alpha\sqrt{2^{1/\beta} - 1}$. The $r_{\rm nps}$ radius is given by

$$r_{\rm nps}(x,\, y) = \sqrt{x^2 + y^2}\,, \tag{2.16}$$

while the total luminosity of the NPS profile is given by

$$\begin{aligned} L_{\rm nps} &= 2\pi \int_0^\infty I_{\rm nps}(r) r dr \\ &= 2\pi I_{0,\,\rm nps} \frac{\alpha^2}{2(\beta - 1)} \end{aligned} \quad . \tag{2.17}$$

GASP2D allows the user to keep the NPS intensity either free to vary or fixed at a given value:

Central nuclear point source intensity (0 → fixed, 1 → variable)
0

As for the bar component, several works have recently pointed out the importance of including a NPS to properly derive the bulge parameters when the galaxy host nuclear stellar clusters (NSCs, Balcells et al. 2007) or active galactic nuclei (AGNs, Benítez et al. 2013). However, in this work (e.g., Chapter 3) the inclusion of a NPS does not intend to model an extra component (NSC, AGN) but rather to model an unresolved bulge with a size comparable to the image PSF. Indeed, this can lead to erroneous results, usually producing extreme values of the Sérsic index ($n > 7$). Therefore, the use of a NPS in the modeling of a galaxy rules out the simultaneous fitting with a bulge component. Although one of our aims is giving solid estimates of the bulge parameters, high values of n might also have a significant impact on disk or bar parameters. Therefore, we preferred to fit these galaxies using a NPS instead of the Sérsic parameterization for the bulge. A visual inspection of the two-dimensional residual is used to determine whether the final fit is reliable (see Section 3.5.1 for further details).

Finally, besides each substructure parameter, also the galaxy center (x, y) can either be kept fixed at a given value or free to vary:

Galaxy x center (0 $\rightarrow$ fixed, 1 $\rightarrow$ variable)

1

Galaxy y center (0 $\rightarrow$ fixed, 1 $\rightarrow$ variable)

1

2.1.2 Image analysis and fitting procedure

A detailed analysis of the galaxy images is fundamental in order to accomplish the most accurate photometric decomposition and to properly weight the structural parameters. Regarding the instrumental setup for the science images, the Readout Noise (RON) and gain of the Charge-coupled device (CCD) are required to create the image that describes the instrumental noise:

Readout noise (e^-)

5.44725

Gain (e^-/ADU)

4.035

2.1.2.1 Sky background

The study of the faintest part of disk galaxies highlighted the necessity to properly account for the sky background estimation (Méndez-Abreu et al. 2017; Pagotto et al. 2017). The sky estimation provided for all the images in the SDSS archive (i.e., the median value of every pixel after a σ-clipping is applied), has been proved to be insufficient (Pohlen & Trujillo 2006; Hyde & Bernardi 2009). We applied the sky subtraction procedure introduced by Pohlen & Trujillo (2006) and used in the recent work of Corsini et al. (2017). After masking all the foreground stars, companion and background galaxies, and spurious sources, such as residual cosmic rays and bad pixels close to the galaxy, we measured the surface-brightness radial profile of the galaxy with the `ellipse` task in IRAF[2] (Jedrzejewski 1987).

[2]IRAF is distributed by the National Optical Astronomy Observatory, which is operated by the Association of Universities for Research in Astronomy (AURA) under cooperative agreement with the National Science Foundation.

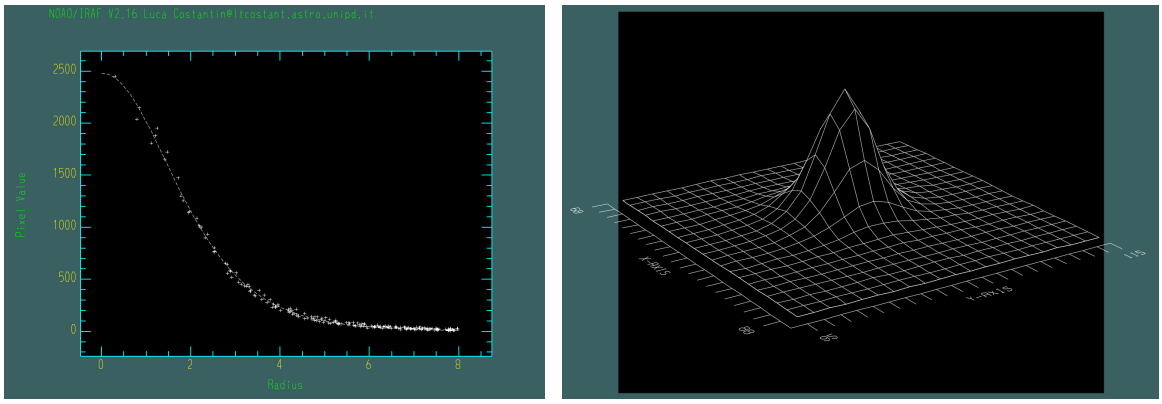

Figure 2.1: Two-dimensional (*left panel*) and three-dimensional (*right panel*) PSF for a background star in the image frame as obtained from the IRAF task `imexamine`.

First, the center, ellipticity, and position angle of the fitting ellipses were allowed to vary. Then, fitting again the isophotes, we adopted the center of the inner ellipses and the ellipticity and position angle of the outer ellipses. Finally, a constant value of the surface brightness measured at large radii, where the galaxy contributed no light, was assumed as the sky level to be subtracted from each science frame. The standard deviation $\sigma_{\rm sky}$ of the background in the sky-subtracted image was calculated by analyzing several regions, where no sources were present with the IRAF task `imexamine`. The user has to impose these values before the fitting procedure as:

Sky values (ADU)

64.9

Sky rms: $\sigma_{\rm sky}$ (ADU)

4.2

2.1.2.2 Point Spread Function

The PSF describes how a point source is seen by an imaging system. The ground-based images are mostly affected by atmospheric turbulence; the seeing scatters the light of astronomical objects and produces a loss of spatial resolution. In order to retrieve reliable structural parameters of the galactic bulge, which dominates the surface brightness profile at small radii, it becomes critical to accurately shape the PSF (Fig. 2.1). In particular, errors of 2% in the PSF FWHM produces variations up to 10% in $r_{\rm e}$ and n (Méndez-Abreu

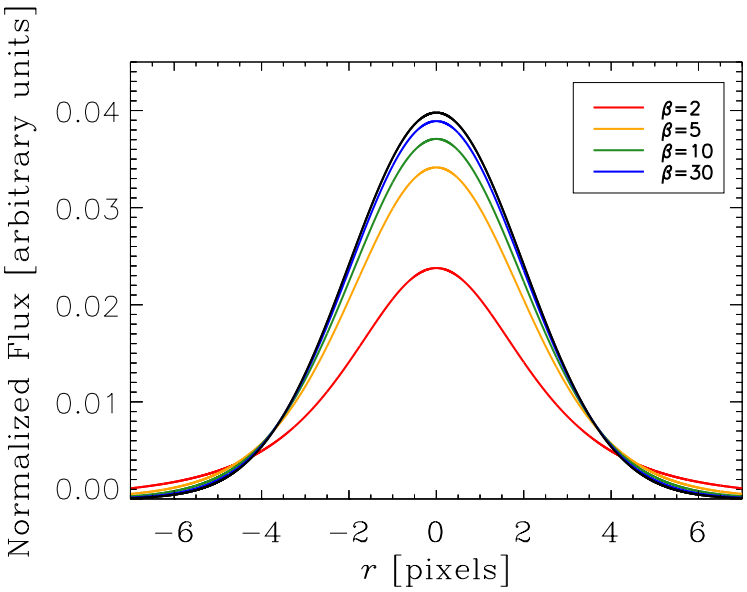

Figure 2.2: A Gaussian PSF (black line) is compared to different Moffat PSFs (blue, green, orange, and red lines). All the PSFs are computed with the same $FWHM = 4.7$ pixels; for the Moffat PSFs, different colors stand for different values of the β shape parameter (see Eq. 2.19).

et al. 2008a); moreover, the effective radius has to be larger than $\sim 80\%$ of the Half Width at Half Maximum ($\mathrm{HWHM_{PSF}}$) to obtain a reliable estimation (Gadotti 2008, but see also Chapter 4). Finally, Trujillo et al. (2001a,b) have extensively discussed the seeing effects on the surface brightness profile described by a Sérsic light distribution. In GASP2D, the model image of the galaxy is convolved with the adopted PSF during each interaction. GASP2D addresses this issue either using the Fourier transform or by solving directly the convolution integrals.

GASP2D allows the user to choose between three different PSFs. First, it is possible to select a two-dimensional Gaussian PSF modeled as

$$PSF_{\mathrm{Gauss}}(x,\, y) = \frac{1}{2\pi\sigma^2} e^{-\dfrac{r^2(x,\, y)}{2\sigma^2}}\,, \tag{2.18}$$

where the standard deviation σ is related to the FWHM as $FWHM = 2\sqrt{2\ln(2)}\sigma$. Second, a two-dimensional Moffat PSF modeled as

$$PSF_{\mathrm{Moffat}}(x,\, y) = \frac{\beta - 1}{\pi\alpha^2}\left(1 + \left(\frac{r(x,\, y)}{\alpha}\right)^2\right)^{-\beta}\,, \tag{2.19}$$

where the profile shape is defined by the parameters α and β. The relation between the FWHM and the shape parameters is $FWHM = 2\alpha\sqrt{2^{1/\beta} - 1}$. The Gaussian and Moffat functions differ mainly in the outer wings of the profile, indeed, when $\beta \to \infty$ the Moffat function becomes a Gaussian (Fig. 2.2). The PSF radius $r(x, y)$ is given by

$$r(x, y) = \sqrt{x^2 + y^2}\,. \tag{2.20}$$

Finally, an image of an user-supplied PSF is also allowed to perform the photometric decomposition:

Convolution: 0 → FFT, 1 → integrals
0
PSF: 0 → Gaussian, 1 → Moffat
1
PSF image name
none
If you select a Moffat function, enter the β parameter, if not → 0
3.848
PSF FWHM (in pixels)
3.616

We stressed that GASP2D is implemented to automatically normalize the total flux in all input PSFs in order to ensure the flux conservation in the convolution process.

2.1.2.3 Physical initial parameters

The science image can be trimmed in order to reduce the computing time to perform the two-dimensional photometric decomposition. Using the sky-subtracted trimmed images, we ran `ellipse` again allowing the isophotes to freely reproduce the values of surface brightness, ϵ, and PA. This allows to detect possible changes in the morphology. This task can be performed either automatically or manually within the algorithm itself, making GASP2D powerful in dealing with a large sample of galaxies:

Do you want to run `ellipse`? (0 → yes, 1 → no)

0

Do you want to run `ellipse` fitting automatically? (0 → yes, 1 → no)

0

Do you want to run `ellipse` on the model images? (0 → no, 1 → yes)

1

The ellipse-averaged surface brightness, ellipticity, and position-angle radial profiles are adopted to derive the guess values for the structural parameters by performing a standard one-dimensional photometric decomposition as in Kormendy (1977) or Prieto et al. (2001). Alternatively, the user can provide his own guesses for the initial parameters:

Initial guesses (0 → Automatic, 1 → Manual, 2 → File)

1

If initial guesses → 2 indicate the file name (e.g., ./2Dfit.fits)

2Dfit.fits

The one-dimensional photometric decomposition which defines the automatic initial guesses is done by fitting with GASP2D an exponential law to the radial surface brightness profile at large radii measured with `ellipse`; indeed, the fainter part of the light profile is expected to be dominated by the disk component. In this way, the algorithm retrieves the initial guesses for I_0 and h. Then, the fitted exponential profile is extrapolated to small radii and then subtracted from the initial radial profile; thus, the residual radial surface brightness profile is assumed to be an estimation of the bulge light distribution. The bulge component is fit with a Sérsic law, which provides the initial guesses for $r_{\rm e}$, $I_{\rm e}$, and n, respectively. The initial guesses on the geometrical parameters of the disk ($\epsilon_{\rm disk}$ and $PA_{\rm disk}$) are retrieved averaging the outermost region of the corresponding `ellipse` profile. Finally, the initial guesses on the geometrical parameters of the bulge ($\epsilon_{\rm bulge}$ and $PA_{\rm bulge}$) are estimated by interpolating their radial profiles at the effective radius.

Finally, the last aspect of the image analysis regards masking all spurious sources in the science frame, in order to avoid light contaminations. GASP2D allows the user either to adopt masks previously processed during the `ellipse` image preparation or to make the

algorithm itself to provide the mask through the photometric package `SExtractor` (Bertin & Arnouts 1996):

Do you want an automatic mask to run `ellipse`? (0 → yes, 1 → no)

1

Do you want to use this mask also in the two-dimensional fit? (0 → yes, 1 → no)

1

Flag image mask

0

Image mask name

none

Flag image weight

0

Image weight name

none

2.1.2.4 Two-dimensional fitting

In order to find the best solution in the parameter space, GASP2D iteratively fits a model of the raw intensity $I_{\rm mod}$ to the observations by means of a non-linear least-square minimization method (Bevington & Robinson 2003). The $I_{\rm mod}$ is assumed to be the sum of the intensity of all the components taken into account. All the free parameters are simultaneously adjusted minimizing the χ^2 residual between the data and model image. Being the model of the surface brightness distribution $I_{\rm mod}$ compared with the observed photon counts of the galaxy $I_{\rm obs}$ in each image pixel (x, y), the minimized χ^2 is

$$\chi^2 = \frac{1}{N_{\rm dof}} \sum_{x=1}^{N} \sum_{y=1}^{M} \frac{[I_{\rm mod}(x,y) - I_{\rm obs}(x,y)]^2}{\sigma_{\rm w}^2}\,, \tag{2.21}$$

where $N_{\rm dof}$ represents the number of the degrees of freedom, x and y range over the whole $N \times M$ pixels of the image and $\sigma_{\rm w}$ is the weight function. In GASP2D, two possible weight functions are considered to calculate the χ^2:

How do you want to weight each pixel? (0 → Poisson, 1 → Constant)

0

Indeed, some authors (e.g., Wadadekar et al. 1999; MacArthur et al. 2003) claim that the Poissonian noise better describes the uncertainties in each pixel by modeling the weight function as

$$\sigma_{\rm w} = I_{\rm obs}(x,y) + I_{\rm sky}(x,y) + {\rm RON}^2\,, \tag{2.22}$$

where the contribution of both the galaxy ($I_{\rm obs}$) and the sky ($I_{\rm sky}$) is taken into account. On the other hand, there are authors that prefer to apply a constant weight function (Möllenhoff & Heidt 2001; de Souza et al. 2004).

The two-dimensional fit can be performed on different apertures. The first option is to consider all the pixels within a fixed radius, while the second option is to consider all the pixels with an intensity level from the galaxy over the sky level according to a given threshold expressed in number of $\sigma_{\rm sky}$:

Fitting radius: 0 → Automatic, 1 → Fixed

0

Maximum fixed fitting radius

0

Number of σ over the $\sigma_{\rm sky}$ for the automatic radius

1.0

Finally, if either one side of the galaxy is dominated by dust or the science image does not contain the entire galaxy, the user can decide to reconstruct the image before the fit by symmetrizing it along the major axis:

$$\begin{cases} I(x,\,-y) = I(x,\,y) \\ I(-x,\,-y) = I(-x,\,y) \end{cases} \tag{2.23}$$

Do you want to symmetrize the images before the fit? (0 → yes, 1 → no)

0

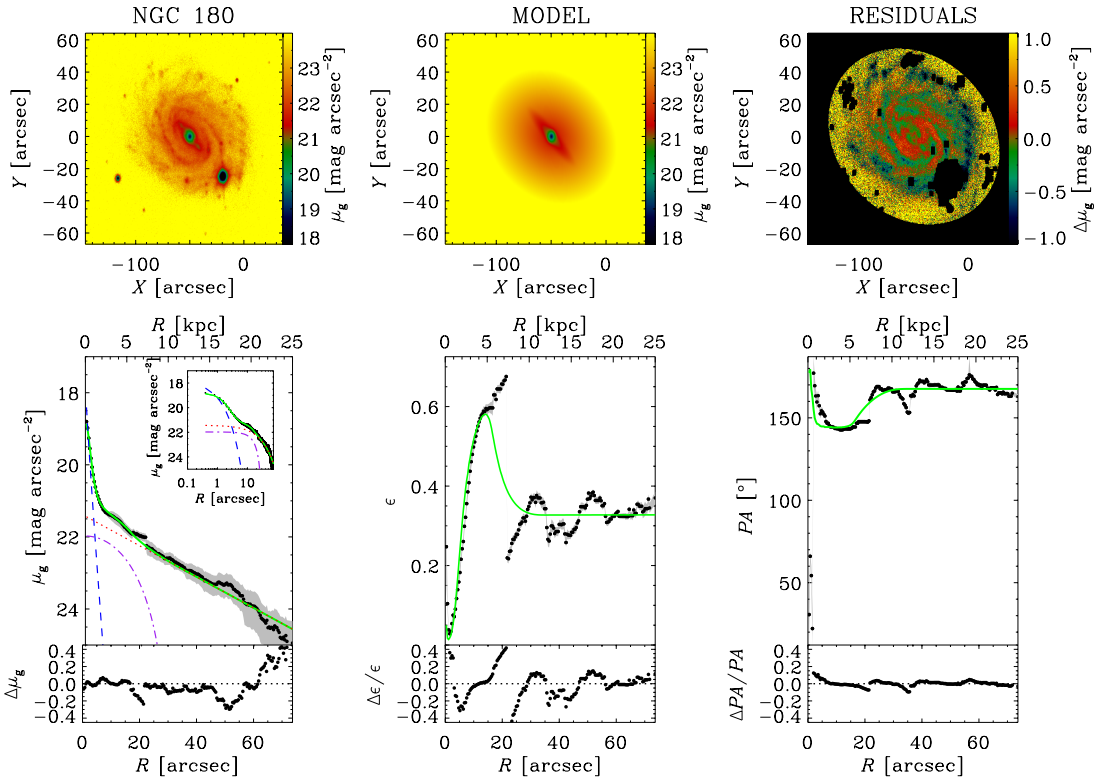

Figure 2.3: Example of two-dimensional photometric decomposition of the spiral galaxy NGC 180 in g band. The upper panels (*from left to right*) show the map of the observed, modeled, and residual (observed−modeled) surface-brightness distributions. The lower panels (*from left to right*) show the ellipse-averaged radial profile of surface brightness, ellipticity, and position angle measured in the observed (black dots with gray error bars) and seeing-convolved modeled image (green solid line) and their corresponding difference. The surface-brightness radial profiles of the best-fit bulge (blue dashed line) and disk (red dotted line) are also shown in both linear and logarithmic scale for the distance to the center of the galaxy.

The final output of GASP2D can be summarized in Fig. 2.3: the galaxy SDSS image in g band and the model are compared to obtain the residual image. Moreover, the trend of the radial ellipse-averaged surface brightness profile as well as the ellipticity and position-angle profiles of the galaxy are compared with the results from the model.

2.2 Three-dimensional shape of galactic bulges

The full description of the probabilistic scheme to derive the three-dimensional shape of bulges is described in Méndez-Abreu et al. (2010), while a summary of the major points is reported in the recent work by Costantin et al. (2018). For the sake of clarity we detailed here the main hypothesis.

2.2.1 Bulge and disk geometry

In order to characterize the intrinsic three-dimensional shape of the bulge we assumed it to be a triaxial ellipsoid with the same equatorial plane of the circular disk. Moreover, the bulge and disk share the same center, which coincides with the center of the galaxy.

Let $(x,\, y,\, z)$ be the Cartesian coordinates on the reference system of the galaxy. The origin of the system is in the galaxy center; the x-axis and y-axis corresponds to the bulge principal axes in the equatorial plane, while the z-axis corresponds to the bulge and disk polar axis. The equation of the bulge on its own reference system is given by

$$\frac{x^2}{A^2} + \frac{y^2}{B^2} + \frac{z^2}{C^2} = 1\,, \tag{2.24}$$

where A, B, and C are the intrinsic lengths of the bulge semi-axes.

Let $(x',\, y',\, z')$ now be the Cartesian coordinates on the reference system of the observer. The origin of the system is in the galaxy center; the polar z'-axis is along the line of sight (LOS) and points toward the galaxy, while $(x',\, y')$ confines the plane of the sky.

The intersection between the equatorial plane of the bulge $(x,\, y)$ and the plane of the sky $(x',\, y')$ is the so-called line of nodes (LON). The angle θ $(0 \leq \theta \leq \pi/2)$ subtended between the polar z-axis and the polar z'-axis defines the inclination of the bulge. Let the angle ϕ $(0 \leq \phi \leq \pi/2)$ be subtended between the x-axis and the LON in the bulge equatorial plane and the angle ψ $(0 \leq \psi \leq \pi/2)$ be subtended between the x'-axis and the LON in the plane of the sky. The three Euler angles $(\theta,\, \phi,\, \psi)$ allow for the transformation from the reference system of the sky to that of the galaxy. If the x'-axis coincides with the LON, consequently it holds that $\psi = 0$.

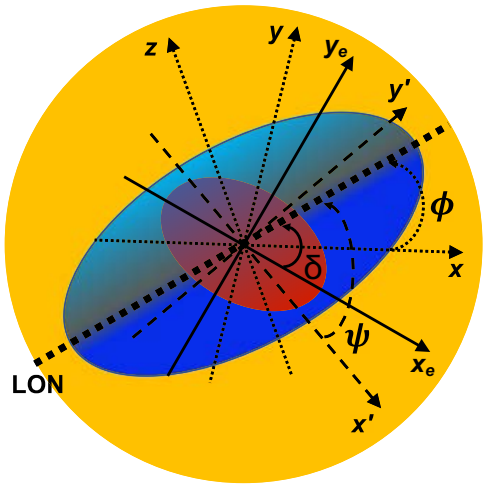

Figure 2.4: Schematic three-dimensional view of a bulge and disk galaxy. The triaxial bulge, the disk plane, and the plane of the sky are shown in red, blue, and orange, respectively. The reference systems of the galaxy (x, y, z) and of the observer (x', y', z') as well as the LON are plotted with thin dotted lines, thin dashed lines, and a thick dashed line, respectively. The axes of symmetry (x_e, y_e) of the ellipse of the bulge in the plane of the sky are represented with thin solid lines. The triaxial bulge is shown as seen along the LOS.

The projection of the triaxial ellipsoidal bulge onto the plane of the sky is an ellipse

$$\frac{x_e^2}{a^2} + \frac{y_e^2}{b^2} = 1\,, \tag{2.25}$$

where x_e and y_e are its axes of symmetry, and a and b are the corresponding semi-major and semi-minor axes. The twist angle δ between the x_e-axis and the LON describes the orientation of the bulge (Fig. 2.4). We always choose $0 \leq \delta \leq \pi/2$, so that a can be either the major or the minor semi-axis, and vice versa for b.

The twist angle δ and the apparent axial ratio $q_{\rm bulge} = b/a$ depend only, and unambiguously, on the direction of the LOS, that is, on θ, ϕ, and ψ, and on the intrinsic shape of the bulge, that is, A, B, and C. Thus, by means of the Euler angles it is possible to impose further constraints to the equations that relate the intrinsic and projected variables in the reference system of the observer (Simonneau et al. 1998).

2.2.1.1 From ellipses to ellipsoids

The real challenge is to describe the three-dimensional shape of a triaxial ellipsoid starting from a two-dimensional projected ellipse. The intrinsic length of the semi-axes of the ellipsoid A, B, and C can be expressed as a function of the length of the semi-axes of the projected ellipse a and b and the twist angle δ (Simonneau et al. 1998). We can define

$$K^2 = \frac{A^2 + B^2}{2} \left(1 + E \cos 2\phi\right) , \tag{2.26}$$

where

$$E = \frac{A^2 - B^2}{A^2 + B^2} \qquad (-1 \leq E \leq 1) \tag{2.27}$$

measures the intrinsic equatorial ellipticity of the bulge. By analogy, we can define a measure of the ellipticity of the observed ellipse as

$$e = \frac{a^2 - b^2}{a^2 + b^2} \qquad (-1 \leq e \leq 1) . \tag{2.28}$$

Thus, the intrinsic lengths of the three-dimensional ellipsoid are

$$A^2 = K^2 \left(1 + \frac{e \sin 2\delta}{1 + e \cos 2\delta} \frac{\tan \phi}{\cos \theta}\right) ; \tag{2.29}$$

$$B^2 = K^2 \left(1 - \frac{e \sin 2\delta}{1 + e \cos 2\delta} \frac{\cot \phi}{\cos \theta}\right) ; \tag{2.30}$$

$$C^2 = K^2 \left(1 - \frac{2\, e \cos 2\delta}{\sin^2 \theta \left(1 + e \cos 2\delta\right)} + \frac{2\, e \cos \theta \sin 2\delta}{\sin^2 \theta \left(1 + e \cos 2\delta\right)} \cot^2 \phi\right) . \tag{2.31}$$

We stress that the values of a, b, δ, and θ can be directly obtained from observations. Unfortunately, the problem cannot be analytically solved because of the spatial position of the bulge (i.e., the angle ϕ), which constitutes the basis of the statistical analysis (see also Méndez-Abreu et al. 2010, for all details).

2.2.1.2 Characteristic angles

Introducing physical constraints on the accessible viewing angles, it is possible to constrain the intrinsic semi-axes of the bulge from its observed properties (i.e., the intrinsic

semi-axes A, B, and C must be definite positive). For any value of the observed variables a, b, δ and θ there are two cases:

1. $a > b$. In this first case we obtain $e > 0$ from Eq. (2.28) and $A > B$ from Eqs. (2.29) and (2.30). According to Eqs. (2.30) and (2.31), the value of B^2 and C^2 can be either positive or negative depending on the value of ϕ. This imposes a limitation on the value of ϕ, since only a positive value for B^2 and C^2 are physically truthful. The semi-axis B^2 is positive only for $\phi > \phi_B$, being the angle ϕ_B defined by $B^2 = 0$ in Eq. (2.30) as

$$\phi_B = \arctan\left(\frac{e\,\sin 2\delta}{\cos\theta\,(1 + e\,\cos 2\delta)}\right). \tag{2.32}$$

   In the same way, C^2 is positive only for $\phi < \phi_C$, being the angle ϕ_C defined by $C^2 = 0$ in Eq. (2.31) as

$$\phi_C = 0.5\arctan\left(\frac{2\,e\,\sin 2\delta\,\cos\theta}{e\,\cos 2\delta\,(1 + \cos^2\theta) - \sin^2\theta}\right). \tag{2.33}$$

   Thus, this limits the value of the angle ϕ in the range $\phi_B \leq \phi \leq \phi_C$.

2. $a < b$. In the second case, from Eq. (2.28) the ellipticity of the observed ellipse results negative ($e < 0$), and the relation between the length of the semi-axis becomes $A < B$ from Eqs. (2.29) and (2.30). With this hypothesis, according to Eqs. (2.29) and (2.31) and depending on the value of ϕ, a positive or negative value of either A^2 or C^2 is possible. The semi-axis A^2 is positive only for $\phi < \phi_A$, being the angle ϕ_A defined by $A^2 = 0$ in Eq. (2.29) as

$$\phi_A = -\arctan\left(\frac{\cos\theta\,(1 + e\,\cos 2\delta)}{e\,\sin 2\delta}\right). \tag{2.34}$$

   In the same way, C^2 is positive only for $\phi > \phi_C$. Thus, this limits the value of the angle ϕ in the range $\phi_C \leq \phi \leq \phi_A$.

Since the problem is symmetric, meaning that either a or b can be the major-axis of the projected ellipse and the major or minor semi-axis are interchangeable, the same mathemat-

ical description applies and the possible values of ϕ are

$$\phi_B \leq \phi \leq \phi_C \,, \tag{2.35}$$

with ϕ_B and ϕ_C defined by Eqs. (2.32) and (2.33), respectively. The length of the intrinsic semi-axes A, B, and C can be expressed as a function of the characteristics angles ϕ_B and ϕ_C as

$$A^2 = K^2 \left(1 + \tan\phi_B \, \tan\phi\right) ; \tag{2.36}$$

$$B^2 = K^2 \left(1 - \frac{\tan\phi_B}{\tan\phi}\right) ; \tag{2.37}$$

$$C^2 = 2K^2 \tan\phi_B \frac{\cos^2\theta}{\sin^2\theta} \left(\cot 2\,\phi - \cot 2\,\phi_C\right) . \tag{2.38}$$

We would like to stress again that the characteristic angles depend on a, b, δ, and θ, therefore they are known functions for each observed bulge. Moreover, as previously explained, the symmetry of the problem allows to always consider $A > B$ without imposing any further constraint on the length of the polar semi-axis C.

The semi-axis B is zero for $\phi = \phi_B$ and it increases when ϕ goes from ϕ_B to ϕ_C. These semi-axes are equal when $B^2 = C^2$ at

$$\phi_{BC} = \arctan\left(\frac{\tan\delta}{\cos\theta}\right) . \tag{2.39}$$

In the range $\phi_{BC} < \phi < \phi_C$ both B^2 and C^2 are smaller than A^2. Moreover, since C^2 increases when ϕ decreases, there is an angle

$$\phi_{AC} = \arctan\left(\cos\theta \tan\delta\right) , \tag{2.40}$$

for which $C^2 = A^2$. Thus, we have $C^2 > A^2 > B^2$ for $\phi < \phi_{AC}$. Finally, the quadratic mean radius of the equatorial ellipse of the bulge is defined as

$$R^2 = \frac{A^2 + B^2}{2} = K^2 \tan\phi_B \left(\cot\phi_B - \cot 2\,\phi\right) , \tag{2.41}$$

which depends only on the unknown angle ϕ. Since it is always possible to study the system

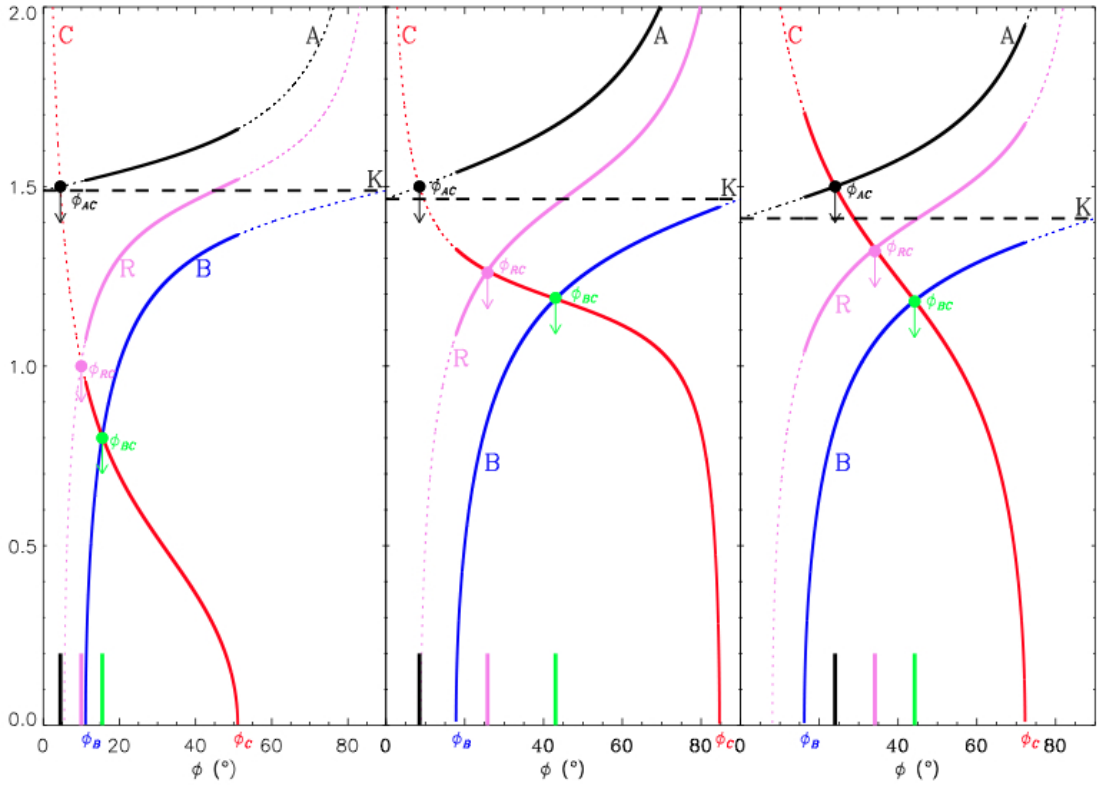

Figure 2.5: The lengths A, B, and C of the semi-axes of the bulge ellipsoid and its mean equatorial radius R as a function of the unknown angle ϕ. The solid lines represent the ranges of physically possible values of A, B, C, and R, while the dotted lines correspond to their overall trends within $0 \leq \phi \leq \pi/2$. A bulge with $\phi_{AC} < \phi_{RC} < \phi_B$, $\phi_{AC} < \phi_B < \phi_{RC}$, and $\phi_B < \phi_{AC} < \phi_{RC}$ is shown in the left, central, and right panel, respectively. From Méndez-Abreu et al. (2010).

where$A^2 > B^2$, the value of quadratic mean radius of the equatorial ellipse is in the range $A^2 \geq R^2 \geq B^2$. There exists a value for the angle ϕ corresponding to the case $C^2 = R^2$ expressed as

$$\phi_{RC} = 0.5 \arctan\left(\tan 2\delta \, \frac{1 + \cos^2\theta}{2\,\cos\theta}\right) . \tag{2.42}$$

An example of the final view of how the characteristic angles influence the statistical analysis is sketched in Fig. 2.5.

2.2.2 Statistical analysis

The observational parameters necessary for the analysis are the apparent shape of the bulge (i.e., the bulge ellipticity $\epsilon_{\rm bulge} = 1 - q_{\rm bulge}$), the apparent shape of the disk (i.e., the

disk ellipticity $\epsilon_{\rm disk} = 1 - q_{\rm disk}$), and the difference between the position angle of the bulge and the disk (i.e., $\delta = PA_{\rm bulge} - PA_{\rm disk}$).

The ellipticity of the disk, under the hypothesis of circularity and infinite thinness, is a measure of the inclination of the bulge

$$\theta = \arccos(q_{\rm disk})\,, \tag{2.43}$$

under the assumption that both the disk and bulge share the same equatorial plane. However, it is well known that disks are not infinitely thin structures (Sandage et al. 1970; Ryden 2004; Sánchez-Janssen et al. 2010). To account for this, we included in our statistical analysis the hypothesis that disks have an intrinsic thickness. Then, we computed the inclination of the galaxy accounting for the distribution of the intrinsic thickness of disk ($q_{0,\,\rm disk}$). We used a normal distribution with mean flattening $\langle q_{0,\,\rm disk}\rangle = 0.267$ and standard deviation $\sigma_{q_{0,\,\rm disk}} = 0.102$ (Rodríguez & Padilla 2013). Thus, the statistical value of the galaxy inclination is given by

$$\theta = \arccos\sqrt{\frac{(q_{\rm disk})^2 - (q_{0,\,\rm disk})^2}{1 - (q_{0,\,\rm disk})^2}}\,, \tag{2.44}$$

where the $q_{0,\,\rm disk}$ value is randomly drawn from the previous normal distribution.

At this stage, we needed to take into account the uncertainties in $\epsilon_{\rm bulge}$, $\epsilon_{\rm disk}$, and δ derived from the photometric decomposition error analysis (Méndez-Abreu et al. 2017). To do so, we used a Gaussian distribution peaked at face values and with standard deviation equal to the uncertainty in the chosen parameter. A similar analysis was previously introduced in Corsini et al. (2012) to measure the shape of the polar bulge of NGC 4698.

2.2.2.1 Intrinsic ellipticity B/A

The axial ratio B/A describes the intrinsic shape of a triaxial bulge in the equatorial plane. It can be defined by

$$\frac{B}{A} = \sqrt{1 - \frac{2\,\sin\phi_B}{\sin\phi_B + \sin\left(2\phi - \phi_B\right)}}\,, \tag{2.45}$$

as resulted using Eqs. (2.36) and (2.37). It is straightforward to show that $B/A = 0$ for $\phi = \phi_B$, while the limiting value of B/A for $\phi = \phi_C$ is

$$\left(\frac{B}{A}\right)_C = \sqrt{1 - \frac{2\,\sin\phi_B}{\sin\phi_B + \sin\left(2\,\phi_C - \phi_B\right)}}\,. \tag{2.46}$$

The axial ratio B/A reaches a maximum value given by

$$\left(\frac{B}{A}\right)_{\rm M} = \frac{1 - \sin\phi_B}{1 + \sin\phi_B}, \tag{2.47}$$

when the angle ϕ ranges between ϕ_B and ϕ_C and corresponds to

$$\phi_{\rm M} = \frac{\pi}{4} + \frac{\phi_B}{2}, \tag{2.48}$$

where $\phi_{\rm M}$ is always larger than ϕ_B.

The value of B/A is zero for $\phi = \pi/2$, while there are no physical values for B/A if $\phi_C < \phi \leq \pi/2$, as previously stated. However, if $\phi_C > \phi_{\rm M}$, B/A monotonically increases reaching the maximum $(B/A)_{\rm M}$ for $\phi = \phi_{\rm M}$ and then monotonically decreases for $\phi > \phi_{\rm M}$ since the limit value $(B/A)_{\rm C}$ for $\phi = \phi_C$. But, if $\phi_C < \phi_{\rm M}$, the maximum value of B/A corresponds to $(B/A)_{\rm C}$, since it does not reach the maximum value given by Eq. (2.47).

To perform a more exhaustive statistical analysis, we computed for each observed bulge the probability $P(B/A)$ corresponding to $0 < (B/A) < (B/A)_C$ by taking into account that ϕ can take any value in the range $\phi_B \leq \phi \leq \phi_C$ with the same probability given by

$$P(\phi) = \frac{1}{\phi_C - \phi_B}\,. \tag{2.49}$$

We have seen that B/A has a different behavior for $\phi_C < \phi_{\rm M}$ and for $\phi_C > \phi_{\rm M}$. Therefore, the probability $P(B/A)$ in the previous case is expressed as

$$P(B/A) = \frac{2\dfrac{B}{A}\sin\phi_B}{\left(\phi_C - \phi_B\right)\left(1 - \dfrac{B^2}{A^2}\right)\sqrt{\left(1 - \dfrac{B^2}{A^2}\right)^2 - \sin^2\phi_B\left(1 + \dfrac{B^2}{A^2}\right)^2}}\,. \tag{2.50}$$

In the latter case, since there is only one value of ϕ for each value of B/A when $0 <$

$B/A < (B/A)_C$ and two values of ϕ for each value of B/A when $(B/A)_C < B/A < (B/A)_M$, the probability

$$P(B/A) = \begin{cases} \dfrac{2\dfrac{B}{A}\sin\phi_B}{(\phi_C - \phi_B)\left(1-\dfrac{B^2}{A^2}\right)\sqrt{\left(1-\dfrac{B^2}{A^2}\right)^2 - \sin^2\phi_B\left(1+\dfrac{B^2}{A^2}\right)^2}} \\ \dfrac{4\dfrac{B}{A}\sin\phi_B}{(\phi_C - \phi_B)\left(1-\dfrac{B^2}{A^2}\right)\sqrt{\left(1-\dfrac{B^2}{A^2}\right)^2 - \sin^2\phi_B\left(1+\dfrac{B^2}{A^2}\right)^2}} \end{cases} \tag{2.51}$$

describes the discontinuity for $B/A = (B/A)_C$, corresponding to $\phi'_C = \frac{\pi}{2} - (\phi_C - \phi_B)$.

2.2.2.2 Intrinsic flattening C/A

The axial ratio C/A usually describes the intrinsic flattening of a triaxial bulge if $A > B > C$. Since no constraints are imposed on the relative length of the three semi-axes, the ellipsoid flattening is redefined as

$$F(\phi) = \frac{C^2}{R^2} = \frac{2C^2}{A^2 + B^2}\,, \tag{2.52}$$

using the definition of the polar semi-axis and mean equatorial radius given by Eqs. (2.31) and (2.41). This description allows to describe the intrinsic flattening as

$$F(\phi) = F_\theta \frac{\sin\phi_B}{\sin 2\phi_C}\frac{\sin(2\phi_C - 2\phi)}{\sin(2\phi - \phi_B)}\,, \tag{2.53}$$

where

$$F_\theta = \frac{2\,\cos^2\theta}{\sin^2\theta} \tag{2.54}$$

accounts for the effect of inclination.

At this stage, we can constrain the intrinsic shape of the observed triaxial ellipsoid by mean of the known characteristic angles ϕ_B and ϕ_C, which depend on the observed quantities a, b, δ, and θ. The relation between Eqs. (2.27) and (2.52) allows to correlate the intrinsic

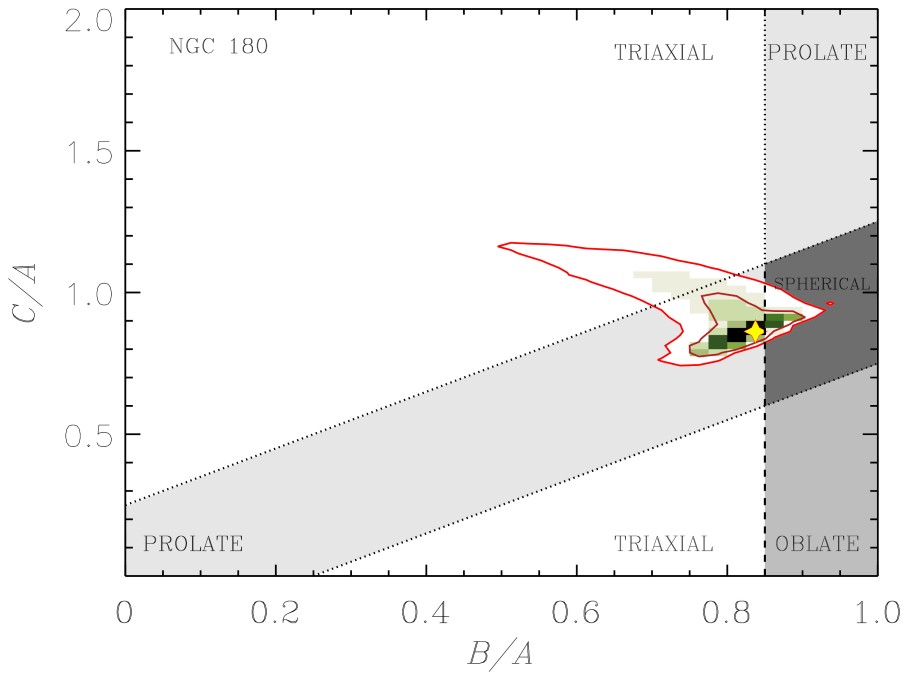

Figure 2.6: Distribution of the intrinsic axial ratios B/A and C/A of the bulge of the galaxy NGC 180. The yellow star corresponds to the most probable values of B/A and C/A. The inner and outer red solid contours encompass respectively the 68.3% and 95.4% of the realizations of (B/A, C/A) consistent with the geometric parameters of bulge and disk measured from our photometric decomposition of the galaxy image. The white, light gray, gray, and dark gray regions mark the regimes of triaxial, prolate, oblate, and spherical bulges, respectively.

equatorial ellipticity E with the redefined flattening F as

$$\sqrt{E^2 - \sin^2\phi_B} = \frac{\frac{F}{F_\theta}\sin 2\phi_C + \sin\phi_B \cos\left(2\phi_C - \phi_B\right)}{\sin\left(2\,\phi_C - \phi_B\right)}\,. \tag{2.55}$$

Thus, we can express the intrinsic axial ratio C/A as

$$\begin{aligned}\frac{C^2}{A^2} =& \frac{F_\theta \sin(2\phi_C - \phi_B)}{2\sin(2\phi_C)}\sqrt{\left(1 - \frac{B^2}{A^2}\right)^2 - \sin^2\phi_B\left(1 + \frac{B^2}{A^2}\right)^2} \\ &- \frac{F_\theta \sin\phi_B \cos(2\phi_C - \phi_B)}{2\sin(2\phi_C)}\left(1 + \frac{B^2}{A^2}\right)\,.\end{aligned} \tag{2.56}$$

2.2.2.3 (B/A, C/A) diagram

The theoretical framework based on the statistical analysis of the ϕ angle allowed us to retrieve the intrinsic three-dimensional shape of individual bulges in disk galaxies. The probabilities of B/A and C/A are equivalent since they are both functions of the same variable ϕ. Indeed, for a given value of B/A with probability $P(B/A)$, the corresponding value of C/A obtained by Eq. (2.56) has a probability $P(C/A) = P(B/A)$.

We generated 1000 geometric configurations for the geometrical initial parameters ($\epsilon_{\rm bulge}$, $\epsilon_{\rm disk}$, δ, and θ) according to their errors, using the galaXYZ code written in IDL. Thus, for each geometric configuration we derived via Monte Carlo (MC) simulations 5000 values of B/A according to its probability function. In this way, taking advantage of the relation between the intrinsic axial ratios, we populated the plane (B/A, C/A) that determines the most probable value of the three-dimensional shape of the bulge. Finally, we computed the 1σ and 2σ contour levels which contain the 68.27% and 95.45% of the computed configurations and represent the statistical uncertainty on the most probable (B/A, C/A). An example of the diagram (B/A, C/A) to compute the most probable three-dimensional shape of the bulge in the spiral galaxy NGC 180 is given in Fig. 2.6.

3

STRUCTURAL PARAMETERS OF CALIFA GALAXIES

We presented the two-dimensional multi-component photometric decomposition of 404 galaxies from the CALIFA data release 3. They represented all possible galaxies not strongly inclined and with no clear signs of interaction in the final CALIFA data release. Galaxies were modeled in the g, r, and i Sloan Digital Sky Survey images including, when appropriate, a nuclear point source, a bulge, a bar, and a disk component. We used a human-supervised approach to determine the optimal number of structures to be included in the fit. The dataset, including the photometric parameters of the CALIFA sample, was released together with statistical errors and a visual analysis of the quality of each fit. The analysis of the photometric components revealed a clear segregation of the structural composition of galaxies with stellar mass. At high masses ($\log(M_\star/\mathrm{M}_\odot) > 11$), the galaxy population is dominated by galaxies modeled with a single Sérsic or a bulge+disk with a bulge-to-total luminosity ratio $B/T > 0.2$. At intermediate masses ($9.5 < \log(M_\star/\mathrm{M}_\odot) < 11$), galaxies described with bulge+disk and $B/T < 0.2$ are preponderant, whereas, at the low mass end ($\log(M_\star/\mathrm{M}_\odot) < 9.5$), the prevailing population is constituted by galaxies modeled with either pure disks or nuclear point sources+disks (i.e., with no discernible bulge). We obtained that 57% of the volume corrected sample of disk galaxies in the CALIFA sample host a bar. This bar fraction shows a significant drop with increasing galaxy mass in the range $9.5 < \log(M_\star/\mathrm{M}_\odot) < 11.5$. The analysis of the extended multi-component radial profile resulted in a volume corrected distribution of 62%, 28%, and 10% for the so-called Type I (pure exponential), Type II (down-bending), and Type III (up-bending) disk profiles, respectively. These fractions are in discordance with previous findings. We argued that the different methodologies used to detect the double-exponential profiles were the main cause for these differences.

3.1 Introduction

The constant development of the morphological classification schemes, from the Hubble tuning fork diagram (Hubble 1926) to the more sophisticated Comprehensive de Vaucouleurs Revised Hubble-Sandage catalogue (CVRHS; Buta et al. 2015), illustrates the morphological complexity of galaxy systems. Even apparently simple systems, like elliptical galaxies, can host a wealth of other structures such as outer shells or nuclear cores (Malin & Carter 1980; Morelli et al. 2004). The properties of the different stellar structures that make up galaxies (e.g., bulges, bars, and disks) are the direct result of their formation and evolution. Therefore, the quantification of the properties of galaxies and their distinct stellar structures is a fundamental step toward understanding how galaxies form and evolve.

Despite their limitations, two-component (bulge+disk) photometric decompositions are still the common procedure when dealing with large surveys at low and high redshift (e.g., Allen et al. 2006; Simard et al. 2011; Lackner & Gunn 2012; Häußler et al. 2013). This is mainly because current methodologies to find the best-fit model to the galaxy images using two-component models are relatively easy to automatize. However, when more structures are added to the fitting process, finding the solution becomes more degenerate and human supervision is usually needed. A number of studies have attempted to produce multi-component photometric decompositions of samples with several hundreds of galaxies. Recently, Salo et al. (2015) performed the largest multi-component decomposition to date, analyzing 2352 galaxies from the Spitzer Survey of Stellar Structure in Galaxies (S^4G, Sheth et al. 2010).

In this Chapter, we presented the two-dimensional multi-component photometric decomposition of 404 galaxies drawn from the final DR of the CALIFA survey (Sánchez et al. 2012). The sample galaxies represent all galaxies in the CALIFA survey that are suitable for our photometric analysis, that is, they are not in interaction with other galaxies, heavily disturbed, or highly inclined. The CALIFA survey is an integral field spectroscopy (IFS) survey of 667 galaxies that provides spatially resolved information, such as stellar and gas kinematics, stellar populations, and gas-phase physical properties, over a large field of view (2-3 galaxy effective radii). The CALIFA data have significantly improved our understanding of the physical processes leading to the observed population of galaxies in the nearby Universe. The aim of this Chapter is to provide the CALIFA dataset with an accurate

photometric characterization of the multiple stellar structures shaping the CALIFA galaxies (bulges, bars, and disks). To this aim, we had used the homogeneous imaging provided by the SDSS DR7 (Abazajian et al. 2009) for the whole CALIFA sample. This Chapter focused on the technical aspects of the photometric decomposition and the incidence of the different galaxy structures in the CALIFA sample galaxies. The detailed photometric description of the galaxy structures presented in this Chapter opens a new set of possibilities to the wealth of two-dimensional spatially resolved spectroscopic information provided by the CALIFA survey.

The Chapter is organized as follows. Section 3.2 describes the final CALIFA DR3 and the sample used in this study. Section 3.3 details the technical aspects of the two-dimensional photometric decomposition analysis. Section 3.4 describes the fitting process and the main types of multi-component decomposition carried out in this Chapter. The incidence of the main stellar structures found in our sample is analyzed in the context of the global properties of the galaxies. Section 3.5 presents a complete description of the uncertainties inherent to our analysis. Section 3.6 describes the synergies between the photometric decomposition analysis and the CALIFA survey. The conclusions are given in Section 3.7. Throughout the Chapter we assumed a flat cosmology with $\Omega_{\rm m} = 0.3$, $\Omega_{\Lambda} = 0.7$, and a Hubble constant H_0 = 70 km s^{-1} Mpc^{-1}.

■ 3.2 Sample selection

The CALIFA final DR (DR3 Sánchez et al. 2016) comprises two different samples of galaxies: galaxies belonging to the CALIFA mother sample and galaxies that are considered the extension sample. The first group represents the natural expansion of the galaxies presented in the previous CALIFA DR1 (Husemann et al. 2013) and DR2 (García-Benito et al. 2015), and it is fully characterized in Walcher et al. (2014). The second group corresponds to a compendium of different sets of galaxies that were observed using the same setup as CALIFA, as part of ancillary science projects within the CALIFA collaboration. The final CALIFA DR3 comprises 667 galaxies.

From the final DR3, and after performing a visual inspection of the SDSS images, we carried out a discard/exclusion process of those galaxies not suitable for our photometric

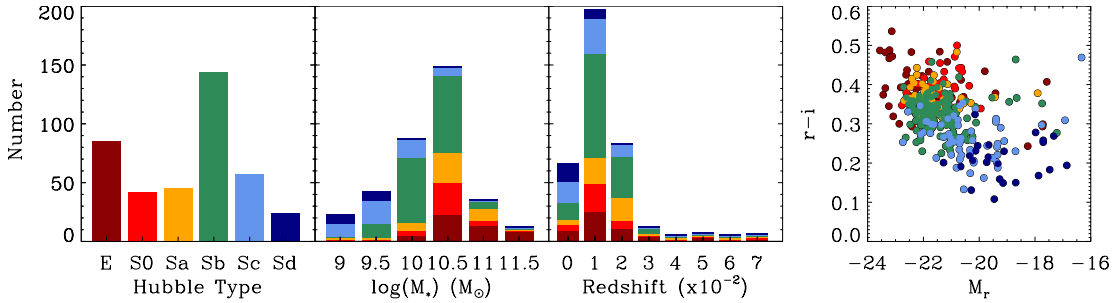

Figure 3.1: (*from left to right*) Distribution of our sample galaxies in Hubble type, stellar mass, redshift, and on the $r-i$ vs. r band color magnitude relation. Colors in all panels represent the different galaxy Hubble types. The parameters for each galaxy were obtained from Walcher et al. (2014).

study. First, we rejected paired and interacting objects (57 galaxies) as well as those systems with a heavily distorted morphology (19 galaxies). Since we aimed to provide an accurate description of the galaxy stellar structures using only symmetric models, galaxies with distorted features cannot be successfully modeled. Then, we checked for the presence of bright stars contaminating our target galaxies and removed them from the analysis (5 galaxies). Finally, the identification and subsequent characterization of structures in highly inclined galaxies was usually not possible due to projection effects, thus those galaxies close to edge-on ($\theta > 70°$) were also removed from the sample (183 galaxies). This latter process was performed by a visual inspection of individual galaxies since we found that a typical disk axial ratio cut did not work for early-type edge-on galaxies with circular stellar haloes. The final sample presented in this Chapter contains 404 galaxies. The distribution of their main global characteristics extracted from Walcher et al. (2014) is shown in Fig. 3.1.

The CALIFA mother sample presents the notable characteristic that its selection criteria are well understood. Therefore, although the final observed sample is not complete in volume, it is possible to reconstruct volume-corrected sample properties. The complete procedure is described in Walcher et al. (2014) and assigns a volume correction to each individual galaxy that can be used to correct for the selection function. Fig. 3.2 shows the luminosity function of the sample in this study, the CALIFA mother sample, and the final observed sample in the CALIFA DR3. It is worth noting that volume corrections are not applicable to the extended sample due to their complicated selection. Thus, the luminosity function represented in Fig. 3.2 contains only those galaxies drawn from the CALIFA mother sample

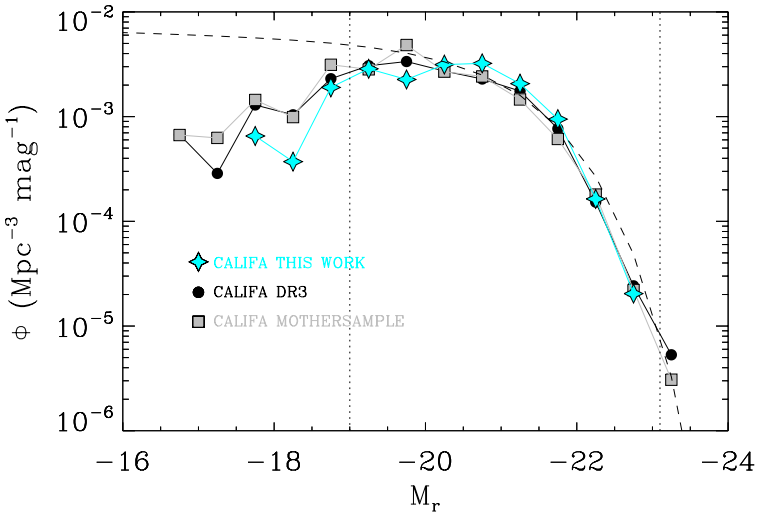

Figure 3.2: Luminosity functions of the CALIFA mother sample (gray squares), final CALIFA observed sample in the DR3 (black dots), and the sample described in this Chapter (cyan stars). The dotted lines denote the mother sample completeness limits. The SDSS luminosity function of Blanton et al. (2003) is shown with a black dashed line.

(297 galaxies). We found a good match among the luminosity functions of the three different samples, as well as for the SDSS luminosity function given by Blanton et al. (2003), within the completeness limits described in Walcher et al. (2014), that is, $-23.1 < M_r < -19$ mag. Our sample contains 285 galaxies within these limits.

3.3 Data reduction

The structural parameters of the CALIFA sample were derived by applying the GASP2D code to fit the two-dimensional surface-brightness distribution of galaxies with a versatile set of model components, as discussed in Section 2.1.1.

We stressed again that due to the high degree of degeneracy that the $n_{\rm bar}$ parameter introduced during the fit, we decided to keep it as a fixed parameter during the fitting process in this particular analysis. The default value used was $n_{\rm bar} = 2$ (see also Laurikainen et al. 2005). Moreover, we mentioned that two galaxies in the sample appeared to host a nuclear bar after a careful inspection of the two-dimensional residuals and their surface brightness distribution was also fit using a Ferrers profile. To derive the photometric parameters of the different structures present in a given galaxy, we iteratively fit a composite model made of a suitable combination of the stellar components described in Section 2.1.1. The actual fitting

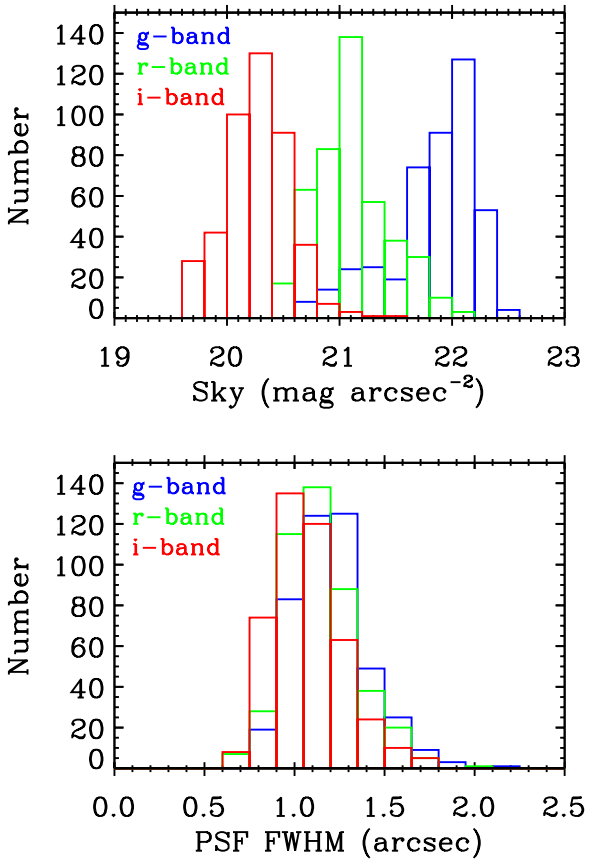

Figure 3.3: (*Top panel*) Distribution of the average surface brightness of the sky subtracted from our galaxy images. (*Bottom panel*) Distribution of the PSF FWHM in our galaxy images. In both panels the blue, green, and red histograms represent the g, r, and i bands, respectively.

for each galaxy was human supervised. This means that the final number of components included in the fit was based on the judgement of the code-user. Usually, at least two different component combinations were tested for each galaxy before the best solution was found. The decision was based on the two-dimensional distribution of the intensity residuals and one-dimensional surface brightness, ellipticity, and position-angle radial profiles.

An exception to the previous human supervised fitting procedure was the case of featureless ETGs. If a given galaxy was visually classified as early-type (E, S0, or S0a) and other structures such as bars or double-exponential profiles were not evident in the image, the number of components, that is, whether the galaxy was fit with a single Sérsic (E) or a bulge+disk (S0/S0a), was decided through an automatic criteria. More details about this procedure can be found in Section 3.4.1.

Increasing the level of complexity of the galaxy model, by including extra components such as lenses, ovals, spiral arms, or barlenses, might improve the quality of the final fit, and provide extra information about the galaxy structure. However, it comes at the cost of greatly increasing the degeneracy on the final parameters, making their interpretation difficult. Therefore, we decided not to include any further structure in our analysis.

In order to perform the two-dimensional photometric decomposition, GASP2D needed a series of input files: (1) a sky-subtracted image of the galaxy; (2) a mask created to avoid foreground stars, background galaxies, and other galactic features departing from the smooth light distribution of the galaxy; and (3) the radial profiles of ellipticity, position angle, and surface brightness (see Section 2.1, for all details). To compute such inputs, we made use of the fully-calibrated g-, r-, and i-band images from the SDSS DR7.

The distribution of the derived values of the surface brightness of the sky for the images of the sample galaxies are shown in the top panel of Fig. 3.3. We found typical values of 21.8 $\pm$ 1.2, 21.1 $\pm$ 1.2, and 20.2 $\pm$ 1.2 mag arcsec^{-2} for g, r, and i band, respectively.

It is well-known that accurate measurements of the image PSF are critical for recovering the structural parameters of the galaxy central components. In this analysis, this mainly refers to the properties of bulges and NPSs. The mean values of the FWHM for our sample galaxies are shown in the bottom panel of Fig. 3.3. We found typical values of 1.2 $\pm$ 0.2, 1.1 $\pm$ 0.2, and 1.1 $\pm$ 0.2 arcsec for the g, r, and i band, respectively.

3.4 Two-dimensional photometric decomposition analysis

This Section describes the main procedures we followed to carry out the photometric decomposition. We separated our sample into early-type (127 galaxies) and spiral galaxies (277 galaxies) since for the former an automatic methodology was used to find the optimal number of components to obtain the best-fit, whereas for the latter a human supervised approach was used. Table 3.1 shows the best-fit parameters obtained for some example galaxies covering different combinations of structural components[1], while some of their GASP2D fits are shown in Fig. 3.3.

[1]The full version of the table for the entire sample galaxies, and similar tables in the g and i bands, are available on-line at: `http://vizier.u-strasbg.fr/viz-bin/VizieR?-source=J/A%2BA/598/A32`.

Table 3.1: Structural parameters of the sample galaxies in the r band.

Galaxy	NGC 5684	NGC 364	NGC 6497	NGC 7489	MCG −02 − 06 − 016
$\mu_{\rm e}$ [mag arcsec^{-2}]	22.4 ± 0.2	18.4 ± 0.3	19.7 ± 0.2	–	–
$r_{\rm e}$ [arcsec]	28 ± 3	1.7 ± 0.3	2.8 ± 0.3	–	–
n	4.8 ± 0.2	1.4 ± 0.2	3.1 ± 0.4	–	–
$q_{\rm bulge}$	0.711 ± 0.009	0.91 ± 0.05	0.77 ± 0.04	–	–
$PA_{\rm bulge}$ [°]	115 ± 1	41 ± 6	112 ± 5	–	–
B/T	1	0.20	0.26	–	–
μ_0 [mag arcsec^{-2}]	–	20.34 ± 0.09	20.67 ± 0.08	20.265 ± 0.007	21.933 ± 0.008
h [arcsec]	–	12.6 ± 0.5	20 ± 1	12.9 ± 0.3	22.2 ± 0.2
$r_{\rm break}$ [arcsec]	–	–	27 ± 3	–	38 ± 2
$h_{\rm out}$ [arcsec]	–	–	6.8 ± 0.9	–	27 ± 2
$q_{\rm disk}$	–	0.72 ± 0.01	0.472 ± 0.009	0.56 ± 0.01	0.646 ± 0.008
$PA_{\rm disk}$ [°]	–	33.4 ± 0.7	110.5 ± 0.5	164.1 ± 0.7	87.8 ± 0.7
D/T	–	0.70	0.61	0.99	1
$\mu_{0,\,\rm bar}$ [mag arcsec^{-2}]	–	20.09 ± 0.07	20.51 ± 0.07	–	–
$a_{\rm bar}$ [arcsec]	–	12.8 ± 0.3	18.6 ± 0.6	–	–
$q_{\rm bar}$	–	0.558 ± 0.007	0.373 ± 0.007	–	–
$PA_{\rm bar}$ [°]	–	91.2 ± 0.4	159.5 ± 0.4	–	–
Bar/T	–	0.10	0.13	–	–
$\mu_{0,\,\rm nps}$ [mag arcsec^{-2}]	–	–	–	19.0 ± 0.1	–
NPS/T	–	–	–	0.01	–
Flag	$1, a$	$1, a$	$1, c$	$1, a$	$1, a$

Notes. Best-fit parameters for a subsample of five galaxies modeled with a different combination of structures. (*From left to right*): single Sérsic, bulge+disk+bar, bulge+disk+bar (including double-exponential profile), NPS+disk, and disk (including double-exponential profile). Each column represents the best-fit parameters for a given galaxy. (*From top to bottom*): bulge parameters (effective surface brightness $\mu_{\rm e}$, effective radius $r_{\rm e}$, Sérsic index n, axial ratio $q_{\rm bulge}$, position angle $PA_{\rm bulge}$, and bulge-to-total luminosity ratio B/T), disk parameters (central surface brightness μ_0, inner scale length h, break radius $r_{\rm break}$, outer scale length $h_{\rm out}$, axial ratio $q_{\rm disk}$, position angle $PA_{\rm disk}$, and disk-to-total luminosity ratio D/T), bar parameters (central surface brightness $\mu_{0,\,\rm bar}$, bar radius $a_{\rm bar}$, axial ratio $q_{\rm bar}$, position angle $PA_{\rm bar}$, and bar-to-total luminosity ratio Bar/T), NPS parameters (central surface brightness $\mu_{0,\,\rm nps}$ and NPS-to-total luminosity ratio NPS/T), and the visual quality flag explained in Section 3.5.1. Each row shows the best-fit values of the given parameters and their associated errors (see Section 3.5.2). Position angles are measured counterclockwise from North to East. When a given structure is not present in the model, its corresponding parameters are left empty. The parameters in this table have not been corrected for galactic extinction, K-correction, or cosmological dimming.

The photometric properties of the different stellar structures were derived independently for the three SDSS bands (g, r, and i) used in this analysis. This means that the structural parameters were not limited and/or tied between the different band images. However, in order to avoid discordant results we decided to relate the initial conditions required for the fit in the three bands. In its standard configuration, GASP2D found the best set of initial guesses to initialize the non-linear fit in an automatic way, as discussed in Section 2.1.2.3.

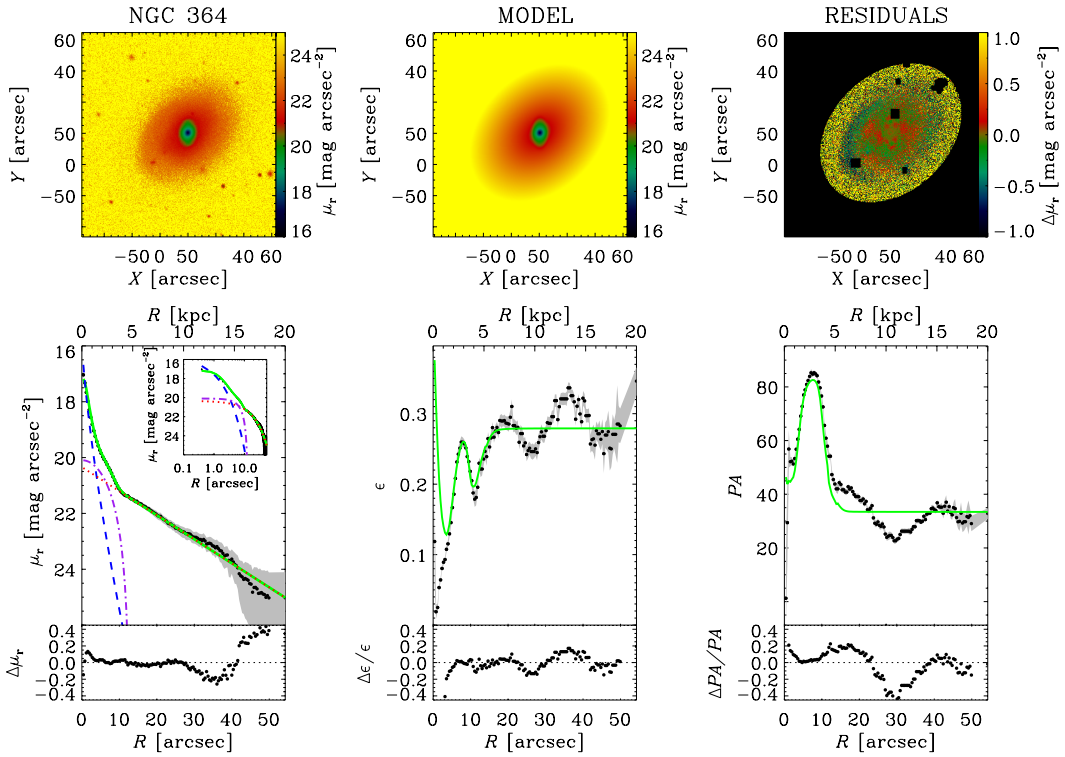

Figure 3.3: Examples of two-dimensional photometric decompositions of the r-band images obtained from GASP2D. The upper panels (*from left to right*) show the map of the observed, modeled, and residual (observed−modeled) surface-brightness distributions. The field of view is oriented with North up and East left. The black areas in the residual image correspond to pixels excluded from the fit. The lower panels (*from left to right*) show the ellipse-averaged radial profile of surface brightness, position angle, and ellipticity measured in the observed (black dots with gray error bars) and seeing-convolved modeled image (green solid line) and their corresponding difference. The surface-brightness radial profiles of the best-fit bulge (blue dashed line), disk (red dotted line), and bar component (magenta dot-dashed line) are also shown in both linear and logarithmic scale for the distance to the center of the galaxy.

In this study, the galaxy images in the r band were fit following this standard procedure with automatic initial guesses or, in some cases, fine-tuning them after a visual inspection. Once a successful fit was achieved, the best-fit parameters in the r band were used as initial guesses for the g and i bands. We found that this strategy generally produced consistent results among different bands without constraining the final photometric parameters.

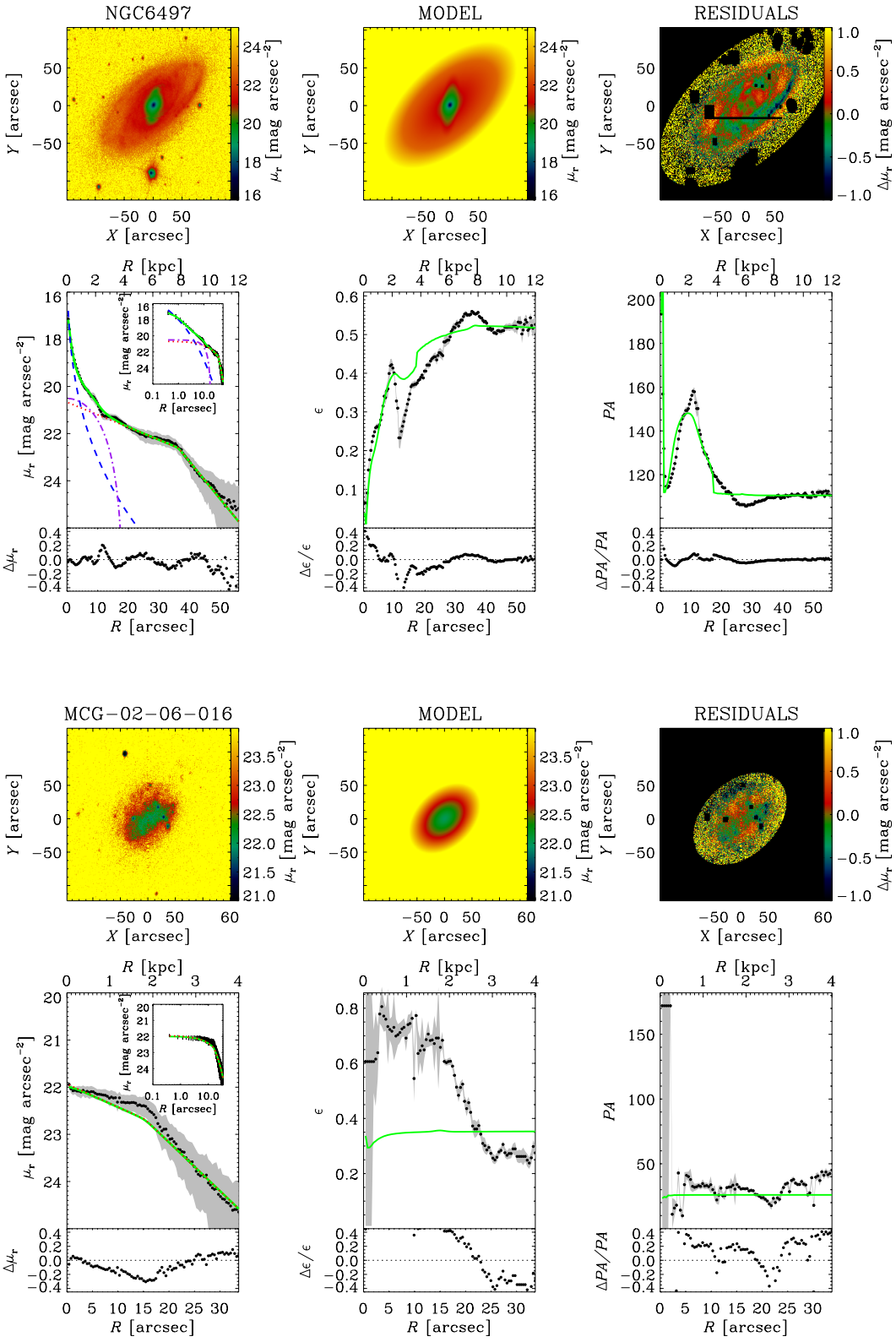

Figure 3.3: continued.

3.4.1 Early-type galaxies

The problem of model selection, that is, of selecting the most appropriate model that represents your data among a set of possibilities, is a well-studied topic in statistics (i.e., Mackay 2003). In astronomy, the photometric properties of ETGs, encompassing elliptical and lenticular galaxies, have been extensively studied in the literature (see Kormendy et al. 2009; Aguerri 2012, for reviews). However, the problem of identifying whether a stellar disk is present or not in these smooth and featureless galaxies is still under discussion (Gomes et al. 2016). From a photometric point of view, elliptical galaxies are stellar systems well described by a single Sérsic profile. On the other hand, the simplest description of a lenticular galaxy galaxy is a two-component model, that is, a Sérsic profile describing the surface brightness distribution of the bulge and a pure exponential representing the outer disk. It is worth noting that this definition is purely photometric and, therefore, it is not directly related to the dynamical status of the galaxies (see Emsellem et al. 2011).

From a photometric point of view, advances in the field have been driven by the application of statistical techniques on model selection, such as the F-test (see Simard et al. 2011, for an application), Bayesian inference criterion (BIC; Schwarz 1978), or Akaike information criterion (AIC; Akaike 1974). These techniques work by adding a penalization to the standard χ^2 accounting for the number of free parameters included in the fit. Thus, these criteria can be applied to determine whether or not adding an extra component (i.e., an outer disk) would statistically improve the best-fit (e.g., Simard et al. 2011; Head et al. 2014). On the other hand, these automatic criteria do not account for the possibility that, even if a given model is statistically preferred, its solution might be unphysical. Therefore, to provide the best mathematical fit with a physical meaning, some authors proposed the use of a 'logical filter' (Allen et al. 2006). In this Chapter we combined the two aforementioned approaches to assess the appropriateness of different model decompositions and decide when a complex model, bulge+disk, was preferred over a single Sérsic profile. The final aim was to obtain a bona-fide sample of lenticular galaxies defined in the canonical way, that is, composed of a photometric bulge dominating the central galaxy regions and an outer disk dominating the light in the galaxy outskirts.

The main features of the logical filter (Fig. 3.4) consist of classifying as elliptical galaxies

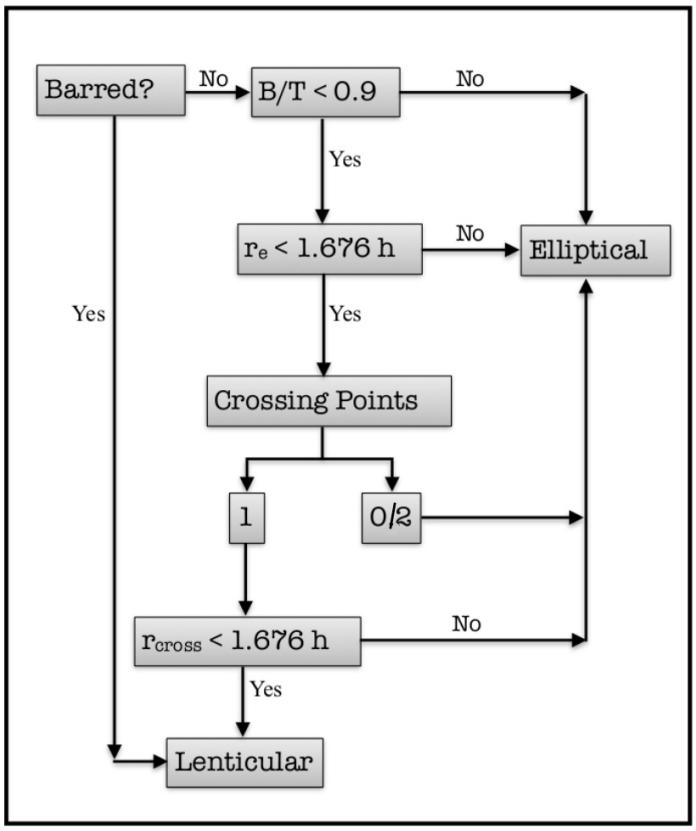

Figure 3.4: Logical filter applied to our complete sample of ETGs. Depending on the answer to each question galaxies were accepted as two-component structures (lenticular galaxies) or classified as elliptical galaxies. The term crossing point is referred to the number of times the bulge profile (Sérsic) intersects the disk profile (exponential) within the maximum radius used for the fit. $r_{\rm cross}$ indicates the radius at which this crossing point occurs.

those galaxies where two-component models produce either:

i) a large B/T ($B/T > 0.9$);

ii) a large $r_{\rm e}$ ($r_{\rm e} > 1.676\,h$);

iii) an even number (0 or 2) of crossing points between the surface brightness distribution of the disk and the bulge;

iv) the previous crossing point happening before one effective radius of the disk ($r_{\rm cross} < 1.676\,h$).

Note that galaxies hosting stellar bars were relatively easy to identify. Since bars could be used to detect the presence of stellar disks (Méndez-Abreu et al. 2010, 2012), they were

Table 3.2: Schematic of the sample selection process of ETGs.

CALIFA VISUAL (1)	L. Filter (2)	L. Filter + ΔBIC (3)	FINAL (4)
85 E	35 E	35 E	41 E 36 B/BD 50 S0
	50 S0	30 B/BD 20 S0	
42 S0	6 E	6 E	
	36 S0	6 B/BD 30 S0	

Notes. Elliptical (E), lenticular (S0), and elliptical or lenticular (B/BD) galaxies. (1) Number of galaxies using the CALIFA visual classification. (2) Number of galaxies after the logical filtering (L. Filter). (3) Number of galaxies after the logical filtering and BIC classification. (4) Final classification used in this Chapter.

directly classified as lenticular galaxies without the need to satisfy either the logical filtering or BIC criteria.

Those galaxies accepted by the logical filtering as possibly hosting two components, that is, lenticular galaxies, are then compared to the single Sérsic fit of the whole galaxy using the BIC. Under the hypothesis of normal errors, the BIC statistic can be written as

$$BIC = \chi^2 + k \ln(m)\,, \tag{3.1}$$

where k is the number of free parameters and m is the number of independent data points. Since in a galaxy image not all the pixels are independent, we followed the prescriptions of Simard et al. (2011) and substituted the number of pixels by the number of resolution elements $m_{\rm res} = m/A_{\rm PSF}$, where $A_{\rm PSF}$ is the size area of the PSF at FWHM. Then, Eq. (3.1) can be rewritten as

$$BIC = \chi^2 A_{\rm PSF} + k \ln \frac{m}{A_{\rm PSF}}\,. \tag{3.2}$$

In this scheme, models with lower values of BIC were considered the preferred models. Thus, as in Méndez-Abreu et al. (2018), we took advantage of simulated mock galaxies to set at ΔBIC = BIC(bulge) − BIC(bulge + disk) > -18 the threshold that statistically sets the distinction between elliptical and lenticular galaxies.

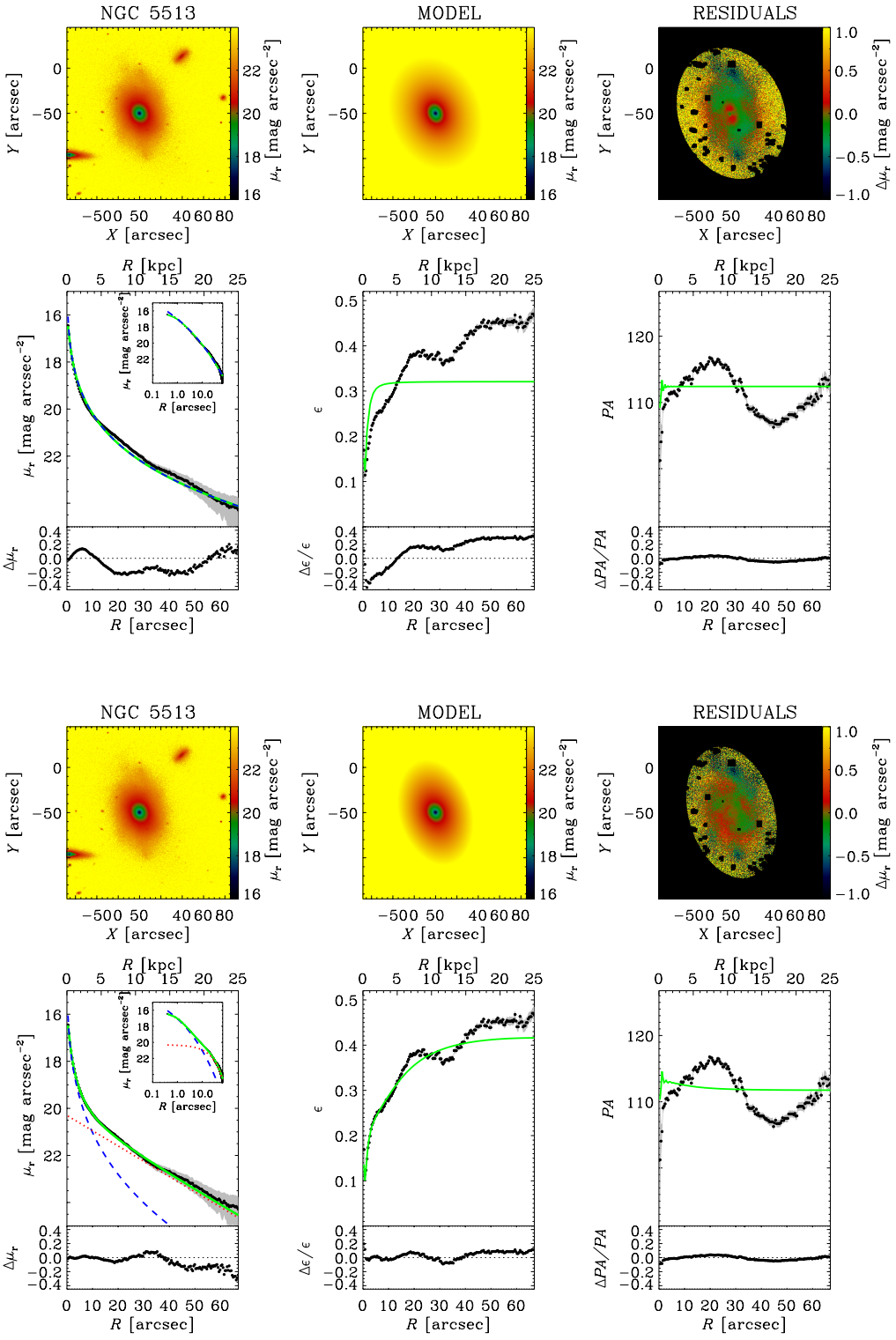

Figure 3.4: As in Fig. 3.3, but for the lenticular galaxy NGC 5513, either using a single Sérsic component (*top panels*) or a bulge+disk model (*bottom panels*).

We therefore applied this two-step process to our sample of 127 ETGs. As an example, Fig. 3.4 shows the photometric decompositions of the lenticular galaxy NGC 5513 either using a single Sérsic component or a bulge+disk model, while Table 3.2 shows the outcome of our analysis. Galaxies were first divided into elliptical and lenticular based on the outcome of the logical filter. Then, for those galaxies where the two models were compatible, the BIC analysis was performed to discern whether there was statistical evidence against one of the models or not. Still, some galaxies remained with unclear classification, equally compatible with being a single Sérsic or a two-component galaxy. Indeed, those galaxies accepted by the logical filter as two-component and with $\Delta\mathrm{BIC} < -18$ cannot be safely classified. This last sample was labeled in the tables as B/BD morphology and highlights the intrinsic difficulties of separating elliptical from lenticular galaxies using photometric data. The best-fit obtained from both the single Sérsic and the bulge+disk was provided for these galaxies to allow the users to decide which decomposition is more suitable for their science case. We ended up with a final sample of 41 elliptical galaxies, 50 lenticular galaxies, and 36 galaxies with B/BD morphology.

3.4.2 Spiral galaxies

The final decomposition of our CALIFA sample of spiral galaxies was performed using a human-supervised approach fitting up to three components: bulge/NPS, disk (including double-exponential profiles), and bar. For each galaxy, a given combination of these structures provided the best-fit.

Small bulges with sizes comparable to the SDSS PSF can lead to erroneous fits, usually producing extreme values of the Sérsic index ($n > 7$). Although one of our goals was to produce reliable estimates of the bulge parameters, high values of n might also had a significant impact on the parameters of the other components. Therefore, we also fit these galaxies using a NPS instead of the Sérsic parameterization for the bulge. A visual inspection of the two-dimensional residual was then used to determine which component was preferred. As a consequence, a bulge and a NPS would never be fit simultaneously in the same galaxy, and galaxies better represented by a NPS should not be understood as necessarily hosting a nuclear star cluster or AGN. GASP2D also allowed for different behaviors of the

Table 3.3: Different combinations of structures present in the photometric decomposition of our sample galaxies.

Structure	Number
(1)	(2)
B	43
D	6
BD	74
ND	12
BD_{br}	67
D_{br}	4
BDBar	88
DBar	7
NDBar	10
BD_{br}Bar	47
D_{br}Bar	3
ND_{br}Bar	5
BDBarNBar	2
B/BD	36

Notes (1) Type of structure. B: single Sérsic, D: pure disk, BD: bulge+disk, ND: nuclear point source+disk, BD_{break}: bulge+disk with double-exponential profile, D_{break}: pure disk with double-exponential profile, BDBar: bulge+disk+bar, DBar: disk+bar, NDBar: nuclear point source+disk+bar, BD_{break}Bar: bulge+disk with double-exponential profile+bar, D_{break}Bar: disk with double-exponential profile+bar, ND_{break}Bar: nuclear point source+disk with double-exponential profile+bar, BDBarNBar: bulge+disk+bar+nuclear bar, B/BD: either single Sérsic or bulge+disk. (2) Number of galaxies.

outer disk component (Type I, Type II, and Type III). Our CALIFA sample was fit using 13 different combinations of the previous structures (see Table 3.3). This demonstrated the morphological variety of our galaxies and the necessity of performing accurate multi-component photometric decompositions.

In Sect 3.4.1 we described the particular case of fitting ETGs. The detection of stellar disks in spiral galaxies was more direct than for ETGs due to the presence of star formation following the characteristic spiral pattern. The strategy followed to perform the photometric decomposition of a spiral galaxy started with a two-component bulge+disk fit. Right after, or from the start if its presence was readily apparent in the galaxy image, we checked for the addition of a bar component (see Sect 3.4.2.1). If the bar was not obvious in the galaxy image, both the bulge+disk and bulge+disk+bar fitting solutions were performed. Then, a careful visual analysis of the two-dimensional surface-brightness distribution residuals, as well of the one-dimensional ϵ and PA profiles (see Aguerri et al. 2009, for a description of

bar identification through the galaxy ϵ and PA) was carried out to reveal whether a bar was actually present or not. It is worth noting that the detection of bars was limited to those central structures with an axial ratio $q_{\rm bar} < 0.7$. The next step was to check for the presence of double-exponential disks and, if the following conditions were fulfilled, included them in the fit:

i) after a careful revision of the two-dimensional surface-brightness distribution residuals we confirmed potential double-exponential profiles were not misidentified with spiral arms and/or outer rings;

ii) they appeared at a surface brightness level $\mu_i < 24$ mag arcsec^{-2} so they could be robustly measured with the SDSS imaging.

The different combinations of structures used for our final sample galaxies are shown in Table 3.3. In the following Sections we will describe the incidence of the different galaxy structures in the CALIFA sample.

3.4.2.1 Barred galaxies

The inclusion of the bar surface brightness distribution in the photometric decomposition has been proven to be critical in order to recover accurate bulge parameters (e.g., Aguerri et al. 2005; Laurikainen et al. 2005). Several studies have shown that both the Sérsic index and B/T can artificially increase if the bar is not properly accounted for in the fit (Gadotti 2008; Salo et al. 2015).

It is worth noting that the inclusion of a stellar bar in our photometric decomposition was independent of the visual morphological classification (see Walcher et al. 2014, for details). Therefore, we could quantify the impact of different bar classification methods on studies of the galaxy bar fraction. Fig. 3.5 shows the distribution of the bar fraction either using the visual classification or the photometric decomposition method with respect to the galaxy Hubble type and stellar mass. In addition, we included the volume-corrected bar fractions for the photometric decomposition method applied to those galaxies extracted from the CALIFA mother sample (see Section 3.2). A summary of the results is presented in Table 3.4. In general, we found a good agreement in the observed bar fractions obtained using the visual and photometric decomposition method. The uncertainty in the visual identification of a bar

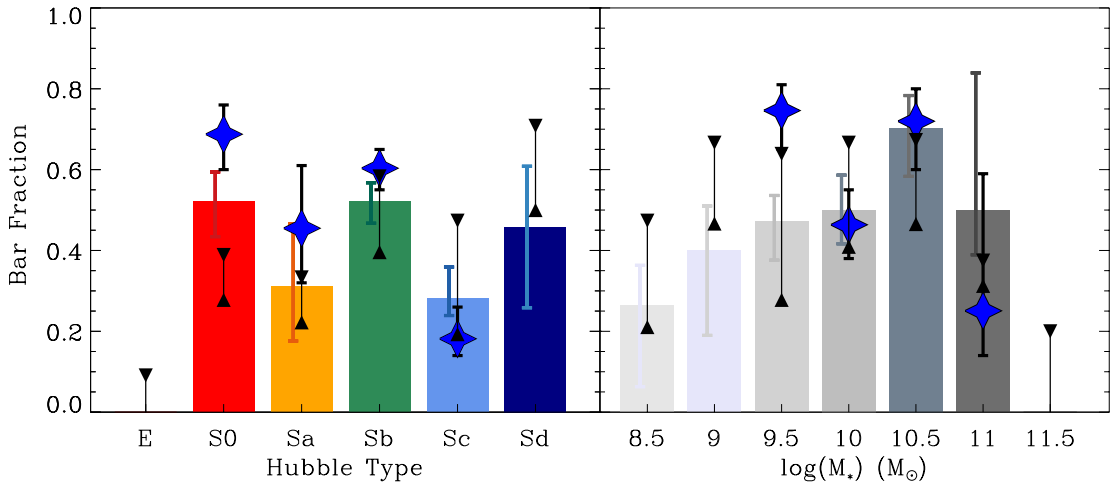

Figure 3.5: Distribution of the bar fraction as a function of the Hubble type (*left panel*) and stellar mass (*right panel*). Color bars represent the photometric bar fraction derived from this study. Lines with darker colors show the 1σ rms. Blue stars show the volume-corrected bar fraction using only those galaxies drawn from the mother sample and with luminosities within the CALIFA completeness limits (285 galaxies). The black lines represent the visual classification from Walcher et al. (2014) with the upper limits including both weak (AB) and strong (B) bars and the lower limit accounting only for strong bars. Note that since the Walcher et al. (2014) Hubble type and bar identification are the average among different independent classifications, some elliptical galaxies were classified as weakly barred. Bins with less than 5 galaxies are not shown.

was enough to account for the differences with respect to the photometric decompositions for all cases except for the galaxies classified as S0 and Sd. In the case of the lenticular galaxy, not only the presence of a bar but also the morphological classification as S0 itself depends on the method (see Section 3.4.1). We attributed the differences in the Sd galaxies to the small number statistics (only 24 galaxies are Sd). The volume corrected fractions could deviate substantially from the estimates from the photometric decomposition method.

The influence of galaxy morphology on the bar fraction has been extensively discussed in the literature with contradictory results. Several authors have claimed that the bar fraction increases toward ETGs (Masters et al. 2011, 2012; Lee et al. 2012) with this trend being consistent with some models of bar formation and evolution (Athanassoula et al. 2013). Nevertheless, other studies have found the opposite trend with Hubble type (Laurikainen et al. 2007; Barazza et al. 2008; Aguerri et al. 2009; Buta et al. 2015). Our volume-corrected bar fraction was relatively constant for early-type disk galaxies (S0, Sa, and Sb) but it dramatically dropped for Sc galaxies. Unfortunately, small number statistics for the Sd type

Table 3.4: Volume-corrected bar fraction distribution in our sample galaxies.

Hubble Type	Bar fraction
S0	68.7% ± 7.2%
Sa	45.5% ± 15.5%
Sb	60.3% ± 4.7%
Sc	18.2% ± 7.8%
Sd	–
Stellar Mass	**Bar fraction**
$9 < \log(M_\star/\mathrm{M}_\odot) < 9.5$	–
$9.5 < \log(M_\star/\mathrm{M}_\odot) < 10$	74.6% ± 6.4%
$10 < \log(M_\star/\mathrm{M}_\odot) < 10.5$	46.4% ± 8.6%
$10.5 < \log(M_\star/\mathrm{M}_\odot) < 11$	72.0% ± 8.0%
$11 < \log(M_\star/\mathrm{M}_\odot) < 11.5$	25.1% ± 22.1%

precluded further analysis of that bin, so we could not confirm the drop in the bar fraction for all late-type galaxies. We found a mean value for the volume-corrected bar fraction of 57%. This number was similar to that obtained using the observed sample (54%) and visual classification (51%). Recently, Buta et al. (2015) found a lower bar fraction in ETGs (56%) than in late-type galaxies (80%) using a visual classification of the S^4G sample galaxies (Sheth et al. 2010). They suggested that the different mass distribution of galaxies with both early- and late-type morphologies could, however, be driving this result.

In fact, the previous, apparently contradictory results could be reconciled when the galaxy stellar mass was accounted for in the sample selection (Nair & Abraham 2010). The incidence of bars in galactic disks is a strong function of stellar mass with a maximum bar fraction at $M_\star \sim 2\times10^9$ $\mathrm{M}_\odot$ for field galaxies (Méndez-Abreu et al. 2010, 2012). The volume corrected fraction showed an increase of the bar fraction toward lower stellar masses. This trend is in good agreement with the results of Méndez-Abreu et al. (2012), although the CALIFA sample is not complete at $M_\star \sim 10^9$ $\mathrm{M}_\odot$, where the bar incidence is predicted to be highest. The observed bar fraction showed a different picture, being nearly independent of stellar mass within the errors for both the visual and photometric decomposition method.

An interesting subsample of barred systems contained nested bars, that is, galaxies hosting both a large-scale bar (described previously) and an inner, secondary bar embedded in the main one (Erwin & Sparke 2002; Corsini et al. 2007; de Lorenzo-Cáceres et al. 2012,

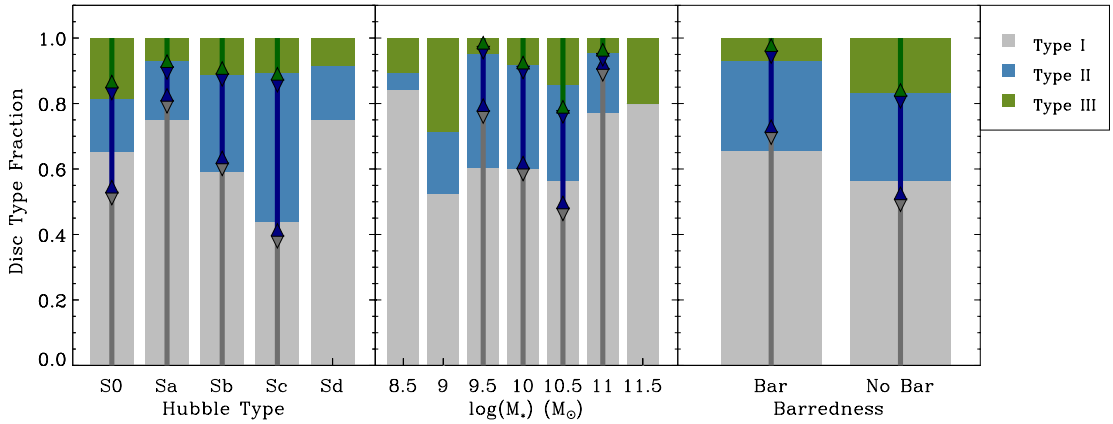

Figure 3.6: Distribution of the three different disk profiles used in this study with Hubble type (*left panel*), stellar mass (*middle panel*), and presence of a bar (*right panel*). Color bars represent our observed fractions for Type I (gray), Type II (blue), and Type III (green). Lines with darker colors show the volume corrected fraction. Bins with less than 5 galaxies are not represented.

2013). Whilst they were not the main focus of this analysis, they were thought to be present in ∼30% of barred galaxies (Laine et al. 2002; Erwin 2004) and might had an impact on the bulge parameters (de Lorenzo-Cáceres et al. in prep). Therefore, when necessary we included a secondary bar using another Ferrers profile in our photometric decomposition. We found only two galaxies with nested bars; NGC 23 and NGC 7716, which represented a much lower fraction (1.5%) with respect to previous findings. Angular resolution likely explained these differences. The sample presented in Erwin (2004) is located at an average distance of 29 Mpc (0.144 kpc arcsec^{-1}), with some of the inner bars detected by using imaging from the HST Wide Field Planetary Camera 2 (WFPC2) with a typical 0.07 arcsec resolution. On the other hand, our sample of barred galaxies was located at 72 Mpc (0.346 kpc arcsec^{-1}) limited to the ∼ 1.1 arcsec SDSS resolution. Thus, a low double-bar fraction was expected in our sample.

3.4.2.2 Double-exponential profiles in disk galaxies

Galactic disks with double-exponential profiles represent an important fraction of the disks in the local Universe and are known to appear in galaxies independently of their Hubble type (e.g., Erwin et al. 2008; Gutiérrez et al. 2011; Marino et al. 2016). The ubiquity of stellar disks with double-exponential profiles is manifest even at high redshift (Pérez 2004; Trujillo & Pohlen 2005; Azzollini et al. 2008), suggesting that they are key features in understanding

Table 3.5: Volume corrected distribution of disk type in our sample galaxies.

Hubble Type	Type I	Type II	Type III
S0	52.8%	32.1%	15.1%
Sa	80.8%	10.3%	8.9%
Sb	61.7%	27.3%	11.0%
Sc	39.6%	47.7%	12.7%
Sd	–	–	–
Stellar Mass	Type I	Type II	Type III
$9 < \log(M_\star/\mathrm{M}_\odot) < 9.5$	–	–	–
$9.5 < \log(M_\star/\mathrm{M}_\odot) < 10$	77.7%	21.7%	0.6%
$10 < \log(M_\star/\mathrm{M}_\odot) < 10.5$	60.1%	33.1%	6.8%
$10.5 < \log(M_\star/\mathrm{M}_\odot) < 11$	48.0%	31.8%	20.2%
$11 < \log(M_\star/\mathrm{M}_\odot) < 11.5$	90.6%	6.6%	2.8%
Barredness	Bar fraction		
Bar	71.2%	24.9%	3.9%
No Bar	50.8%	31.6%	17.6%

how galaxies form and evolve.

From the photometric decomposition point of view, double-exponential profiles have an impact on the properties of the remaining components included in the fit (Kim et al. 2014). Therefore, a complete and robust analysis of the photometric properties of galaxies must include the possibility of disk galaxies displaying double-exponential profiles. Previous studies of the light distribution in the galaxy outskirts have mainly been based on the analysis of one-dimensional azimuthally averaged profiles, and thus are not representative of the two-dimensional nature of the problem of galaxies. GASP2D is able to perform a multi-component decomposition of the galactic light including double-exponential profiles and this work is a pioneering study on the incidence of double-exponential profiles in disk galaxies based on the two-dimensional approach.

Fig. 3.6 shows the distribution of the different disk profiles as a function of the Hubble type, stellar mass, and presence of a bar. We found that 62%, 28%, and 10% of our volume corrected sample of disk galaxies was best represented with a Type I, Type II, and Type III, respectively. This represented a significantly lower fraction of double-exponential disk profiles when compared to one-dimensional analyses present either in the literature (e.g., Gutiérrez et al. 2011; Laine et al. 2014) or in the CALIFA sample (Marino et al. 2016; Ruiz-

Lara et al. 2017). We performed a detailed analysis to understand these differences and concluded that the discrepancy was mainly caused by our new two-dimensional approach instead of due to selection effects in the sample galaxies. In general, multi-component two-dimensional decompositions build the galaxy model as a combination of different galaxy components that contribute differently to the total luminosity depending on the galactocentric radius. This is important in regions with a strong overlap of the components, such as the area where the bulge, disk, and bar coexist. On the contrary, most of the previous studies using one-dimensional profiles used pre-defined regions of the surface brightness profile where a single exponential is fit, without taking into account any superposition with other galaxy components (see Muñoz-Mateos et al. 2013 for an estimation of errors associated to the pre-defined disk regions). This different methodology leads to a higher fraction of double-exponential profiles in one-dimensional analysis (in particular Type II), since it is straightforward to accommodate piecewise exponentials to different sections of the profile, but it is not straightforward to associate these piecewise exponentials with an actual change in disk structure. At the same time, Type III profiles usually occur at lower surface brightness than Type II (Pohlen & Trujillo 2006), so they are intrinsically more difficult to identify. In two-dimensional multi-component analysis the addition of this new structure (i.e., two new free structural parameters $r_{\rm break}$ and $h_{\rm out}$) is not always justified in statistical terms, whereas one-dimensional analysis methods can easily deal with fitting a pre-defined region even if at low surface brightness.

The differences of this work with respect to previous studies lie not only in the different techniques (one-dimensional vs. two-dimensional), but also in the different samples under analysis. The sample analyzed in Pohlen & Trujillo (2006) consisted of 94 late-type spiral galaxies (11% Type I, 66% Type II, and 33% Type III), whereas Erwin et al. (2008) and Gutiérrez et al. (2011) analyzed 66 barred (27% of Type I, 42% Type II, and 24% Type III) and 47 unbarred (28% of Type I, 21% Type II, and 51% Type III) early-type disk galaxies, respectively. Fig. 3.6 shows that, according to our two-dimensional approach, the fraction of Type I profiles decreases with later Hubble types whereas the fraction of Type II profiles increases (with the exception of Sd galaxies) in agreement with previous findings using one-dimensional analyses (although with different fractions). For Type III profiles, we found that the fraction of galaxies displaying this profile remained constant with Hubble type. No

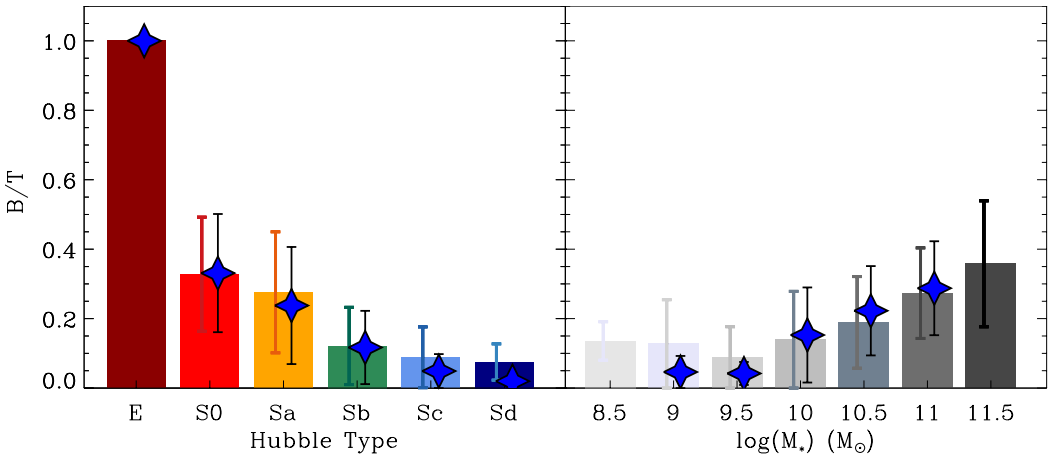

Figure 3.7: Distribution of the B/T luminosity ratio with Hubble type (*left panel*) and stellar mass (*right panel*). Color bars represent the mean values of B/T for the observed distributions. Lines with darker colors show the 1σ rms. Blue stars show the volume-weighted mean values of the B/T ratios with its corresponding 1σ rms. Elliptical galaxies have been excluded from the distribution in the right panel. Bins with less than 5 galaxies are not represented.

significant trends were found in terms of the stellar mass or presence of a bar in agreement with Marino et al. (2016). A summary of our results is shown in Table 3.5.

3.4.2.3 Nuclear point sources and pure disk galaxies

There is compelling evidence that low B/T and pure disk galaxies are common in the local Universe, especially in low-mass or late-type galaxies (Böker et al. 2002; Salo et al. 2015). Recent works using large samples of galaxies drawn from the SDSS survey have found that 15–20% of disk galaxies out to $z \sim 0.03$ appear as pure disks (Kautsch et al. 2006; Barazza et al. 2008; Kautsch 2009). The high observational incidence of both pure disks and low B/T galaxies in the local Universe is challenging for cosmological galaxy formation simulations to reproduce (Abadi et al. 2003; Governato et al. 2004; Peebles & Nusser 2010) and only recently, galaxies with realistic B/T distributions have been obtained (see Brooks & Christensen 2016, for a review).

Fig. 3.7 shows the distribution of B/T as a function of the Hubble type and galaxy mass. The relative size of the bulge with respect to the galaxy is one of the primary features that distinguishes different Hubble types, therefore the drop of B/T from early- to late-type galaxies is not surprising. Our result was also quantitatively in agreement with previous works in the literature. Indeed, Laurikainen et al. (2010) found a decline in the mean

Table 3.6: Volume-corrected B/T distribution in our sample galaxies.

Hubble Type	$\langle B/T \rangle$
S0	0.33 ± 0.16
Sa	0.24 ± 0.17
Sb	0.12 ± 0.11
Sc	0.05 ± 0.09
Sd	0.02 ± 0.05
Stellar Mass	$\langle B/T \rangle$
$9 < \log(M_\star/\mathrm{M}_\odot) < 9.5$	0.05 ± 0.13
$9.5 < \log(M_\star/\mathrm{M}_\odot) < 10$	0.05 ± 0.09
$10 < \log(M_\star/\mathrm{M}_\odot) < 10.5$	0.15 ± 0.14
$10.5 < \log(M_\star/\mathrm{M}_\odot) < 11$	0.22 ± 0.13
$11 < \log(M_\star/\mathrm{M}_\odot) < 11.5$	0.29 ± 0.13

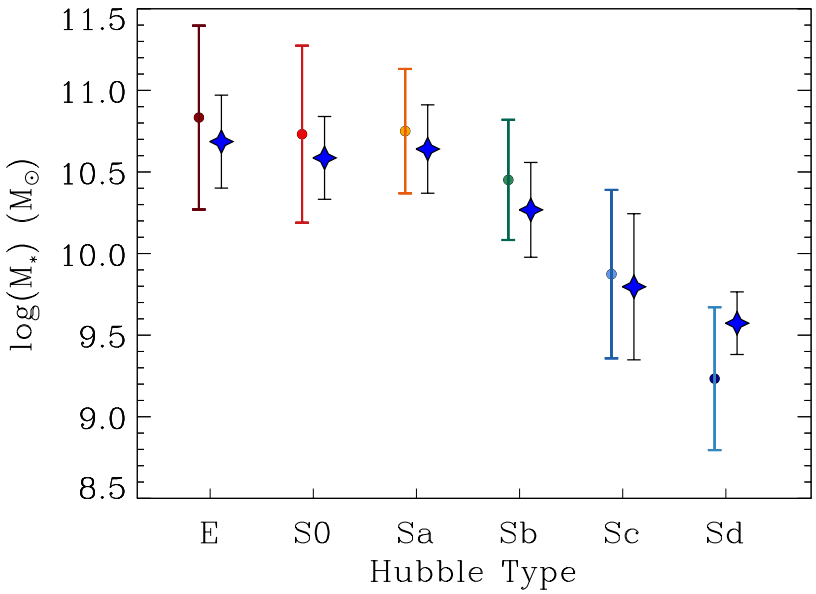

Figure 3.8: Distribution of galaxy stellar mass with Hubble type for our sample galaxies. Color points and bars represent the mean values and 1σ rms of stellar mass for the observed distributions. Blue stars show the volume-weighted mean values of the mass with its corresponding 1σ rms.

B/T values from 0.32 to 0.07 for S0 and Sd galaxies, respectively. Similar values were more recently obtained by Salo et al. (2015) and were consistent with our volume corrected measurements of 0.33 and 0.02 for S0 and Sd galaxies, respectively (see Table 3.6 for a summary of the B/T values). We also found a clear trend of B/T increasing with the galaxy stellar mass for the volume corrected sample (right panel on Fig. 3.7). Nonetheless, these

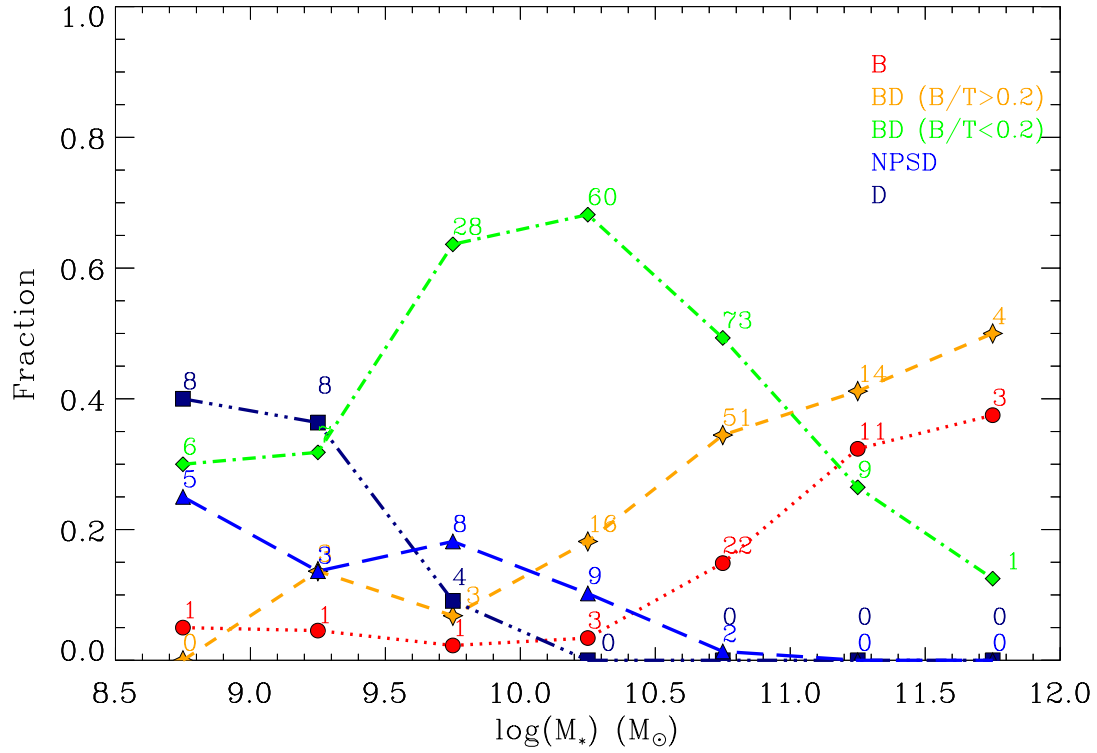

Figure 3.9: Fraction of the final models used in the photometric decomposition as a function of stellar mass. Red circles represent single Sérsic models (B). Orange stars show models composed of a bulge+disk (BD) with $B/T > 0.2$. Green diamonds display models composed of a bulge+disk with with $B/T < 0.2$. Navy blue squares show models with no bulge but pure disk (D). Blue triangles represent models with a NPS+disk (NPSD). The 5 different combinations of structures include double-exponential profiles and/or bars. The number of galaxies in each bin is also shown.

two relations were not completely independent since, in our sample, later Hubble types were systematically less massive than early types (Fig. 3.8). This trend between the Hubble type and stellar mass held for the observed, but also for the volume corrected quantities, and was already found by Huertas-Company et al. (2011) and Torres-Papaqui et al. (2012).

We found that 24% and 76% of our volume-corrected disk galaxies have $B/T > 0.2$ and $B/T < 0.2$, respectively. The relative fraction of galaxies with different B/T imposes strong constraints on the galaxy evolution scenarios. Weinzirl et al. (2009) found that 34% and 66% of their high-mass ($\log(M_\star/\mathrm{M}_\odot) > 10$) sample spiral galaxies have $B/T > 0.2$ and $B/T < 0.2$, respectively. Limiting our sample to this mass limit, we found that 36% and 64% of our volume-corrected disk galaxies have $B/T > 0.2$ and $B/T < 0.2$, respectively, in remarkably good agreement with Weinzirl et al. (2009).

Fig. 3.9 shows the fraction of the final decomposition models used to represent our sample galaxies as a function of the stellar mass. Here, we focused on the incidence of bulge components in the photometric decomposition, and therefore we grouped together all possible model combinations (see Table 3.1) in 5 groups depending only on their central component, and neglecting other structures such as double-exponential disk profiles or bars:

i) galaxies well represented by a single Sérsic model (42 elliptical galaxies);

ii) bulge+disk galaxies with $B/T > 0.2$ (91 galaxies);

iii) bulge+disk galaxies with $B/T < 0.2$ (184 galaxies);

iv) galaxies with no bulge and pure disk (22 galaxies);

v) galaxies with a NPS+disk (27 galaxies).

Fig. 3.9 shows a clear segregation of galaxy types depending on their stellar mass. The fractions of single Sérsic and bulge+disk with $B/T > 0.2$ galaxies steadily increase with galaxy mass. Indeed, they are the dominant population of galaxies with $M_\star > 10^{11}$ $M_\odot$. On the other hand, bulge+disk with $B/T < 0.2$ galaxies are the preponderant galaxy population in the mass range $10^{9.5} < M_\star/M_\odot < 10^{11}$, whilst galaxies with negligible bulges, both pure disk and NPS+disk models, prevail at low masses $M_\star < 10^9$ $M_\odot$.

3.5 Quality assessment and photometric uncertainties

Determining the uncertainties in the photometric parameters in multi-component decompositions such as the one presented in this Chapter is a complicated task. Here, we described our attempts to provide meaningful uncertainties for the different parameters using two different approaches: a visual quality control analysis and quantitative error measurement based on mock galaxies.

3.5.1 Visual quality check

The galaxies in this analysis are drawn from the CALIFA DR3 sample by applying two main criteria: i) they are not interacting or merging and ii) they are relatively face-on

($\theta \lesssim 70$), as stated in Section 3.2. However, there could still be issues related either to the original SDSS imaging, the presence of strong extra components not included in the fit (spiral arms or rings), or difficulties inherent to the fitting process that can compromise the quality of the final decomposition. In order to assess the reliability of the fits and to quantify the incidence of these issues in our sample galaxies, we carried out a visual check of each individual fit assigning a 'quality flag', that is provided in the tables together with the results of the decompositions (see Table 3.1, for an example).

The quality flag is defined as a number (1, 2, 3, or 4) followed by a letter (a, b, or c). Different numbers correspond to galaxies with:

(1) both good imaging and no other strong extra galaxy components affecting the fit;

(2) good imaging but strong extra components that might influence the final fit;

(3) poor imaging but no strong extra components affecting the final fit;

(4) poor imaging and strong extra components affecting the final fit.

We referred to problems with the original imaging as those due to the presence of other bright galaxies whose stellar haloes overlapped with our galaxy, and/or strong fluctuations of the local sky background around the galaxy.

The different letters are related to the fitting process. Due to the highly degenerate parameter space we were dealing with (some fits include up to 17 free parameters), in some cases it was not possible to achieve a reasonable fit without fixing some parameters to a value given by our one-dimensional analysis. We assigned the letter:

(a) if all the parameters were free to vary during the fitting process;

(b) if only geometrical parameters such as PA or ϵ were kept fixed;

(c) whenever we also needed to fix size-related quantities.

This quality check classification scheme for each galaxy was performed by at least two reviewers. In the case of disagreement, another reviewer checked the quality flag and provided the final classification. The number of galaxies with each particular flag is shown in Table 3.7.

Table 3.7: Results from the visual quality check of the photometric decompositions.

Flag number (1)	Flag letter (2)	Number (3)
1	a	190
	b	14
	c	122
2	a	22
	b	5
	c	26
3	a	13
	b	0
	c	10
4	a	1
	b	0
	c	1

Notes (1) Different numbers represent galaxies with both good imaging and no other strong extra components (spiral arms or rings) affecting the fit (flag 1), good imaging but strong extra components that can influence the final fit (flag 2), poor imaging but no strong extra components affecting the final fit (flag 3) and poor imaging and strong extra components (flag 4). (2) Different letters represent whether or not: (a) all the parameters are allowed to vary during the fitting process, (b) only geometrical parameters such as PA or ϵ are kept fixed, and (c) size-related quantities are also fixed.

Only 6% of the images were classified as poor quality and 14% presented strong extra components that might significantly affect the fit. On the other hand, 58% of the fits were performed allowing all the parameters to vary during the fit. This highlights the high level of convergency in our fits since 73% of our models require the constraint of more than 10 parameters. Regarding those fits with fixed quantities, only 5% of the fits required the ellipticities or PA of any of the components to be fixed to the values obtained from the one-dimensional radial profiles. However, 37% of the fits have been performed fixing a size-related quantity of the model. We found that in approximately half of these cases the fixed parameter was the break radius of the disk in the Type II and Type III profiles. As explained in Section 3.4.2.2, constraining the parameters of double-exponential disk profiles in a multi-component decomposition is not straightforward, but it is the only way to consistently compare with the other galaxy structures. It is worth noting that fixing the break radius did not affect our classification nor the results shown in Section 3.4.2.2.

3.5.2 Statistical and systematic errors

The formal errors obtained from the minimization procedure are usually not representative of the real errors on the fitted parameters (Méndez-Abreu et al. 2008a). This is mainly because possible covariance terms are neglected in the error computation process. Therefore, to provide our structural parameters with a robust error estimate we carried out different tests applying MC techniques to mock galaxies. This procedure allowed us to improve both the accuracy of our error estimates, avoiding the otherwise necessary exploration of the full parameter space to account for the covariance of the parameters, and to determine the observational limits of our photometric decomposition.

We devised a set of tailor-made simulations for each combination of structures fit to our sample galaxies (see Table 3.3). For each set, we simulated 500 mock galaxies with structural parameters constrained within the limits of our real sample galaxies. For the sake of simplicity we assumed the i-band parameters as representative of our galaxies. Altogether we created 7000 mock galaxies that were built in the following way. First, the total apparent magnitude of the galaxy was randomly selected within the observed range m_i = [11, 14] mag. Then, the values of the relative luminosity ratios of the bulge (B/T), disk (D/T), bar (Bar/T), and NPS (NPS/T) were set according to the observed values for each combination of structures. The distribution of the luminosity ratios also matched that of the real galaxies, and a given luminosity was associated to each structure. The interval ranges for the size and shape parameters for each structure covered by our simulations are: $r_{\rm e}$ = [0.9, 14] arcsec, n = [0.5, 5], h = [4, 25] arcsec, $r_{\rm break}$ = [16, 50] arcsec, $h_{\rm out}$ = [4, 25] arcsec, and $a_{\rm bar}$ = [5, 30] arcsec. Once the mock galaxy structure was defined, the values of the surface brightness for the bulge ($\mu_{\rm e}$), disk (μ_0), bar ($\mu_{0,\,\rm bar}$), and NPS ($\mu_{0,\,\rm nps}$) were derived using the equations to compute the total luminosity for each analytical representation of the galaxy structure (see Section 2.1.1). Finally, the axial ratio of the bulge ($q_{\rm bulge}$), disk ($q_{\rm disk}$), and bar ($q_{\rm bar}$) components as well as the value of the position angle of the bulge ($PA_{\rm bulge}$), disk ($PA_{\rm disk}$), and bar ($PA_{\rm bar}$) were generated from a random uniform distribution, where no constraints were adopted. In the particular case of the double barred galaxies the typical values for the mock galaxy generation were obtained from de Lorenzo-Cáceres et al. (in prep).

Mock galaxies were placed at a distance of 67 Mpc that corresponded to the median value

of our real sample. The galaxy models were then convolved with the mean PSF of the i-band SDSS images (see Section 3.3) to reproduce the typical spatial resolution. In addition, we adopted the pixel scale (0.396 arcsec px^{-1}), typical values of the CCD gain (4.86 e$^-$ ADU^{-1}), and RON (5.76 e$^-$) to mimic the instrumental setup of the SDSS data. Finally, a background and photon noise were added to the artificial images to yield a signal-to-noise ratio (S/N) to match the observed one.

The mock galaxies were then fit using GASP2D as if they were real galaxies. The comparison between the input and output values of the fitted parameters was used to compute the errors. Mock galaxies were split into three different bins of magnitude ($11 < m_i < 12$ mag, $12 < m_i < 13$ mag, $13 < m_i < 14$ mag). In each bin, the mean and the standard deviation of the relative errors were adopted as the systematic and statistical errors for the observed galaxies for the parameters ($\mu_{\rm e}$, $r_{\rm e}$, n, μ_0, h, $h_{\rm out}$, $r_{\rm break}$, $\mu_{0,\,\rm bar}$, $a_{\rm bar}$, $\mu_{0,\,\rm nps}$), whereas the mean and standard deviation of the absolute errors were adopted as the systematic and statistical errors for the observed galaxies for the set ($q_{\rm bulge}$, $PA_{\rm bulge}$, $q_{\rm disk}$, $PA_{\rm disk}$, $q_{\rm bar}$, $PA_{\rm bar}$). Since the systematic errors were generally smaller than the statistical errors they were added in quadrature. Errors were then assigned to each galaxy depending on its apparent magnitude. The final errors for each parameter are included in Table 3.1.

3.6 Photometric decomposition and synergies with the CALIFA survey

The detailed photometric description of the galaxy structures results critical to properly deal with the IFS information provided by the CALIFA survey. Indeed, some of the information presented in this Chapter has already been used within the collaboration, combining the accuracy of the photometric analysis with the potential of spatially resolved spectroscopic data.

Sánchez-Menguiano et al. (2016) analyzed the radial oxygen abundance gradient of the arm and interarm star forming regions of 63 face-on spiral galaxies to shed some light onto the mechanism responsible for generating the spiral structure. We morphologically separated the sample into flocculent versus grand design spiral galaxies (Elmegreen & Elmegreen 1982, 1987) and barred versus unbarred galaxies. However, the best characterization of the

spiral pattern needed a deprojection of the galaxy disk; this was performed by means of the two-dimensional photometric decomposition results provided in this Chapter. We found subtle but statistically significant differences between the arm and interarm distributions for flocculent galaxies, suggesting that the mechanisms generating the spiral structure in these galaxies may be different to those producing grand design systems, for which no significant differences are found. We also found small differences in barred galaxies, not observed in unbarred systems, hinting that bars may affect the chemical distribution of these galaxies but not strongly enough as to be reflected in the overall abundance distribution. In light of these results, we proposed bars and flocculent structures as two distinct mechanisms inducing differences in the abundance distribution between arm and interarm star forming regions.

Ruiz-Lara et al. (2017) investigated the role of radial migration on the light distribution and the radial stellar content by comparing the inner color, age, and metallicity gradients for galaxies with different surface brightness profiles. We defined these inner parts avoiding the bulge and bar regions and up to around three disk scale lengths (Type I profile) or the break radius (Type II and Type III profiles). We made use of photometric data presented in this Chapter to characterize the light distribution of 214 CALIFA spiral galaxies and to obtain color profiles. The stellar age and metallicity profiles were computed using a methodology based on full-spectrum fitting techniques, that is, pPXF, GANDALF, and STEllar Content and Kinematics via Maximum A Posteriori likelihood (STECKMAP; Ocvirk et al. 2006a,b), to the IFS CALIFA data. We found a trend in which Type II galaxies show the steepest profiles of all and Type III the shallowest, with Type I galaxies displaying an intermediate behavior. These results are consistent with a scenario in which radial migration is more efficient for type III galaxies than for Type I systems with Type II galaxies presenting the lowest radial migration efficiency. In such scenario, radial migration mixes the stellar content flattening the radial stellar properties and shaping different surface brightness profiles. However, in light of these results we could not further quantify its importance in shaping spiral galaxies, and other processes such as recent star formation or satellite accretion might play a role.

Kalinova et al. (2017) presented a new galaxy classification system for 238 CALIFA galaxies (E1–Sdm) based on the shapes and amplitudes of their circular velocity curves (CVCs). We inferred the CVCs from the deprojected surface brightness of the galaxies

obtained in this Chapter, after scaling by a constant mass-to-light ratio based on stellar dynamics. We solved axisymmetric Jeans equations via fitting the second velocity moment $v_{\rm rms} = \sqrt{v^2 + \sigma^2}$ of the stellar kinematics. We used principal component analysis applied to the CVC shapes to find characteristic features and separated circular curves into 4 different classes: slow-rising, flat, round-peaked, and sharp-peaked circular curves. We found that slow-rising profiles are typical for low-mass, late-type (Sb–Sdm), young, faint, metal-poor and disk-dominated galaxies. Sharp-peaked curves are typical for high-mass, early-type (E1–E7), old, bright, metal-rich and bulge-dominated galaxies. Finally, flat and round-peaked profiles are typical for galaxies with intermediate mass, age, luminosity, metallicity, B/T and morphologies (E4–S0a, Sa–Sbc). This new classification based on circular velocity curves presents an alternative to typical morphological classification and appears more tightly linked to galaxy evolution.

Catalán-Torrecilla et al. (2017) estimated the current extinction-corrected Hα star formation rate (SFR) of the different morphological components that shape galaxies (bulges, bars, and disks). We combined the multi-component photometric decomposition from this Chapter with the spectral information from the CALIFA datacubes for a sample of 219 galaxies. This analysis reveals an enhancement of the central SFR and specific SFR (sSFR = SFR/$M_\star$) in barred galaxies. Along the Main Sequence, we found that more massive galaxies have undergone efficient quenching of their star formation. We discovered that more massive disks have had their star formation quenched as well. The presence of type-2 AGNs (Seyfert/LINER) seems to play a role at damping the sSFR in bulges and less efficiently in disks. Moreover, the decrease in the sSFR of the disk component becomes more noticeable for stellar masses around $10^{10.5}$ $M_\odot$; for bulges, it is already present at $M \sim 10^{9.5}$ $M_\odot$. The analysis of the velocity dispersion of the bulge component and of the corresponding FJR shows that AGNs tend to have slightly higher velocity dispersion values than star-forming galaxies for the same mass. Finally, we also evaluated the impact of the environment, finding that the SFR of both bulges and disks decreases in intermediate-to-high density environments.

Finally, Méndez-Abreu et al. (2018) combined the accurate two-dimensional multi-component photometric decomposition provided in this Chapter with the 2D kinematic properties of bulges in 28 nearby lenticular galaxies to shed light on their formation scenario. We performed mock spectroscopic simulations mimicking the observed galaxies to quantify

the impact of the underlying disk in the bulge kinematic measurements. We compared the sample bulges corrected kinematic measurements with the results from Schwarzschild dynamical modeling (Schwarzschild 1979); the good agreement confirms the robustness of our results. We found that the photometric and kinematic properties of bulges in 28 field lenticular galaxies are not correlated. We demonstrated that this morpho-kinematic decoupling is intrinsic to the bulges and it is not due to projection effects. We concluded that photometric diagnostics usually used to separate different types of bulges (disk-like vs. classical) might not be useful for lenticular galaxies. The morpho-kinematic properties of lenticular bulges suggest that they are mainly formed by dissipative processes happening at high redshift.

■ 3.7 Conclusions

We presented the multi-component photometric decomposition of 404 galaxies from the CALIFA DR3 survey. Our aim was to provide the community with an accurate photometric characterization of the multiple stellar structures shaping the CALIFA galaxies, namely bulges, bars, and disks.

The sample galaxies cover all galaxies included in the CALIFA final DR3, both from the mother sample and the extension sample, except those in mergers, showing interaction features, or with high inclination. We adopted a human-supervised strategy, where bulge/NPS, disk (including double-exponential profiles), and bar components were used to provide the best-fit for each galaxy. The final combination of structures was individually determined by the code-user after checking several possibilities. We had thoroughly compared our results with previous works from the literature (Simard et al. 2011; Salo et al. 2015) obtaining a reasonable agreement when the different galaxy components are carefully selected, but different results when automatic methods were used. We considered this as an indication of the robustness of the human-supervised multi-component photometric decomposition techniques. Counting double-exponential disk profiles as different structures, we used 13 different combinations of structures to describe our sample galaxies.

We focused on the incidence of the different structures in our sample. Since the properties of the galaxies extracted from the mother sample can be volume corrected, we had studied

the frequency of the different structures for the whole observed sample as well as taking into account for volume correction. Our main conclusions are:

- We found an average bar fraction in our volume corrected sample of 57%, which is consistent with previous results in the literature. The volume-corrected bar fraction shows a drop toward late-type galaxies; unfortunately, the number of galaxies in the late-type bin is too small to draw statistical conclusions. The observed bar fraction (using the whole sample) is relatively constant with Hubble type. Regarding the mass dependance of the bar fraction, the volume-corrected bar fraction drops from 75% at $M_\star = 10^{9.5}$ $\mathrm{M}_\odot$ to 25% at $M_\star = 10^{11}$ $\mathrm{M}_\odot$.

- We explored the frequency of different disk types by using two-dimensional surface-brightness models including double-exponential profiles and found that 62%, 28%, and 10% of our volume corrected sample of disk galaxies is better represented with a Type I (pure exponential), a Type II (down-bending), and a Type III (up-bending) profile, respectively. These fractions are in strong disagreement with previous results (Erwin et al. 2008; Gutiérrez et al. 2011). We argued that the different methodologies are the main explanation for these differences. In our two-dimensional analysis, we were simultaneously fitting all different galaxy components, whereas one-dimensional studies usually fit only piecewise exponentials to pre-defined regions of the surface brightness profile. Despite the quantitative differences, we found the same trends observed in the previous works, that is, a decrease in the fraction of Type I profiles with Hubble type (from Sa to Sc), an increase for the Type II profiles, and an almost constant fraction for Type III galaxies. No significant trends were found in terms of the stellar mass or the presence of bars.

- We also studied the incidence of pure disks and/or small unresolved bulges in our sample. Regarding the presence of a bulge and its prominence, we found a clear segregation of the structural composition of galaxies according to stellar mass. At high masses ($\log(M_\star/\mathrm{M}_\odot) > 11$), galaxies modeled with a single Sérsic or a bulge+disk with $B/T > 0.2$ represented the dominant population. At intermediate masses ($9.5 < \log(M_\star/\mathrm{M}_\odot) < 11$), galaxies described with bulge+disk but $B/T < 0.2$ were preponderant, whereas in the low mass end ($\log(M_\star/\mathrm{M}_\odot) < 9.5$), the prevailing population

was constituted by galaxies modeled with either pure disks or NPS+disks (i.e., with no discernible bulge). This trend of the fitted model with galaxy mass was also consistent with the trend of the B/T luminosity ratio with both Hubble type and mass. We found a clear decrease of B/T with both increasing Hubble type and decreasing mass with an average volume-corrected B/T value of 0.14.

This work focused on describing the photometric decomposition pipeline and the incidence of the different structural components in the final CALIFA DR. Moreover, it set the basis for new studies combining photometric information with the wealth of two-dimensional spatially resolved spectroscopic information provided by the CALIFA survey. Indeed, our photometric analysis allowed to accurately study the mechanisms responsible for generating the spiral structures (Sánchez-Menguiano et al. 2016), investigate the role of stellar radial migration (Ruiz-Lara et al. 2017), present a new galaxy classification system based on the shapes and amplitudes of their CVCs (Kalinova et al. 2017), estimate the current extinction-corrected Hα SFR of the different galaxy components (bulges, bars, and disks), and deeply study the relation between morphology and kinematics of bulges in lenticular galaxies (Méndez-Abreu et al. 2018).

4

SMALL BULGES IN NEARBY LATE-TYPE SPIRAL GALAXIES

About 20% of low-redshift galaxies are late-type spiral galaxies with a small or no bulge component. Although they are the simplest disk galaxies in terms of structure and dynamics, the role of the different physical processes driving their formation and evolution is not yet fully understood. We investigated whether small bulges of late-type spiral galaxies follow the same scaling relations traced by elliptical galaxies and large bulges and if small bulges are disk-like or classical bulges. We derived the photometric and kinematic properties of nine nearby late-type spiral galaxies. To this aim, we analyzed the surface brightness distribution from the i-band images of the Sloan Digital Sky Survey and obtained the structural parameters of the galaxies from a two-dimensional photometric decomposition. We measured the line-of-sight stellar velocity distribution within the bulge effective radius from the long-slit spectra taken with high spectral resolution at the Telescopio Nazionale Galileo. We used the photometric and kinematic properties of the sample bulges to study their location in the fundamental plane, Kormendy, and Faber-Jackson relations defined for elliptical galaxies and large bulges. We found that our bulges satisfy some of the photometric and kinematic prescriptions for being considered disk-like bulges, such as small size and mass with nearly exponential light profile, small bulge-to-total luminosity ratio, low stellar velocity dispersion, and ongoing star formation. However, each of these bulges follows the same scaling relations of elliptical galaxies, massive bulges, and compact early-type galaxies so they cannot be classified as disk-like systems. We found a single population of galaxy spheroids that follow the same scaling relations, where the mass seems to lead to a smooth transition in the photometric and kinematic properties from less to more massive bulges and elliptical galaxies.

4.1 Introduction

The population of late-type spiral galaxies comprises about 20% of the galaxies at low redshift (Nair & Abraham 2010) and is composed of disks with a small or no bulge component. Late-type spiral galaxies are characterized by the presence of large amounts of dust, ongoing star formation, and small-scale substructures both in the nucleus and along the arms (Carollo et al. 1997). Moreover, some of these spiral galaxies show a light excess and peculiar kinematics in the inner hundred parsecs due to the presence of a nuclear cluster (Böker et al. 2002; Seth et al. 2006), nuclear stellar disk (Morelli et al. 2010; Corsini et al. 2012), or nuclear bar (Erwin 2004; de Lorenzo-Cáceres et al. 2013). Thus, measuring and interpreting the properties of their bulges is particularly challenging. The extremely late-type spiral galaxies located at the end of the Hubble morphological sequence do not actually have a bulge component and are pure disk galaxies (Böker et al. 2002, 2003).

Although bulgeless spiral galaxies are the simplest disk galaxies in terms of structure and dynamics, the role of the different physical processes driving their formation and evolution is not yet fully understood. Indeed, hierarchical clustering scenarios are successful in explaining the assembly and growth of massive elliptical galaxies, but do not fully account for the building of disk-dominated galaxies with little or no bulge (Kautsch et al. 2006). Despite the fact that Hopkins et al. (2009) showed that the gas content in mergers plays a significant role in the efficiency of disk destruction and enables disks to survive, numerical simulations still have difficulty reproducing the observed fraction of extremely-late spiral galaxies in the local Universe (Weinzirl et al. 2009; Kormendy et al. 2010; Zavala et al. 2012).

The proper way to classify galactic bulges would be distinguishing between their different formation scenarios, which led to different observed properties. Reconstructing the formation mechanism from observations is a hard task, but the way in which scaling relations are satisfied by galaxies reflects the general dynamical principles of how baryons settle into dark matter potential wells. Previous works reported some hints about differences between less and more massive bulges, suggesting different formation scenarios and/or evolution pathways (Graham & Guzmán 2003; Méndez-Abreu et al. 2008a). However, since observational studies on bulges were mostly focused on the prominent bulges, further efforts are required to explore the photometric and kinematic properties of small and low-mass bulges in nearby late-type

spiral galaxies. In this Chapter, we aimed to extend the scaling relations of bulges all the way down to the lowest mass regime studied so far.

The Chapter is organized as follows. The galaxy sample is presented in Section 4.2. The acquisition, reduction, and analysis of the photometric and spectroscopic data are explained in Sections 4.3 and 4.4, respectively. In Section 4.5 the position of our small bulges in the scaling relations traced by elliptical galaxies and large bulges is investigated. Our results and conclusions are presented in Sections 4.6 and 4.7, respectively. We adopted $H_0 = 75$ km s^{-1} Mpc^{-1}, $\Omega_{\rm M} = 0.3$, and $\Omega_\Lambda = 0.7$ as cosmological parameters throughout this Chapter.

■ 4.2 Sample selection

We selected a volume-limited sample of 309 disk galaxies located within a radius of 100 Mpc and with $M_r \leq -18$ mag using the SDSS DR6 catalog (Adelman-McCarthy et al. 2008). Since small bulges are preferentially located in late-type spiral galaxies, we considered only galaxies with a light concentration index $C = R_{90}/R_{50} < 2.5$, where R_{50} and R_{90} are the radii enclosing 50% and 90% of the total galaxy luminosity, respectively. This corresponds to a Sérsic index $n \leq 1.5$ (Conselice 2003; Graham et al. 2005). Since galaxies are randomly oriented, it is possible to derive their properties by taking into account only the objects within a inclination interval. Therefore, we restricted to low inclination galaxies with $\theta < 45°$ in order to perform a successful photometric decomposition. Finally, we chose the 30 closest objects to be representative of the low-inclined late-type galaxies, but we observed only nine of these objects due to time and weather constraints during the spectroscopic observations.

The main properties of the sample galaxies are listed in Table 4.1, while the distributions of the r-band magnitudes of the volume-limited, representative, and final samples of galaxies are shown in Fig. 4.1. Our sample galaxies are all late-type spiral galaxies (Fig. 4.2), despite their morphological classification in Huertas-Company et al. (2011) and Makarov et al. (2014).

Table 4.1: Properties of the sample galaxies.

Galaxy		RA	DEC		Type	$B_{\rm T}$	θ	z	D	Scale	$D_{25} \times d_{25}$	$M^0_{B_T}$
SDSS name	Alternative name	[h m s]	[deg arcmin arcsec]			[mag]	[°]		[Mpc]	[pc arcsec^{-1}]	[arcsec]	[mag]
(1)	(2)	(3)	(4)	(5)	(6)	(7)	(8)	(9)	(10)	(11)	(12)	(13)
SDSS J104054.43+143202.4	...	10 40 54.43	+14 32 02.4	...	Sa-Sb (0.48)	16.00	22.4	0.021	81.4	395	21×20	-19.0
SDSS J112139.74+112924.6	...	11 21 39.74	+11 29 24.6	...	Sc-Sd (0.47)	16.77	20.3	0.020	77.6	378	19×17	-18.1
SDSS J113642.30+545045.7	IC 2943	11 36 42.30	+54 50 45.7	Sa	Sc-Sd (0.49)	15.18	39.5	0.019	75.8	368	24×19	-19.6
SDSS J115243.42+014428.0	UGC 6854	11 52 43.42	+01 44 28.0	SBbc	Sa-Sb (0.49)	14.52	39.6	0.020	79.6	386	56×43	-20.2
SDSS J133253.11−011531.1	PGC 47684	13 32 53.11	−01 15 31.1	S?	Sa-Sb (0.35)	15.70	40.6	0.012	47.1	228	29×22	-18.3
SDSS J143227.42+272538.7	IC 4452	14 32 27.42	+27 25 38.7	Sa	Sc-Sd (0.62)	14.92	20.6	0.014	55.9	271	29×27	-19.2
SDSS J144425.40+415140.6	PGC 2188136	14 44 25.40	+41 51 40.6	...	S0 (0.36)	15.79	36.0	0.018	69.0	335	39×31	-18.6
SDSS J160324.17+205328.4	NGC 6035	16 03 24.17	+20 53 28.4	Sc	Sc-Sd (0.64)	14.20	29.0	0.016	62.2	301	59×52	-20.4
SDSS J170128.21+634128.0	IC 1241	17 01 28.21	+63 41 28.0	Sc	Sc-Sd (0.63)	14.37	38.2	0.016	63.4	308	70×56	-20.0

Notes. (1) Full name of the galaxy according to SDSS. (2) Alternative name. (3), (4) Right ascension and declination (J2000.0). (5) Morphological classification from HyperLeda (Makarov et al. 2014). (6) Morphological classification and corresponding probability from Huertas-Company et al. (2011). (7) Apparent total blue magnitude from HyperLeda. (8) Inclination from HyperLeda. (9) Spectroscopic redshift from SDSS DR6. (10) Angular diameter distance. (11) Conversion factor from arcsec to parsec. (12) Major and minor diameters of the isophote at a surface brightness level of $\mu_B = 25$ mag arcsec^{-2} from the HyperLeda. (13) Absolute total blue magnitude corrected for inclination and extinction from the HyperLeda.

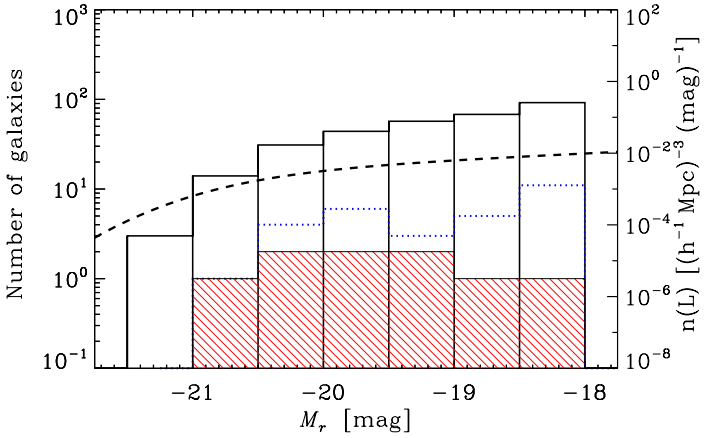

Figure 4.1: Distribution of the absolute r-band magnitude of the volume-limited sample (309 galaxies, black solid line), representative sample of late-type spiral galaxies (30 galaxies, blue dotted line), and observed sample nine galaxies, red filled histogram). The dashed line corresponds to the r-band luminosity function of SDSS galaxies by Tempel et al. (2011).

4.3 Surface photometry

We summarized here the main steps (i.e., data reduction and two-dimensional decomposition) of the photometric analysis of the final sample galaxies.

4.3.1 Data reduction

We retrieved the flux-calibrated i-band images of the sample galaxies from the SDSS DR9 (Ahn et al. 2012). The choice of i band ensured us a sufficient spatial resolution ($FWHM \simeq 1$ arcsec) and depth (out to $\mu_i \simeq 25$ mag arcsec^{-2}), and minimized the dust effects with respect to the other SDSS passbands to resolve the bulge component with an accurate photometric decomposition of the galaxy surface-brightness distribution.

We estimated the background sky level and its standard deviation using the procedure described in Section 2.1.2.1. We found that our estimates of the sky level are systematically lower by 0.2% than those given by SDSS. We trimmed the sky-subtracted images to reduce the computing time to perform a reliable photometric decomposition. Each galaxy was centered in a field of view of at least 50×50 pixels corresponding to 20×20 arcsec^2.

We ran `ellipse` on the trimmed images to derive the radial profiles of the ellipse-averaged surface brightness μ, ellipticity ϵ, and position angle PA of the galaxy isophotes in the i band. We adopted these photometric profiles and the mask images to estimate the sky level for

Table 4.2: Characteristics of the i-band SDSS images of the sample galaxies.

Galaxy	Gain	RON	Sky	$FWHM$	β
	$[e^-$ ADU$^{-1}]$	$[e^-]$	[ADU]	[arcsec]	
(1)	(2)	(3)	(4)	(5)	(6)
SDSSJ1040	4.8	10.7	212 ± 6	1.0	3.0
SDSSJ1121	6.6	16.4	177 ± 5	1.1	3.4
SDSSJ1136	4.9	13.4	230 ± 6	1.0	4.8
SDSSJ1152	6.6	16.4	121 ± 4	1.0	2.7
SDSSJ1332	4.8	10.7	184 ± 5	1.3	3.8
SDSSJ1432	6.6	16.4	150 ± 5	1.0	5.6
SDSSJ1444	4.9	13.4	199 ± 5	0.7	3.6
SDSSJ1603	6.6	16.4	128 ± 4	0.9	4.7
SDSSJ1701	4.9	10.4	119 ± 5	1.0	4.1

Notes. (1) Short name of the galaxy according to SDSS. (2) Image gain provided by SDSS. (3) Image RON provided by SDSS. (4) Measured sky level and corresponding standard deviation. (5), (6) FWHM and β parameter measured for the circular Moffat PSF.

the photometric decomposition. Finally, we modeled the PSF of each galaxy with a circular Moffat profile (Table 4.2), deriving its parameters fitting five unsaturated stars.

4.3.2 Two-dimensional photometric decomposition analysis

We derived the structural parameters of the sample galaxies by performing a two-dimensional photometric decomposition of their surface brightness distribution using the GASP2D algorithm (Méndez-Abreu et al. 2008a, 2014) presented in Section 2.1. We assumed the surface brightness distribution of the sample galaxies to be the sum of a Sérsic bulge, exponential disk, and Ferrers bar component as explained in Section 2.1.1. We did not consider any other additional component, such as spiral arms, lenses, or ovals. When possible, we masked their corresponding regions in the galaxy images and excluded them from the fitting process. In addition, we masked out the dust patches and lanes as much as possible to recover a reliable model of the surface brightness distribution.

We detected a bulge component in seven out of nine sample galaxies, whereas the remaining two (namely SDSSJ1040 and SDSSJ1121) were better fit only with a disk component. We detected a bar component in four out of nine galaxies (namely SDSSJ1152, SDSSJ1444, SDSSJ1603, and SDSSJ1701). The best-fit structural parameters of the sample galaxies are available in Table 4.3 while their GASP2D fits are shown in Fig. 4.2.

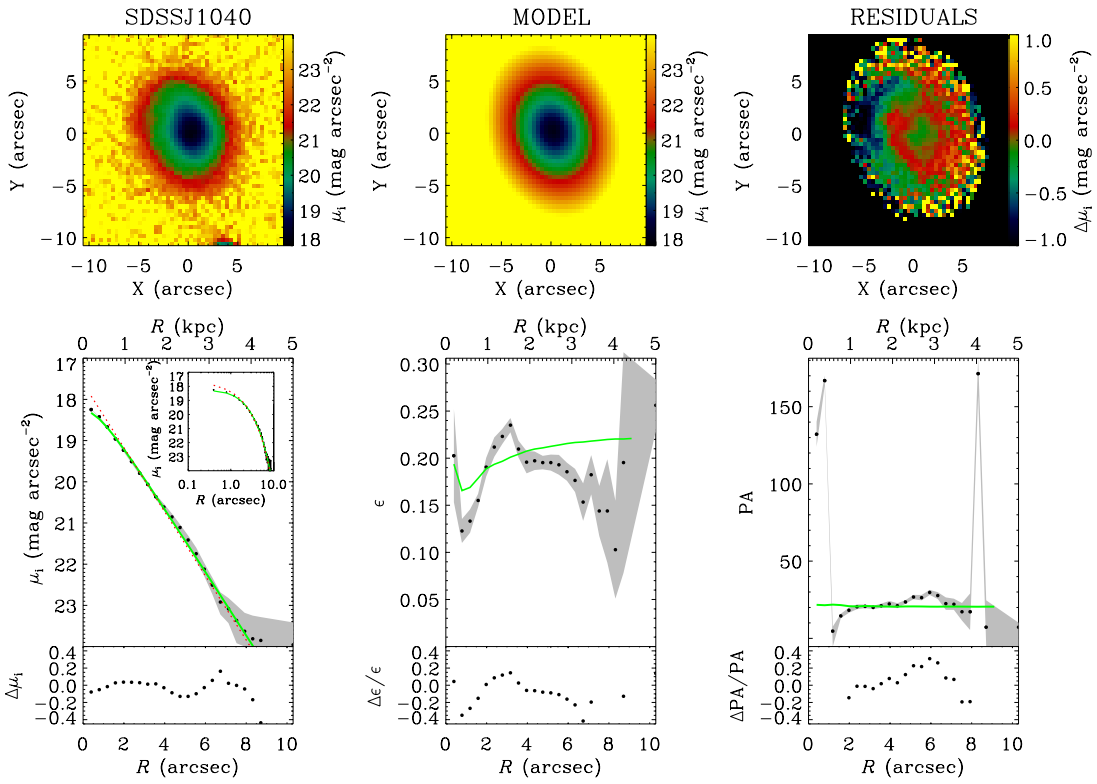

Figure 4.2: Two-dimensional photometric decomposition of the i-band images of the sample galaxies obtained from GASP2D. For each galaxy the upper panels (*from left to right*) show the map of the observed, modeled, and residual (observed−modeled) surface-brightness distributions. The field of view is oriented with North up and East left. The black areas in the residual image correspond to pixels excluded from the fit. The lower panels (*from left to right*) show the ellipse-averaged radial profile of surface brightness, position angle, and ellipticity measured in the observed (black dots with gray error regions) and seeing-convolved modeled image (green solid line) and their corresponding difference. The surface-brightness radial profiles of the best-fit bulge (blue dashed line), disk (red dotted line), and bar component (magenta dot-dashed line) are also shown in both linear and logarithmic scale for the distance to the center of the galaxy.

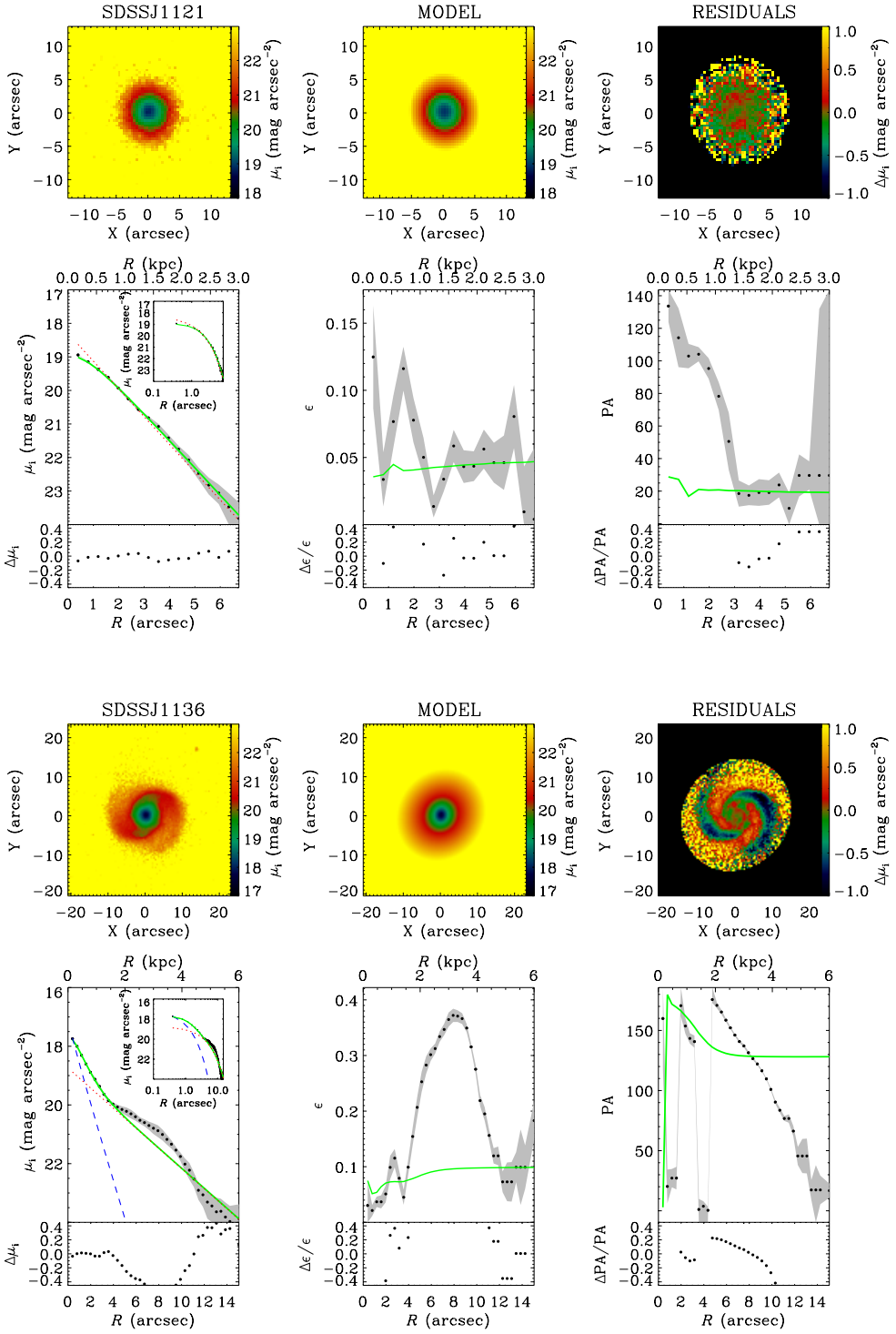

Figure 4.2: continued.

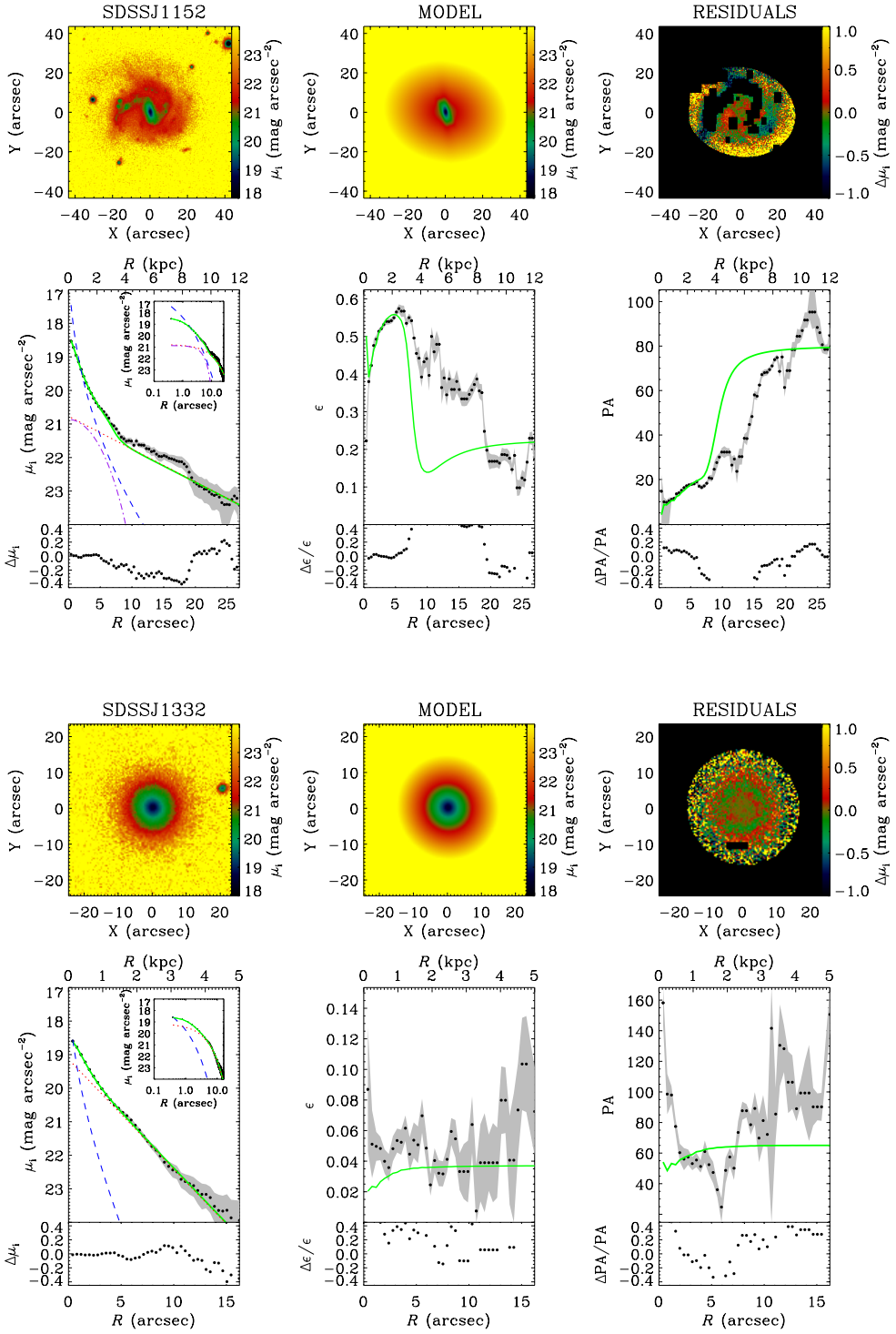

Figure 4.2: continued.

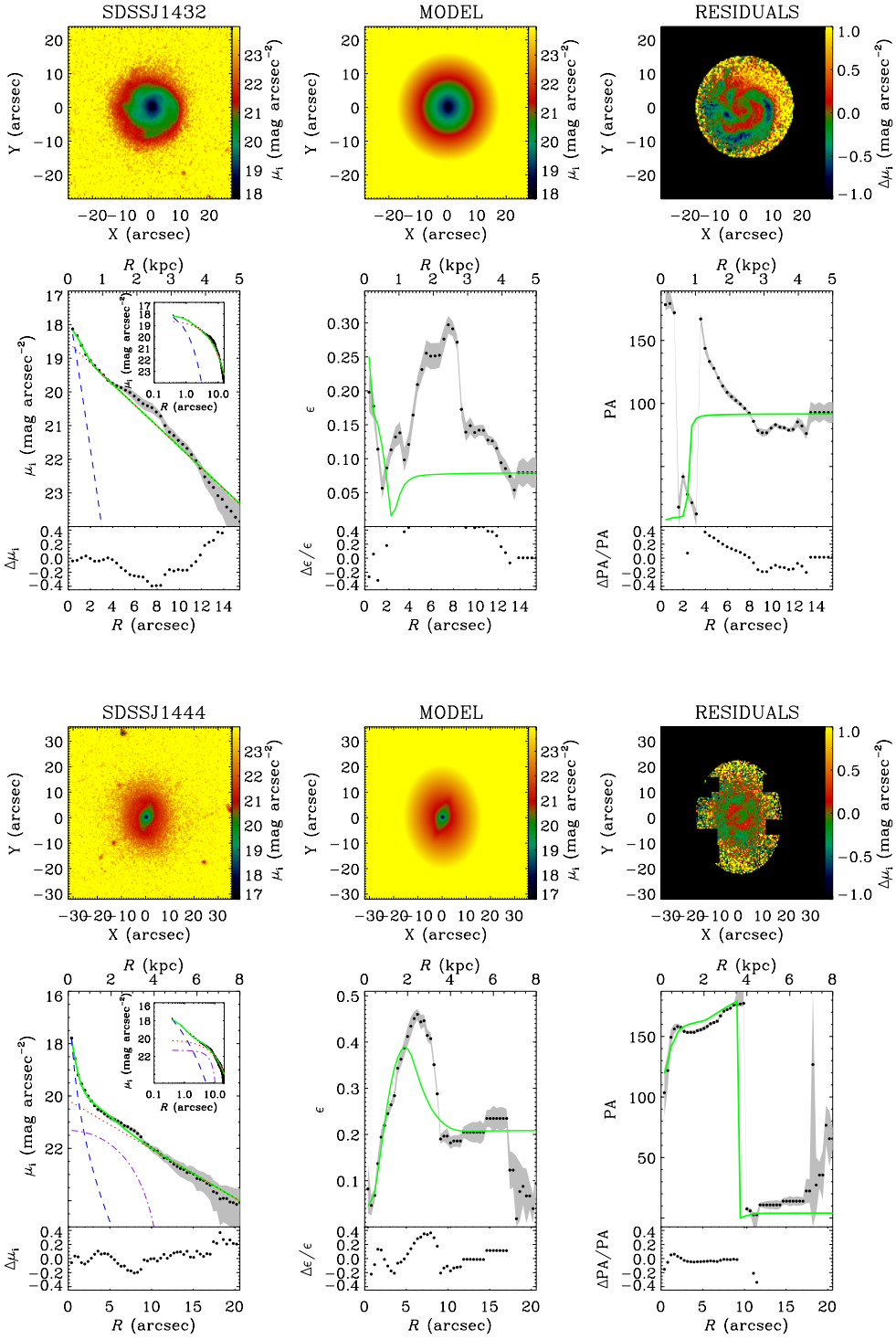

Figure 4.2: continued.

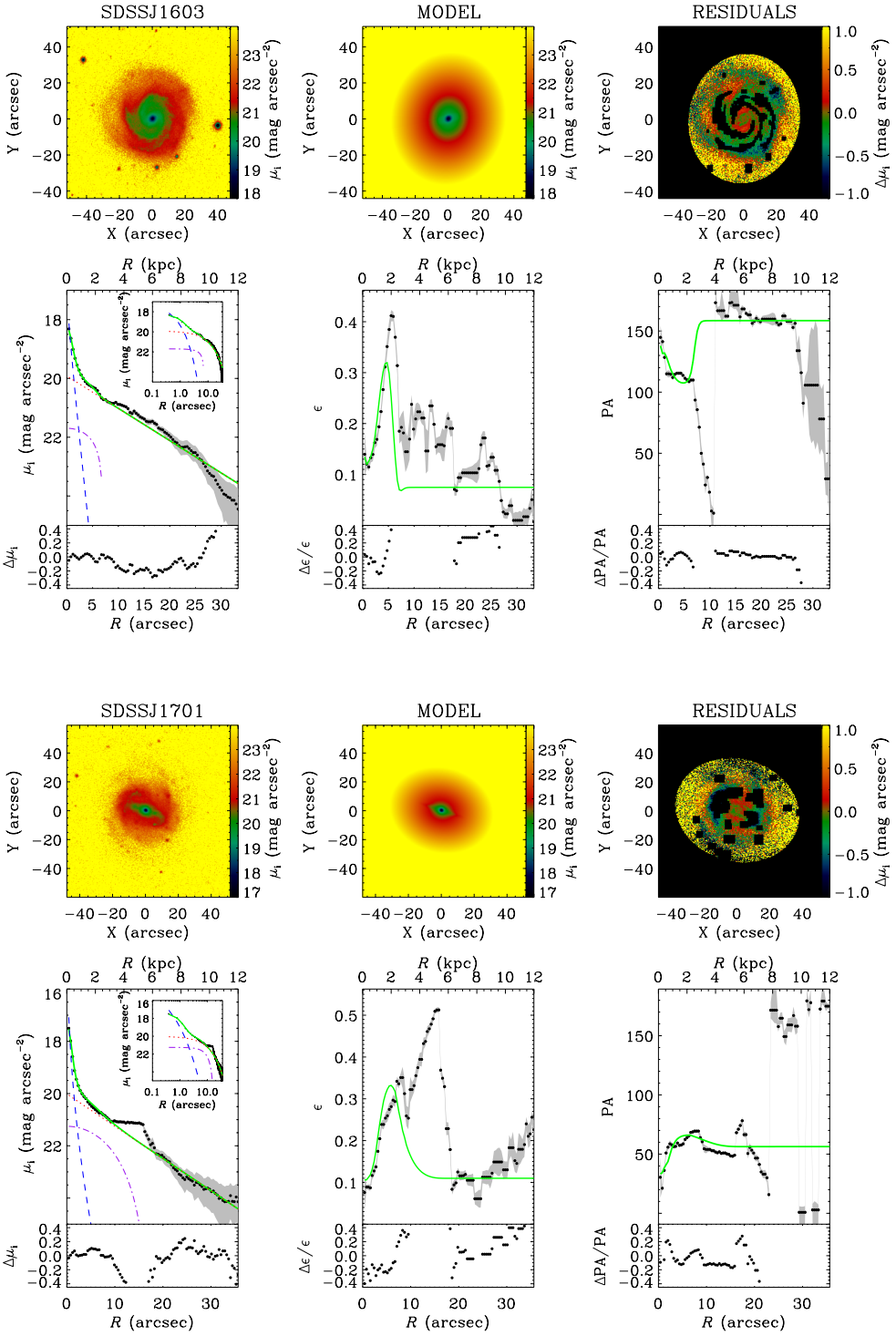

Figure 4.2: continued.

Table 4.3: Structural parameters of the sample galaxies.

galaxy [name] (1)	μ_e [mag arcsec^{-2}] (2)	$\langle\mu_e\rangle$ [mag arcsec^{-2}] (3)	r_e [arcsec] (4)	n (5)	ϵ_{bulge} (6)	PA_{bulge} [°] (7)	μ_0 [mag arcsec^{-2}] (8)	h [arcsec] (9)	ϵ_{disk} (10)	PA_{disk} [°]
SDSSJ1040	...	...	...	...	...	...	17.61 ± 0.01	1.39 ± 0.01	0.24 ± 0.01	20.4 ± 0.5
SDSSJ1121	...	...	...	...	...	...	18.30 ± 0.01	1.31 ± 0.01	0.05 ± 0.01	19.0 ± 0.5
SDSSJ1136	19.0 ± 0.1	18.3 ± 0.1	1.3 ± 0.1	1.06 ± 0.07	0.15 ± 0.02	172 ± 2	18.74 ± 0.04	3.17 ± 0.05	0.10 ± 0.01	128 ± 2
SDSSJ1152	20.1 ± 0.2	19.0 ± 0.5	2.9 ± 0.4	2.3 ± 0.2	0.75 ± 0.01	7 ± 2	20.77 ± 0.08	11.1 ± 0.3	0.23 ± 0.02	80 ± 2
SDSSJ1332	20.2 ± 0.1	19.3 ± 0.2	1.3 ± 0.1	1.6 ± 0.1	0.05 ± 0.02	56 ± 2	19.12 ± 0.04	3.30 ± 0.06	0.04 ± 0.01	60 ± 2
SDSSJ1432	19.2 ± 0.1	18.6 ± 0.1	0.85 ± 0.07	0.94 ± 0.06	0.38 ± 0.02	3 ± 2	18.53 ± 0.04	3.49 ± 0.06	0.08 ± 0.01	90 ± 2
SDSSJ1444	18.7 ± 0.2	17.5 ± 0.5	0.63 ± 0.09	2.7 ± 0.3	0.15 ± 0.01	122 ± 2	20.18 ± 0.08	5.9 ± 0.1	0.21 ± 0.02	180 ± 2
SDSSJ1603	19.2 ± 0.2	18.5 ± 0.2	0.92 ± 0.09	0.99 ± 0.07	0.19 ± 0.01	126 ± 1	19.82 ± 0.08	9.9 ± 0.2	0.06 ± 0.01	160 ± 1
SDSSJ1701	17.5 ± 0.2	16.7 ± 0.4	0.54 ± 0.05	1.23 ± 0.09	0.22 ± 0.01	39 ± 1	19.87 ± 0.08	8.9 ± 0.2	0.11 ± 0.01	60 ± 1

galaxy [name] (12)	μ_{bar} [mag arcsec^{-2}] (13)	a_{bar} [arcsec] (14)	n_{bar} (15)	ϵ_{bar} (16)	PA_{bar} [°] (17)	c (18)	B/T (19)	Bar/T (20)
SDSSJ1040	...	...	...	...	...	...	0	0
SDSSJ1121	...	...	...	...	...	...	0	0
SDSSJ1136	...	...	...	...	...	...	0	0
SDSSJ1152	20.87 ± 0.09	15 ± 2	6 ± 3	0.77 ± 0.02	32.6 ± 0.3	0.43 ± 0.06	0.10	0.03
SDSSJ1332	...	...	...	...	...	...	0.12	0
SDSSJ1432	...	...	...	...	...	...	0.04	0
SDSSJ1444	21.22 ± 0.09	12 ± 2	2.0 ± 0.8	0.73 ± 0.02	159.3 ± 0.3	0.01 ± 0.01	0.12	0.06
SDSSJ1603	21.99 ± 0.08	6 ± 1	0.11 ± 0.04	0.72 ± 0.01	102.0 ± 0.2	2.0 ± 0.2	0.03	0.01
SDSSJ1701	21.03 ± 0.08	17 ± 3	2.0 ± 0.8	0.75 ± 0.01	69.3 ± 0.2	−1.0 ± 0.1	0.06	0.03

Notes. (1), (12) Short name of the galaxy according to SDSS. (2), (3), (4), (5), (6) and (7) Surface brightness at effective radius, mean surface brightness within effective radius, effective radius, Sérsic index, ellipticity ($\epsilon_{bulge} = 1 - q_{bulge}$), and position angle of the bulge, respectively. (8), (9), (10) and (11) Central surface brightness, scalelength, ellipticity ($\epsilon_{disk} = 1 - q_{disk}$), and position angle of the disk, respectively. (13), (14), (15), (16), (17) and (18) Central surface brightness, length, Sérsic index, ellipticity ($\epsilon_{bar} = 1 - q_{bar}$) , position angle, and isophotal shape parameter of the bar, respectively. (19) Bulge-to-total luminosity ratio. (20) Bar-to-total luminosity ratio.

4.3.3 Error budget

We estimated the errors by analyzing a sample of mock galaxies built through a series of MC simulations to test the sensibility of the best-fit parameters and understand if any systematic error affect them, as also done in Section 3.5.2. However, instead of randomly generating the mock galaxies, we created them taking into account the correlations among the structural parameters of bulge and disk. For this purpose, we used the sample of nearby galaxies of Gadotti (2009). Firstly, we divided the nine galaxies of our sample into three subsamples, according to the number of their components: (1) disk only, (2) bulge and disk, (3) bulge, disk, and bar. This allowed us to define bins of magnitude in which we created the corresponding sample of mock galaxies: four bins for subsamples (1) and (2) in the magnitude range $-20.5 < M_i < -18.5$ mag and four bins for subsample (3) in the magnitude range $-21.5 < M_i < -19.5$ mag. Each bin is composed of about 200 mock galaxies. Then, we generated a B/T random value from a uniform distribution in the range $[0, 0.45]$, and starting from this value we determined the Sérsic index n from a normal distribution using the correlation

$$n = 5.73 \cdot B/T + 1.25, \tag{4.1}$$

which we obtained by fitting the Gadotti (2009) sample (Fig. 4.3).

After that, we produced a random value of $r_{\rm e}$ from a normal distribution and determined a value of h using the correlation

$$r_{\rm e}/h = 0.69 \cdot B/T + 0.19, \tag{4.2}$$

which we obtained from the sample of Gadotti (2009) (Fig. 4.4).

Unfortunately, we could not use this sample to investigate the properties of the bar, so we randomly generated the structural parameters of the bar in the same intervals as those obtained from the photometric decomposition of our sample. The interval ranges explored for all the parameters were $r_{\rm e} = [0.5, 4]$ arcsec, $n = [0.5, 4]$, $h = [1, 14]$ arcsec, $a_{\rm bar} = [5, 25]$ arcsec, $n_{\rm bar} = [0, 7]$, and $c = [-2, 5]$. Finally, we randomly generated the apparent flattening of the bulge $q_{\rm bulge}$, disk $q_{\rm disk}$, and bar $q_{\rm bar}$ and the values of the position angle of the bulge $PA_{\rm bulge}$, disk $PA_{\rm disk}$, and bar $PA_{\rm bar}$ from uniform distributions, where no constraints were

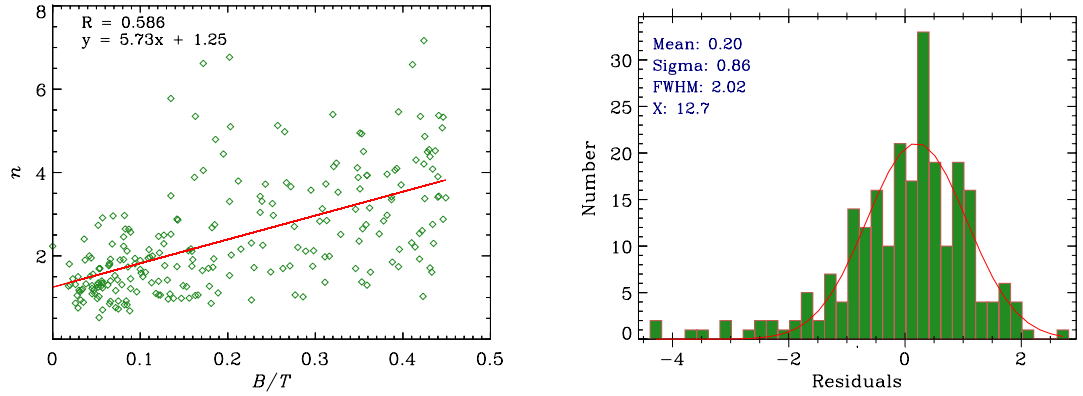

Figure 4.3: Correlation between the bulge-to-total luminosity ratio B/T and Sérsic index n (*left panel*) extrapolated from the sample in Gadotti (2009) and residuals histogram (*right panel*).

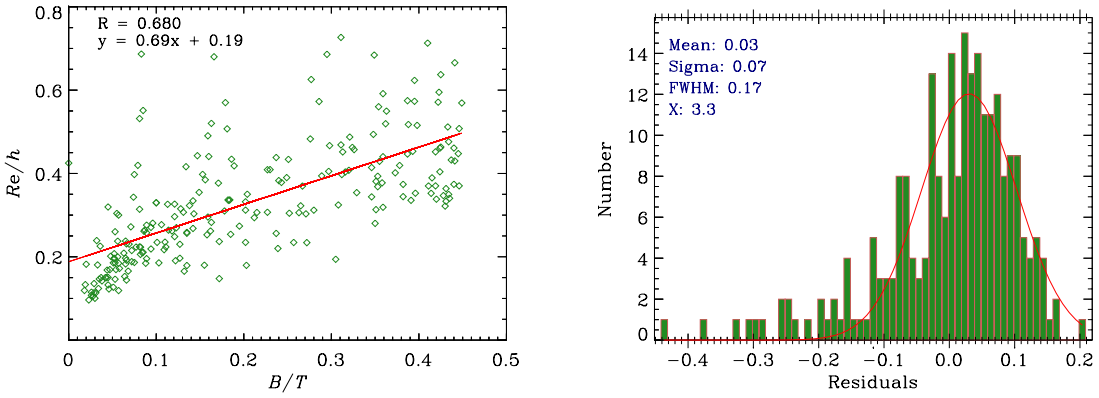

Figure 4.4: Correlation between the bulge-to-total luminosity ratio B/T and scale length ratio r_e/h (*left panel*) extrapolated from the sample in Gadotti (2009) and residuals histogram (*right panel*).

adopted.

We assumed the mock galaxies to be at a distance of 69 Mpc, which corresponds to the median distance of our sample galaxies. We chose the pixel scale (0.396 arcsec pixel^{-1}), gain (6.6 e^- ADU^{-1}), RON (16.4 e^- rms), and size of the simulated images (400 $\times$ 400 pixels) to mimic the instrumental setup of the photometric observations. Moreover, we added a background level (170 ADU) and a Poissonian photon noise to yield, in the simulated images,

S/N similar to those of the observed images.

We analyzed the images of the mock galaxies as if they were real using GASP2D. Thus, we evaluated the initial conditions in the fitting procedure starting from the values of the generated parameters for each model galaxy. We estimated the errors on the fitted parameters by comparing the input and measured values, assuming they were normally distributed. For $I_{\rm e}$, $r_{\rm e}$, n, I_0, h, $I_{0,\rm bar}$, $a_{\rm bar}$, $n_{\rm bar}$, and c we adopted the mean and standard deviation of the relative errors of the mock galaxies as the systematic and statistical errors of the observed galaxies, respectively. For $q_{\rm bulge}$, $q_{\rm disk}$, $q_{\rm bar}$, $PA_{\rm bulge}$, $PA_{\rm disk}$, and $PA_{\rm bar}$ we adopted the mean and standard deviation of the absolute errors of the mock galaxies as the systematic and statistical errors of the observed galaxies, respectively. The computed errors $\sigma^2 = \sigma^2_{\rm stat} + \sigma^2_{\rm syst}$ are provided in Table 4.3. In the analysis we did not consider the systematic errors derived from the uncertainties on the estimates of the PSF FWHM or sky level. Therefore, the errors reported in Table 4.3 could be slightly underestimated (see Méndez-Abreu et al. 2008a, for a discussion).

4.3.4 Spatial resolution of the bulge component

We performed a further analysis to ensure that our bulges are spatially resolved because the angular sizes of most of them are close to the size of the image PSF ($1.3 < r_{\rm e}/\sigma_{\rm PSF} < 6.9$), resulting from the photometric decomposition (Table 4.3).

To this aim, we built a large number of images of mock galaxies with a Sérsic bulge and an exponential disk belonging to the faintest magnitude bin ($m_i = 15$ mag); the galaxies have a Moffat PSF with $FWHM = 1$ arcsec consistent with observations and are characterized by different values of $r_{\rm e}$ so that $r_{\rm e}/\sigma_{\rm PSF} = [1.2, 1.8, 2.4, 3.0, 3.5, 4.1, 4.7, 5.3, 5.9, 6.5, 7.1]$. We chose the value of the Sérsic index to be $n = [0.5, 1, 1.5, 2, 2.5, 3, 3.5, 4, 4.5, 5]$. We generated the remaining structural parameters of the mock galaxies in two different ways. First, we adopted $B/T = 0.1$ and derived h using the $(r_{\rm e}/h, B/T)$ correlation given in Eq. (4.2) to inspect galaxies with different disk sizes. Then, we adopted $h = 5.6$ arcsec that is consistent with the disk scale lengths of our sample galaxies (Table 4.3) and randomly derived B/T from a uniform distribution in the range $[0, 0.45]$ to examine the impact of the bulge component. We investigated all the possible permutations and built two final samples of 110 mock galaxies

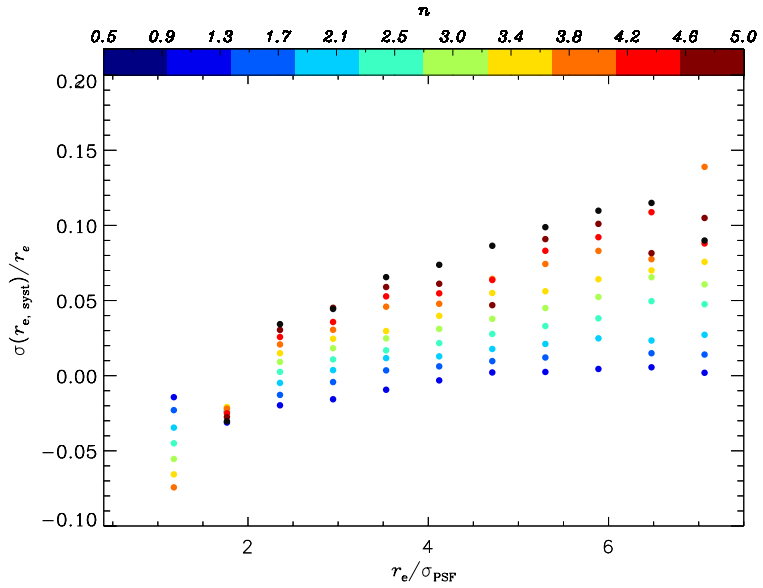

Figure 4.5: Relative difference between $r_{\mathrm{e,\,output}}$ and $r_{\mathrm{e,\,input}}$ as function of $r_{\mathrm{e}}/\sigma_{\mathrm{PSF}}$ adopting $B/T = 0.1$. Positive/negative values correspond to an over/underestimation of r_{e}. The different values of n are shown in different colors.

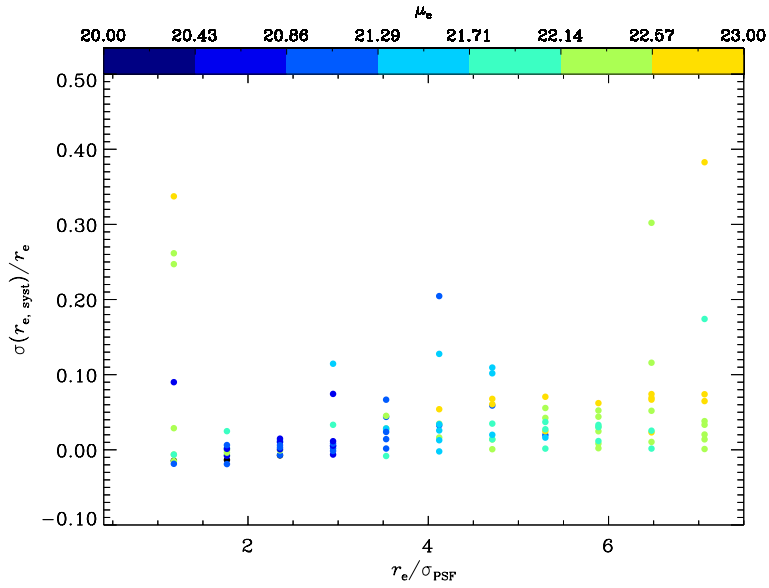

Figure 4.6: Relative difference between $r_{\mathrm{e,\,output}}$ and $r_{\mathrm{e,\,input}}$ as function of $r_{\mathrm{e}}/\sigma_{\mathrm{PSF}}$ adopting $h = 5.6$ arcsec. Positive/negative values correspond to an over/underestimation of r_{e}. The different values of μ_{e} are shown in different colors.

each, where all the geometrical parameters are the same for all the galaxies in the same sample. We analyzed the images of the mock galaxies as if they were real using GASP2D.

The two different sets of mock galaxies lead to the same results (Fig. 4.5 and 4.6). The bulge component can be actually measured even if $r_{\rm e}/\sigma_{\rm PSF} = 1.2$ with a relative error $\sigma_{r_{\rm e},\,{\rm syst}}/r_{\rm e} \lesssim 0.1$ in agreement with the photometric errors from the MC analysis. If brighter galaxies are considered (e.g., with $m_i = 13$ mag) the errors on $r_{\rm e}$ become smaller ($\sigma_{r_{\rm e},\,{\rm syst}}/r_{\rm e} \sim 0.01$). Therefore, all the sample bulges are spatially resolved. We also considered the role of n (Fig. 4.5) and $\mu_{\rm e}$ (Fig. 4.6). Galaxies with smaller n are better fit than those with larger n. Moreover, galaxies with larger $\mu_{\rm e}$ show a larger scatter around the actual value. This combined effect could be explained by the fact that smaller bulges are also brighter and so their parameters are retrieved with greater accuracy.

4.4 Long-slit spectroscopy

We summarized here the main steps (i.e., data reduction and stellar kinematics) of the spectroscopic analysis of the final sample galaxies.

4.4.1 Observations and data reduction

We carried out the spectroscopic observations of the sample galaxies on 2009 April 1–4 at the Telescopio Nazionale Galileo (TNG) in La Palma (Spain).

In the setup we used the DOLORES spectrograph with the V510 grism covering the wavelength range 4875–5325 Å and the 1-arcsec wide slit. The spectrograph was equipped with a E2V 4240 camera and a thinned back-illuminated, deep-depleted, Astro-BB coated CCD with 2048 × 2048 pixels of 13.5 × 13.5 μm^2, gain 0.97 e^- ADU^{-1}, and RON 9 e^- (rms). We used the mean of the Gaussian FWHMs measured for a number of unblended arc-lamp lines over the whole spectra range of a wavelength-calibrated spectrum to derive the instrumental resolution. We found $FWHM_{\rm inst} = 1.04 \pm 0.08$ Å, corresponding to a velocity dispersion $\sigma_{\rm inst} = 25.4 \pm 0.4$ km s^{-1} at 5100 Å, far below the instrumental resolution of the SDSS spectra. The angular sampling was 0.252 arcsec pixel^{-1} with a reciprocal dispersion of 0.235 Å pixel^{-1}. The median value of the seeing FWHM during the observing nights was 1.22 arcsec. This value was measured fitting a circular Gaussian on the guide stars.

Table 4.4: Log of spectroscopic observations and stellar kinematics of the sample galaxies

Galaxy	PA	Single Exp. Time	Total Exp. Time	$\sigma_{\rm e}$	$\sigma_{1.5\,\rm arcsec}$
	[°]	[s]	[h]	[km s^{-1}]	[km s^{-1}]
(1)	(2)	(3)	(4)	(5)	(6)
SDSSJ1040	16.9	$1 \times 1800 + 2 \times 2700$	2	...	54 ± 4
SDSSJ1121	53.2	$1 \times 1800 + 2 \times 2700$	2	...	37 ± 4
SDSSJ1136	24.9	4×1800	2	61 ± 3	61 ± 3
SDSSJ1152	99.2	4×1800	2	55 ± 11	58 ± 11
SDSSJ1332	88.4	4×1800	2	35 ± 2	35 ± 2
SDSSJ1432	101.8	$1 \times 2400 + 1 \times 2700$	1.4	37 ± 4	42 ± 3
SDSSJ1444	−115.0	$3 \times 1800 + 1 \times 2700$	2.25	55 ± 9	68 ± 7
SDSSJ1603	9.8	4×1800	2	57 ± 5	56 ± 4
SDSSJ1701	−24.0	4×1800	2	71 ± 7	69 ± 6

Notes. (1) Short name of the galaxy according to SDSS. (2) Position angle of the slit measured North to East. (3) Exposure time of the spectra. (4) Total exposure time. (5) Measured velocity dispersion within $r_{\rm e}$. (6) Measured velocity dispersion within 1.5-arcsec radius.

For each object, we centered the slit on the galaxy nucleus and visually aligned it along the galaxy major axis. Details about the slit position angles and exposure times are given in Table 4.4.

Each spectrum was bias-subtracted, flat-field corrected, cleaned of cosmic rays, corrected for bad columns, and wavelength and flux calibrated via standard IRAF tasks. We used the bias frames obtained during the observing nights to determined the bias level. We performed the flat-field correction for pixel-to-pixel sensitivity variations and large-scale illumination patterns arising from slit vignetting with thorium lamp and twilight sky spectra, respectively, which were normalized and divided into all spectra. We carried out the identification of the cosmic rays by comparing the counts in each pixel with the local mean and standard deviation as obtained from Poisson statistics considering the gain and RON of the CCD and then we corrected by interpolating over. If cosmic rays were detected, we corrected them by interpolating over with the `lacos_spec` task in IRAF (van Dokkum 2001). If residual cosmic rays were present, we manually removed them by editing the spectra.

We rebinned all the spectra using the wavelength solution obtained from the corresponding arc-lamp spectrum and flux-calibrated using the sensitivity function acquired from the flux standard star spectra of the corresponding night. We estimated the contribution from the sky by interpolating along the outermost regions at the two edges of the slit, where the

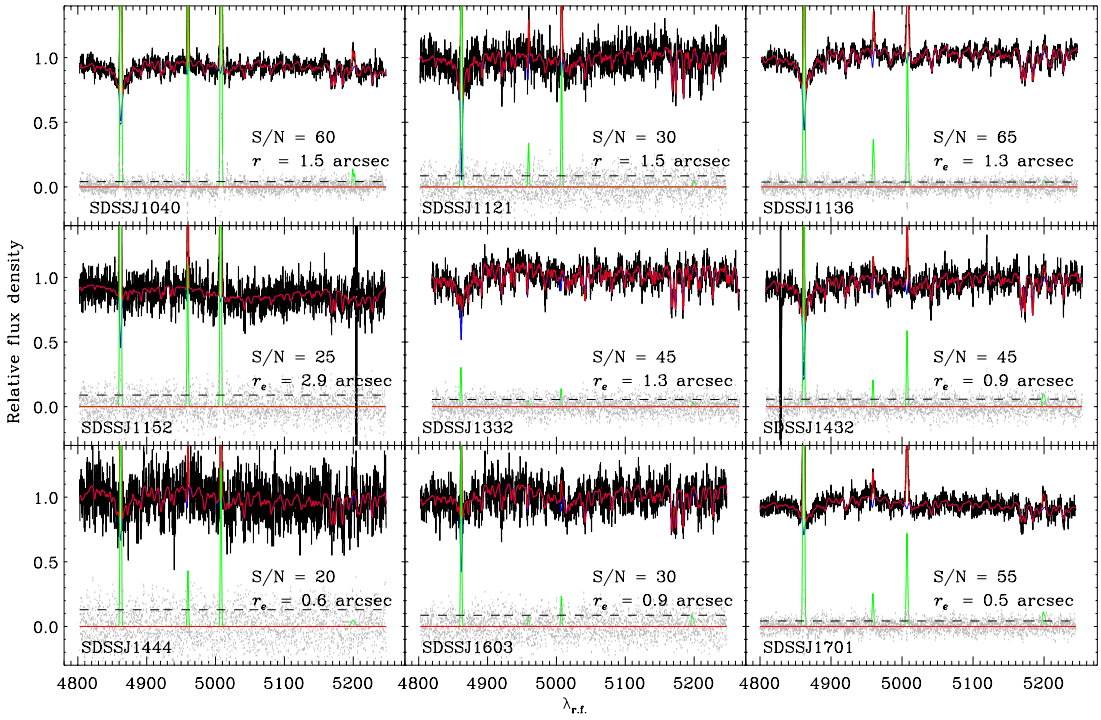

Figure 4.7: Long-slit spectra of the sample galaxies. Relative fluxes have false zero points for viewing convenience. In each panel the best-fit model (red line) is the sum of the spectra of the ionized gas (green line) and stellar component (blue line). The residuals (gray dots) are obtained by subtracting the best-fit model from the observed spectrum. The S/N is given per resolution element.

galaxy or stellar light is negligible, and then we subtracted it. Finally, in order to improve the S/N of the final two-dimensional spectrum, we coadded the major-axis spectra using the center of the stellar continuum as reference.

4.4.2 Stellar kinematics

We measured the stellar kinematics of the sample galaxies from the absorption features in their spectra. We used the penalized pixel-fitting method (pPXF; Cappellari & Emsellem 2004), including the Gas and Absorption Line Fitting algorithm (GANDALF; Sarzi et al. 2006), adapted for dealing with our setup. We rebinned the spectra along the spatial direction to provide the kinematic parameters within 1.5 arcsec and $r_{\rm e}$.

The convolution of a linear combination of stellar spectra from the ELODIE library ($FWHM$ = 0.48 Å; Prugniel & Soubiran 2001) with the LOSVD, described by Gauss-Hermite expansion (Gerhard 1993; van der Marel & Franx 1993), allowed us to fit the

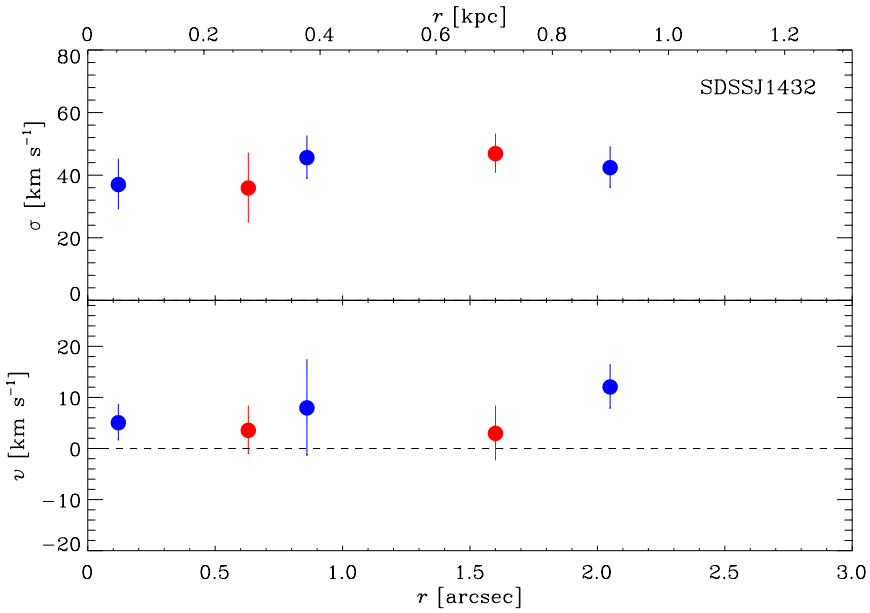

Figure 4.8: Long-slit stellar kinematics of SDSSJ1432. The curves are folded around the nucleus. Blue circles and red circles refer to data measured along the approaching and residing sides of the galaxy, respectively. The upper panel shows the velocity-dispersion radial profile, while the bottom panel shows the velocity radial profile, after the subtraction of the systemic velocity.

observed galaxy spectrum by χ^2 minimization in pixel space. Before the convolution, we degraded the spectral resolution of the ELODIE spectra by convolving them with a Gaussian function to match the galaxies spectral resolution. We properly masked bad pixels coming from imperfect subtraction of cosmic rays and sky emission lines and we excluded them from fitting procedure. In this way, we determined the value of the mean velocity $v_{\rm los}$, velocity dispersion $\sigma_{\rm los}$, and third- h_3 and fourth-order h_4 moments of the LOSVD. The measured values of h_3 and h_4 were compatible with zero, thus we fixed their values and we again performed the fit adopting a Gaussian LOSVD and obtaining only $v_{\rm los}$ and $\sigma_{\rm los}$. All the analyzed spectra had a $S/N \geq 20$ per resolution element (Fig. 4.7). We adopted a low-order multiplicative polynomial in the template fitting to deal with the effect of dust and possible residuals of the data reduction procedure. Thus, the method minimizes the effects of reddening because it is more sensitive to the absorption lines than the continuum shape.

To allow for additional structure not addressed by our model, we estimated the uncertainties in the kinematic parameters from the formal errors of the fitting procedure by

evaluating the χ^2 values. We achieved $\chi^2 = N_{\rm dof} = N_{\rm data} - N_{\rm fit}$ for the best-fit model, where $N_{\rm dof}$, $N_{\rm data}$, and $N_{\rm fit}$ are the numbers of the degrees of freedom, data points, and fitting parameters, respectively (Press et al. 1986). The measured stellar velocity dispersion and corresponding errors are reported in Table 4.4, while the folded kinematic profiles of SDSSJ1432 are shown in Fig. 4.8 as an example.

■ 4.5 Scaling relations

The luminosity, surface brightness, size, and velocity dispersion of elliptical galaxies and bulges of disk galaxies are used to identify a set of well-defined scaling relations, namely the FPR, KR, and FJR. These relations unveil the structure of galaxy spheroids and provide valuable clues regarding the physics driving their formation and evolution history.

We investigated whether small bulges follow the same scaling relations traced by elliptical galaxies and large bulges by comparing our galaxy sample to the sample of nearby galaxies, in which structural parameters and velocity dispersion are measured by Gadotti (2009) and Oh et al. (2011) from SDSS i-band images and spectra, respectively.

We marked all the comparison galaxies by assigning a probability to be E–S0, Sa–Sb, or Sc–Sd using the Bayesian automated classification by Huertas-Company et al. (2011). After that, elliptical galaxies ($B/T = 1$) were disentangled from lenticular galaxies ($B/T < 1$). This allowed us to properly consider the structural parameters of the whole galaxy for elliptical galaxies and of the bulge component only for disk galaxies.

We are particularly interested in having low-σ galaxies in the comparison sample. But, given the typical S/N and instrumental resolution of the SDSS spectra ($\sigma_{\rm inst,SDSS} \simeq 70$ km s^{-1}), as a rule the use of SDSS galaxies with $\sigma < 70$ km s^{-1} is not recommended because their velocity dispersion could be unreliable (Bernardi et al. 2003a). Oh et al. (2011) defined a new criterion to assess the reliability of the SDSS-based σ values by rejecting galaxies with a ratio rN/s$N > 3$ between the rms of the residuals of the spectral fit (rN) and the expected statistical rms (sN). We eventually included in the comparison sample all the galaxies with $\sigma < 70$ km s^{-1} that meet the prescription by Oh et al. (2011).

For all the comparison galaxies we calculated the velocity dispersion $\sigma_{\rm e}$ within $r_{\rm e}$ from

the SSDS σ measured within a fixed aperture of 3 arcsec using a power-law function

$$\left(\frac{\sigma}{\sigma_{\rm e}}\right) = \left(\frac{r}{r_{\rm e}}\right)^{\alpha} , \tag{4.3}$$

where α is

$$\alpha_{\rm ETG} = -0.055 \pm 0.020$$

for the ETGs, and

$$\begin{cases} \alpha_{\rm LTG}(M_r < -22) = 0.047 \pm 0.021 \\ \alpha_{\rm LTG}(-20 < M_r < -22) = 0.086 \pm 0.013 \\ \alpha_{\rm LTG}(M_r > -20) = 0.153 \pm 0.063 \end{cases} ,$$

for the late-type galaxies, as derived by Falcón-Barroso et al. (2017) from the analysis of 300 galaxies drawn from the CALIFA DR3 (Sánchez et al. 2016).

Finally, the comparison sample includes 234 elliptical galaxies and 626 bulges (79 in lenticular galaxies, 192 in Sa-Sb galaxies, and 355 in Sc-Sd galaxies). For the sake of completeness, although only seven out of nine galaxies in our sample present a bulge component, the entire sample was superimposed on the scaling relations for a comparison. Owing to the small size of our sample, in the following we only discussed the properties of our individual late-type bulges and not of the whole population. Further observations of a complete sample of late-type bulges would be needed to infer their global properties as a distinct class of bulges.

4.5.1 Fundamental plane

The FPR (Djorgovski & Davis 1987; Dressler et al. 1987; D'Onofrio et al. 2008; Cappellari et al. 2013) is the most widely studied scaling relation providing information about structure and kinematics of galaxy spheroids. Observable quantities, such as the mean effective surface brightness $\langle\mu_{\rm e}\rangle$, $r_{\rm e}$, and σ are commonly adopted in the FPR as proxies of the physical properties of the galaxy (Bender et al. 1992). When spiral galaxies are considered, as in this work, the previous properties only refer to the bulge component instead of the whole galaxy as in elliptical galaxies.

The common way to express the FPR is $\log(r_\mathrm{e}) = \alpha \log(\sigma_\mathrm{e}) + \beta\langle\mu_\mathrm{e}\rangle + \gamma$ in order to separate r_e from σ_e and $\langle\mu_\mathrm{e}\rangle$, which do not depend on distance. Fig. 4.9 shows the FPR for the comparison sample of elliptical galaxies and bulges with the best-fit line given by

$$\log(r_\mathrm{e}) = 0.99 \log(\sigma_\mathrm{e}) + 0.24\langle\mu_\mathrm{e}\rangle - 6.46\,, \tag{4.4}$$

where r_e is given in kpc, σ_e in km s^{-1}, and $\langle\mu_\mathrm{e}\rangle$ in mag arcsec^{-2}. We derived the FPR coefficients with a direct fit approach using the `cramer` routine in IDL. They are consistent with those found by Bernardi et al. (2003b) considering a sample of 8022 ETGs and analyzing their i-band images from the SDSS. The rms deviation in $\log(r_\mathrm{e})$ from the fitted relation (rms = 0.15) is larger than that obtained by Bernardi et al. (2003b), but similar to the K-band and B-band values of Falcón-Barroso et al. (2002) and to the V-band value of Falcón-Barroso et al. (2011), respectively. In the literature there is a general agreement that the typical scatter of the FPR (rms $\simeq$ 0.10) is independent of the photometric passband (Jorgensen et al. 1996; La Barbera et al. 2010; Kim et al. 2016). But most works concentrate on elliptical and lenticular galaxies and adopt different fitting methods.

As a matter of fact, it is observationally easier to study the large and bright bulges of lenticular and early-type spiral galaxies than the small and faint bulges of late-type spiral galaxies, which are more affected by dust patches and lanes and require more complex photometric decompositions (Laurikainen et al. 2010). Since they share similar properties, it is considered that elliptical galaxies and early-type bulges usually follow the same FPR in optical and near-infrared passbands, whereas late-type bulges deviate from the relation (Falcón-Barroso et al. 2002). Some authors explained the deviation of late-type bulges from the FPR by taking into account the total kinetic energy of the system (Bender et al. 1992; Falcón-Barroso et al. 2002). Correcting the velocity dispersion for this missing contribution allows the placement of bulges of different morphological types on the same FPR (Bender et al. 1992; Falcón-Barroso et al. 2002). We measured the rotational velocity of our sample bulges within r_e. After correcting for slit orientation and galaxy inclination, we found that in the bulge region the maximum rotational velocity $|v_\mathrm{max}|_{r<r_\mathrm{e}}$ is much smaller than the corresponding σ_e, which is $|v_\mathrm{max}|_{r<r_\mathrm{e}} \simeq 50$ km s^{-1} for SDSSJ1152 and $|v_\mathrm{max}|_{r<r_\mathrm{e}} < 30$ km s^{-1} for the remaining galaxies. The slit misalignment does not affect σ_e which we measured

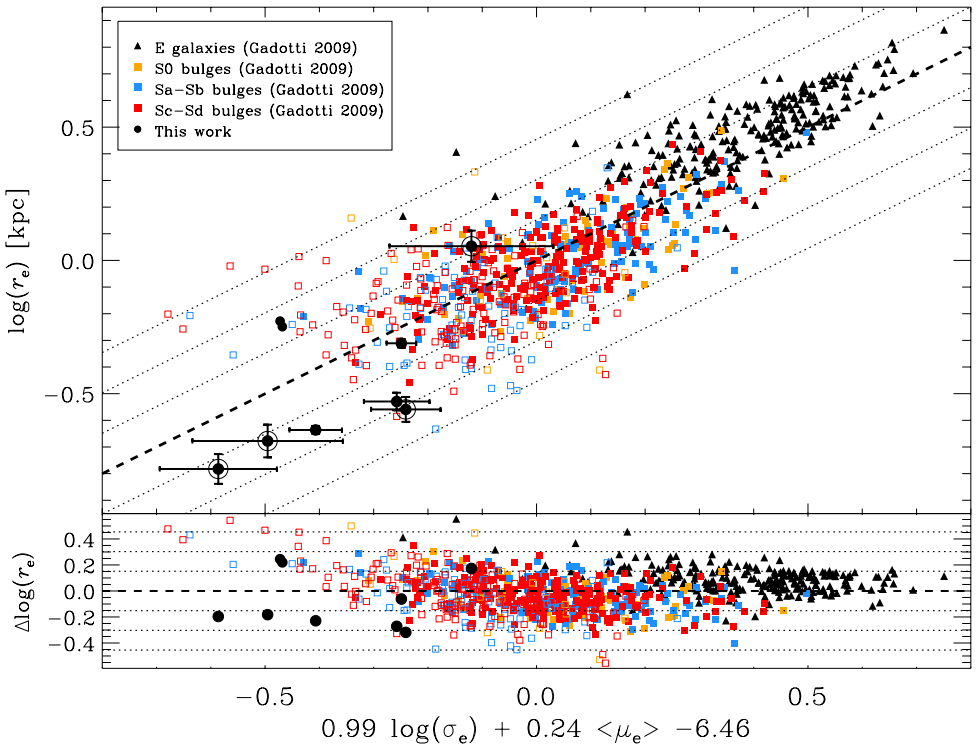

Figure 4.9: Fundamental plane relation for the galaxies of our (larger symbols) and comparison sample (smaller symbols). The elliptical galaxies (black triangles) and bulges in S0 (orange squares), Sa–Sb (blue squares), and Sc–Sd galaxies (red squares) of the comparison sample are shown with filled ($\sigma > 70$ km s^{-1}) and empty symbols ($\sigma < 70$ km s^{-1}) according to their calculated velocity dispersion. Filed circles with and without error bars correspond to the galaxies in our sample with and without bulge, respectively. Open circles denote the barred galaxies. The dashed line is the best-fit relation for the comparison sample. The dotted lines show the 1 rms, 2 rms, and 3 rms deviation in $\log(r_e)$ regions, respectively.

over nearly squared apertures. Thus, the correction of the velocity dispersion values does not affect the position of the bulges in the FPR, although these measurements are subject to our observational limits in terms of both the large PSF FWHM of our spectra with respect to r_e and possible contamination from the underlying disk. However, the surface brightness distribution is dominated by the bulge contribution by a factor 2–10 with respect to the disk inside r_e. Therefore, we are confident that our luminosity-weighted spectroscopic measurements are probing the bulge kinematics.

Each of our bulges is consistent with the FPR of the comparison sample (Fig. 4.9). No obvious differences appear in the residuals when galaxies are divided according to their

morphological type. Moreover, the FPR suggests that a single population of bulges share the same physical properties. This is also true when our small bulges are considered.

4.5.2 Kormendy relation

According to the KR (Kormendy 1985; Nigoche-Netro et al. 2008) larger galaxies are fainter than smaller galaxies. Fig. 4.10 shows the KR for the comparison sample of elliptical galaxies and bulges with the best-fit line given by

$$\langle \mu_{\rm e} \rangle = 0.77(\pm 0.08) \log(r_{\rm e}) + 18.84(\pm 0.02)\,, \tag{4.5}$$

where $\langle \mu_{\rm e} \rangle$ is expressed in mag arcsec^{-2} and $r_{\rm e}$ in kpc. We derived the KR coefficients using the `poly_fit` routine in IDL. The low value of the Pearson correlation coefficient ($\rho = 0.3$) reflects the large scatter of the relation when all the comparison galaxies are considered together. The rms deviation in $\langle \mu_{\rm e} \rangle$ from the fitted relation (rms = 0.7 mag arcsec^{-2}) is slightly larger than values quoted in earlier works (e.g., Hamabe & Kormendy 1987; La Barbera et al. 2003) making it difficult to observe a clear trend, contrary to previous findings (e.g., Aguerri et al. 2004; Ravikumar et al. 2006). However, comparing galaxies with different absolute magnitudes could be misleading because of the strong bias caused by selecting systems with different stellar masses (Nigoche-Netro et al. 2008). Indeed, we found a clear trend when different intervals of absolute magnitude are considered in agreement with Nigoche-Netro et al. (2007, 2008), who pointed out how the KR coefficients and rms deviation from the fitted relation change when choosing fixed-width intervals of progressively brighter absolute magnitude.

Our bulges are consistent with the magnitude-dependent trend of the KR, and 5 of them lie in the poorly populated region of the low-mass systems characterized by small $r_{\rm e}$ and large $\langle \mu_{\rm e} \rangle$ (Fig. 4.10). The offset of the bulge of SDSSJ1152 is explained by the large errors on $r_{\rm e}$ and $\langle \mu_{\rm e} \rangle$. Indeed, the data point is consistent within 3 rms with its magnitude bin. Owing to the large scatter and overall dependance on the mass of the KR, we cannot infer any difference in the populations of bulges using such a relation, which is indeed a poor proxy to disentangle bulge properties.

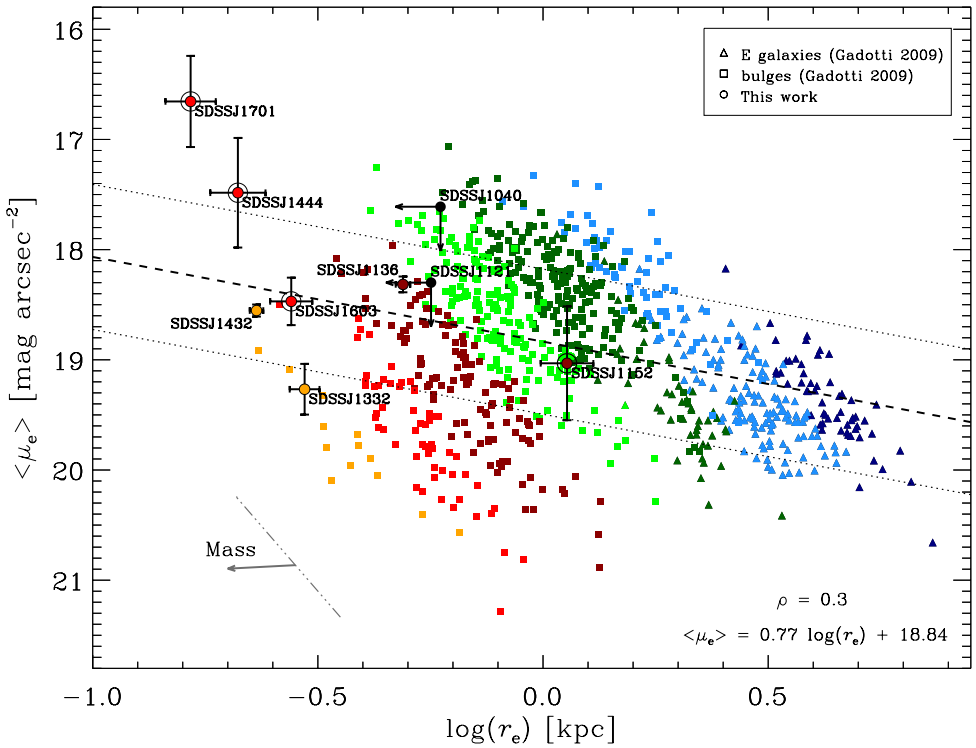

Figure 4.10: Kormendy relation for the galaxies of our (larger symbols) and comparison sample (smaller symbols). The elliptical galaxies and bulges of the comparison sample are shown with triangles and squares, respectively. Filled circles with and without error bars correspond to the galaxies in our sample with and without bulge, respectively. Open circles indicate the barred galaxies. The galaxies are divided according to their absolute magnitude in the following bins: $M_i < -22$ mag (dark blue), $M_i = [-22, -21]$ mag (light blue), $M_i = [-21, -20]$ mag (dark green), $M_i = [-20, -19]$ mag (light green), $M_i = [-19, -18]$ mag (dark red), $M_i = [-18, -17]$ mag (light red), and $M_i = [-17, -16]$ mag (orange). The dashed line is the best-fit relation for the comparison sample. The dotted lines show the rms deviation in $\langle\mu_e\rangle$ from the fit. The dash-dotted line gives the slope of the KR for the magnitude bin $M_i = [-20, -19]$ mag, while the arrow indicates the KR trend for decreasing masses (Nigoche-Netro et al. 2008). The best-fit relation and Pearson correlation coefficient are also given.

4.5.3 Faber-Jackson relation

The FJR (Faber & Jackson 1976; Falcón-Barroso et al. 2011) states that brighter galaxies exhibit larger velocity dispersion. Fig. 4.11 shows the FJR for the comparison sample of elliptical galaxies and bulges with the best-fit line given by

$$\log(\sigma_e) = -0.152(\pm 0.003) M_i - 1.07(\pm 0.07)\,, \tag{4.6}$$

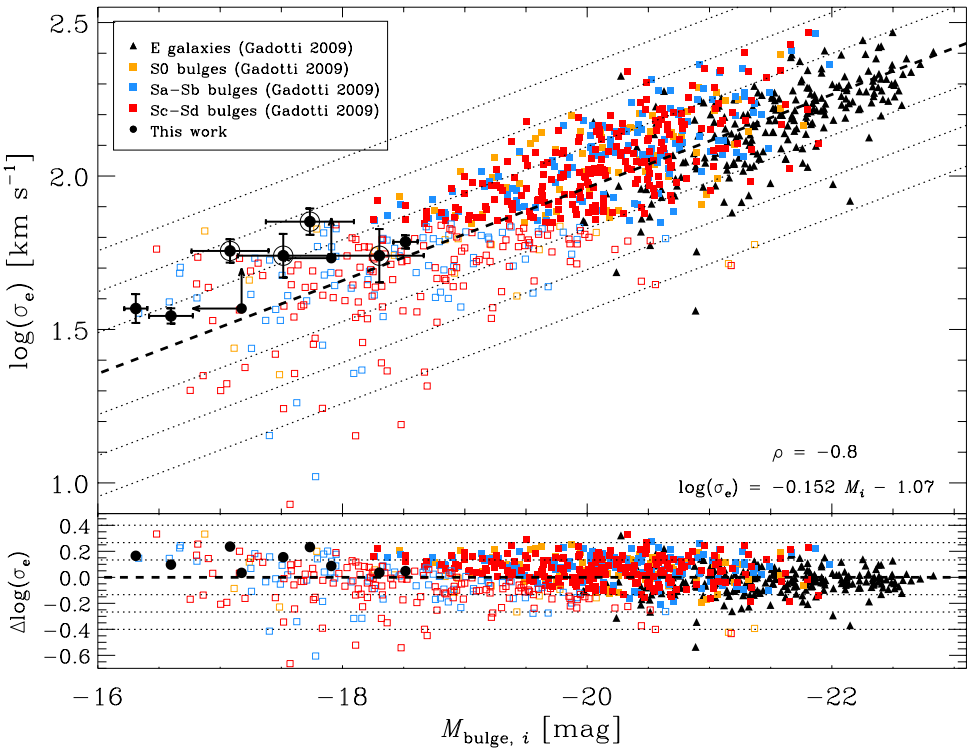

Figure 4.11: As in Fig. 4.9 but for the FJR and with the rms deviation in $\log(\sigma_e)$ from the fit. The best-fit relation and Pearson correlation coefficient are also given.

where σ_e is provided in km s^{-1} and M_i is the i-band absolute magnitude of the galaxy spheroid. We derived the FJR coefficients using the `poly_fit` routine in IDL. Eq. (4.6) results in $L \propto \sigma^{2.64\pm0.01}$, which deviates from the theoretical virial relation $L \propto \sigma^4$, but it is consistent with $L \propto \sigma^{2.9\pm0.5}$ found by Balcells et al. (2007) for a sample of bulges observed with the HST in the K band. The Pearson correlation coefficient is $\rho = -0.8$, reflecting a tight correlation between galaxies properties in this plane.

The scatter increases in the low-σ end of the relation, showing a trend mimicking the expected down-bending of the FJR (Falcón-Barroso et al. 2011). This regime of the FJR is populated by the small bulges of the comparison sample. Their velocity dispersion are far below the instrumental resolution of the SDSS spectra. Moreover, they are measured within a fixed aperture of 3 arcsec, where a significant contamination from the disk component is expected because of the small B/T of these galaxies. On the contrary, no hint of

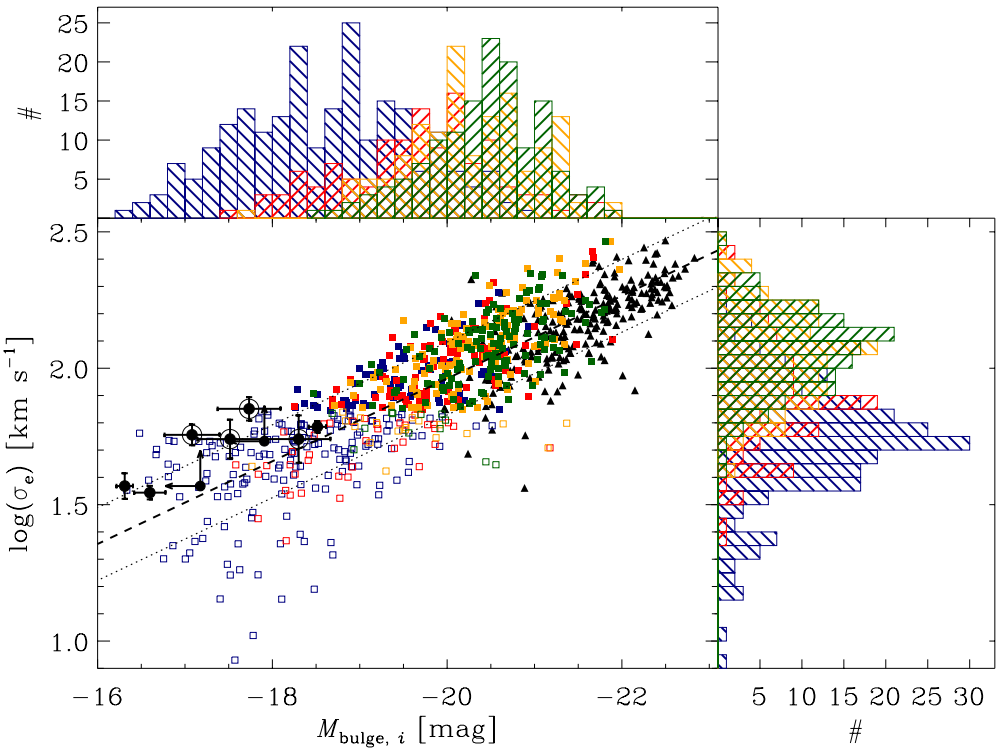

Figure 4.12: Faber-Jackson relation for the galaxies of our (larger symbols) and comparison sample (smaller symbols). The elliptical galaxies (triangles) and bulges (squares) of the comparison sample are shown with filled ($\sigma > 70$ km s^{-1}) and empty symbols ($\sigma < 70$ km s^{-1}) according to their calculated velocity dispersion. Filled circles with and without error bars correspond to the galaxies in our sample with and without bulge, respectively. Open circles indicate the barred galaxies. The galaxies are divided according to their Sérsic index in the following bins: $1 < n < 2$ (blue), $2 < n < 3$ (red), $3 < n < 4$ (orange), and $n > 4$ (green). The dashed line is the best-fit relation for the comparison sample. The dotted lines show the rms deviation in $\log(\sigma_e)$ given in Fig. 4.11. The distribution of galaxies of the different bins of n as function of their absolute magnitude and effective velocity dispersion are also shown.

down-bending is observed for our bulges, which have measured σ larger than instrumental resolution. At face values, they are above the FJR whereas disk-like bulges are expected to be low-σ outliers, being rotation rather than pressure supported. As a matter of fact, each of our bulges follows the same FJR of the brighter elliptical galaxies and bulges of the comparison sample. Moreover, we could infer that both elliptical galaxies and bulges share the same properties when the FJR is used. The FJR down-bending highlighted in other works (Méndez-Abreu et al. 2008a; Kim et al. 2016) could be due to selection effects, when

only high- or low-mass systems are considered. Indeed, the slope of the relation changes when galaxies with increasing values of absolute magnitudes are considered (Nigoche-Netro et al. 2010).

We did not observe any trend when bulges are divided according to the morphological type of their host galaxies (Fig 4.11), in agreement with the results by Thomas & Davies (2006). They found that the stellar populations of less massive bulges are typically younger, less metal-rich, and less overabundant of α elements than ETGs with no dependance on the morphological type. This also supports the correlation between the structural parameters (e.g., $r_{\rm e}/h$ and B/T) and bulge luminosity and mass rather than morphological type.

We observed a smooth transition from larger to smaller values of n according both to σ and $M_{\rm bulge,\,i}$ when the sample is divided in terms of the Sérsic index (Fig. 4.12). This suggests that n strongly depends on the mass of the system. The same trend is visible when B/T is considered (see Eq. (4.1) in Section 4.3.3). Recently, Kim et al. (2016) have shown that faint galaxies ($-19 < M_{r,\,\rm bulge} < -17$ mag) with smaller B/T have systematically lower σ than those with larger B/T. They concluded that bulges in low-B/T galaxies are rotation supported (i.e., disk-like bulges). However, this is due to a bias caused by *a priori* selection of the B/T range used for fitting the FJR. Moreover, this selection leads to contradictory results because for brighter galaxies ($M_r \lesssim -20$ mag) a smaller B/T corresponds to a larger σ (see their Fig. 9).

■ 4.6 Discussion

The 7 late-type bulges we studied in this work are small and have a low mass, as confirmed by their position in the FPR (Fig. 4.9), KR (Fig. 4.10), and FJR (Fig. 4.11). Although they are located at the low-$r_{\rm e}$ and low-σ ends of the scaling relations, they follow the same trend of elliptical galaxies and larger and more massive bulges. To address the statistical significance of our claim, we computed the probability of each bulge to be compatible with the fitted relations by means of MC simulations. The deviation of each bulge from the FPR and FJR is less than 2.1 rms, therefore we can not consider them outliers. We found no differences between photometric and kinematic properties of barred and unbarred galaxies. The remaining two galaxies SDSSJ1040 and SDSSJ1121 were better fit only with a disk

component. This means that either they have no bulge or their bulge is really small and beyond our possibility to detect it. The latter reinforces the finding that small bulges are not low-σ outliers in FJR.

As far as the structure and kinematics of disk-like bulges concerns, they are expected to share the properties of the surrounding host disks and be more rotation-dominated than classical bulges. Our bulges bulges fulfill many of the observational prescriptions originally provided by Kormendy & Kennicutt (2004) and later revised by Kormendy (2016) as classified as disk-like bulges. They have a late-type morphology with a nearly exponential light profile, small B/T, low velocity dispersion, and ongoing star formation, as proved by the presence of strong Hβ and [OIII]5007 emission lines in their spectra. All the galaxies of our sample exhibit either a spiral structure all the way down to the galaxy center or a bar component (Fig. 4.2). In this case the bulge dynamics should be more similar to that of a disk rather than a spheroidal component, making the bulge a low-σ outlier in the FJR. But our bulges are not rotation-dominated systems (i.e., the maximum velocity value inside the bulge region is $|v_{\rm max}|_{r<r_{\rm e}} \leq 50$ km s^{-1}), although they are characterized by very low values of velocity dispersion ($\sigma_{\rm e} \lesssim 70$ km s^{-1}). Each of them follows the same scaling relations of elliptical galaxies, massive bulges, and compact ETGs so they cannot be classified as disk-like systems.

We explored the possibility that our bulges could actually be similar to other spheroidal systems, such as globular clusters (GCs) and compact ETGs (cETGs). To this aim, we further extended the M_i and $\sigma_{\rm e}$ ranges of the FJR by including 125 GCs of the nearby giant elliptical NGC 5128 (Taylor et al. 2015) and 8 low-mass cETGs of the Virgo cluster (Guérou et al. 2015). We transformed the absolute magnitude of the GCs in the i band using the prescriptions from SDSS-DR8[1] (Aihara et al. 2011). Fig. 4.13 shows that our bulges do not share the same position of GCs in the FJR even though they have similar values of velocity dispersion ($\sigma_{\rm e} \simeq 30$ km s^{-1}). The absolute magnitude of GCs is indeed several orders of magnitude fainter than that of small bulges. On the contrary, cETGs follow the same FJR as our bulges and more massive bulges. This supports the idea that the low SDSS-based values of velocity dispersion are in reality affected by instrumental resolution

[1]The equations are available on the website: `https://www.sdss3.org/dr8/algorithms/sdssUBVRITransform.php#Lupton2005`.

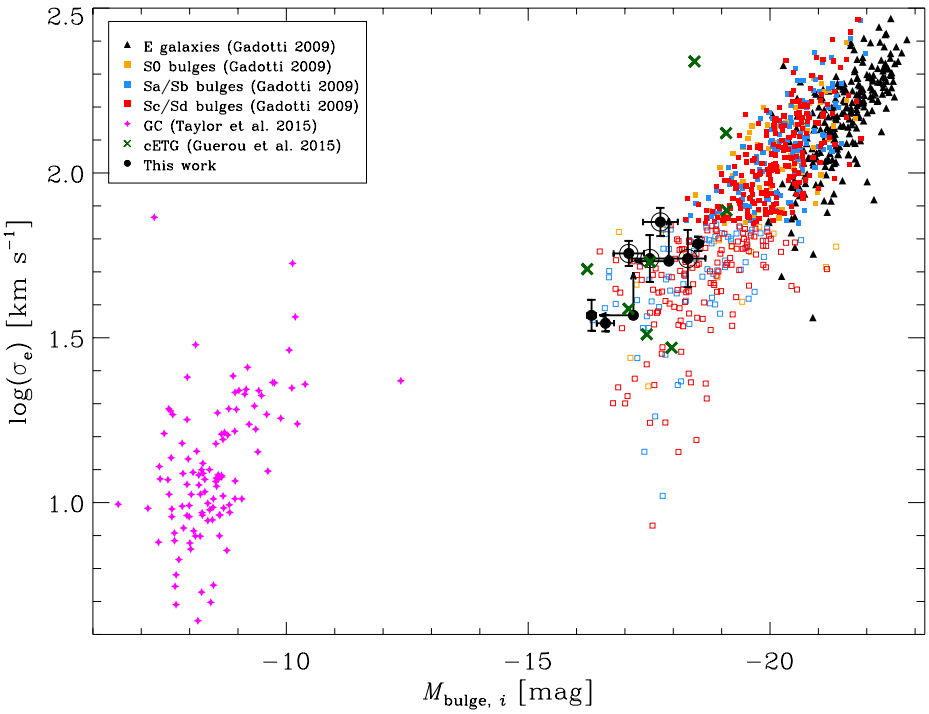

Figure 4.13: As in Fig. 4.11 but including the GCs from Taylor et al. (2015, pink stars) and cETGs from Guérou et al. (2015, green crosses).

and disk contamination, and suggests that the less massive bulges follow the same scaling relations as elliptical galaxies and more massive bulges.

We found no correlation between the location of our bulges in the FPR or FJR and Hubble type of their host galaxies. The lack of correlation between the structural and kinematical properties of bulges and galaxy morphology is in agreement with the findings of Thomas & Davies (2006), who focused on the stellar population properties of bulges. The mass rather than the morphology seems to be the driver of the intrinsic physical properties of bulges. As a matter of fact, we found a single population of galaxy spheroids that follows the same scaling relations, where the mass leads to a smooth transition in the photometric and kinematic properties from less to more massive bulges and elliptical galaxies.

It is worth noting that classical and disk-like bulge are usually separated only using the Sérsic index of their surface-brightness radial profile or even worse the Sérsic index of their host galaxy. This is a misuse of the findings of Fisher & Drory (2008, 2010), who pointed

out a bimodal distribution of the Sérsic index of bulges. Once bulge-disk decomposition was performed on galaxies separated according to their visual morphology, they found that classical bulges have $n > 2$ while disk-like bulges have $n < 2$. To date, no physical explanation has been found for this behavior. Moreover, since the Sérsic index correlates with B/T in classical bulges (Fisher & Drory 2008; Gadotti 2009), the common belief is that disk-like bulges have $B/T < 0.35$. However, the photometric and kinematic properties of our bulges in the framework of the scaling relations of elliptical galaxies and bulges show that small values of n and B/T do not guarantee that a bulge is disk-like.

4.7 Conclusions

We analyzed the surface brightness distribution and stellar kinematics of a sample of late-type spiral galaxies. They were selected to investigate the photometric and kinematic properties of small bulges in order to understand whether they follow the same scaling relations traced by elliptical galaxies and large bulges and if they are disk-like or classical bulges.

We obtained the structural parameters of the sample galaxies by performing a two-dimensional photometric decomposition of their SDSS i-band images. The surface brightness distribution of each galaxy was assumed to be the sum of the contribution of a Sérsic bulge and an exponential disk. We included a Ferrers bar in fitting the images of 4 sample galaxies. We found a bulge component in 7 galaxies, while the remaining 2 resulted in pure disk galaxies. We measured the stellar velocity dispersion within the bulge effective radius from long-slit spectra taken with high spectral resolution. All the sample bulges have small $r_{\rm e}$, nearly exponential light profiles, small B/T, low σ, and ongoing star formation.

We combined the photometric ($r_{\rm e}$, $\langle\mu_{\rm e}\rangle$, and M_i) and kinematic parameters ($\sigma_{\rm e}$) of the sample bulges to study their location in the FPR, KR, and FJR. To this aim, we built the scaling relations defined for a comparison sample of nearby elliptical galaxies and bulges with structural parameters and velocity dispersion measured from SDSS i-band images and spectra by Gadotti (2009) and Oh et al. (2011), respectively. Our data extend the scaling relations to the regime of bulges with $r_{\rm e} \simeq 0.2$ kpc, $\sigma_{\rm e} \simeq 35$ km s^{-1}, and $M_i \simeq -16$ mag. The FPR coefficients are consistent with the findings of Bernardi et al. (2003b), which are based

on a much larger sample of ETGs and characterized by a smaller scatter. The location of the elliptical galaxies and bulges in the FPR suggests that there is a single population of galaxy spheroids sharing the same physical properties. This is also true when our small bulges are considered. No differences appear in the residuals when galaxies are divided according to their morphological type. The sample bulges are actually small in size and mass, resulting from their location in the KR. We confirmed that this relation is a poor proxy of the bulge properties due to its large intrinsic scatter and magnitude bias (Nigoche-Netro et al. 2008, 2010), although it is commonly used to disentangle between classical and disk-like bulges (e.g., Vaghmare et al. 2013; Mishra et al. 2017). Our small bulges with resolved velocity dispersion are not following the down-bending previously reported in the low-σ end of the FJR, but trace the same trend as elliptical galaxies and large bulges. This supports the idea that the lowest values of the SDSS-based σ are actually affected by instrumental resolution and disk contamination. We observed a smooth transition in FJR from larger to smaller values of n according both to $\sigma_{\rm e}$ and M_i when the comparison sample is divided in terms of the Sérsic index. This suggests that n strongly depends on the mass of the system rather than on the morphology of the host galaxy.

Our bulges fulfill most of the observational prescriptions (Kormendy & Kennicutt 2004; Kormendy 2016) for being disk-like bulges. But they are not rotation dominated and follow the same scaling relations of elliptical galaxies and larger and more massive bulges, where the mass seems to lead to a smooth transition in the photometric and kinematic properties from less to more massive systems. We conclude that small values of n and B/T do not guarantee that a bulge is disk-like and not classical.

5

INTRINSIC SHAPE OF CALIFA BULGES

The intrinsic shape of galactic bulges in nearby galaxies provides crucial information to separate bulge types. We intended to derive accurate constraints to the intrinsic shape of bulges to provide new clues on their formation mechanisms and set new limitations for future simulations. We retrieved the intrinsic shape of a sample of CALIFA bulges using a statistical approach. Taking advantage of `GalMer` numerical simulations of binary mergers we estimated the reliability of the procedure. Analyzing the i-band mock images of resulting lenticular remnants, we studied the intrinsic shape of their bulges at different galaxy inclinations. Finally, we introduced a new (B/A, C/A) diagram to analyze possible correlations between the intrinsic shape and properties of bulges. We tested the method on simulated lenticular remnants, finding that for galaxies with inclinations $25^\circ < \theta < 65^\circ$ we can safely derive the intrinsic shape of their bulges. We found that our CALIFA bulges tend to be nearly oblate systems (66%), with a smaller fraction of prolate spheroids (19%) and triaxial ellipsoids (15%). The majority of triaxial bulges are in barred galaxies (75%). Moreover, we found that bulges with low Sérsic indices or in galaxies with low bulge-to-total luminosity ratios form a heterogeneous class of objects; additionally, bulges in late-type galaxies or in less massive galaxies have no preference for being oblate, prolate, or triaxial. On the contrary, bulges with high Sérsic index, in early-type galaxies, or in more massive galaxies are mostly oblate systems. We concluded that various evolutionary pathways may coexist in galaxies, with merging events and dissipative collapse being the main mechanisms driving the formation of the most massive oblate bulges and bar evolution reshaping the less massive triaxial bulges.

5.1 Introduction

In observational extragalactic astrophysics, our measurements of the light distribution of galaxies are confined to the two-dimensional framework of the sky plane. Although observations can only access the projected rather than intrinsic luminosity density of galaxies, we can disentangle their different luminous components, including bulges. Constraining the three-dimensional light distribution of the galaxy components, and therefore their intrinsic shape, is a crucial piece of information in our understanding of how galaxies form and evolve.

Several studies addressed the intrinsic shape of the elliptical galaxies (Sandage et al. 1970; Tremblay & Merritt 1996; Rodríguez & Padilla 2013). Although many elliptical galaxies were initially thought to be oblate or prolate spheroids, some photometric (i.e., the twisting of the isophotes; Carter 1978; Bertola & Galletta 1979) and kinematic properties (i.e., the low rotation of stars or the kinematic misalignment; Bertola & Capaccioli 1975; Illingworth 1977; Krajnović et al. 2011) promptly supported the idea that some of them could be triaxial ellipsoids. In general, faint elliptical galaxies are more flattened with a tendency to be oblate spheroids, whereas bright elliptical galaxies are rounder and more frequently triaxial ellipsoids (Weijmans et al. 2014; Foster et al. 2017). It should be noticed that most of the works about the intrinsic shape of elliptical galaxies deal with the distribution function of the intrinsic axial ratios of the whole population through statistical analyses of their apparent flattenings (see Méndez-Abreu 2016, for a review). As a matter of fact, it is not possible to recover the intrinsic shape of an individual elliptical galaxy by only studying its light distribution (Statler et al. 2001). Indeed, deprojecting the apparent shape of an elliptical into its intrinsic shape represents a typical ill-posed problem, caused by the lack of observational constraints on the three Euler angles (θ, ϕ, ψ) that provide the transformation. Further details about the galaxy structure, like the presence of dust lanes, gaseous disks or embedded stellar disks (e.g., NGC 5077, Bertola et al. 1991a) or the knowledge of the stellar velocity field (e.g., NGC 4365, van den Bosch et al. 2008) are needed to overcome this problem. On the contrary, in disk galaxies it is possible to derive the intrinsic shape of individual bulges because of the presence of the disk component. Its observed ellipticity provides a proxy for the bulge inclination, under the assumptions that both the bulge and disk share the same equatorial plane of symmetry and that disks are highly-flattened oblate

spheroids (but, see also Ryden 2004, 2006, for different findings).

The bulge is photometrically defined as the structural component responsible for the light excess measured in the galaxy central regions, above the inward extrapolation of the exponential surface brightness profile of the disk (Andredakis et al. 1995; Balcells et al. 2007). The main concern for bulges is separating their light contribution from that of the other galaxy components. This is usually done by means of the photometric decomposition of the galaxy surface brightness into the contribution of the bulge and disk, and possibly of a lens, a bar, inner or outer rings, nuclear unresolved components, and spiral arms (Peng et al. 2002; Laurikainen et al. 2005; Gadotti 2009; Benítez et al. 2013; Erwin 2015).

Nowadays, it is widely accepted that bulges are not simple axisymmetric structures in the center of galaxies (see Méndez-Abreu 2016, for a review). The misalignment between the bulge and disk isophotes observed in many spiral galaxies (e.g., M31, Lindblad 1956; Williams & Schwarzschild 1979) resembles the isophotal twist of elliptical galaxies and it is similarly interpreted as the signature of bulge triaxiality. The first quantitative estimate of the triaxiality of bulges was carried out by Bertola et al. (1991b) by studying the misalignment between the major axes of the bulge and disk in a sample of 32 early-type disk galaxies. They found that the mean intrinsic axial ratio of bulges in the disk plane is $\langle B/A \rangle = 0.86$, while their mean intrinsic flattening in the plane perpendicular to the disk plane is $\langle C/A \rangle = 0.65$, where A, B, and C are the lengths of the semi-axes of the bulge ellipsoid. This result was later confirmed by Fathi & Peletier (2003), who analyzed the deprojected axial ratio of the galaxy isophotes within the bulge radius in a sample of 70 disk galaxies, ranging from lenticular to late-type spiral galaxies. They found $\langle B/A \rangle = 0.79$ and $\langle B/A \rangle = 0.71$ for the bulges in earlier and later morphological types, respectively. By means of a two-dimensional photometric decomposition, Méndez-Abreu et al. (2008a) measured the structural parameters of both bulges and disks in a sample of 148 early-to-intermediate spiral galaxies, increasing the statistics of Bertola et al. (1991b) by an order of magnitude. They found that about 80% of the sample bulges are triaxial ellipsoids with $\langle B/A \rangle = 0.85$. More recently, Méndez-Abreu et al. (2010) introduced a novel statistical method to constrain the intrinsic shape of individual bulges (see Section 2.2, for details). The knowledge of the geometric properties (i.e., the apparent ellipticity and major-axis position angle) of the bulge and disk makes it possible to simultaneously compute the probability distribution function

of the intrinsic axial ratios B/A and C/A for every single bulge. They revisited the galaxies of the sample of Méndez-Abreu et al. (2008a) and concluded that 65% of them host oblate triaxial bulges while the remaining ones have prolate triaxial bulges.

Nevertheless, further efforts are required to better characterize the intrinsic shape of bulges and, in particular, a higher number statistics is needed to investigate the correlations between the bulge shape and galaxy properties. Knowing the intrinsic shape of bulges completes our understanding of the potential well and orbital distribution of the stars in the inner regions of galaxies. This will also help us to explain the origin of the different populations of classical and disk-like bulges, as well as to address the assembly processes of their host galaxies. (e.g., Athanassoula 2005; Brooks & Christensen 2016). Currently, the observational separation between classical and disk-like bulges is usually done by analyzing their observed photometric, kinematic, or stellar population properties (Morelli et al. 2008; Coelho & Gadotti 2011). However, the demarcation lines are often blurred making difficult to understand the actual frequency of different bulge types (see Chapter 4, for all details). Furthermore, bulges can suffer from different processes during their lifetime with some of them giving rise to similar observational properties. As a consequence, different kind of bulges can coexist in the same galaxy (Athanassoula 2005; Méndez-Abreu et al. 2014; Erwin et al. 2015). The measurements of the intrinsic shape of bulges might provide a fundamental additional constraint to separate bulge types, as well as limitations for future numerical simulations willing to reproduce realistic galaxies.

In this Chapter, we analyzed the intrinsic shape of the bulges of some of the disk galaxies observed in the CALIFA DR3 (Sánchez et al. 2016). We aimed at investigating the possible links between the intrinsic shape of bulges and their observed photometric properties. Here, we improved the previous results by Méndez-Abreu et al. (2008a, 2010) by testing the reliability of their statistical method and setting limits on the galaxy inclination to its successful application with the help of mock images of a set of simulated remnant galaxies.

The Chapter is organized as follows. The galaxy sample is presented in Section 5.2. In Section 5.3 mock images of simulated remnant galaxies seen at different inclinations are used to understand the limits of our analysis. The intrinsic shape of the bulges of the sample galaxies is derived in Section 5.4. The discussion about the possible implications of our results for galaxy formation is given in Section 5.5. Our conclusions are presented in

Section 5.6. $H_0 = 70$ km s^{-1} Mpc^{-1}, $\Omega_{\rm M} = 0.3$, and $\Omega_\Lambda = 0.7$ are adopted as cosmological parameters throughout this Chapter.

5.2 Sample selection

We selected our galaxies sample from the final sample of galaxies included in the CALIFA DR3, which was drawn from the SDSS DR7 (Abazajian et al. 2009) and comprises 667 nearby galaxies ($0.005 < z < 0.03$) with an angular isophotal diameter between 45 and 79.2 arcsec at a surface brightness level of 25 mag arcsec^{-2} in the r band.

First, we focused onto the 314 disk galaxies of CALIFA DR3, not interacting or merging, with a photometric decomposition obtained in Chapter 3. These galaxies were fit with either bulge and disk only (177 galaxies), or with a bar in addition to bulge and disk (137 galaxies) using the GASP2D algorithm (see Section 2.1, for all details).

Then, we took into account only the galaxies with good imaging, that is the absence of either strong fluctuations of the local sky background around the galaxy or other bright component affecting the photometric decomposition (e.g., a lens, inner and/or outer rings, and spiral arms), and all the structural parameters of the bulge, disk, and bar left free to vary during the fitting process (i.e., the galaxies flagged as 1,a in Table 3.7). This allowed us to obtain a subsample of 118 robustly fitted galaxies (67 unbarred and 51 barred galaxies), with no bias on the measured structural parameters that could hamper our analysis of the bulge intrinsic shape.

Finally, we set a limit onto the galaxy inclination ($25^\circ < \theta < 65^\circ$) to exclude both the low-inclined galaxies, for which it is not possible to constrain the bulge shape along the direction perpendicular to the disk plane, and the highly-inclined ones, for which the results of the GASP2D photometric decomposition are not reliable (see Section 3.2, for all details) and the bulge shape on the disk plane is unconstrained (see Section 5.3.2, for a discussion). This selection criterion reduced the galaxy sample to 83 objects (43 unbarred and 40 barred galaxies).

We considered only galaxies with i-band images to better resolve the bulge component minimizing the dust effects with respect to the other SDSS passbands. The choice of i band assured a sufficient spatial resolution ($FWHM = 1.1 \pm 0.2$ arcsec) and depth (out to $\mu_i \simeq 26$

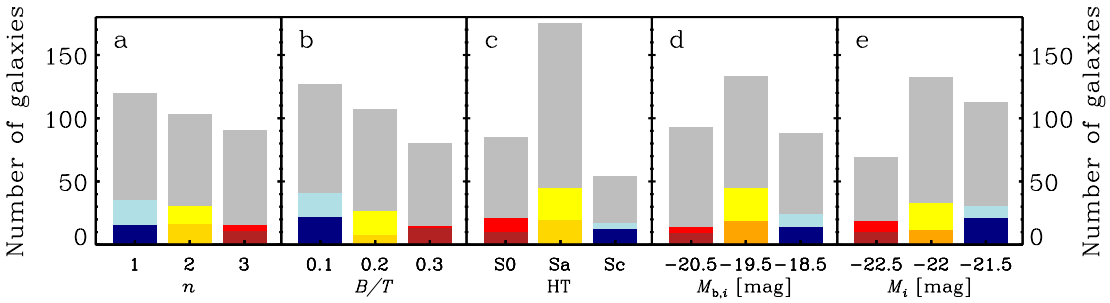

Figure 5.1: Distribution of the Sérsic index of the bulge (*panel a*), bulge-to-total luminosity ratio (*panel b*), Hubble type (*panel c*; Sa bin comprises Sa-Sab-Sb-Sbc galaxies, while Sc bin comprises Sc-Scd-Sd-Sdm galaxies), i-band absolute magnitude of the bulge (*panel d*), and i-band absolute magnitude of the galaxy (*panel e*) for our final sample of 43 unbarred (dark color histograms) and 40 barred galaxies (light color histograms). The gray histograms show the distribution of the remaining 231 galaxies of the sample of 314 disk galaxies selected from CALIFA DR3. The galaxy properties are taken from Méndez-Abreu et al. (2017).

mag arcsec^{-2}), as retrieved in Chapter 3. Their basic properties (i.e., Sérsic index of the bulge n, bulge-to-total luminosity ratio B/T, Hubble type HT, i-band absolute magnitude of the bulge $M_{\mathrm{b},i}$, and i-band absolute magnitude of the galaxy M_i presented in Chapter 3) are shown in Fig. 5.1 and compared with those of the selected sample of 314 disk galaxies from CALIFA DR3. This final sample is not complete in volume. However, we thought that the selection in diameter of the CALIFA sample should not introduce any major bias in our results, since the distribution of bulge observed properties is well sampled, as shown in Fig. 5.1.

■ 5.3 Bulge shape of simulated galaxies

In order to test our statistical method for recovering the intrinsic shape of bulges (see Section 2.2, for all details) and to understand its limitations, we measured the intrinsic axial ratios of the bulge against different galaxy inclinations. To this aim, we used a subset of 11 numerical simulations from the `GalMer` database[1](Chilingarian et al. 2010). We used remnant galaxies of a variety of merger experiments between pairs of galaxies with different mass, morphology, gas content, and orbital parameters. These remnant galaxies strongly resemble lenticular galaxies, according to their morphological, photometric, and kinematic

[1]The `GalMer` database is a public library of hydrodynamics N-body simulations of galaxy mergers with intermediate resolution available at `http://www.project-horizon.fr/`.

Table 5.1: Intrinsic shape of the bulges of the simulated lenticular remnants seen at different inclinations.

Galaxy	B/A					C/A		
	(0°)	(180°)	(30°)	(45°)	(60°)	(30°)	(45°)	(60°)
(1)	(2)	(3)	(4)	(5)	(6)	(7)	(8)	(9)
gE0gSbo5	1.00	1.00	1.00	1.00	1.00	0.99	0.59	0.59
gE0gSdo5	0.79	0.79	0.91	0.89	0.86	0.46	0.26	0.26
gS0dE0o98	0.46	0.49	0.49	0.64	0.56	0.51	0.21	0.36
gS0dE0o99	0.46	0.46	0.54	0.59	0.69	0.64	0.64	0.64
gS0dE0o100	0.46	0.46	0.49	0.54	0.56	0.59	0.14	0.39
gS0dS0o99	0.59	0.59	0.56	0.61	0.76	0.64	0.41	0.21
gS0dSao103	0.51	0.51	0.51	0.56	0.56	0.96	0.21	0.34
gS0dSbo106	0.44	0.44	0.41	0.46	0.61	0.69	0.39	0.29
gS0dSdo100	0.51	0.51	0.49	0.51	0.74	0.54	0.41	0.24
gSbgSbo9	0.71	0.71	0.76	0.76	0.76	1.06	0.74	0.54
gSbgSdo5	0.81	0.84	0.84	0.81	0.84	0.36	0.26	0.21

Notes. (1) Identifier in the `GalMer` database of the merger experiment resulting in a lenticular remnant, which we adopted as the name of the simulated galaxy. (2), (3), (4), (5), (6) Intrinsic axial ratio B/A of the bulge obtained from the mock images of the simulated lenticular remnants seen at an inclination $\theta = 0°$, 180°, 30°, 45°, and 60°, respectively. (7), (8), (9) Intrinsic axial ratio C/A of the bulge obtained from the mock images of the simulated lenticular remnants seen at an inclination $\theta = 30°$, 45°, and 60°, respectively.

properties (Borlaff et al. 2014; Querejeta et al. 2015b,c; Tapia et al. 2017, Eliche-Moral et al. in prep.).

We chose to analyze simulated lenticular remnants resulting from binary mergers instead of N-body realizations of analytical expressions, as those adopted for building the progenitor galaxies of the remnants, because we required a certain degree of bulge triaxiality. Such a triaxiality is a common feature of merger remnants, although their progenitors could be axisymmetric by construction (Cox et al. 2006a; Tapia et al. 2014). All the simulated lenticular remnants of the analyzed merger experiments are either unbarred galaxies if resulting from a major merger, or weakly barred galaxies if resulting from a minor merger (Eliche-Moral et al. in prep.). We discarded the merger experiments producing elliptical or E/S0 remnants, in order to have simulated galaxies with a well-defined bulge embedded into a large disk, similarly to the observed CALIFA galaxies.

The progenitor galaxies were modeled with a spherical non-rotating dark-matter halo, which contains a stellar and/or a gaseous disk and/or a central non-rotating bulge, depending

Table 5.2: Orbital parameters of the merger experiments resulting in the simulated lenticular remnants listed in Table 5.1.

ID_{orb}	Spin-orbit	i_2	d_{per}	E_0
	[P/R]	[°]	[kpc]	[10^4 km^2 s^{-2}]
(1)	(2)	(3)	(4)	(5)
5	P	0	16	0
9	P	0	24	0
98	P	33	8	2.5
99	P	33	8	5
100	P	33	8	15
103	R	33	8	0
106	R	33	8	15

Notes. (1) Identifier in the `GalMer` database of the orbit used in the merger experiment. (2) Spin-orbit coupling (P: prograde; R: retrograde). (3) Inclination of the secondary progenitor with respect to the orbital plane. (4) Pericenter distance. (5) Initial orbital energy.

on their morphological type. The primary galaxy consisted of a giant galaxy (hereafter gE0 for a giant-like elliptical, gS0 for a giant-like lenticular, gSa for a giant-like Sa spiral, gSb for a giant-like Sb spiral, and gSd for a giant-like Sd spiral) interacting either with another giant galaxy of similar mass or with a dwarf galaxy (hereafter dE0, dS0, dSa, dSb, and dSd), whose total mass is ten times smaller than that of the giant galaxy. Several simulations were performed varying the initial orbital energy, pericenter distance, and inclination with respect to the orbital plane of the interacting galaxies. Indeed, for each interacting pair the disk (when present) of one of the two galaxies is kept in the orbital plane, while the companion disk can have a different inclination. Direct and retrograde orbits were also taken into account, where direct or retrograde spin-orbit coupling refer to progenitors having either parallel or antiparallel spins, respectively. The merger experiments have a total of 240 000 and 528 000 particles for the major and minor merger events, respectively. The particles have a mass $M = 3.5\text{–}20.0 \times 10^5$ $M_\odot$ each. The merger experiments have a duration of 3–3.5 Gyr and were evolved using a `Tree-SPH` code (Semelin & Combes 2002), adopting the same softening length for all particle types $\epsilon = 280$ pc for the giant-giant galaxy mergers and $\epsilon = 200$ pc for the giant-dwarf galaxy mergers. The effects of gas and star formation (such as the stellar mass loss, metallicity enrichment of the interstellar medium, and energy injection due to supernova explosions) were considered using the method described in Mihos & Hernquist

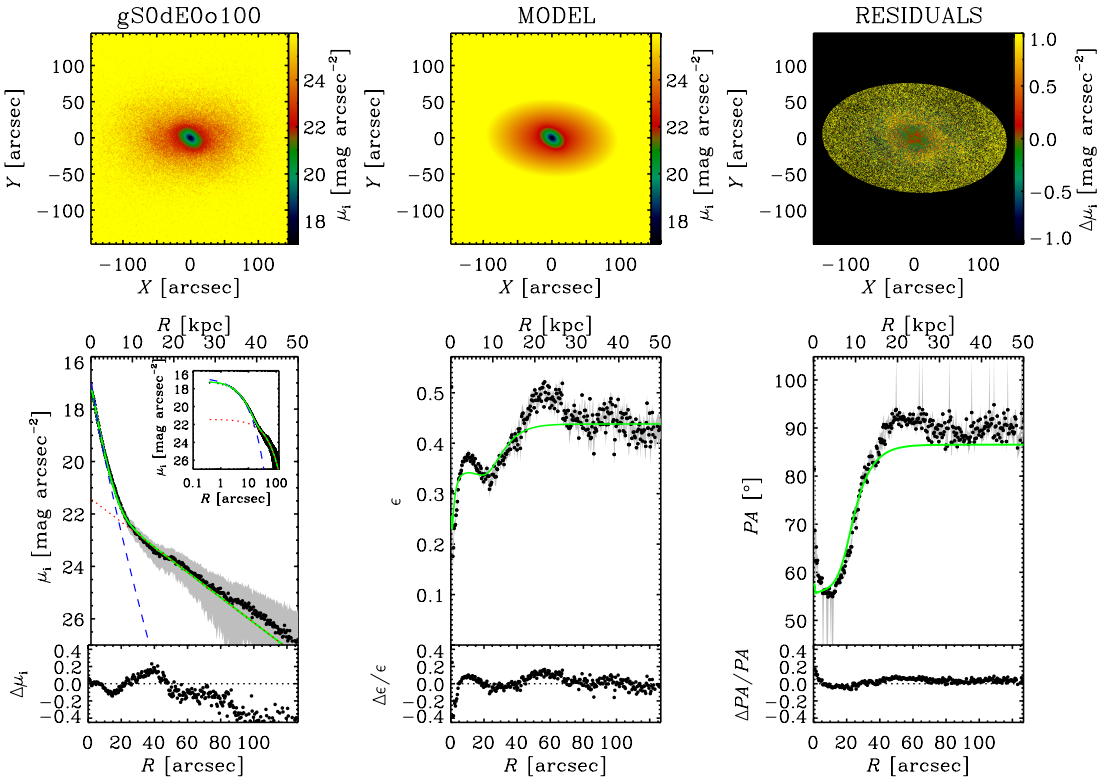

Figure 5.2: Two-dimensional photometric decomposition of the mock i-band image of the simulated lenticular remnant gS0dE0o100 seen at an inclination $\theta = 60°$ obtained with GASP2D. The upper panels (*from left to right*) show the map of the observed, modeled, and residual (observed−modeled) surface-brightness distributions. The lower panels (*from left to right*) show the ellipse-averaged radial profile of surface brightness, ellipticity, and position angle measured in the observed (black dots with gray error bars) and seeing-convolved modeled image (green solid line) and their corresponding difference. The surface-brightness radial profiles of the best-fit bulge (blue dashed line) and disk (red dotted line) are also shown in both linear and logarithmic scale for the distance to the center of the galaxy.

(1994a). The stellar mass of the lenticular remnants is in the range $M = 1$–3×10^{11} $M_\odot$ for major mergers and $M = 1.2$–1.3×10^{11} $M_\odot$ for minor ones.

The merger experiments we analyzed were chosen to cover the whole range of morphologies, mass ratios, and orbital configurations of the progenitors. They are listed in Table 5.1 and labeled considering both the morphological type of the progenitors and the unique numerical identifier given to the orbit in the `GalMer` database. The orbital configuration of each merger experiment is provided in Table 5.2. For example, the experiment gS0dE0o100 corresponds to the accretion of a dwarf elliptical by a giant-like lenticular. It follows the

orbit tagged as 100 in the `GalMer` database with an inclination of 33° with respect to the orbital plane, a pericenter distance of 8 kpc, and a initial energy of 15×10^4 km^2 s^{-2} in a prograde spin-orbit coupling.

5.3.1 Photometric decomposition of the simulated lenticular remnants

To perform a fair comparison between the results from our sample of simulated bulges and the final observed sample from CALIFA, we built mock images of the simulated lenticular remnants under the observing setup of the CALIFA galaxies.

Therefore, we mimicked SDSS i-band images of the simulated lenticular remnants assuming they are at a distance of 67 Mpc, which corresponds to the median distance of the CALIFA DR3 galaxies. We modeled the PSF with a circular Moffat profile (Moffat 1969) with $FWHM = 1.2$ arcsec and $\beta = 5$, which represent typical values for the SDSS images of the galaxies in CALIFA DR3 (see Chapter 3, for all details). Moreover, we considered a Poissonian photon noise to yield $S/N = 1$ at a limiting magnitude of $\mu_i = 25.7$ mag arcsec^{-2}. We chose a pixel scale of 0.396 arcsec pixel^{-1} and, for simplicity, we assumed a gain of 1 e^- ADU^{-1} and RON of 1 e^- rms.

We converted the mass of each particle of the simulated lenticular remnants into light by adopting the i-band mass-to-light ratio (M/L) corresponding to the stellar population of the same age and metallicity of the particle. For the old stellar particles, we assumed that they have evolved previous to the merger following a typical star formation history (SFH), according to the morphological type of the progenitors as found in real galaxies (Eliche-Moral et al. 2010). Since the SF is transferred to the hybrid particles at the start of the merger simulation, the SFH of the old stellar particles is stopped at that moment and they are assumed to evolve passively since then. We thus adopted a present-day age of 11 Gyr for the old stellar component because it is the average age of the old stellar population in the disks of nearby lenticular galaxies (Sil'chenko et al. 2012; Sil'chenko 2013). The SFHs were estimated using the stellar population synthesis models by Bruzual & Charlot (2003) with a Chabrier initial mass function (Chabrier 2003), and the evolutionary tracks by Bertelli et al. (1994). Concerning the hybrid particles, the SF in the galaxies that merge is transferred to them during the simulation. So, part of their initial mass (totally gaseous at the start

Table 5.3: Structural parameters of the simulated lenticular remnants resulting from numerical experiments of giant-giant galaxy mergers.

Galaxy	θ [°]	r_e [arcsec]	n	h [arcsec]	q_b	q_d	$\lvert\delta\rvert$ [°]
(1)	(2)	(3)	(4)	(5)	(6)	(7)	(8)
	0	0.8	3.8	9.0	0.95	0.98	90
	180	0.8	3.8	9.0	1.00	0.98	32
gE0gSbo5	30	0.9	4.9	9.1	1.00	0.97	19
	45	0.9	3.9	9.4	0.86	0.78*	4
	60	1.0	4.1	9.7	0.78	0.67*	1
	0	1.0	1.1	8.7	0.80	0.99	6
	180	1.0	1.1	8.7	0.80	0.99	6
gE0gSdo5	30	0.9	1.2	8.7	0.90	0.90*	23
	45	0.9	1.3	8.9	0.81	0.83*	18
	60	0.8	1.5	9.1	0.64	0.70*	7
	0	1.3	3.5	10.9	0.72	0.97	90
	180	1.3	3.5	10.9	0.72	0.97	90
gSbgSbo9	30	1.2	3.8	11.0	0.78	0.87	63
	45	1.1	4.2	11.3	0.81	0.74	42
	60	1.1	4.9	11.6	0.73	0.57	18
	0	2.3	3.6	18.0	0.83	0.99	58
	180	2.4	4.0	18.1	0.84	0.99	59
gSbgSdo5	30	2.3	3.8	18.0	0.82	0.92	29*
	45	2.2	3.6	17.4	0.75	0.82	21*
	60	2.1	3.5	17.4	0.64	0.67	12*

Notes (1) Identifier of the simulated lenticular remnant. (2) Galaxy inclination. (3) Effective radius of the bulge. (4) Sérsic index of the bulge. (5) Scale length of the disk. (6), (7) Apparent axial ratio of the bulge and disk, respectively. (8) Difference of the position angles of bulge and disk. Nominal values are marked with *.

of the simulation) turns into stellar mass during the merger depending on the local gas concentration. The SFH of these particles is specifically computed during the experiment and it is different for each particle (Chilingarian et al. 2010). Although it may be quite complex, most of their SF accumulates into one or two short peaks occurred soon after the first pericenter passage and the full merger, mostly in this last one (see Di Matteo et al. 2007, 2008; Lotz et al. 2008, and Eliche-Moral et al. in prep.). Therefore, we have approximated the complex SFH of each hybrid particle by simple stellar populations (SSPs), assuming the mean age and metallicity that each hybrid particle presents at the end of the simulation, to estimate a M/L for each one and convert their newly formed stellar mass into luminosity. For this goal, we have used the same stellar population synthesis models mentioned before.

Table 5.4: As in Table 5.3, but simulated lenticular remnants resulting from numerical experiments of giant-dwarf galaxy mergers.

Galaxy	θ [°]	r_e [arcsec]	n	h [arcsec]	q_b	q_d	$\lvert\delta\rvert$ [°]
(1)	(2)	(3)	(4)	(5)	(6)	(7)	(8)
gS0dS0o99	0	7.0	1.1	18.9	0.60	0.97	59
	180	7.0	1.1	19.2	0.60	0.96	82
	30	6.8	1.1	18.9	0.59	0.89	33
	45	6.6	1.1	18.8	0.57	0.76	18
	60	6.3	1.1	18.5	0.53	0.59	11
gS0dSao103	0	7.7	1.5	22.1	0.54	0.97	20
	180	7.8	1.5	22.1	0.54	0.98	20
	30	7.4	1.5	21.6	0.56	0.93	46
	45	6.9	1.6	21.5	0.60	0.80	47
	60	6.2	1.6	21.1	0.63	0.63	37
gS0dSdo106	0	7.7	1.1	24.1	0.46	0.93	83
	180	7.7	1.0	24.1	0.46	0.93	83
	30	7.4	1.1	22.2	0.46	0.92	36
	45	6.8	1.0	21.2	0.45	0.77	20
	60	8.3	1.3	30.1	0.43	0.59	9
gS0dSdo100	0	7.9	1.6	26.3	0.53	0.93	73
	180	7.9	1.6	26.3	0.53	0.93	74
	30	7.9	1.6	24.9	0.50	0.91	13
	45	8.0	1.7	25.1	0.47	0.76	4
	60	8.3	1.7	25.7	0.44	0.56	1

We transformed the intrinsic physical values of lengths into projected angular values and we corrected the resulting surface brightness by cosmological dimming (see Tapia et al. 2017, for more details).

For each simulated lenticular remnant, we created six mock images corresponding to different inclinations with respect to the direction of the total angular momentum vector of the simulated lenticular remnant (i.e., $\theta = 0°$, $30°$, $45°$, $60°$, $90°$, and $180°$). The face-on views $\theta = 0°$ and $180°$ correspond to the cases where the angular momentum vector points toward to and away from the observer, respectively. This allowed us to compare the reliability of the photometric decomposition results of both cases (which should be identical) and the dependence of our method to derive the intrinsic shape of bulges on the galaxy inclination. We analyzed the mock images of the simulated lenticular remnants as if they were real by performing a photometric decomposition with GASP2D, as explained in Section 2.1. An example of the GASP2D photometric decomposition of the mock images of the simulated

Table 5.5: As in Table 5.3, but simulated lenticular remnants resulting from numerical experiments of (giant S0)-(dwarf E0) galaxy mergers with different orbital parameters.

Galaxy	θ [°]	$r_{\rm e}$ [arcsec]	n	h [arcsec]	$q_{\rm b}$	$q_{\rm d}$	$\lvert\delta\rvert$ [°]
(1)	(2)	(3)	(4)	(5)	(6)	(7)	(8)
	0	7.8	1.1	21.5	0.49	0.90	9
	180	7.9	1.1	21.6	0.49	0.91	13
gS0dE0o98	30	7.4	1.1	21.7	0.52	0.82	30
	45	6.8	1.2	21.9	0.54	0.70	26
	60	6.4	1.2	22.4	0.54	0.53	19
	0	7.8	1.1	20.8	0.49	0.99	16
	180	7.8	1.1	20.7	0.49	0.97	16
gS0dE0o99	30	6.7	1.1	18.5	0.56	0.91	7
	45	5.9	1.2	18.5	0.66	0.89	54
	60	4.9	1.2	18.7	0.76	0.66	40
	0	8.0	1.1	21.2	0.48	0.85	1
	180	8.0	1.1	21.1	0.47	0.87	1
gS0dE0o100	30	7.3	1.2	20.9	0.53	0.87	38
	45	6.6	1.2	22.1	0.59	0.74	44
	60	5.8	1.2	22.9	0.65	0.56	31

galaxies is shown in Fig. 5.2 for the lenticular remnant resulting from the merger experiment gS0dE0o100 seen at an inclination $\theta = 60°$.

We listed the more relevant best-fit structural parameters (i.e., the effective radius $r_{\rm e}$, Sérsic index n, and axial ratio $q_{\rm b}$ of the bulge, the scale length h and axial ratio $q_{\rm d}$ of the disk, and the difference between the position angles of bulge and disk δ) of the mock images of the simulated lenticular remnants seen at different inclinations in Table 5.3 for the giant-giant galaxy mergers, Table 5.4 for the giant-dwarf galaxy mergers, and Table 5.5 for the giant S0-dwarf E0 galaxy mergers with different orbital parameters. Following what we found in Chapter 3, we adopted $\sigma_q = 0.01$ and $\sigma_{PA} = 1°$ as uncertainties on the axial ratio and position angle of both bulge and disk, respectively.

5.3.2 Three-dimensional shape of simulated lenticular remnants bulges

We made use of our statistical method to retrieve from the mock images the probability distribution of the intrinsic axial ratios B/A and C/A of the bulges of the simulated lenticular remnants seen at different inclinations ($\theta = 0°, 30°, 45°, 60°$, and $180°$). We excluded from the analysis the edge-on configurations ($\theta = 90°$) because they do not allow us to constrain B/A and C/A due to the unknown orientation of the triaxial bulge in the disk plane. The

probability distribution of B/A and C/A for the bulge of the simulated lenticular remnants resulting from the merger experiment gS0dE0o100 and seen at an inclination $\theta = 60^\circ$ is shown as an example in Fig. 5.3.

The face-on configurations of the simulated lenticular remnants ($\theta = 0^\circ$ and 180°) provided the same result in terms of the probability distribution of B/A and C/A for all the simulated bulges, as expected if no observational and theoretical bias affected the adopted statistical method. Furthermore, we confirmed that the tightest constraints for B/A are given when galaxies are seen face on, whereas C/A remains unconstrained for these galaxies. We also found consistent probability distributions of B/A and C/A for the same simulated lenticular remnant seen at intermediate inclinations ($\theta = 30^\circ$, 45°, and 60°). Because of this, we were confident of having correctly recovered the bulge intrinsic shape and suggested us to set a limit on the inclination of real galaxies ($25^\circ < \theta < 65^\circ$) to robustly apply our statistical method to their bulges (see Section 5.2). In general, the probability distribution of B/A and C/A is tighter at $\theta = 60^\circ$ with respect to $\theta = 30^\circ$ or 45°. Therefore, we considered this inclination as the ideal viewing angle for future analyses of the bulge intrinsic shape in real galaxies.

The probability distributions of B/A and C/A of the bulge of the simulated lenticular remnant resulting from the merger experiment gS0dE0o100 seen at different inclinations are shown in Fig. 5.4, while the remaining galaxies are shown in Fig. 5.5. The values of B/A and C/A derived for all the simulated lenticular remnants seen at different inclinations are listed in Table 5.1.

We realized that the accuracy of the photometric decomposition is critical to successfully constrain the bulge intrinsic shape. All the structural parameters of the bulge, disk, and bar in the photometric decomposition of the mock images with GASP2D were left free to vary. For a few galaxies, we found that the 1σ level contours of the probability distributions of B/A and C/A obtained at different inclinations did not overlap. We double checked the photometric decomposition of these galaxies and noticed that the ellipticity and/or position angle of their disks were not well fit by the model. As a matter of fact, we fit the surface brightness distribution of all these disks with a double-exponential profile and assumed they had the same ellipticity and position angle both in the inner and outer regions.

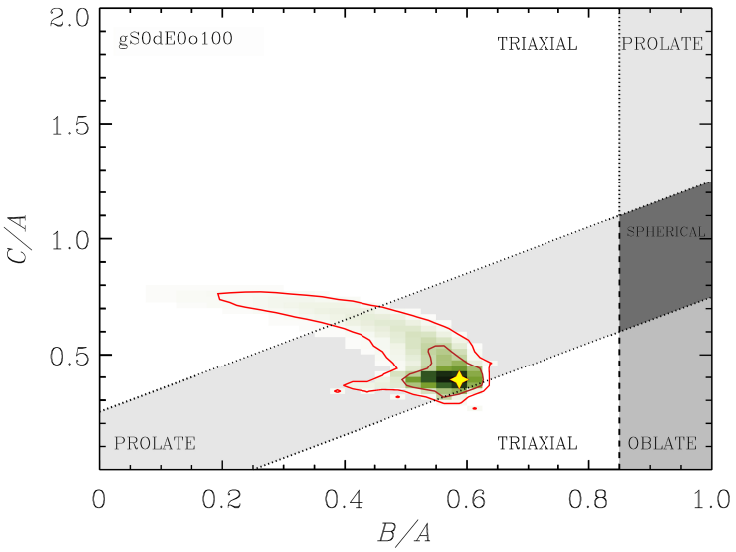

Figure 5.3: Distribution of the intrinsic axial ratios B/A and C/A of the bulge of the simulated lenticular remnant gS0dE0o100 seen at an inclination $\theta = 60°$. The yellow star corresponds to the most probable values of B/A and C/A. The inner and outer red solid contours encompass respectively the 68.3% and 95.4% of the realizations of $(B/A, C/A)$ consistent with the geometric parameters of bulge and disk measured from our photometric decomposition of the mock image of the simulated lenticular remnant. The white, light gray, gray, and dark gray regions mark the regimes of triaxial, prolate, oblate, and spherical bulges, respectively.

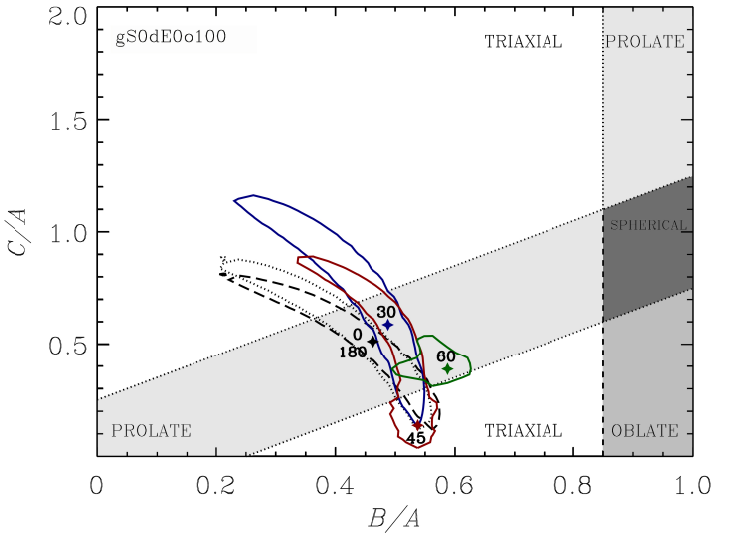

Figure 5.4: Distribution of the intrinsic axial ratios B/A and C/A of the bulge of the simulated lenticular remnant gS0dE0o100 seen at different inclinations. The contours encompass the 68.3% of the realizations of $(B/A, C/A)$ consistent with the geometric parameters of bulge and disk measured from our photometric decomposition of the mock images of the simulated lenticular remnant at $\theta = 0°$ (black dashed line), 30° (blue), 45° (red), 60° (green), and 180° (black dotted line). The stars correspond to the most probable values of B/A and C/A for the different galaxy inclinations and are color coded as their corresponding contours. The white, light gray, gray, and dark gray regions mark the regimes of triaxial, prolate, oblate, and spherical bulges, respectively.

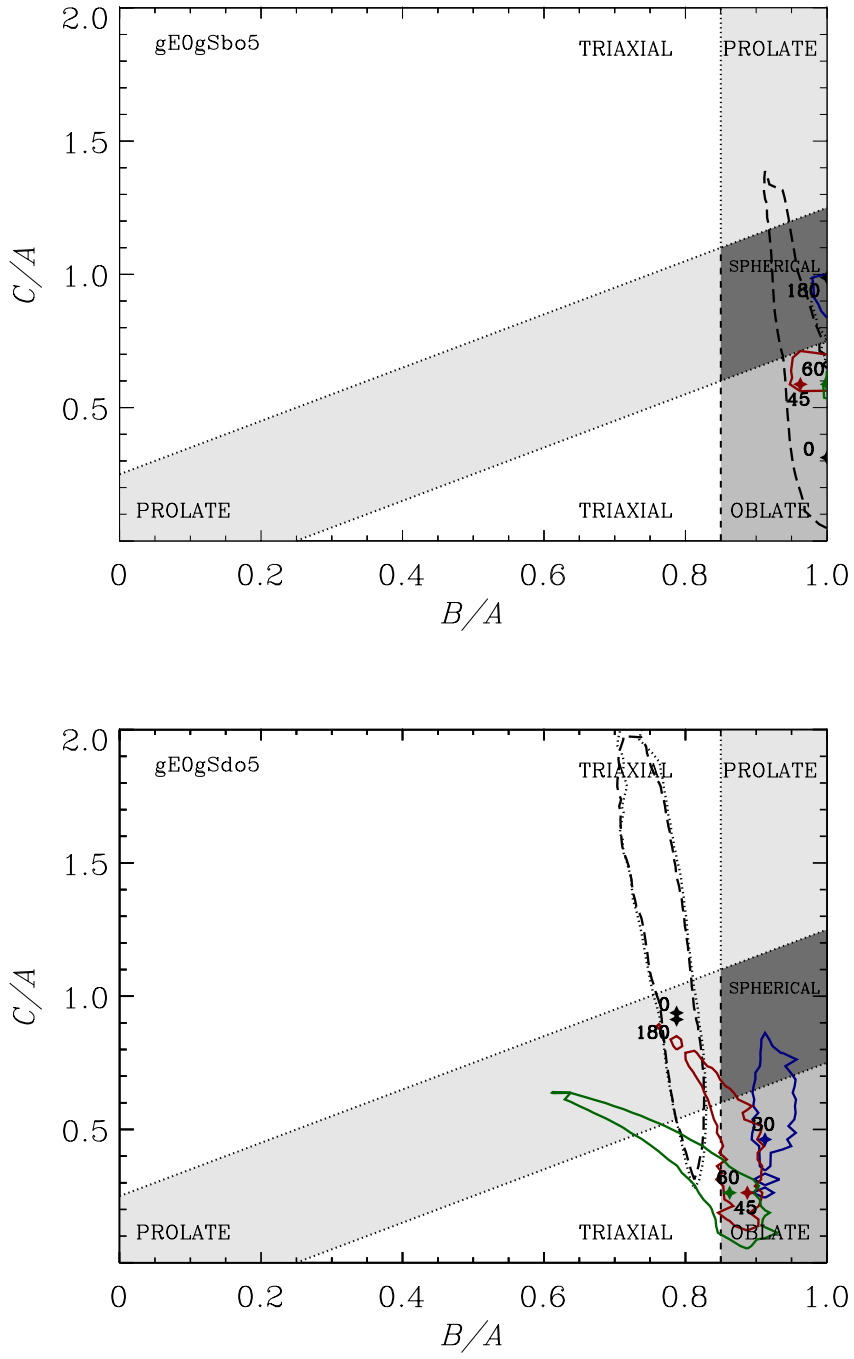

Figure 5.5: As in Fig. 5.4, but for the remaining simulated lenticular remnants. The most probable $(B/A, C/A)$ values for the simulated lenticular remnant gE0gSbo5 at $\theta = 180°$ and $\theta = 30°$ practically overlap.

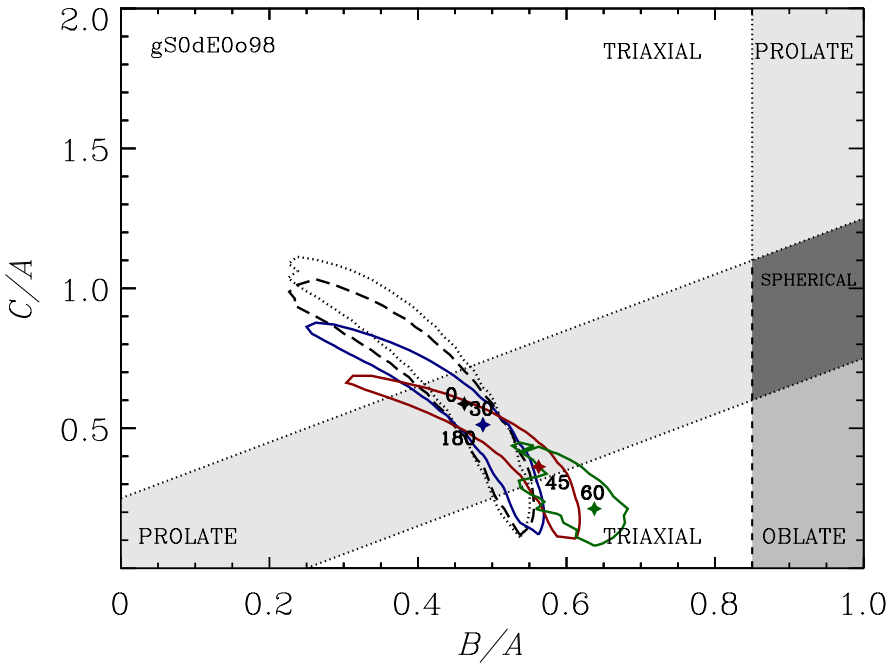

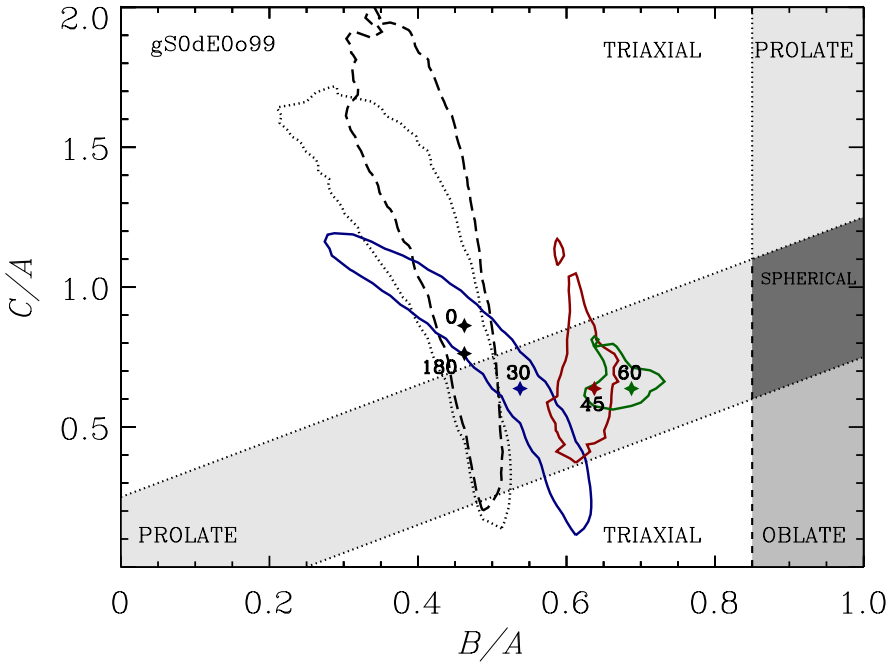

Figure 5.5: continued.

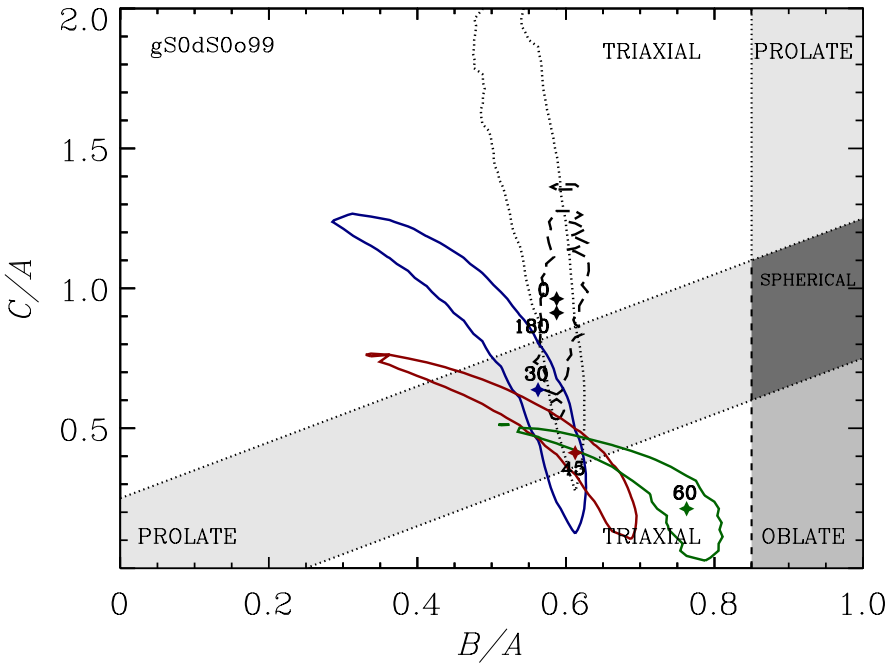

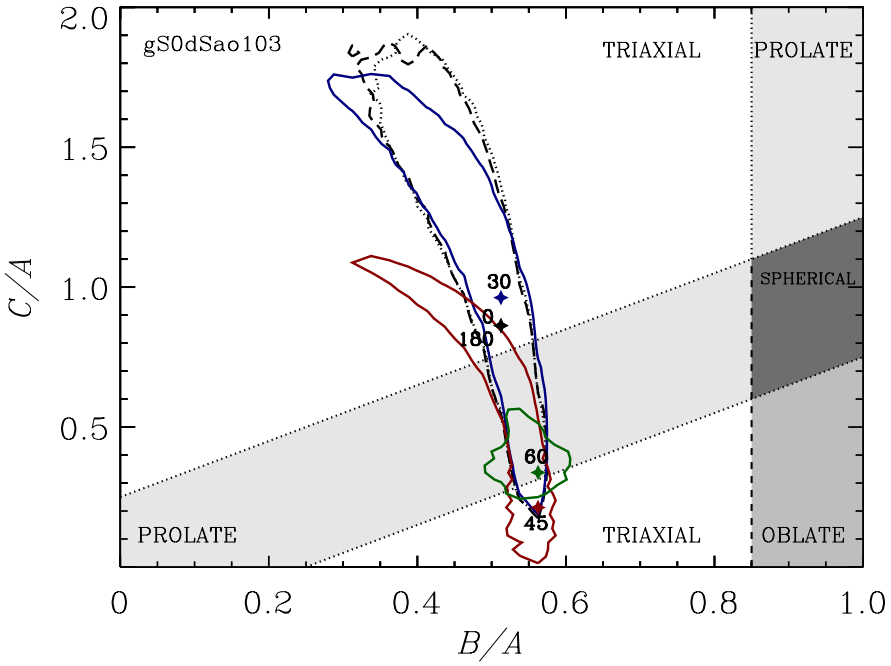

Figure 5.5: continued.

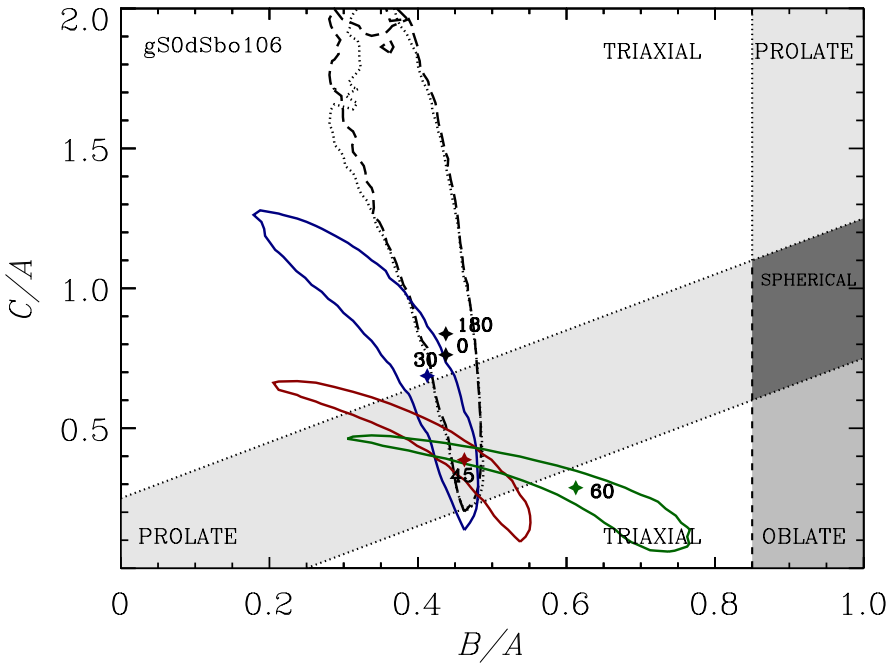

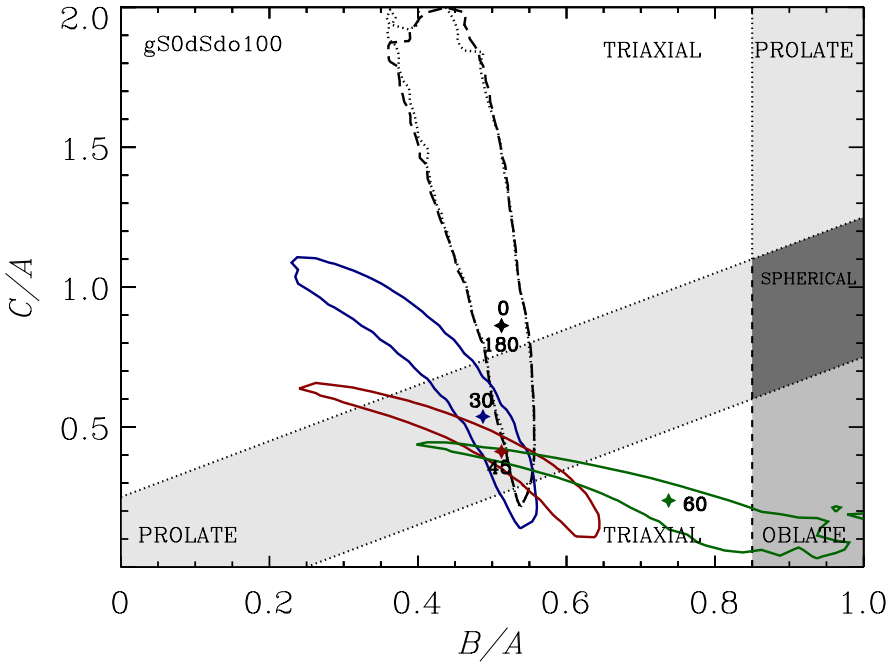

Figure 5.5: continued.

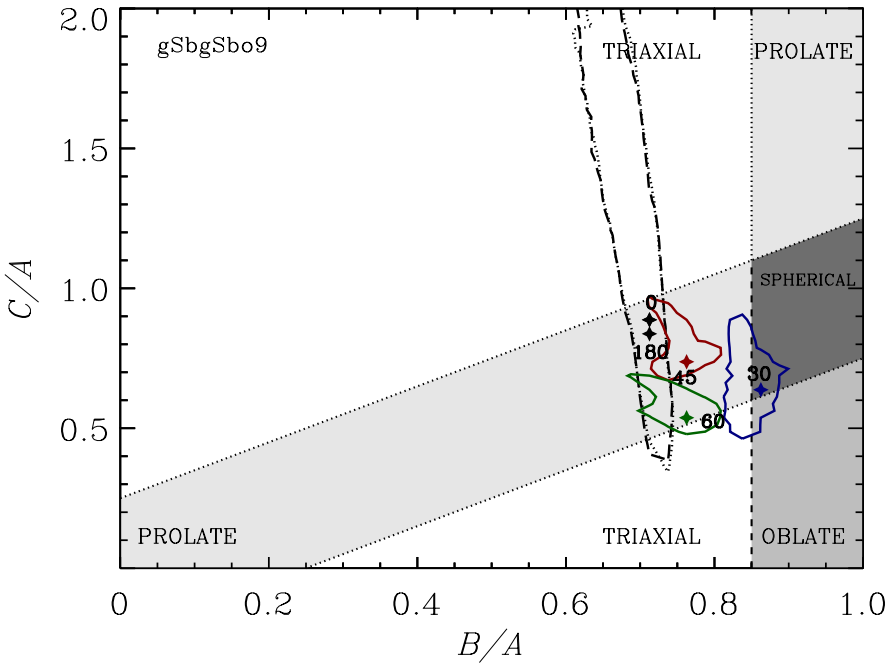

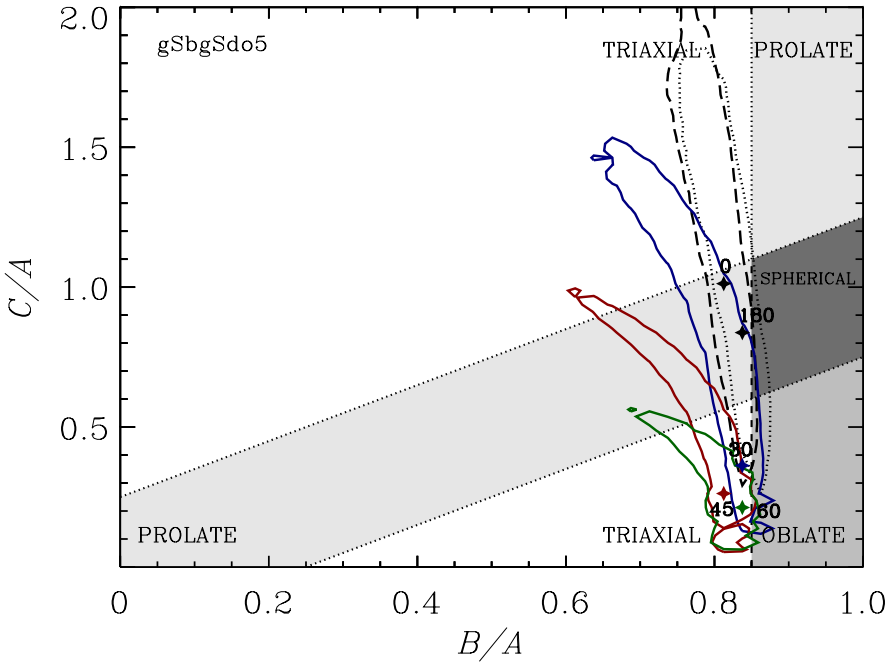

Figure 5.5: continued.

We found that in some cases (e.g., gE0gSbo5) the change in the ellipticity and position angle measured at the break radius was probably due to the fact that there were two distinct structural components (i.e., a lens and a disk) with different geometrical parameters, instead of a single down- or up-bending exponential disk. As a consequence, the adopted photometric model did not exquisitely match the surface brightness distribution of the simulated lenticular remnant. In other cases (e.g., gSbgSdo5), the change was due a moderate degree of granularity observed in the mock images at large galactocentric distances caused by light spots coming from isolated group of stellar particles orbiting the galaxy outskirts. To address these issues, we refined the estimate of $\epsilon_{\rm d}$ and $PA_{\rm d}$ by assuming the average ellipticity and position angle of the galaxy isophotes fit at large radii with the IRAF task `ellipse` (nominal values in Table 5.3).

5.4 Bulge shape of CALIFA galaxies

We made use of our statistical method to retrieve the probability distribution of B/A and C/A of the bulges of our CALIFA galaxy sample. The probability distribution of B/A and C/A for the bulge of NGC 1 is shown as an example in Fig. 5.6, while the most probable values of B/A and C/A of our CALIFA bulges in Fig. 5.7 and Table 5.6 and 5.6.

We derived for each of our CALIFA bulges the projection of the 1σ contour along the B/A and C/A axes and adopted the median values of such projections as the uncertainties on the derived values of B/A and C/A. We estimated $\sigma_{B/A} = 0.15$ and $\sigma_{C/A} = 0.25$, respectively. At this point, we considered as oblate spheroids all the bulges with $B/A > 0.85$ and $C/A < B/A - 0.25$ (oblate in-plane) or with $B/A < 0.85$ and $0.75 < C/A < 1.25$ (oblate off-plane), as prolate spheroids all the bulges with both $B/A < 0.85$ and $B/A - 0.25 < C/A < B/A + 0.25$ (prolate in-plane) or with $B/A > 0.85$ and $C/A > B/A + 0.25$ (prolate off-plane), as spherical all the bulges with both $B/A > 0.85$ and $B/A - 0.25 < C/A < B/A + 0.25$, and as triaxial all the remaining bulges. Spherical bulges will be treated as oblate spheroids in the analysis below.

Table 5.6: Structural parameters of our CALIFA unbarred galaxies.

Galaxy	$\log(M_{\rm galaxy})$	$q_{\rm bulge}$	$PA_{\rm bulge}$	$q_{\rm disk}$	$PA_{\rm disk}$	B/A	C/A
(1)	(2)	(3)	(4)	(5)	(6)	(7)	(8)
NGC 0001	10.6	0.79 ± 0.02	127 ± 3	0.64 ± 0.01	94 ± 1	0.71	0.64
NGC 0160	10.9	0.71 ± 0.02	50 ± 4	0.508 ± 0.003	48.4 ± 0.2	0.96	0.61
NGC 0237	10.2	0.45 ± 0.02	47 ± 3	0.60 ± 0.01	178 ± 1	0.29	0.41
NGC 0234	10.6	0.92 ± 0.02	77 ± 4	0.861 ± 0.003	76.8 ± 0.2	1.00	0.71
NGC 0257	10.8	0.68 ± 0.01	96 ± 2	0.621 ± 0.008	94.1 ± 0.6	0.96	0.44
NGC 0496	10.3	0.86 ± 0.05	46 ± 5	0.57 ± 0.01	33.4 ± 0.8	0.91	0.81
NGC 0677	10.9	0.92 ± 0.01	31 ± 2	0.820 ± 0.008	171.2 ± 0.6	0.91	0.91
NGC 0873	10.2	0.63 ± 0.01	129 ± 2	0.840 ± 0.008	140.2 ± 0.6	0.66	0.54
NGC 1070	10.8	0.97 ± 0.02	28 ± 4	0.814 ± 0.003	1.5 ± 0.2	0.96	0.94
NGC 1094	10.6	0.76 ± 0.03	97 ± 4	0.688 ± 0.008	93.1 ± 0.4	0.96	0.49
NGC 1349	10.8	0.95 ± 0.02	98 ± 3	0.88 ± 0.01	98 ± 1	1.00	0.76
NGC 1665	10.5	0.80 ± 0.01	54 ± 2	0.559 ± 0.008	48.1 ± 0.6	0.94	0.69
NGC 2476	10.5	0.71 ± 0.02	144 ± 4	0.664 ± 0.003	148.7 ± 0.2	0.96	0.46
IC 2341	10.8	0.55 ± 0.03	5 ± 4	0.533 ± 0.008	1.8 ± 0.4	0.94	0.29
NGC 2592	10.3	0.80 ± 0.01	58 ± 2	0.803 ± 0.008	57.9 ± 0.6	1.0	0.31
NGC 2916	10.5	0.82 ± 0.02	7 ± 4	0.651 ± 0.003	15.0 ± 0.2	0.94	0.66
NGC 3106	11.0	0.96 ± 0.01	144 ± 2	0.901 ± 0.008	135.3 ± 0.6	1.00	0.81
NGC 3158	11.6	0.78 ± 0.01	70 ± 2	0.868 ± 0.008	71.0 ± 0.6	0.89	0.39
UGC 05520	9.5	0.34 ± 0.03	112 ± 4	0.53 ± 0.02	100 ± 1	0.46	0.24
UGC 07012	9.1	0.43 ± 0.05	159 ± 5	0.58 ± 0.01	13.8 ± 0.8	0.34	0.29
IC 0776	9.3	0.64 ± 0.05	40 ± 5	0.54 ± 0.01	91.2 ± 0.8	0.46	0.49
NGC 4711	10.3	0.66 ± 0.03	48 ± 4	0.476 ± 0.008	41.9 ± 0.4	0.84	0.54
NGC 5376	...	0.72 ± 0.02	59 ± 4	0.577 ± 0.003	65.3 ± 0.2	0.91	0.56
UGC 09110	10.1	0.65 ± 0.02	19 ± 3	0.44 ± 0.01	21 ± 1	0.94	0.54
NGC 5732	9.9	0.72 ± 0.05	39 ± 5	0.57 ± 0.01	40.1 ± 0.8	1.00	0.59
NGC 5772	10.8	0.80 ± 0.01	38 ± 2	0.531 ± 0.008	36.9 ± 0.6	1.00	0.74
NGC 6060	10.8	0.51 ± 0.01	100 ± 2	0.435 ± 0.008	100.4 ± 0.6	1.00	0.36
NGC 6155	10.1	0.45 ± 0.03	118 ± 4	0.707 ± 0.008	146.6 ± 0.4	0.41	0.39
NGC 6301	10.8	0.63 ± 0.03	110 ± 4	0.603 ± 0.008	109.6 ± 0.4	1.00	0.36
NGC 6314	11.1	0.51 ± 0.02	173 ± 3	0.56 ± 0.01	175 ± 1	0.89	0.19
NGC 7047	10.7	0.52 ± 0.03	111 ± 4	0.491 ± 0.008	107.0 ± 0.4	0.89	0.29
UGC 12224	9.9	0.56 ± 0.02	103 ± 3	0.84 ± 0.01	34 ± 1	0.51	1.04
IC 5309	10.2	0.41 ± 0.03	14 ± 4	0.50 ± 0.02	26 ± 1	0.64	0.24
NGC 7653	10.5	0.89 ± 0.02	20 ± 3	0.84 ± 0.01	164 ± 1	0.89	0.81
NGC 7782	11.1	0.71 ± 0.01	179 ± 2	0.556 ± 0.008	176.5 ± 0.6	0.96	0.56
NGC 5481	10.3	0.93 ± 0.02	114 ± 4	0.738 ± 0.003	114.8 ± 0.1	1.00	0.86
UGC 09708	10.1	0.81 ± 0.05	138 ± 6	0.76 ± 0.04	151 ± 3	0.91	0.59
UGC 01370	10.6	0.55 ± 0.05	156 ± 5	0.43 ± 0.01	156.5 ± 0.8	0.94	0.41
NGC 5145	9.9	0.58 ± 0.01	88 ± 2	0.807 ± 0.008	56.0 ± 0.6	0.54	0.56
MCG −01−52−012	10.3	0.47 ± 0.02	86 ± 3	0.80 ± 0.01	43 ± 1	0.39	0.54
UGC 09837	9.1	0.61 ± 0.05	31 ± 5	0.81 ± 0.01	137.7 ± 0.8	0.59	1.26
NGC 2526	10.2	0.68 ± 0.05	142 ± 5	0.51 ± 0.01	130.9 ± 0.8	0.76	0.51
MCG +09−22−053	9.4	0.79 ± 0.05	93 ± 5	0.77 ± 0.01	127.9 ± 0.8	0.79	0.64

Notes Galaxy name. (2) Stellar mass of the galaxy from Walcher et al. (2014). (3), (4) Apparent axial ratio and position angle of the bulge. (5), (6) Apparent axial ratio and position angle of the disk. (7), (8) Most probable intrinsic axial ratios B/A and C/A of the bulge.

Table 5.7: As in Table 5.6, but for barred galaxies.

Galaxy	$\log(M_{\rm galaxy})$	$q_{\rm bulge}$	$PA_{\rm bulge}$	$q_{\rm disk}$	$PA_{\rm disk}$	B/A	C/A
(1)	(2)	(3)	(4)	(5)	(6)	(7)	(8)
NGC 0171	10.4	0.73 ± 0.02	124 ± 3	0.885 ± 0.004	97.6 ± 0.3	0.71	0.76
NGC 0309	10.7	0.88 ± 0.03	136 ± 3	0.894 ± 0.007	108.4 ± 0.3	0.91	0.61
NGC 0364	10.6	0.88 ± 0.05	45 ± 6	0.73 ± 0.01	33.3 ± 0.7	0.93	0.76
NGC 0551	10.6	0.64 ± 0.05	126 ± 6	0.44 ± 0.01	135.9 ± 0.7	0.78	0.53
NGC 0842	10.8	0.64 ± 0.02	137 ± 3	0.525 ± 0.004	145.1 ± 0.3	0.86	0.46
NGC 1666	10.5	0.88 ± 0.02	138 ± 3	0.880 ± 0.004	147.5 ± 0.3	0.96	0.41
NGC 1667	10.7	0.57 ± 0.03	171 ± 3	0.687 ± 0.007	172.1 ± 0.3	0.81	0.26
UGC 03253	10.4	0.65 ± 0.05	92 ± 6	0.60 ± 0.01	78.4 ± 0.7	0.78	0.43
NGC 2486	10.6	0.83 ± 0.04	85 ± 5	0.591 ± 0.009	90.7 ± 0.5	0.93	0.76
UGC 04145	10.6	0.60 ± 0.05	135 ± 6	0.50 ± 0.01	138.2 ± 0.7	0.93	0.48
NGC 2572	10.9	0.59 ± 0.07	126 ± 13	0.43 ± 0.02	137.4 ± 0.9	0.51	0.33
NGC 2880	10.4	0.79 ± 0.02	129 ± 3	0.571 ± 0.003	143.2 ± 0.1	0.86	0.66
NGC 3381	9.6	0.70 ± 0.05	80 ± 6	0.83 ± 0.01	45.2 ± 0.7	0.76	0.28
NGC 4185	10.6	0.67 ± 0.02	173 ± 3	0.666 ± 0.004	167.0 ± 0.3	0.91	0.31
NGC 4210	10.3	0.75 ± 0.02	78 ± 3	0.731 ± 0.004	94.1 ± 0.3	0.83	0.38
NGC 4961	9.6	0.67 ± 0.04	111 ± 5	0.692 ± 0.009	99.9 ± 0.5	0.83	0.31
NGC 5056	10.6	0.58 ± 0.05	97 ± 6	0.55 ± 0.01	179.4 ± 0.7	0.46	0.96
NGC 5157	11.1	0.73 ± 0.05	114 ± 6	0.78 ± 0.01	105.7 ± 0.7	0.91	0.28
NGC 5473	10.6	0.92 ± 0.01	137 ± 2	0.787 ± 0.003	155.0 ± 0.1	0.93	0.81
IC 0994	11.1	0.78 ± 0.05	19 ± 6	0.51 ± 0.01	14.6 ± 0.7	0.91	0.71
NGC 5602	10.5	0.83 ± 0.08	163 ± 8	0.52 ± 0.03	167 ± 2	1.00	0.81
NGC 5720	10.8	0.82 ± 0.05	125 ± 6	0.65 ± 0.01	129.2 ± 0.7	1.00	0.73
NGC 5735	10.1	0.78 ± 0.05	73 ± 6	0.90 ± 0.01	32.6 ± 0.7	0.78	0.36
UGC 09492	11.1	0.65 ± 0.05	47 ± 6	0.45 ± 0.01	54.2 ± 0.7	0.78	0.48
IC 4534	10.7	0.65 ± 0.04	158 ± 5	0.564 ± 0.009	162.9 ± 0.5	0.93	0.48
NGC 5888	11.2	0.69 ± 0.04	154 ± 5	0.596 ± 0.009	153.2 ± 0.5	0.96	0.51
UGC 09777	10.2	0.95 ± 0.05	129 ± 5	0.61 ± 0.02	145.9 ± 0.9	1.00	0.93
NGC 6278	10.7	0.81 ± 0.02	123 ± 3	0.531 ± 0.004	126.8 ± 0.3	0.96	0.73
NGC 6941	10.9	0.68 ± 0.05	118 ± 6	0.72 ± 0.01	130.5 ± 0.7	0.86	0.23
UGC 11649	10.4	0.82 ± 0.05	132 ± 6	0.86 ± 0.01	71.8 ± 0.7	0.81	1.00
NGC 7321	10.9	0.63 ± 0.05	15 ± 6	0.65 ± 0.01	22.2 ± 0.7	0.86	0.33
UGC 12185	10.5	0.71 ± 0.05	141 ± 5	0.46 ± 0.02	155.0 ± 0.9	0.73	0.58
NGC 7591	10.7	0.85 ± 0.05	167 ± 6	0.48 ± 0.01	148.4 ± 0.7	0.83	0.76
NGC 7671	10.7	0.83 ± 0.02	142 ± 3	0.596 ± 0.004	135.1 ± 0.3	0.93	0.71
NGC 7716	10.3	0.51 ± 0.04	56 ± 5	0.822 ± 0.008	39.4 ± 0.4	0.51	0.48
UGC 04455	10.9	0.73 ± 0.08	174 ± 8	0.74 ± 0.03	11 ± 2	0.81	0.41
NGC 6977	10.9	0.94 ± 0.05	171 ± 6	0.83 ± 0.01	152.7 ± 0.7	0.96	0.88
UGC 12250	11.1	0.78 ± 0.04	13 ± 5	0.626 ± 0.009	12.7 ± 0.5	1.00	0.63
NGC 5947	10.6	0.88 ± 0.04	39 ± 5	0.811 ± 0.009	63.7 ± 0.5	0.88	0.71
NGC 2767	10.8	1.00 ± 0.04	178 ± 5	0.733 ± 0.009	169.6 ± 0.5	1.0	0.98

Notes(1) Galaxy name. (2) Stellar mass of the galaxy from Walcher et al. (2014). (3), (4) Apparent axial ratio and position angle of the bulge. (5), (6) Apparent axial ratio and position angle of the disk. (7), (8) Most probable intrinsic axial ratios B/A and C/A of the bulge.

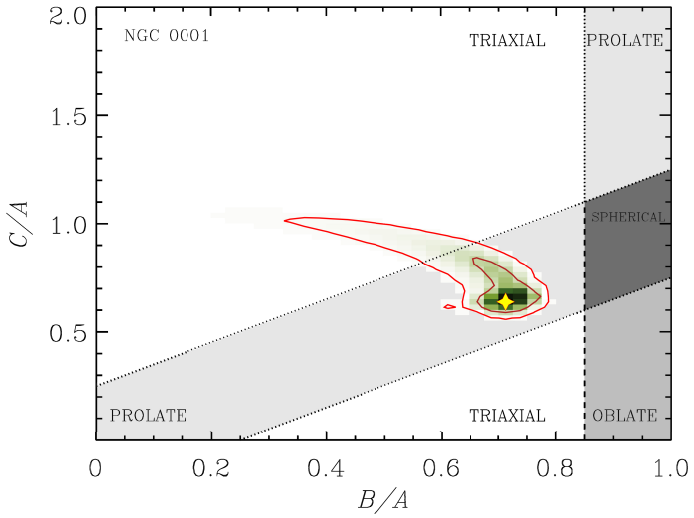

Figure 5.6: As in Fig. 5.3, but for the bulge of NGC 1. The inner and outer red solid contours encompass respectively the 68.3% and 95.4% of the realizations of $(B/A, C/A)$ consistent with the geometric parameters of bulge and disk measured by Méndez-Abreu et al. (2017) with a photometric decomposition of the SDSS i-band image of the galaxy.

It is worth noting that 4 of our CALIFA bulges are oblate spheroids off-plane, while there are no prolate spheroids off-plane. Such rare central structures swelling out the disk plane have been recently studied by Corsini et al. (2012), who found a slightly triaxial polar bulge with axial ratios $B/A = 0.95$ and $C/A = 1.60$ in NGC 4698. We inspected the probability distribution of our 4 bulges and found that they presented a great scatter compatible also with being triaxial, as expected. Therefore, due to the peculiarity and the great uncertainty in the properties and formation mechanisms of polar bulges, they should be considered as a particular kind of bulges and not include them in the main groups described in the forthcoming analysis. Thus, the final sample of our CALIFA bulges comprises 79 objects (41 in unbarred galaxies and 38 in barred galaxies).

We distinguished all different bulges intrinsic shapes (oblate, prolate, or triaxial) in the $(B/A, C/A)$ diagram according to the properties of their host galaxies. As a general behavior, we found that most of our CALIFA bulges tend to be oblate (66%), with a smaller fraction of prolate (19%) or triaxial bulges (15%). The majority of triaxial bulges are in barred galaxies (75%). The B/A and C/A distribution peaks at $\langle B/A \rangle = 0.85$ and $\langle C/A \rangle = 0.55$, respectively.

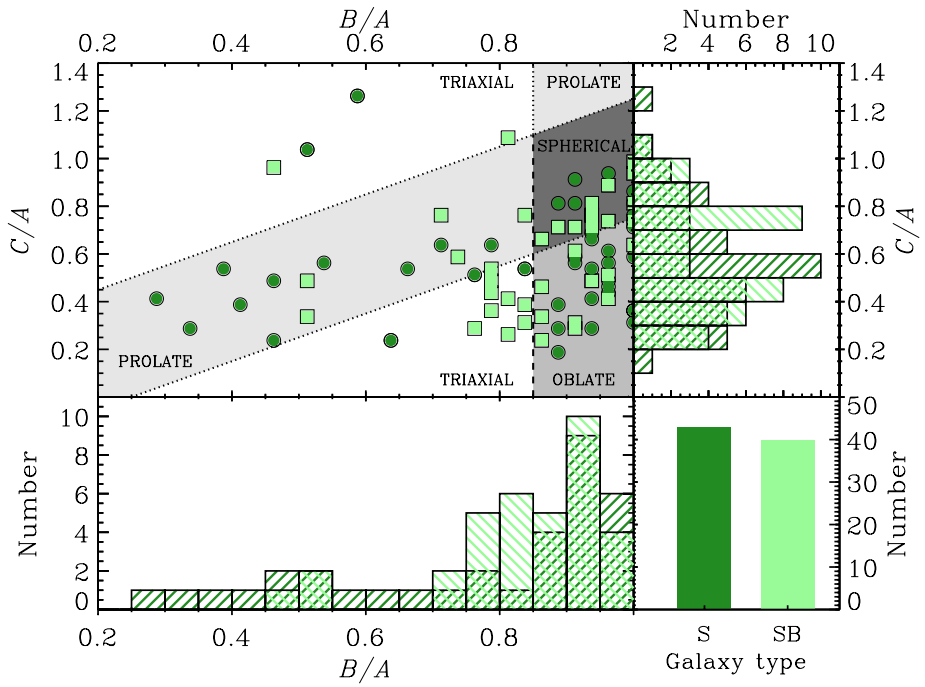

Figure 5.7: (*Top left panel*) Intrinsic axial ratios B/A and C/A of our CALIFA bulges. Dark green circles and light green squares correspond to unbarred and barred galaxies, respectively. The white, light gray, gray, and dark gray regions mark the regimes of triaxial, prolate, oblate, and spherical bulges, respectively. (*Top right panel*) Distribution of C/A. (*Bottom left panel*) Distribution of B/A. (*Bottom right panel*) Distribution of our CALIFA bulges in unbarred (S) and barred galaxies (SB).

We divided our CALIFA bulges according to their Sérsic index in the bins $n \leq 1.5$, $1.5 < n \leq 2.5$, and $n > 2.5$ (Fig. 5.8). The vast majority of our bulges (80%) is characterized by a small Sérsic index ($n \leq 2.5$). A substantial fraction of bulges with $n > 2.5$ (69%) is observed in unbarred galaxies. The bulges with $n \leq 1.5$ have a variety of intrinsic shapes, with comparable fractions of triaxial (30%), oblate (49%), and prolate bulges (21%). By contrast, most of the bulges with $1.5 < n \leq 2.5$ (77%) and $n > 2.5$ (81%) are oblate. Finally, we noticed that almost all the triaxial bulges show very small values of Sérsic index ($n < 1.5$). The same trends were seen by dividing our CALIFA bulges in the bins $B/T \leq 0.1$, $0.1 < B/T \leq 0.3$, and $B/T \leq 0.3$, according to the bulge-to-total luminosity ratio of their host galaxy (Fig. 5.9). Most of the larger bulges are oblate (74%), while the smaller ones show a variety of intrinsic shapes. We also pointed out that the bulges with small values of intrinsic flattening C/A have systematically small values of n and B/T.

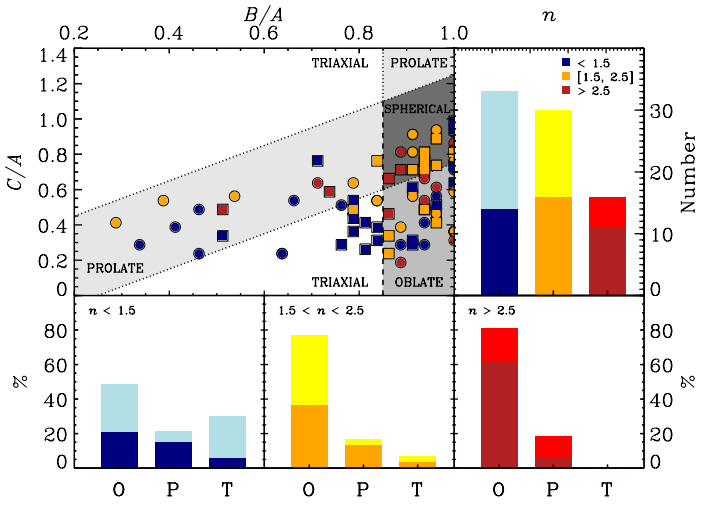

Figure 5.8: (*Top left panel*) Intrinsic axial ratios B/A and C/A of our CALIFA bulges as a function of their Sérsic index ($n < 1.5$: blue symbols; $1.5 < n < 2.5$: yellow symbols; $n > 2.5$: red symbols). Circles and squares correspond to unbarred and barred galaxies, respectively. The white, light gray, gray, and dark gray regions mark the regimes of triaxial, prolate, oblate, and spherical bulges, respectively. (*Top right panel*) Distribution of the Sérsic index of our CALIFA bulges ($n < 1.5$: blue histogram; $1.5 < n < 2.5$: yellow histogram; $n > 2.5$: red histogram). Dark and light colors correspond to unbarred and barred galaxies, respectively. (*Bottom panels*) Distribution of the intrinsic shape of our CALIFA bulges (O: oblate; P: prolate; T: triaxial) as a function of their Sérsic index ($n < 1.5$: blue histograms; $1.5 < n < 2.5$: yellow histograms; $n > 2.5$: red histograms). Dark and light colors correspond to unbarred and barred galaxies, respectively.

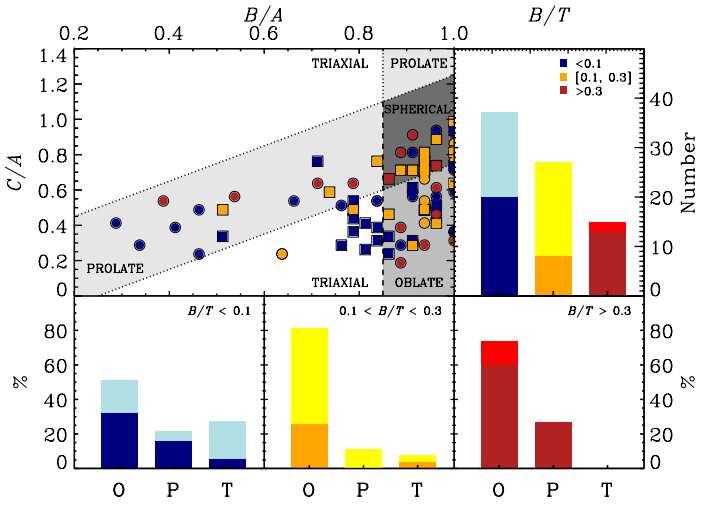

Figure 5.9: As in Fig. 5.8, but for the bulge-to-total luminosity ratio. Our CALIFA bulges are divided in the following bins: $B/T > 0.1$ (blue), $0.1 < B/T < 0.3$ (yellow), and $B/T > 0.3$ (red).

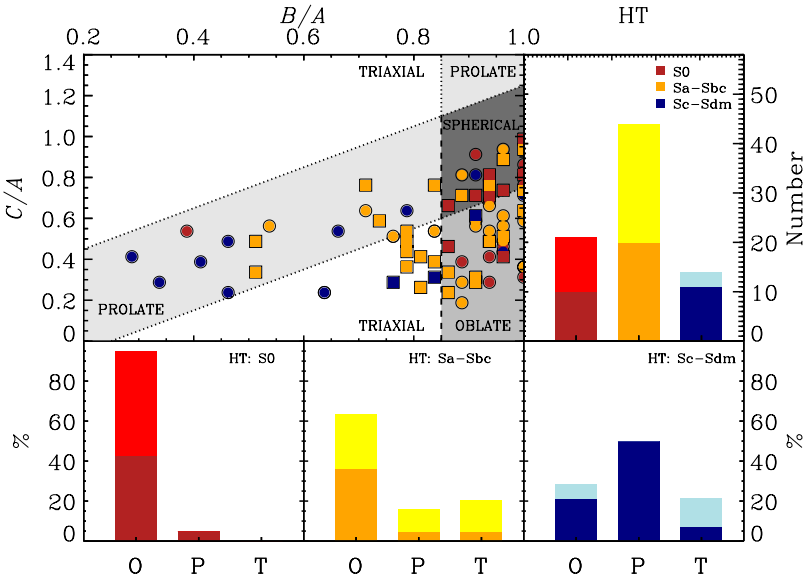

Figure 5.10: As in Fig. 5.8, but for the Hubble type. Our CALIFA bulges are divided in the following bins: S0 (red), Sa–Sbc (yellow), Sc–Sdm (blue).

We also analyzed the bulge intrinsic shape to highlight possible correlations with the morphology of the host galaxy (Fig. 5.10). We separated our CALIFA bulges into three bins by taking into account the bulges in S0 galaxies, bulges in Sa, Sab, Sb, and Sbc galaxies, and bulges in Sc, Scd, Sd, and Sm galaxies. Most of the bulges belong to galaxies in the Sa–Sbc bin (56%). Almost all the bulges in S0 galaxies (95%) are oblate, with a different degree of intrinsic flattening C/A. We did not find any triaxial bulge among the S0 galaxies. On the contrary, the bulges of spiral galaxies present a variety of intrinsic shapes, with oblate bulges (62%) dominating the Sa–Sbc bin. Moreover, we noticed that bulges with small values of C/A are more frequently observed in late-type spiral galaxies.

Finally, we studied the bulge intrinsic shape as a function of i-band absolute magnitude of the bulge (Fig. 5.11) and of the host galaxy (Fig. 5.12). Almost all the most massive bulges ($M_{\mathrm{b},i} < -20.5$ mag) are oblate (86%), whereas the less massive one ($M_{\mathrm{b},i} > -18.5$ mag) are more heterogeneous with a similar fraction of triaxial (41%), oblate (27%), and prolate systems (32%). We obtained the same results when the total galaxy absolute magnitude was examined, with no difference when unbarred and barred galaxies were considered separately.

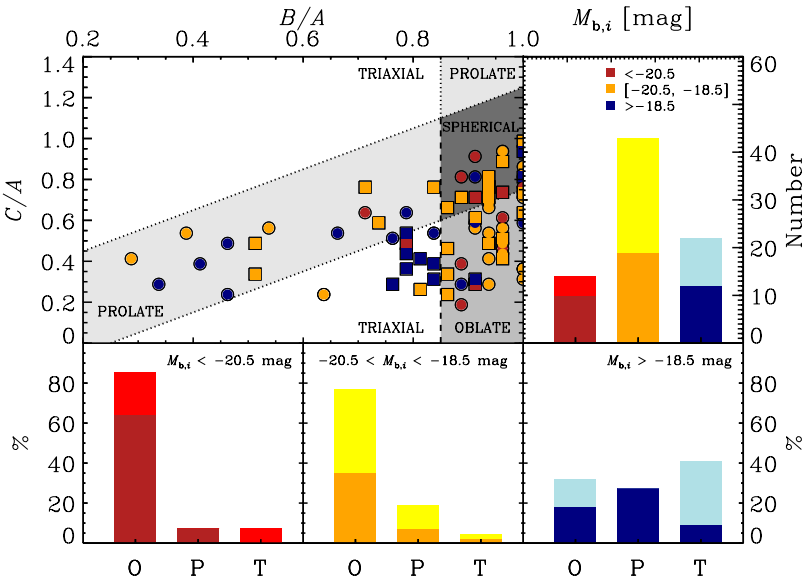

Figure 5.11: As in Fig. 5.8, but for the absolute magnitude of the bulge. Our CALIFA bulges are divided in the following bins: $M_{\mathrm{b},i} < -20.5$ mag (red), $-20.5 < M_{\mathrm{b},i} < -18.5$ mag (yellow), and $M_{\mathrm{b},i} > -18.5$ mag (blue).

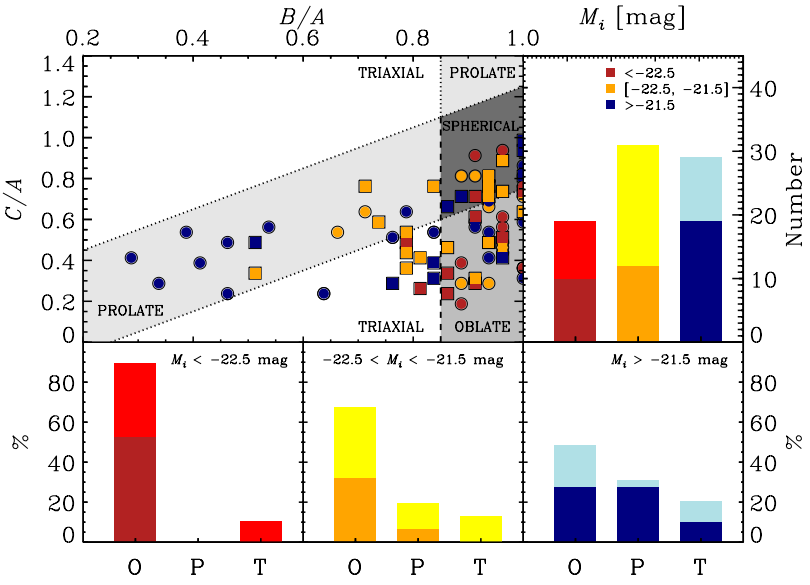

Figure 5.12: As in Fig. 5.8, but for the absolute magnitude of the galaxy. Our CALIFA bulges are divided in the following bins: $M_i < -22.5$ mag (red), $-22.5 < M_i < -21.5$ mag (yellow), and $M_i > -21.5$ mag (blue).

5.5 Discussion

The statistical analysis presented in this Chapter allowed us to individually constrain the intrinsic shape of a sample of bulges in relation to their observed properties. We projected the $(B/A, C/A)$ values in order to compare the bulge shape distribution with previous results (see Fig. 5.7). We found that the mean axial ratio of our CALIFA bulges is $\langle B/A \rangle = 0.85$ and $\langle C/A \rangle = 0.55$, respectively. This result is in agreement with previous analyses by Bertola et al. (1991b), Fathi & Peletier (2003), and Méndez-Abreu et al. (2008a).

Since the cumulative projected distribution mixes all different shapes (oblate, prolate, and triaxial), we preferred to distinguish the properties of our CALIFA bulges in the $(B/A, C/A)$ diagram. Indeed, the actual position of bulges in the $(B/A, C/A)$ diagram is a powerful tool for disentangling bulge types. We found that some of our CALIFA bulges (6%) are very flattened oblate systems ($B/A > 0.85$ and $C/A < 0.3$), which are possible candidate to be disk-like bulges. Moreover, since barred galaxies are found to host the majority of triaxial bulges, they could be interpreted as the signature of boxy/peanut structures. Indeed, the secular evolution of the bar via buckling or resonants effects is known to result in thick triaxial components. Even the inclusion of the bar in the photometric decomposition can not avoid a mild contamination from boxy/peanut structures. Thus, it is not surprising that barred galaxies show a large fraction of triaxial bulges. It is worth noting that in discussing the shape of the sample bulges obtained from the $(B/A, C/A)$ diagram, we considered the statistical meaning of the intrinsic axial ratios that we derived and the empiric definition we adopted for the oblate, spherical, prolate, and triaxial bulges. The 1σ contour level of the distribution of the intrinsic axial ratios of a bulge can tightly or loosely circle the most probable values of its shape (see Fig. 5.4, for an example). Therefore, a certain degree of triaxiality is allowed also for the bulges we classified as oblate or prolate. On the other hand, the definition of the boundaries of the regions marking the different bulge shapes in the $(B/A, C/A)$ diagram might be very conservative.

These results are consistent with a major role of a certain mechanism in the buildup of the most massive bulges (usually identified by higher n, higher B/T, earlier types, more massive systems) which has not significantly contributed to those forming the less massive ones (usually identified by lower n, lower B/T, later types and in less massive galaxies).

Some evolutionary mechanisms may have taken place in all mass ranges similarly (such as internal secular evolution or cluster-related processes), but it is obvious from these results that there are some specific processes that have contributed much more in the most massive bulges to make them more homogeneous in shape (i.e., all oblate) than in the bulges with lower masses (e.g., Ravikumar et al. 2006; Laurikainen et al. 2010; Bernardi et al. 2011a,b). These processes must impose over others and have occurred more frequently in massive systems than in less massive ones, as well as they have also contributed to increase n and B/T in the galaxy at the same time, meaning that they must transform the system toward an earlier type.

In the less massive bulges, the interplay of different evolutionary mechanisms can explain the wide variety of shapes, as they can be more or less relevant in a galaxy depending on its evolutionary history and environment (Buta et al. 2010; Marino et al. 2011). However, the presence of the bar seems to drive the evolution of low-mass triaxial bulges. Indeed, triaxial bulges are mostly hosted in barred galaxies with low values of B/T, $M_{\mathrm{b},i}$, and n. These bulges could be contaminated by the residual light of the low-inclined counterparts of boxy/peanut structures. The lack of triaxial bulges in lenticular barred galaxies could be explained by the larger mass of their bulges: their deep potential well seems to reshape the central region into a more axisymmetric structure, where the bar has a marginal role in perturbing the bulge. Thus, the bulge mass could play a role also in driving the evolution of bulges in barred galaxies.

Many studies report observational evidence of a major role of both major and minor merging and dissipative collapse in the buildup of the most massive galaxies (e.g., Rudick et al. 2009; Eliche-Moral et al. 2010; Thomas et al. 2010; Kaviraj et al. 2011; Bernardi et al. 2011b; Méndez-Abreu et al. 2012; Barway et al. 2013; Prieto et al. 2013; Morelli et al. 2016; Leja et al. 2015; Prieto & Eliche-Moral 2015). Numerical simulations have shown that gas-poor major and minor mergers tend to introduce some triaxiality in bulges that originally were spheroidal (Cox et al. 2006b; Tapia et al. 2014). However, the bulges of dry minor-merger remnants also exhibit higher rotational support at their centers, even though the global rotational support of the galaxy decreases, making the bulge more oblate (Tapia et al. 2014). This happens because part of the orbital angular momentum of the encounter is transferred to the inner regions (see Eliche-Moral et al. 2006, 2011), contributing to the

flattening of the material at the galaxy center. High gas amounts in the progenitors only contribute to make the remnant more axisymmetric (Jesseit et al. 2007), so the trend of dry mergers to make remnant bulges more oblate can be extrapolated to wet ones. Therefore, our results would be consistent with a higher relevance of merging in the formation and evolution of the most massive bulges.

5.6 Conclusions

We derived the intrinsic shape of 83 bulges of a sample of nearby galaxies from CALIFA DR3. To this aim we applied the statistical method by Méndez-Abreu et al. (2008a) to the structural parameters obtained by Méndez-Abreu et al. (2017) with a two-dimensional photometric decomposition of the SDSS i-band images of the sample galaxies.

We made use of a set of simulated galaxies resulting from merger experiments, that closely resemble lenticular galaxies, to test the reliability of the method by Méndez-Abreu et al. (2008a). For each simulated lenticular remnant, we created a set of mock SDSS i-band images at different galaxy inclinations to mimic the observing setup of SDSS images of CALIFA DR3 galaxies. We performed a two-dimensional photometric decomposition of all the mock images applying the same procedure as for real galaxies, in order to retrieve the geometrical parameters of bulge and disk which we used to recover the bulge intrinsic shape. The probability distributions of the axial ratios B/A and C/A obtained for different inclinations for the same simulated lenticular remnant overlap at 1σ level. We concluded that the adopted method allows us to successfully constrain the bulge intrinsic shape when the galaxy inclination is $25^\circ < \theta < 65^\circ$. We also realized that a very accurate photometric decomposition is mandatory to retrieve the bulge intrinsic shape and that a galaxy inclination of $\theta = 60^\circ$ returns the tightest constraints on the intrinsic axial ratios B/A and C/A of the bulge.

We divided our CALIFA bulges according to their intrinsic axial ratios B/A and C/A into oblate (in-plane or off-plane), prolate (in-plane or off-plane), and triaxial. We looked for possible correlations between the intrinsic shape of our bulges and some of the basic properties of their host galaxies (i.e., Sérsic index of the bulge n, bulge-to-total luminosity ratio B/T, Hubble type HT, i-band absolute magnitude of the bulge $M_{\mathrm{b},i}$, and i-band

absolute magnitude of the galaxy M_i) as derived by Méndez-Abreu et al. 2017. Our analysis pointed out that bulges with a small value of n or B/T could be equally axisymmetric or triaxial ellipsoids, while most of the bulges with large values of n or B/T are mostly oblate spheroids. Moreover, less massive bulges and bulges in late-type galaxies presented heterogeneous intrinsic shapes, while more massive bulges and bulges in lenticular galaxies are mostly oblate. Finally, we found the majority of triaxial bulges in barred galaxies.

We concluded that merging events and dissipative collapse could be responsible of driving the formation and evolution of our most massive bulges, although other physical mechanisms, that is, the internal secular evolution caused by the presence of the bar, may be acting at the same time. The coexistence of different pathways is more clear in less massive bulges, where the bar seems to reshape low-mass triaxial bulges. In this context, the role of simulations result crucial in unveiling various evolution pathways in nearby galaxies. Nevertheless, very few numerical studies have focused on the bulge evolution and in particular on the intrinsic shape. Thus, our results have imposed further limitations on forthcoming numerical simulations and may help to disentangle different formation scenarios.

6

OBSERVED PROPERTIES OF BULGES IN LENTICULAR GALAXIES

Secular evolution mechanisms at work in nearby galaxies are considered responsible to build flattened central bulges with disk properties. Separating these systems from classical bulges using a variety of observational criteria has become a common task in extragalactic astronomy. Our aim is to characterize nearby bulges using all the commonly adopted observational diagnostics and to test their ability to identify different bulge types. We derived the photometric, kinematic, stellar population, and intrinsic shape properties of the bulge of nine lenticular galaxies from the ATLAS^{3D} survey. We argued that the bulge Sérsic index is a poor diagnostic to discriminate different bulge types. Moreover, we found that the combination of kinematic properties and line-strength indices of the sample bulges provides contradictory identifications in 45% of the cases. This remains true also when comparing the results obtained from the line-strength indices with those from the photometric analysis. We remarked that, even if the different observational characteristics look well motivated in terms of distinct formation paths, their interplay might result in conflicting outcomes. We proposed to characterize disk-like bulges in terms of their intrinsic shape and dynamical status as the most reliable way to separate them from classical bulges. Thus, we found only one bulge out of nine to be classified as disk-like in our lenticular galaxies. We concluded that, even using multiple criteria, the classification of bulges into different types based on *a priori* classification according to their morphology or Sérsic index has to be carefully reconsidered.

6.1 Introduction

The current distinction of galactic bulges into classical and disk-like spheroids is usually done by comparing their observed photometric, kinematic, and stellar population properties. Different formation and evolution mechanisms have been proposed to be responsible for these different bulge types, given the variety of their distinct features. Thus, studying the observed properties of bulges it might be possible to infer their distinct formation mechanisms.

Recently, Fisher & Drory (2016) reviewed the observed properties of bulges in nearby galaxies extending the criteria provided by Kormendy & Kennicutt (2004). They proposed a number of observational criteria (i.e., category I diagnostics) that allow to mark a relatively clean separation between classical and disk-like bulges and statistically classify all the bulges within a sample. They also identified other observational properties (i.e., category II diagnostics) that can be used to classify single bulges, but can not be applied to the whole bulge population. Finally, they gave a few additional criteria (i.e., category III diagnostics), which are supposed to be necessary (but not sufficient) to identify a bulge as classical or disk like. Here, we provided a summary of the observational criteria given by Fisher & Drory (2016) grouped according to their category.

- Classical bulges are thought to:

$(\text{I–1})_{\text{C}}$ show no spiral or ring structures in the region where they dominate the galaxy light, as shown by optical images taken at high spatial resolution ($FWHM < 100$ pc);

$(\text{I–2})_{\text{C}}$ have Sérsic index $n > 2$;

$(\text{I–3})_{\text{C}}$ show correlations between absorption line-strength indices consistent with those of elliptical galaxies;

$(\text{I–4})_{\text{C}}$ have strongly peaked radial profile of velocity dispersion, with a gradient $\text{dlog}(\sigma)/\text{dlog}(r) < -0.1$ within $[r_{\text{min}}, r_{25\%}]$ (see Section 6.5.1, for all details);

$(\text{II–1})_{\text{C}}$ have central velocity dispersion $\sigma_0 > 130$ km s^{-1};

$(\text{III–1})_{\text{C}}$ be consistent with the fundamental plane relation of elliptical galaxies;

(III–2)$_{\rm C}$ show low specific star formation rate $sSFR < 10^{-11}$ yr^{-1} (but this is not applicable to lenticular galaxies; Kormendy 2016);

(III–3)$_{\rm C}$ rarely present extremely blue colors (e.g., $B - V < 0.65$).

- Disk-like bulges are supposed to:

(I–1)$_{\rm D}$ show spiral or ring structures in the region where they dominate the galaxy light, as shown by optical images taken at high spatial resolution ($FWHM < 100$ pc);

(I–2)$_{\rm D}$ have Sérsic index $n < 2$;

(I–3)$_{\rm D}$ show absorption line-strength offset ΔMg $b < 0.7$ Å compared to the Mg b – σ_0 correlation, or ΔMg $b < 0.7$ Å compared to the Mg b – Fe relation of elliptical galaxies;

(I–4)$_{\rm D}$ present a velocity dispersion radial profile that satisfies dlog(σ)/dlog(r) > -0.1 or $\langle v^2\rangle/\langle\sigma^2\rangle \geq 0.35$ within [$r_{\rm min}$, $r_{25\%}$] (see Section 6.5.1, for all details);

(II–1)$_{\rm D}$ be low surface-brightness outliers from scaling relations of elliptical galaxies such as Kormendy relation;

(II–2)$_{\rm D}$ present high specific star formation rate $sSFR > 10^{-11}$ yr^{-1} (but this is not applicable to lenticular galaxies; Kormendy 2016);

(II–3)$_{\rm D}$ have absorption line-strength indices Fe 5015 < 3.95 Å and Mg $b < 2.35$ Å;

(II–4)$_{\rm D}$ be low-σ outliers in the Faber-Jackson relation of elliptical galaxies;

(II–5)$_{\rm D}$ show blue optical colors (e.g., $B - V < 0.5$).

It is worth noting that, even if the different observational properties of bulges can be explained in terms of formation process and evolutionary history, most of the above criteria are based on an *a priori* separation between classical and disk-like bulges which is usually done with a visual morphological classification. For this reason, different authors (e.g., Graham & Worley 2008; Méndez-Abreu et al. 2018) challenged these criteria by pointing out that they can lead to a strong contamination when one or few of them are adopted to select a particular type of bulge. On the contrary, an accurate combination of photometric

and kinematic properties and the analysis of the bulge intrinsic shape should be adopted in order to disentangle classical and disk-like bulges. In this thesis, we have shown how the bulge intrinsic shape might be used as one of the most powerful tool that disentangle bulge types (Chapter 5). In this Chapter we applied for the first time all these criteria to a well-defined sample of bulges to investigate which or which combination of them is more effective in characterizing classical and disk-like bulges and how they correlate with the bulge intrinsic shape. To address this issue, we selected our sample bulges from the volume-limited ATLAS^{3D} survey of ETGs (Cappellari et al. 2011).

The Chapter is organized as follows. The galaxy sample is presented in Section 6.2. The surface brightness distribution of the sample galaxies is analyzed in Section 6.3. The intrinsic shape of the sample bulges is recovered in Section 6.4. The stellar kinematics and line-strength indices of the sample bulges is analyzed in Section 6.5. In Section 6.6 it is investigated whether our bulges follow the same scaling relations traced by elliptical galaxies and large bulges. The classification of the sample bulges is discussed in Section 6.7. Our conclusions are presented in Section 6.8.

■ 6.2 Sample selection

We selected our sample galaxies among the galaxies studied in the ATLAS^{3D} survey (Cappellari et al. 2011). The ATLAS^{3D} project is based on a local (within 42 Mpc) volume-limited sample of 260 ETGs extracted from a complete parent sample. The potential of the survey resides in the multi-wavelength approach spanning from the radio to millimeter and optical observations. It provides multi-color imaging and two-dimensional kinematics of the atomic, molecular, and ionized gas (Sarzi et al. 2013; Serra et al. 2014; Young et al. 2014), together with the kinematics (Emsellem et al. 2011) and line-strength indices of the stellar component (Scott et al. 2013). The results of this project opened the era of IFU astronomy, giving deeper insights (among the others) on the following issues about ETGs:

- morphological features (Krajnović et al. 2011), such as bars and rings, dust structures, blue nuclei, and evidence of past interactions and mergers;

- stellar dynamical status, both from observations (Emsellem et al. 2011) and simulations

Table 6.1: Properties of the sample galaxies.

Galaxy	RA	DEC	d	m_i	$M_{\mathrm{gal},i}$	θ
	[h m s]	[deg arcmin arcsec]	[Mpc]	[mag]	[mag]	[°]
(1)	(2)	(3)	(4)	(5)	(6)	(7)
NGC 3156	10 12 41.25	+3 07 45.69	21.8	12.05	-19.64	59
NGC 3245	10 27 18.39	+28 30 26.79	20.3	10.39	-21.15	57
NGC 3998	11 57 56.13	+55 27 12.92	13.7	11.04	-19.64	39
NGC 4249	12 17 59.39	+05 35 54.91	38.7	13.07	-19.86	16
NGC 4578	12 37 30.56	+09 33 18.25	16.3	11.07	-20.00	44
NGC 4690	12 47 55.52	−01 39 21.83	40.2	12.26	-20.76	37
NGC 5687	14 34 52.40	+54 28 33.05	27.2	11.71	-20.46	47
NGC 6149	16 27 24.23	+19 35 49.91	37.2	12.65	-20.20	49
PGC 29321	10 05 51.19	+12 57 40.69	40.9	13.80	-19.25	35

Notes. (1) Galaxy name. (2), (3) Right ascension and declination (J2000.0). (4) Galaxy distance from Cappellari et al. (2011). (5) Composite-model apparent i-band magnitude (cmodel) of the galaxy from SDSS. (6) Absolute i-band magnitude of the galaxy. (7) Galaxy inclination from the axial ratio given by 2MASS.

(Naab et al. 2014). This allowed to classify galaxies in slow and fast rotators according to their angular momentum and infer general implications on their formation processes;

- stellar populations, showing that their spectral properties are independent of environment, varying only with the galaxy mass (McDermid et al. 2015).

We first selected a sample of lenticular unbarred galaxies (i.e., SA0 according to the morphological classification of RC3). Lenticular unbarred galaxies are supposed to represent the simplest systems in terms of their morphological structure, that is, they have only a bulge and a disk. Moreover, we selected only galaxies without any morphological (e.g., recent signs of interactions) or kinematic peculiarity (e.g., kinematic distinct cores; Krajnović et al. 2011). We restricted to galaxies with inclination $\theta < 65°$, based on the galaxy axial ratio b/a (2MASS), in order to perform a successful photometric decomposition of the galaxies and carefully retrieve the three-dimensional shape of their bulges as shown in Section 5.3.2. This selection led to a sample of 35 galaxies. We retrieved the flux-calibrated i-band images of the sample galaxies from the SDSS DR9 (Ahn et al. 2012).

This sample of galaxies was further limited after performing the photometric decomposition analysis explained in Section 6.3, which highlighted: (i) the presence of a previously unidentified bar component or spiral structures in six out of 35 galaxies, (ii) a single compo-

Table 6.2: Characteristics of the i-band SDSS images of the sample galaxies.

Galaxy	Gain	RON	Sky	$FWHM$	β
	$[e^-$ ADU$^{-1}]$	$[e^-]$	[ADU]	[arcsec]	
(1)	(2)	(3)	(4)	(5)	(6)
NGC 3156	5.2	14.5	144 ± 5	1.3	3.2
NGC 3245	6.6	16.4	186 ± 6	1.3	4.6
NGC 3998	4.6	13.0	177 ± 5	1.1	4.1
NGC 4249	4.6	13.0	213 ± 6	1.1	5.9
NGC 4578	4.9	10.4	160 ± 5	1.1	4.2
NGC 4690	6.6	16.4	206 ± 5	1.0	3.6
NGC 5687	6.6	16.4	224 ± 5	1.2	3.5
NGC 6149	4.9	10.4	124 ± 4	1.1	4.5
PGC 29321	4.9	13.4	168 ± 5	1.0	8.0

Notes. (1) Galaxy name. (2), (3) Image gain and RON provided by SDSS. (4) Measured sky level and corresponding standard deviation. (5), (6) FWHM and β parameter measured for the circular Moffat PSF.

nent best-fit model for eight out of 35 galaxies which turned out to be elliptical galaxies (see Méndez-Abreu et al. 2018, for all details), and (iii) a high inclination (more than $\theta = 65°$) of 12 out of 35 galaxies. It is worth noting that a careful inspection of the subsample of highly inclined galaxies allowed us to conclude that in some cases the circular halo component was misinterpreted as the bulge component in the fitting procedure, resulting in a very large bulge that dominates the light also in the outskirts of the galaxy. We preferred to discard also these galaxies, since the geometrical parameters are critical in our analysis (see Section 6.4).

The final sample is composed of nine galaxies for which we reported their main properties in Table 6.1.

■ 6.3 Surface photometry

We made use of the procedure described in Section 2.1.2.1 to estimate the background sky level and its standard deviation. We found that our estimates of the sky level are systematically lower by 0.3% than those given by SDSS. We trimmed the sky-subtracted images to reduce the computing time when performing a reliable photometric decomposition. We centered each galaxy in a field of view of at least 300×300 pixels^2 corresponding to 120×120 arcsec^2. We modeled the PSF of the images with a circular Moffat function

(Moffat 1969), with the shape parameters measured directly from the field stars (Table 6.2). Finally, we built mask images and ran `ellipse` on the trimmed images to derive the radial profiles of the azimuthally-averaged surface brightness μ, ellipticity ϵ, and position angle PA of the galaxy isophotes in the i band.

We performed the two-dimensional photometric decomposition of the SDSS images of the 35 unbarred lenticular galaxies taken from the ATLAS^{3D} survey with no morphological and kinematic peculiarities and seen at intermediate inclination using GASP2D. We derived the structural parameters of each galaxy assuming that its surface brightness distribution was the sum of a Sérsic bulge and an exponential disk (Type I, II, or III), as explained in Section 2.1.1. We did not consider any other additional component, such as spiral arms, lenses, or ovals. Under the assumption of circular and infinitesimally thin disk, we calculated the galaxy inclination $\theta = \arccos(q_{\rm disk})$, discarding 12 galaxies because of their high inclination.

We discriminated between elliptical and lenticular galaxies by using the logical filtering and statistical criteria given in Section 3.4.1 to decide whether adopt or not a disk component to model the surface brightness distribution of the selected galaxies. As in Méndez-Abreu et al. (2018), we took advantage of simulated mock galaxies to set at $\Delta{\rm BIC} > -18$ the threshold that statistically sets the distinction between elliptical and lenticular galaxies. This led us to identify eight elliptical galaxies, which we rejected.

We scrutinized the residual images obtained after subtracting the GASP2D model images of the remaining 15 *bona fide* lenticular galaxies from their SDSS images to look for other components than bulge and disk (i.e., a main bar, large-scale spiral arms, inner and outer rings, a lens, or an oval). Six galaxies showed a weak bar and/or a faint spiral structure and were discarded. Furthermore, we visually inspected the optical and near-infrared images of each of the nine remaining galaxies available in the HST Science Archive to double check that they did not host nuclear bars, rings, or spiral arms.

Finally, we estimated the errors on the structural parameters analyzing a sample of mock galaxies built through a series of MC simulations and following the procedure described in Section 4.3.3. We assumed the mock galaxies to be at a distance of $\sim$ 27 Mpc, which corresponds to the median distance of our sample galaxies.

The best-fit structural parameters and the corresponding errors of the nine sample galaxies are available in Table 6.3 while their GASP2D fits are shown in Fig. 6.1.

Table 6.3: Structural parameters of the sample galaxies.

Galaxy	μ_e [mag arcsec^{-2}]	$\langle\mu_e\rangle$ [mag arcsec^{-2}]	r_e [arcsec]	n	q_{bulge}	PA_{bulge} [°]	μ_0 [mag arcsec^{-2}]	h [arcsec]	q_{disk}	PA_{disk} [°]	B/T	ΔBIC
(1)	(2)	(3)	(4)	(5)	(6)	(7)	(8)	(9)	(10)	(11)	(12)	(13)
NGC 3156	20.06 ± 0.02	18.52 ± 0.05	4.7 ± 0.1	5.31 ± 0.04	0.580 ± 0.002	48.7 ± 0.1	18.68 ± 0.02	12.22 ± 0.07	0.495 ± 0.002	48.5 ± 0.2	0.16	103
NGC 3245	17.32 ± 0.01	16.42 ± 0.01	4.03 ± 0.02	1.52 ± 0.01	0.730 ± 0.001	175.7 ± 0.1	18.50 ± 0.01	20.61 ± 0.03	0.518 ± 0.001	176.5 ± 0.1	0.25	49
NGC 3998	17.31 ± 0.01	16.20 ± 0.02	5.40 ± 0.03	2.31 ± 0.01	0.838 ± 0.001	131.6 ± 0.1	19.10 ± 0.01	23.76 ± 0.06	0.790 ± 0.001	139.0 ± 0.1	0.42	2
NGC 4249	18.45 ± 0.04	17.51 ± 0.08	1.31 ± 0.05	1.67 ± 0.03	0.939 ± 0.003	86.9 ± 0.3	19.47 ± 0.03	6.6 ± 0.1	0.949 ± 0.006	93.1 ± 0.4	0.17	−7
NGC 4578	19.32 ± 0.01	18.13 ± 0.02	8.89 ± 0.06	2.71 ± 0.01	0.750 ± 0.001	32.5 ± 0.1	20.37 ± 0.01	32.51 ± 0.08	0.686 ± 0.001	30.6 ± 0.1	0.39	−16
NGC 4690	19.37 ± 0.02	17.91 ± 0.07	2.84 ± 0.09	4.52 ± 0.04	0.779 ± 0.002	148.1 ± 0.1	19.37 ± 0.02	10.4 ± 0.1	0.737 ± 0.002	149.2 ± 0.2	0.19	30
NGC 5687	19.01 ± 0.01	17.92 ± 0.03	6.67 ± 0.07	2.58 ± 0.01	0.686 ± 0.001	103.6 ± 0.1	20.16 ± 0.01	24.26 ± 0.08	0.622 ± 0.001	101.2 ± 0.1	0.40	−17
NGC 6149	18.79 ± 0.02	17.65 ± 0.07	3.0 ± 0.1	2.49 ± 0.03	0.691 ± 0.002	21.2 ± 0.1	19.50 ± 0.02	8.85 ± 0.05	0.660 ± 0.002	18.9 ± 0.2	0.39	0
PGC 29321	18.91 ± 0.04	18.10 ± 0.05	1.28 ± 0.04	1.26 ± 0.02	0.742 ± 0.003	62.1 ± 0.3	18.87 ± 0.03	3.90 ± 0.06	0.873 ± 0.006	54.4 ± 0.4	0.16	12

Notes. (1) Galaxy name. (2), (3), (4), (5), (6) and (7) Surface brightness at effective radius, mean surface brightness within effective radius, effective radius, Sérsic index, apparent axial ratio, and position angle of the bulge, respectively. (8), (9), (10) and (11) Central surface brightness, scalelength radius, apparent axial ratio, and position angle of the disk, respectively. The inner scalelength radius is given for the double-exponential disks. (12) Bulge-to-total luminosity ratio. (13) ΔBIC = BIC(bulge) − BIC(bulge + disk).

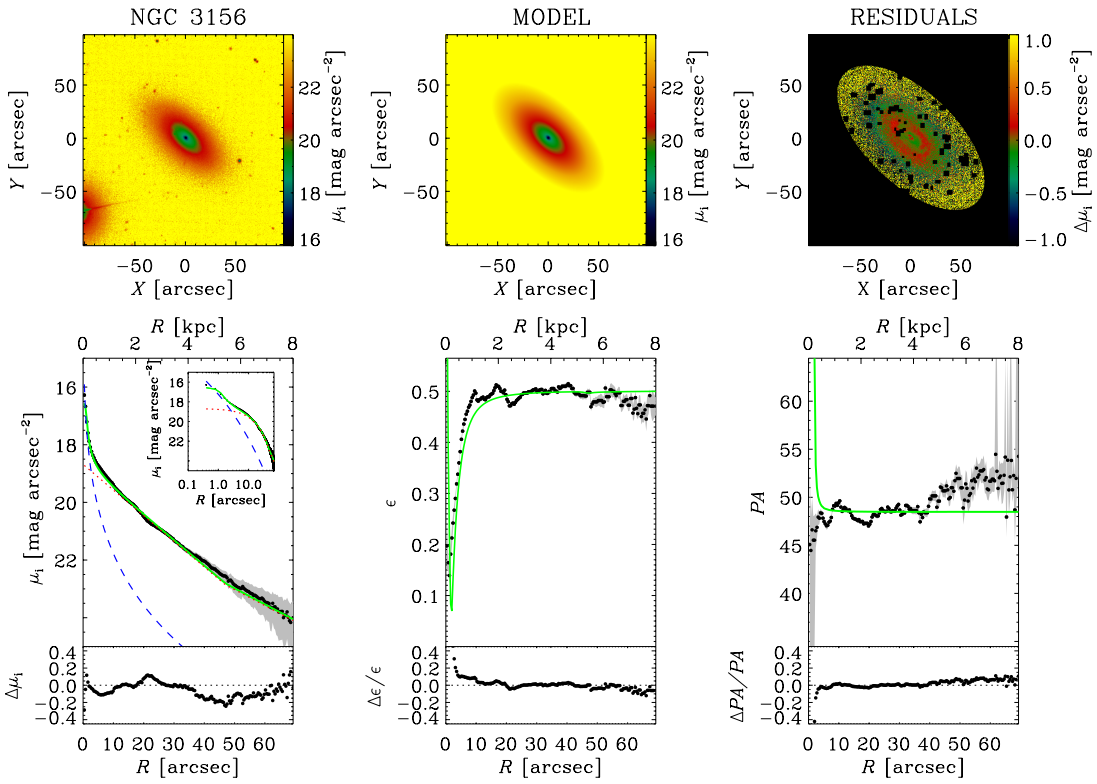

Figure 6.1: Two-dimensional photometric decomposition of the *i*-band images obtained from GASP2D. The upper panels (*from left to right*) show the map of the observed, modeled, and residual (observed−modeled) surface-brightness distributions. The field of view is oriented with North up and East left. The black areas in the residual image correspond to pixels excluded from the fit. The lower panels (*from left to right*) show the ellipse-averaged radial profile of surface brightness, position angle, and ellipticity measured in the observed (black dots with gray error bars) and seeing-convolved modeled image (green solid line) and their corresponding difference. The surface-brightness radial profiles of the best-fit bulge (blue dashed line) and disk (red dotted line) are also shown in both linear and logarithmic scale for the distance to the center of the galaxy.

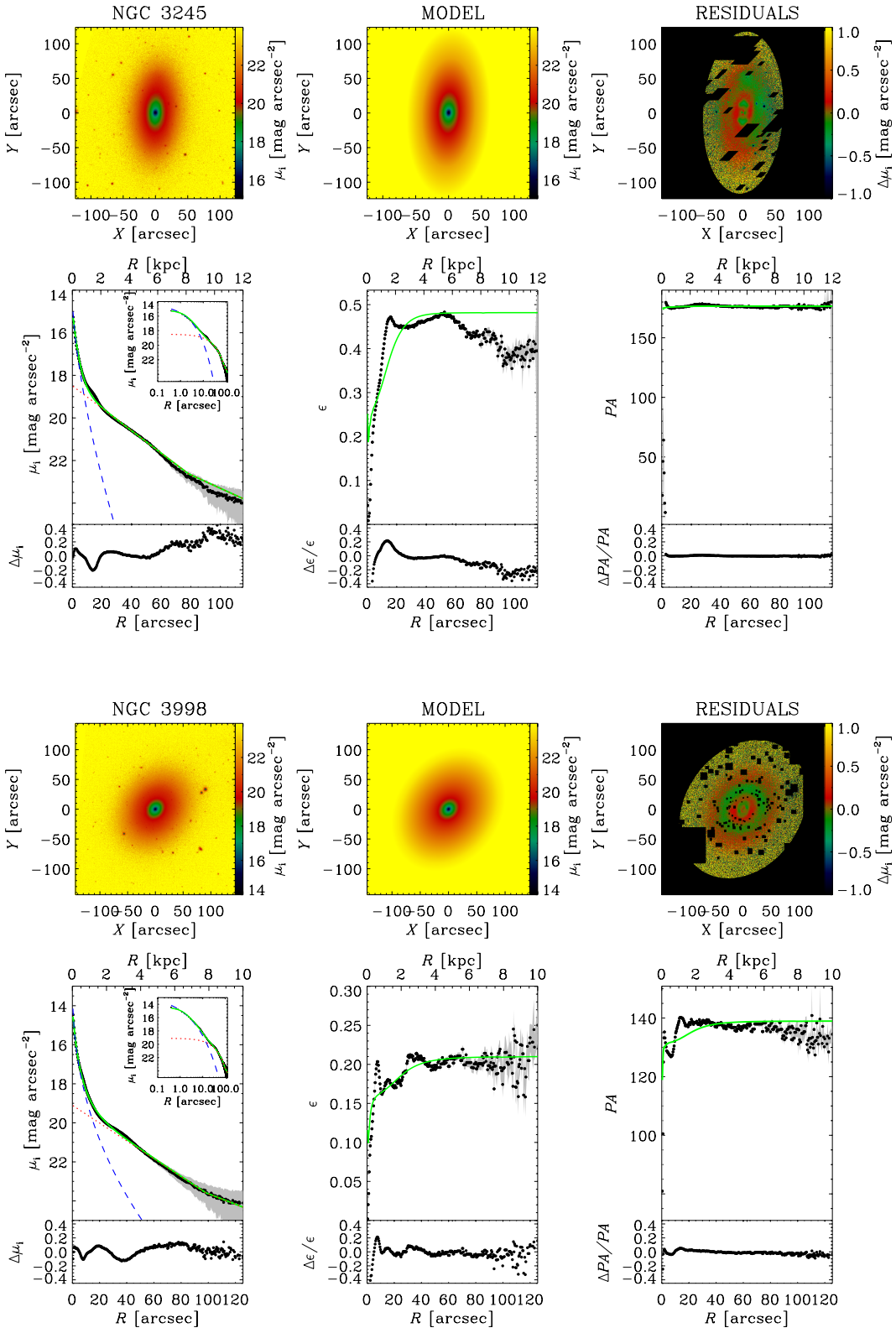

Figure 6.1: continued.

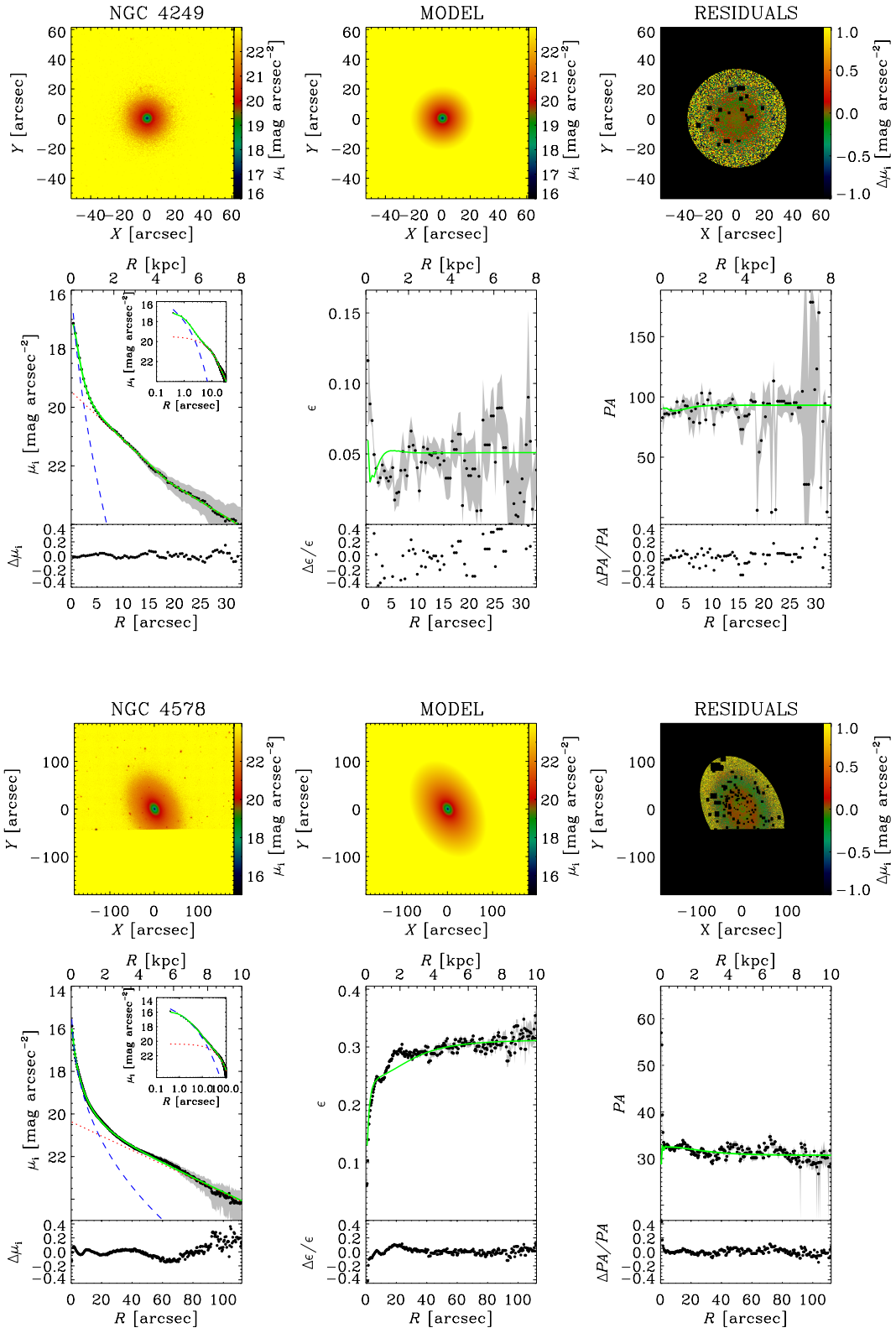

Figure 6.1: continued.

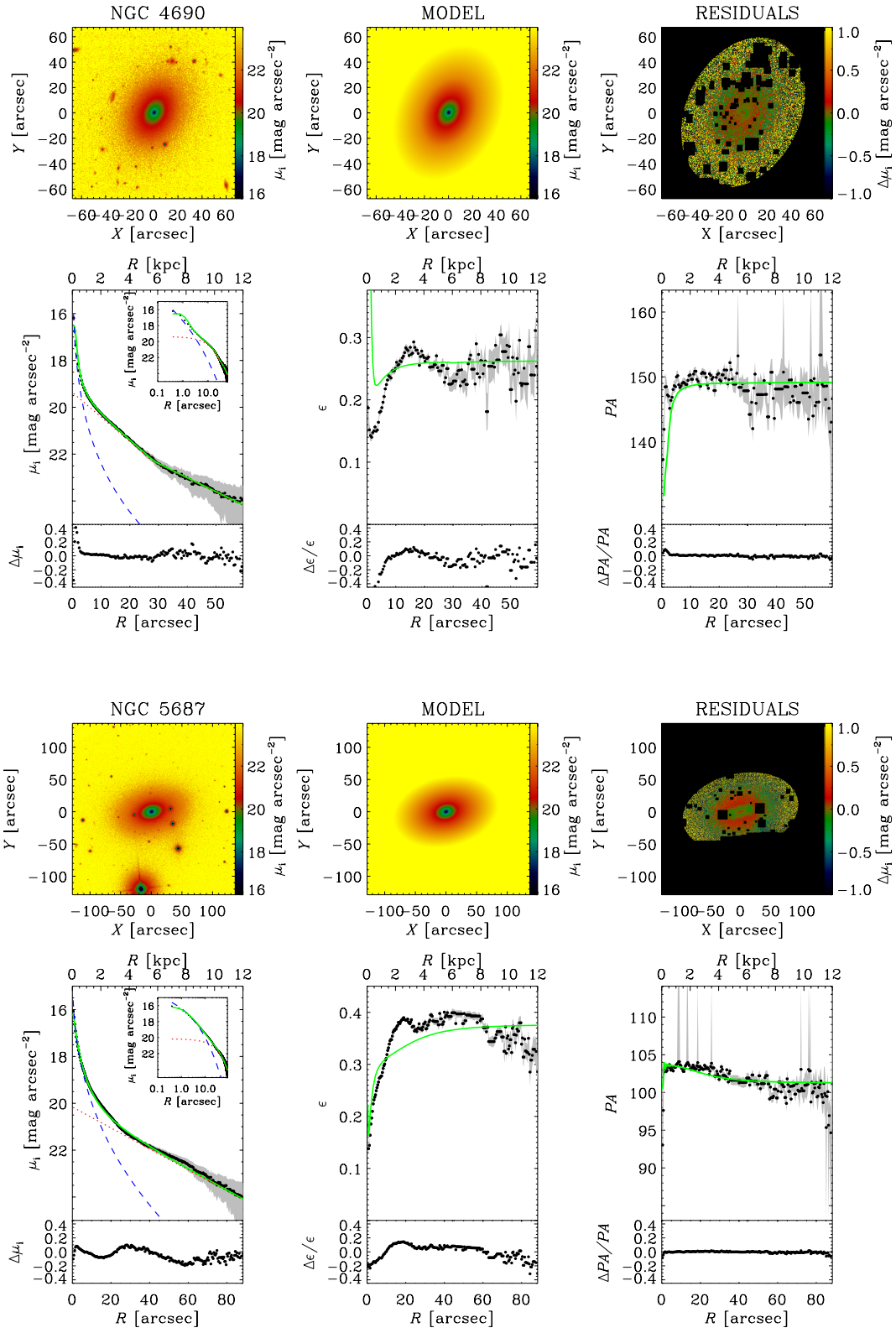

Figure 6.1: continued.

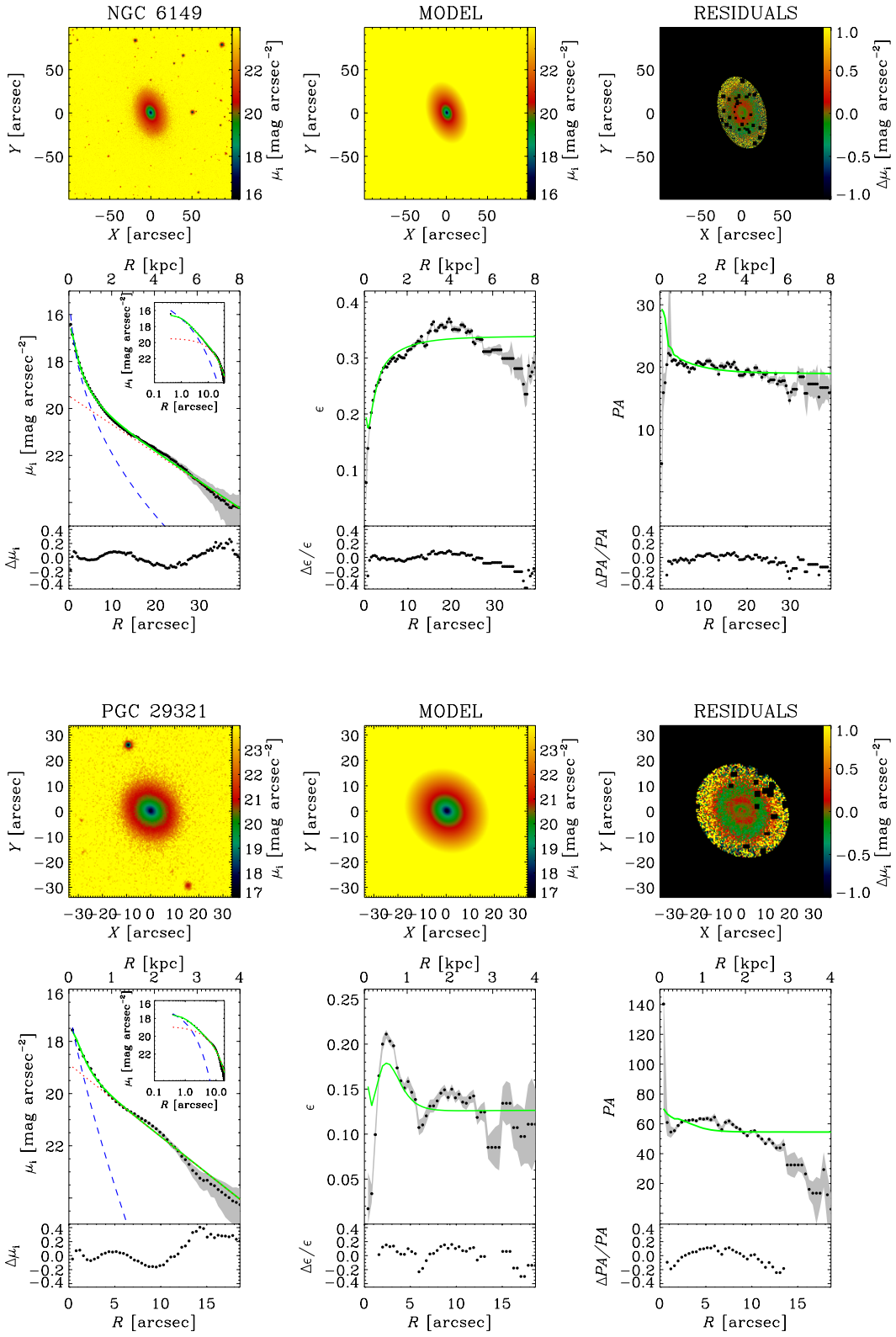

Figure 6.1: continued.

Table 6.4: Most probable intrinsic shape of our sample bulges.

Galaxy	B/A	C/A	P($C/A < 0.4$)	P($C/A < 0.5$)
(1)	(2)	(3)	(4)	(5)
NGC 3156	1.00	0.41	29%	88%
NGC 3245	1.00	0.61	...	...
NGC 3998	0.96	0.51	...	22%
NGC 4249	1.00*	1.08*	...	...
NGC 4578	1.00	0.46	...	51%
NGC 4690	1.00	0.46	4%	65%
NGC 5687	0.94	0.51	...	19%
NGC 6149	0.94	0.36	45%	84%
PGC 29321	0.79	0.59	5%**	5%**

Notes.(1) Galaxy name. (2), (3) Most probable intrinsic axial ratios of the bulge. (4), (5) Probability that the galaxy hosts an oblate bulge ($B/A > 0.85$) with an intrinsic flattening (C/A) less than 0.4 and 0.5, respectively. * symbol is used to mark the low-inclined galaxy NGC 4249, while ** symbol is used to identify the prolate/triaxial bulge of PGC 29321.

■ 6.4 Bulge intrinsic shape

We constrained the intrinsic shape of our sample bulges making use of the statistical method presented in Section 2.2. The most probable values of B/A and C/A are listed in Table 6.4, while the intrinsic shape probability distributions of the bulge are shown in Fig. 6.2. It is worth noting that eight out of nine galaxies in our sample are in the inclination interval $25° < \theta < 65°$, which was defined in Section 5.3.2 as the reliable range for deriving the three-dimensional shape of the bulge component. We also calculated the intrinsic shape of the bulge in NGC 4249, even if this galaxy is nearly face-on ($\theta = 18°$).

In order to fully characterize the three-dimensional shape of our sample bulges taking into account the uncertainties in the (B/A, C/A) diagram, we calculated their probability to present a given degree of flattening. This allowed us to characterize disk-like bulges with a probabilistic approach instead of using a fixed threshold. Considering the mean intrinsic flattening of the disk component in nearby galaxies $\langle q_{0,\,\mathrm{disk}} \rangle = 0.267 \pm 0.102$ (Rodríguez & Padilla 2013), we derived the probability that our bulges presented a flattening similar of that of the disks within 2 rms. Thus, considering the oblate region $B/A > 0.85$, we calculated the probability $P(C/A < 0.4)$ and $P(C/A < 0.5)$ for each sample bulge (Table 6.4). For completeness, we also applied this procedure to the bulge of PGC 29321, even though it results to be the only prolate or mildly triaxial bulge in our sample. We found that the galaxy NGC 6149 hosts the most flattened oblate bulge.

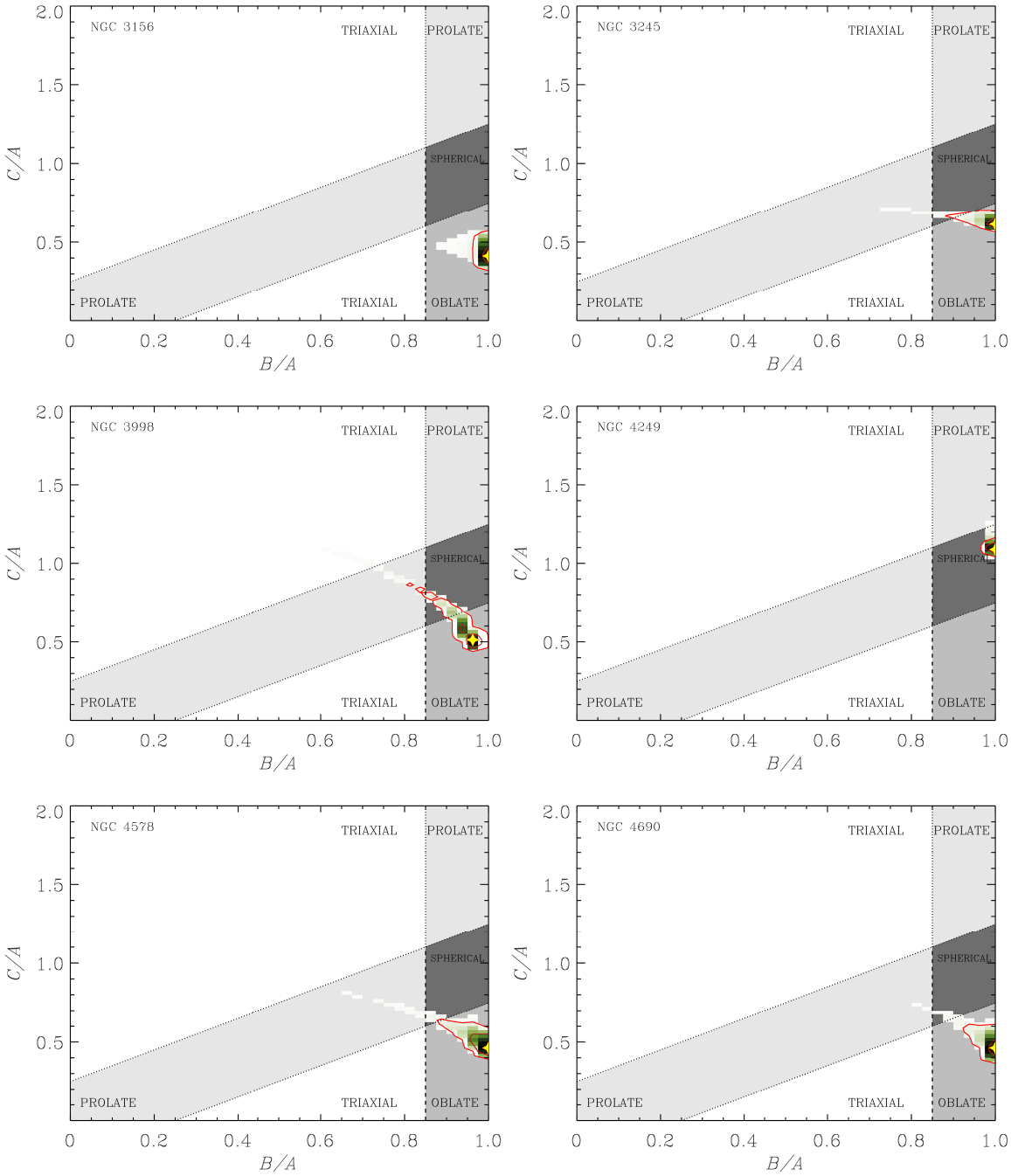

Figure 6.2: Distribution of the intrinsic axial ratios B/A and C/A of the bulge of the sample galaxies. The yellow star corresponds to the most probable values of B/A and C/A. The inner and outer red solid contours encompass respectively the 68.3% and 95.4% of the realizations of (B/A, C/A) consistent with the geometric parameters of bulge and disk measured from our photometric decomposition. The white, light gray, gray, and dark gray regions mark the regimes of triaxial, prolate, oblate, and spherical bulges, respectively.

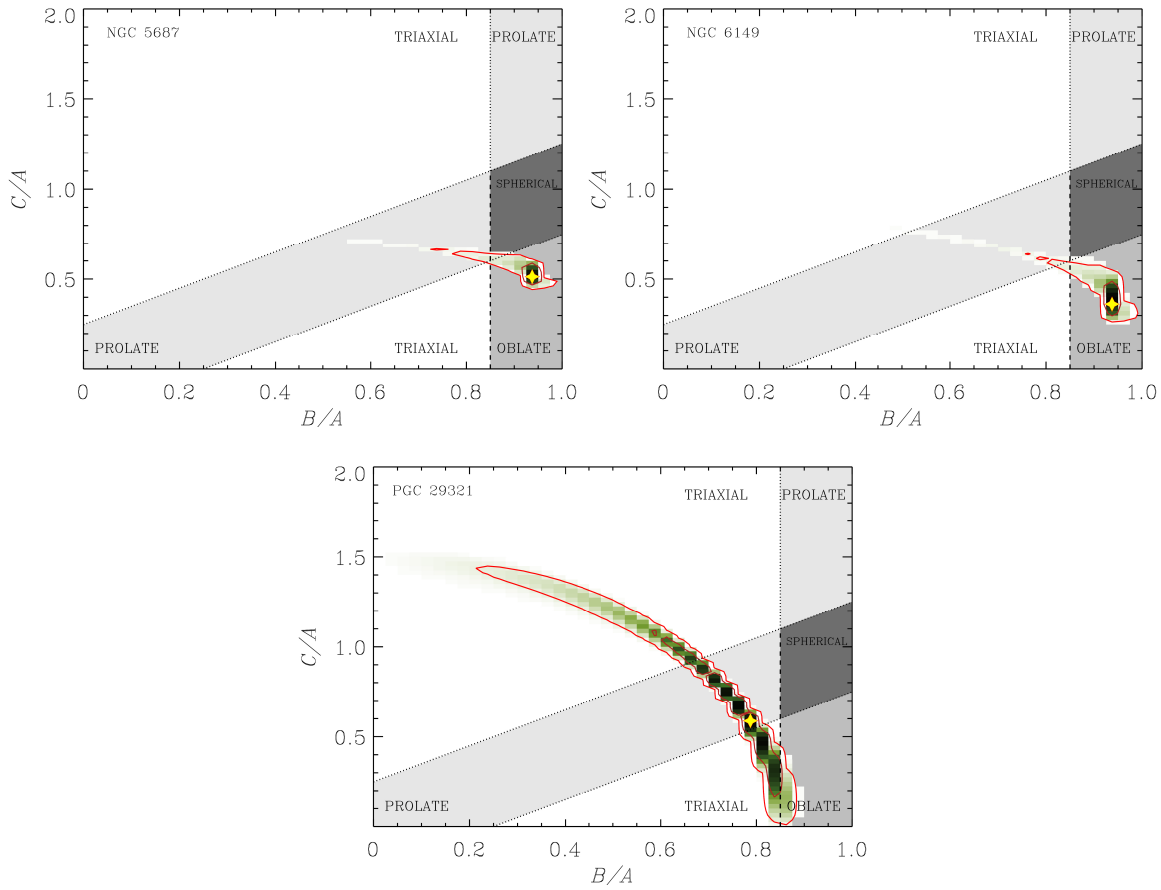

Figure 6.2: continued.

■ 6.5 Integral field spectroscopy

We characterized the two-dimensional kinematics and line-strength indices of the sample bulges taking advantage of the reduced datacubes provided by the ATLAS^{3D} survey (see Emsellem et al. 2004; Cappellari et al. 2011; McDermid et al. 2015, for all details).

The spectroscopic data were obtained using the SAURON IFS (Bacon et al. 2001) mounted on the William Herschel Telescope (WHT) in La Palma (Spain). The observations were conducted in the low spatial resolution mode. The field of view of the SAURON IFS covers 33 $\times$41 arcsec^2, with a spatial sampling of 0.94 $\times$ 0.94 arcsec^2 and a spectral resolution of $FWHM \sim 4$ Å. The spectroscopic data reduction for all the galaxies in the ATLAS^{3D} mother sample follows the procedures described in Bacon et al. (2001) and Emsellem et al. (2004). All the datacubes were merged with 0.8$\times$0.8 arcsec^2 spaxels rebinning,

using a minimum S/N threshold of 40 for the adaptive binning (Cappellari & Copin 2003). They presented a typical $FWHM_{\rm PSF}$ of 1.5 arcsec. The extraction of the stellar kinematics was performed using the pPXF algorithm (Cappellari & Emsellem 2004), the MILES library of stellar templates (Sánchez-Blázquez et al. 2006), and an optimized template per galaxy (see Cappellari et al. 2011, for further details). The line-strength indices were measured in the Lick/IDS system (Worthey et al. 1994) and spatially binned to a constant S/N.

It is worth noting that we did not reduce the data or extract the stellar kinematics, but we only computed the bulge related values of the stellar kinematics and line-strength indices needed to characterize our sample bulges, following the criteria provided by Fisher & Drory (2016).

6.5.1 Stellar kinematics

We characterized the bulge kinematics by extracting the light-weighted velocity dispersion within an elliptical aperture of $r_{\rm e}$. Moreover, we calculated the central light-weighted velocity dispersion within a circular aperture of $r_{\rm e}/10$, using the power-law function for the aperture correction

$$\left(\frac{\sigma}{\sigma_{\rm e}}\right) = \left(\frac{r}{r_{\rm e}}\right)^{\alpha}, \tag{6.1}$$

where $\alpha = -0.055 \pm 0.020$ for ETG, as derived by Falcón-Barroso et al. (2017) analyzing 300 galaxies drawn from the CALIFA DR3 (Sánchez et al. 2016).

We calculated the light-weighted $\langle v^2\rangle/\langle\sigma^2\rangle$ value inside the bulge region, defined as

$$\left.\frac{\langle v^2\rangle}{\langle\sigma^2\rangle}\right|_{r_{\rm e}} = \frac{\sum_{i=1}^{N} F_i v_i^2}{\sum_{i=1}^{N} F_i \sigma_i^2}, \tag{6.2}$$

where F_i is the flux contained inside the i-th Voronoi bin and v_i and σ_i are the corresponding measured inclination-corrected velocity and velocity dispersion (Binney 2005). Furthermore, similarly to Fabricius et al. (2012), we provided another estimation of the light-weighted $\langle v^2\rangle/\langle\sigma^2\rangle$ value as

$$\left.\frac{\langle v^2\rangle}{\langle\sigma^2\rangle}\right|_{r_{\rm min}<r<r_{25\%}}, \tag{6.3}$$

where the minimum radius $r_{\rm min}$ excludes the inner $\rm FWHM_{PSF}$, while the maximum radius $r_{25\%}$ is defined as the radius where the light contribution of the photometric bulge exceeds

that of the disk component by 25%, that is

$$I_{0,\,\mathrm{bulge}}\, e^{-\left(\frac{r_{25\%}}{r_0}\right)^{1/n}} = 1.25\, I_{0,\,\mathrm{disk}}\, e^{-\left(\frac{r_{25\%}}{h}\right)}, \tag{6.4}$$

where the central intensity of the bulge component is defined as

$$I_{0,\,\mathrm{bulge}} = I_{\mathrm{e}}\, e^{b_n} \tag{6.5}$$

and the bulge scale length radius can be expressed as

$$r_0 = \frac{(b_n)^n}{r_{\mathrm{e}}}\,. \tag{6.6}$$

We made sure to avoid a dependence on the particular binning scheme of each kinematic data set, using a circular radial binning of five equally-sized bins in $\log(r)$ (see Fabricius et al. 2012, for details).

Finally, we analyzed the gradient of the bulge velocity dispersion profile defined as

$$\gamma = \left\langle \frac{\mathrm{d}\log(\sigma)}{\mathrm{d}\log(r)} \right\rangle |_{r_{\mathrm{min}} < r < r_{25\%}}\,. \tag{6.7}$$

The values of σ, $\langle v^2\rangle/\langle\sigma^2\rangle$, γ , and of the $r_{25\%}$ radius are provided in Table 6.5. It is worth noting that for the galaxy PGC 29321, since $r_{25\%} < r_{\mathrm{min}}$, we can not apply this method to calculate both $\langle v^2\rangle/\langle\sigma^2\rangle$ and γ.

The stellar kinematics maps of v and σ for the nine sample galaxies are shown in Figure 6.3. We overplotted an ellipse showing the bulge effective radius, ellipticity, and position angle to mark the region where the bulge component dominates the galaxy light. It results that our photometric definition of the bulge component generally coincides with an increase of the velocity dispersion in the center of these galaxies (e.g., NGC 3245 and NGC 3998). It is worth noting that the two-dimensional stellar kinematic maps encompass at least one galaxy effective radius in most of the objects, ensuring a full coverage of our bulges.

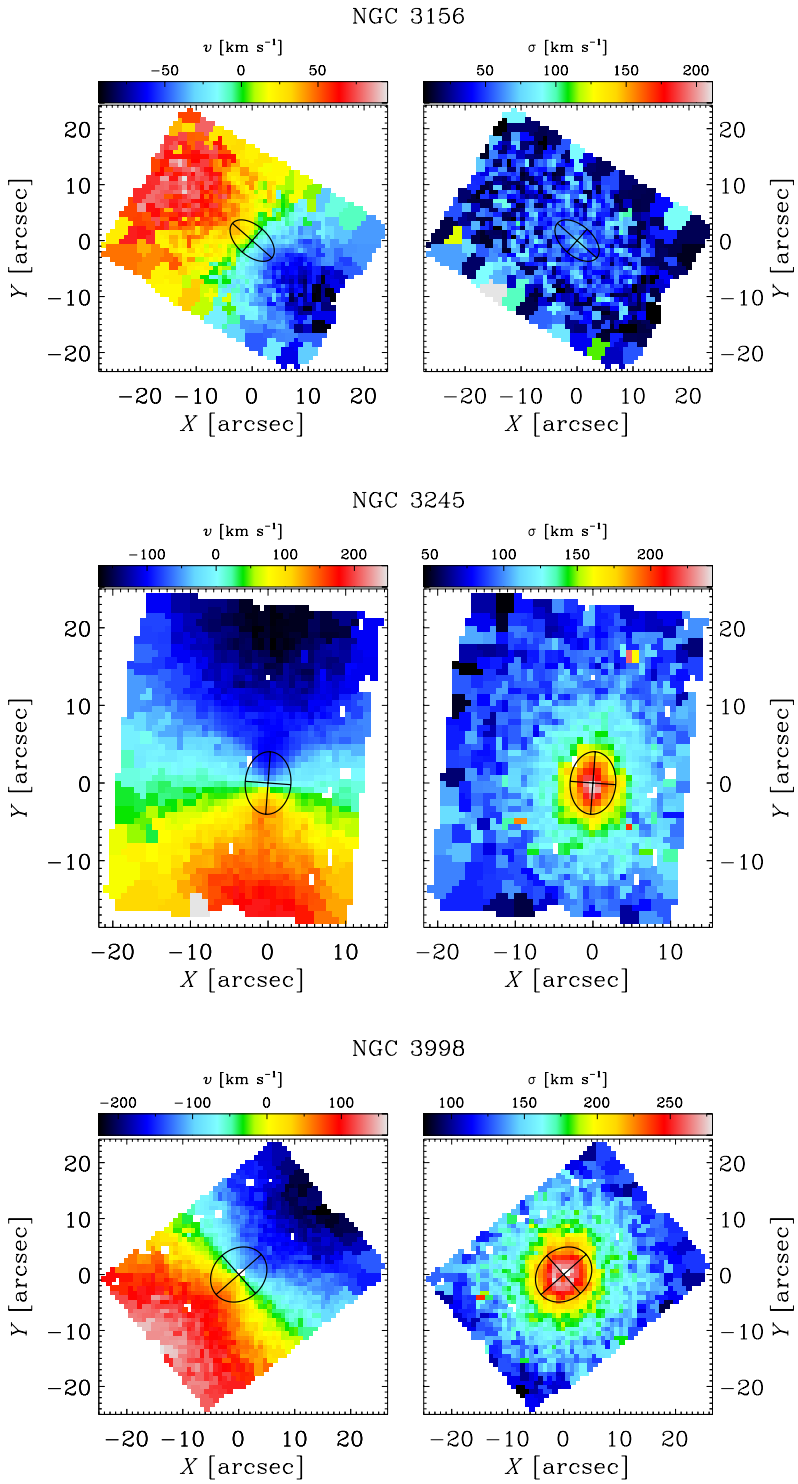

Figure 6.3: Two-dimensional stellar kinematic maps of the sample galaxies, including velocity (*left panel*) and velocity dispersion (*right panel*). The black ellipse marks the bulge effective radius, ellipticity, and position angle.

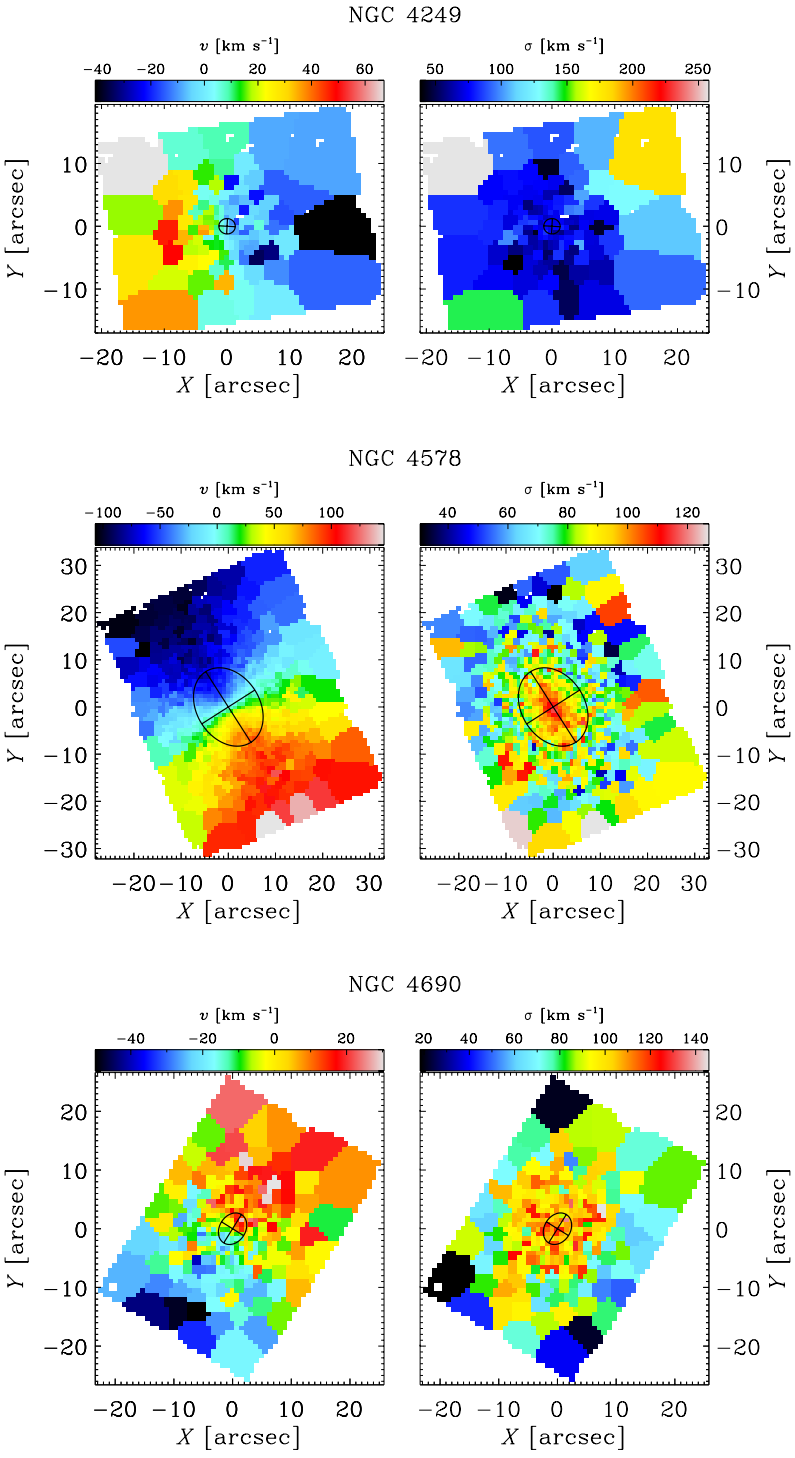

Figure 6.3: continued.

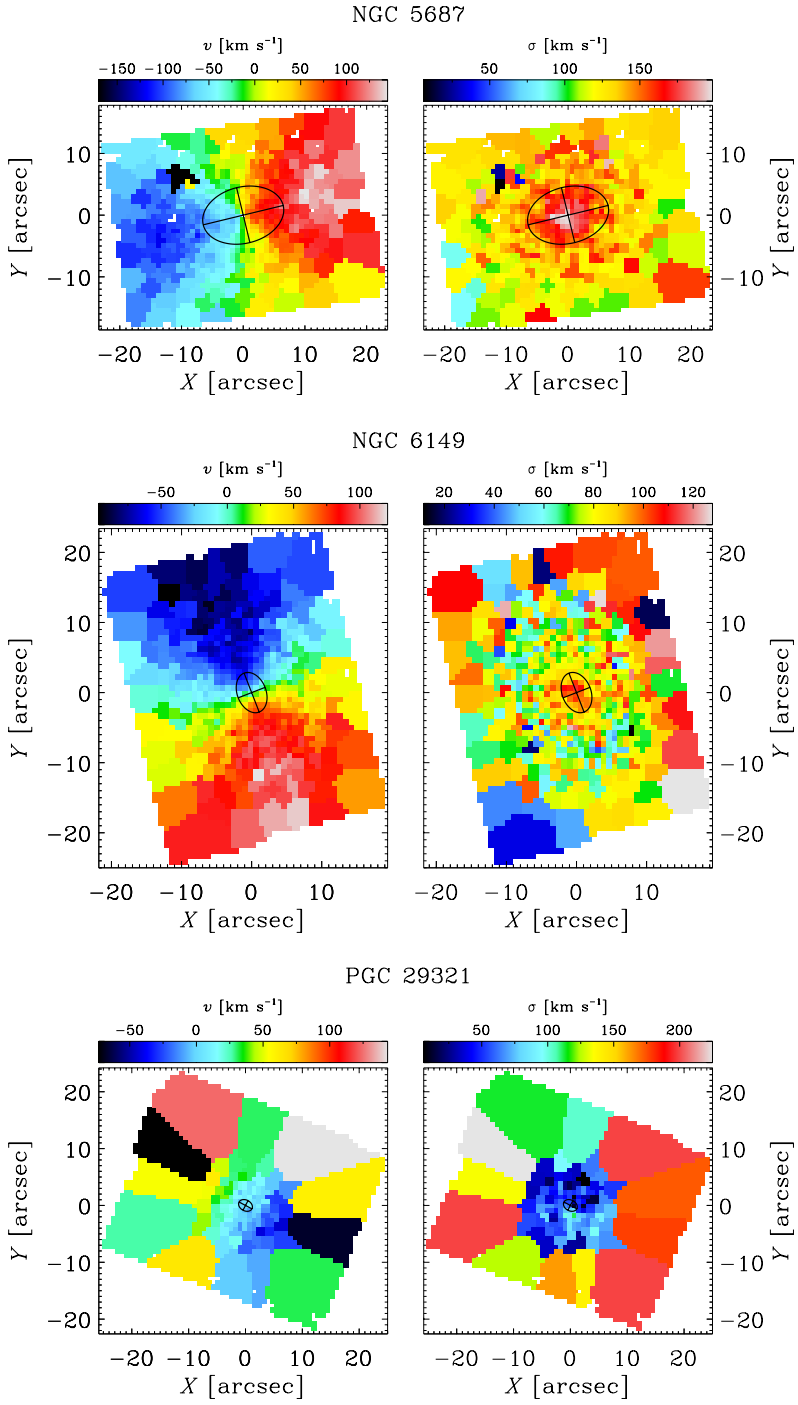

Figure 6.3: continued.

Table 6.5: Kinematics and line-strength indices for the sample galaxies.

Galaxy	$r_{25\%}$ [arcsec]	$\sigma_{r_e/10}$ [km s^{-1}]	σ_e [km s^{-1}]	$\langle v^2\rangle/\langle\sigma^2\rangle\vert r_{25\%}$	$\langle v^2\rangle/\langle\sigma^2\rangle\vert r_e$	Mg b (1.5) [Å]	Mg b (r_e) [Å]	Fe 5015 (1.5) [Å]	Fe 5015 (r_e) [Å]	γ
(1)	(2)	(3)	(4)	(5)	(6)	(7)	(8)	(9)	(10)	(11)
NGC 3156	2.28	71 ± 9	62 ± 8	0.11	0.16	1.50 ± 0.03	1.62 ± 0.06	3.65 ± 0.06	3.4 ± 0.1	-0.11
NGC 3245	7.03	229 ± 5	202 ± 3	0.19	0.16	4.10 ± 0.03	3.97 ± 0.03	5.23 ± 0.06	5.01 ± 0.08	-0.18
NGC 3998	12.93	282 ± 6	249 ± 4	0.22	0.16	4.67 ± 0.03	4.52 ± 0.05	1.39 ± 0.05	3.94 ± 0.09	-0.14
NGC 4249	2.14	84 ± 10	74 ± 9	0.19	0.09	3.37 ± 0.08	3.37 ± 0.08	4.9 ± 0.2	4.9 ± 0.2	-0.05
NGC 4578	16.03	111 ± 7	98 ± 6	0.32	0.33	4.36 ± 0.03	3.70 ± 0.09	5.59 ± 0.06	4.7 ± 0.2	-0.11
NGC 4690	2.94	127 ± 9	112 ± 8	0.02	0.02	3.31 ± 0.07	3.08 ± 0.08	4.5 ± 0.1	4.3 ± 0.2	-0.04
NGC 5687	12.14	193 ± 9	170 ± 6	0.20	0.18	4.28 ± 0.09	3.9 ± 0.1	5.4 ± 0.2	4.8 ± 0.2	-0.11
NGC 6149	4.68	111 ± 6	98 ± 5	0.36	0.28	3.38 ± 0.04	3.24 ± 0.05	4.64 ± 0.08	4.4 ± 0.1	-0.07
PGC 29321	1.21	66 ± 13	58 ± 15	n.a.	n.a.	2.45 ± 0.09	2.37 ± 0.08	0.3 ± 0.2	0.1 ± 0.2	n.a.

Notes. (1) Galaxy name. (2) $r_{25\%}$ radius. (3), (4) Central velocity dispersion within a circular aperture of $r_{e/10}$ and an elliptical aperture of r_e, respectively. (5), (6) $\langle v^2\rangle/\langle\sigma^2\rangle$ value within $r_{25\%}$ and r_e, respectively. (7), (8), (9), and (10) Mg b and Fe 5015 line-strength indices within a circular aperture of 1.5-arcsec radius and an elliptical aperture of r_e. (11) Gradient of the bulge velocity dispersion profile.

6.5.2 Line-strength indices

We extracted the light-weighted values of the line-strength indices within both an elliptical aperture of r_e and a circular aperture of 1.5-arcsec radius, taking advantage of the ATLAS^{3D} maps describing the stellar populations of our galaxies (McDermid et al. 2015). The derived values of Mg b and Fe 5015 indices of the sample bulges are listed in Table 6.5, while their two-dimensional maps are shown in Fig. 6.4.

The choice of extracting the line-strength indices of our bulges within a circular aperture of 1.5-arcsec radius was justified by our aim of a straightforward comparison with literature criteria of bulge classification. Peletier et al. (2007) measured the line-strength indices of a sample of bulges in 24 early-type spiral galaxies within a circular aperture of 1.2-arcsec radius, while Ganda et al. (2007) measured them within a circular aperture of 1.5-arcsec radius for a sample of bulges in 18 late-type spiral galaxies. Fisher & Drory (2016) combined these measurements, stressing that there are not classical bulges presenting either Mg $b < 2.35$ Å or Fe 5015 < 3.97 Å. It has to be strongly remarked that this analysis was carried out once bulges were *a priori* classified as classical or disk-like by analyzing their morphologies and/or Sérsic index values. We found that the bulges of NGC 3156, NGC 3998, and PGC 29321 show Fe 5015 < 3.95 Å, while only the bulge in NGC 3156 presents Mg $b < 2.35$ Å.

Furthermore, we built up the relations (Mg b – σ_0) and (Mg b – Fe 5015), as proposed by Fisher & Drory (2016). We used as comparison sample the bulges from Peletier et al. (2007), where $\sigma_0 = \sigma_{1.2\,\mathrm{arcsec}}$, and Ganda et al. (2007), where $\sigma_0 = \sigma_{1.5\,\mathrm{arcsec}}$, while we selected the elliptical galaxies studied by Kuntschner et al. (2010), where $\sigma_0 = \sigma_{r_e/8}$. The two relations, with the best fit inferred from Fisher & Drory (2016) for the same sample of elliptical galaxies, are shown in Figs. 6.5 and 6.6, respectively. We color coded our sample bulges according to their Sérsic index values distinguishing between $n > 2$ (red circles) and $n < 2$ (blue circles), as proposed by Fisher & Drory (2016). We found that the bulge of NGC 3156 is below the line that is supposed to separate the two bulge classes in both diagrams. It is worth noting that the bulges of NGC 3998 and PGC 29321 show a really small value of Mg b (1.5 arcsec), not consistent with the (Mg b – Fe 5015) relation. However, when measured with an elliptical aperture of r_e, the bulge of NGC 3998 moves towards the expected trend, while the bulge of PGC 29321 remains more or less in the same position.

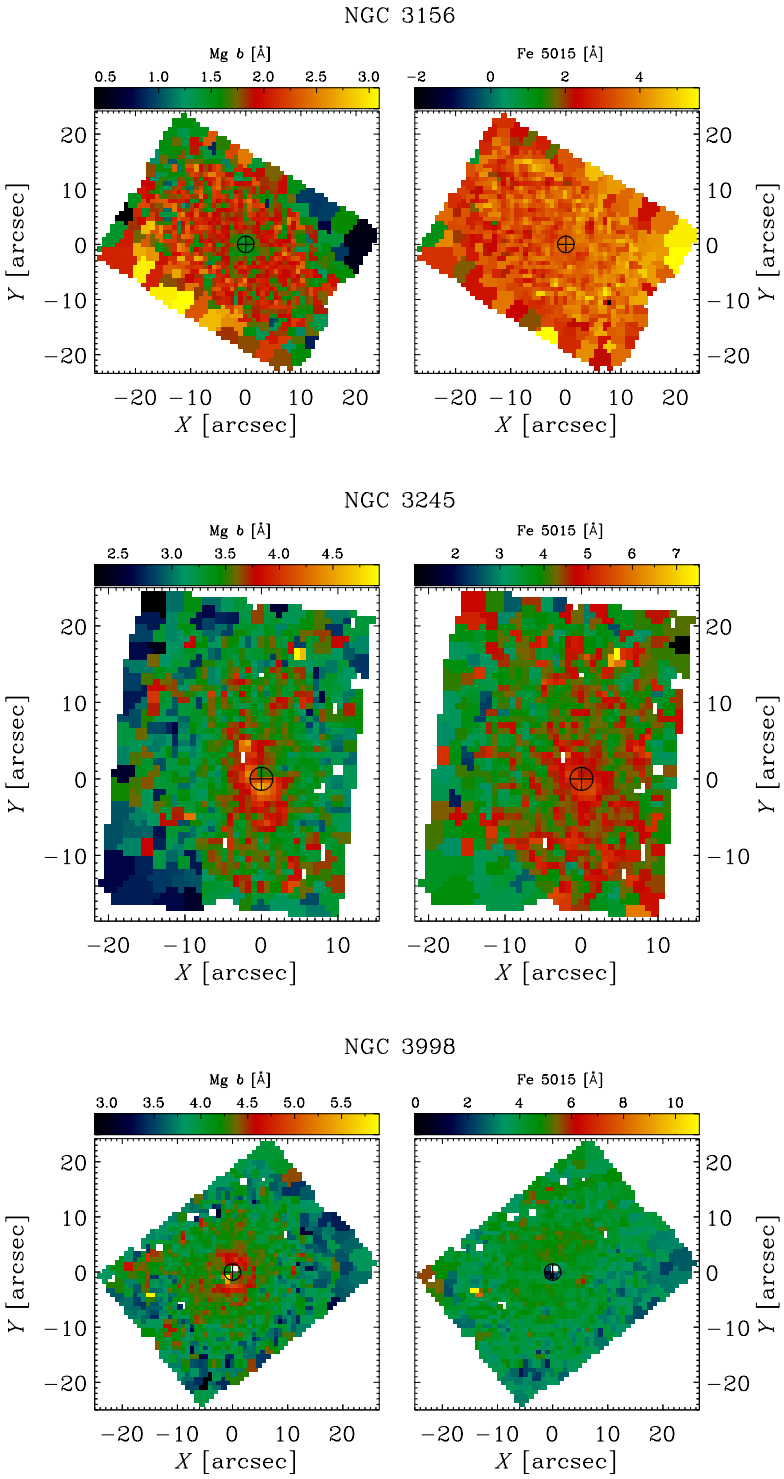

Figure 6.4: Two-dimensional stellar absorption line-strength indices maps, including Mg b (*left panel*) and Fe 5015 (*right panel*). The black circle marks the central 1.5-arcsec radius.

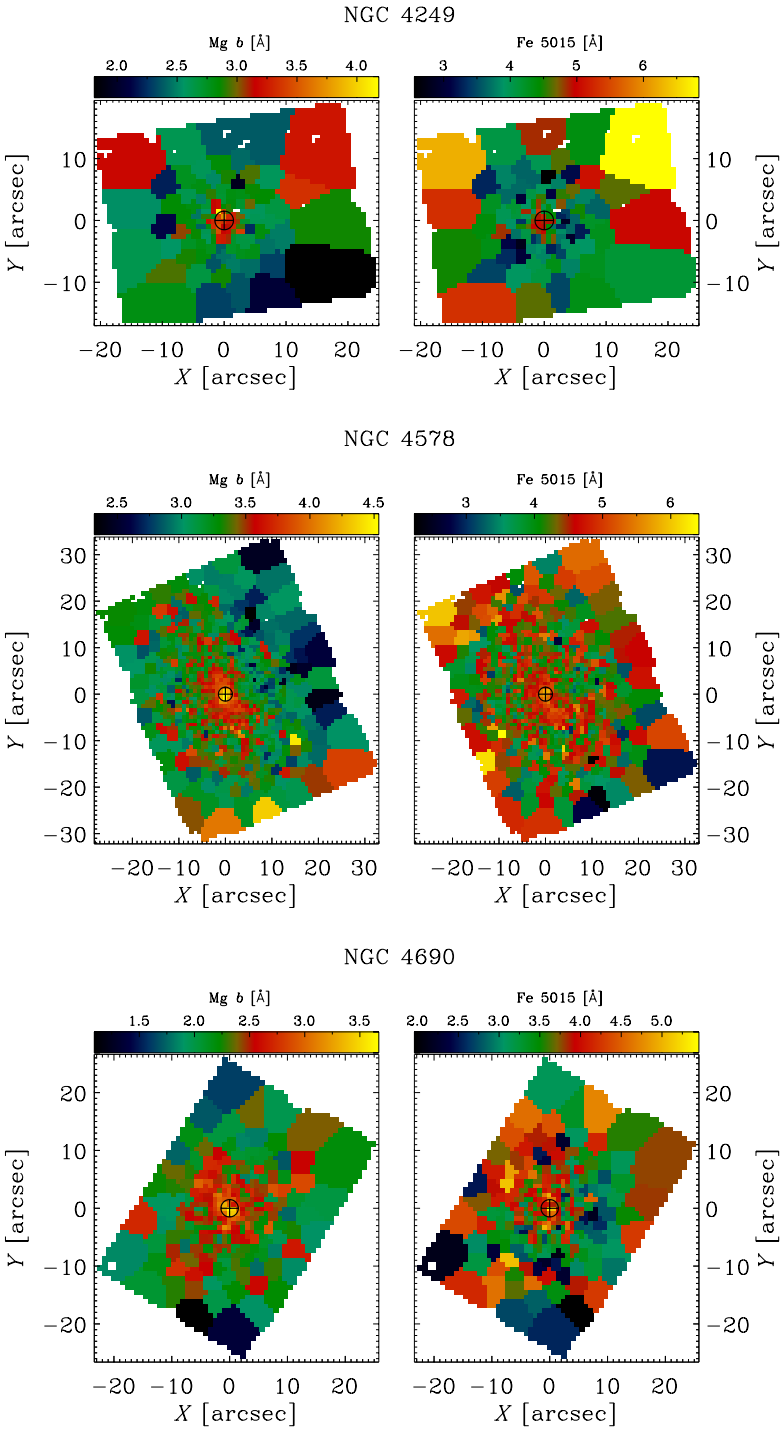

Figure 6.4: continued.

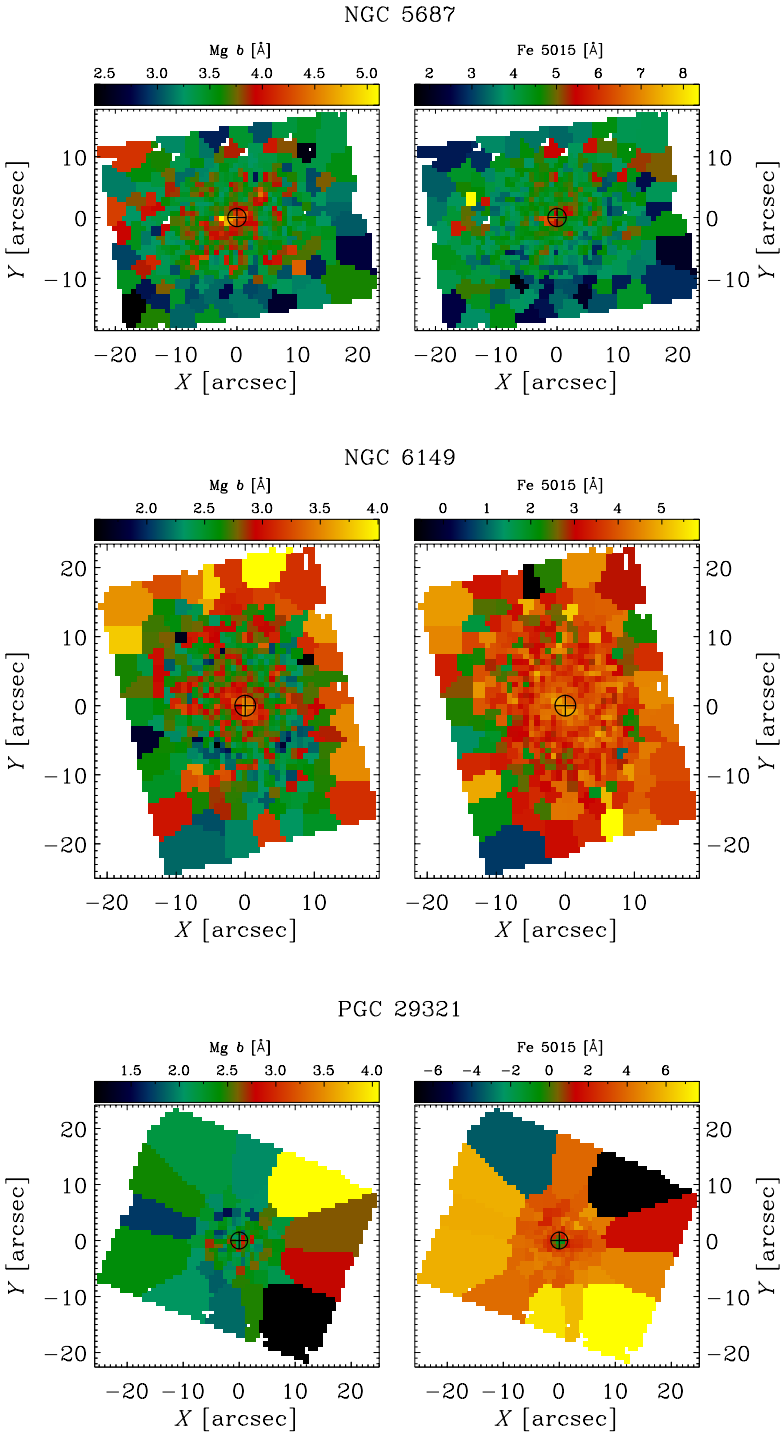

Figure 6.4: continued.

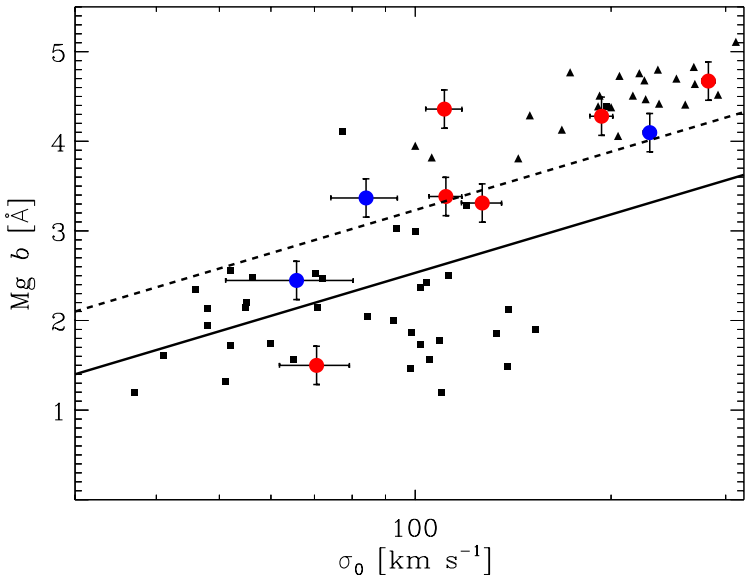

Figure 6.5: Mg b – σ_0 relation. Black symbols represent the comparison sample bulges (squared) and elliptical galaxies (triangles), as taken from Peletier et al. (2007), Ganda et al. (2007), and Kuntschner et al. (2010). Red circles stand for our sample bulges with $n > 2$, while blue circles correspond to our sample bulges with $n < 2$. The black dashed line represents the best fit, as inferred from Fisher & Drory (2016) using elliptical galaxies, while the black solid line corresponds to a deviation of 0.7 from the best-fit relation.

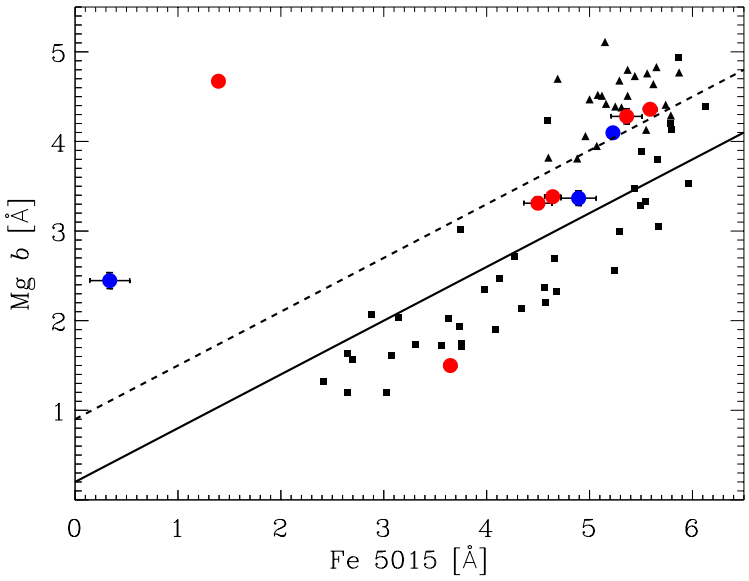

Figure 6.6: As in Fig. 6.5 but for the Mg b – Fe 5015 relation.

6.6 Scaling relations

Scaling relations are a powerful tool to investigate bulge properties, especially when combining both the photometric and kinematic information. Following the procedure explained in Section 4.5, we built the FPR, KR, and FJR using the photometric ($r_{\rm e}$, $\langle\mu_{\rm e}\rangle$, and M_i) and kinematic ($\sigma_{\rm e}$) properties of bulges from the analysis of Gadotti (2009) and Oh et al. (2011), respectively. We superimposed our sample bulges on the different relations to study their locations and infer their global properties.

We combined the photometric and kinematic properties of our bulges in the FPR (Fig. 6.7) and FJR (Fig. 6.8), using the best-fit expressions given by Eqs. (4.4) and (4.6), respectively. We found that none of our sample bulges is a low-σ outlier either to the FPR or the FJR. However, we noticed that our bulges are located systematically below the best-fit trend expected for the FPR and systematically above the best-fit line describing the FJR, even if they are consistent with the global trend within their errors. Only the bulge of NGC 3998 slightly deviates from the FJR.

We investigated the position of our sample bulges in the KR, taking advantage of the equation provided by Gadotti (2009)

$$\langle\mu_{\rm e}\rangle = 1.74\ \log(r_{\rm e}) + 19.17\,, \tag{6.8}$$

that allows to separate classical from disk-like bulges (Fig. 6.9). Firstly, we found that our bulges are compatible with the magnitude trend highlighted in Section 4.5.2, discriminating between less and more massive bulges. Secondly, we noticed that none of our bulges is below the demarcation line of the disk-like systems.

6.7 Discussion

Our sample bulges, with resolved IFS data and accurate two-dimensional photometry, presents a heterogeneous set of properties once compared with the criteria enumerated in Section 6.1. Our analysis reveals that it is difficult to pick out bulges that fulfill all the criteria for being classified either classical or disk-like bulges combining the different diag-

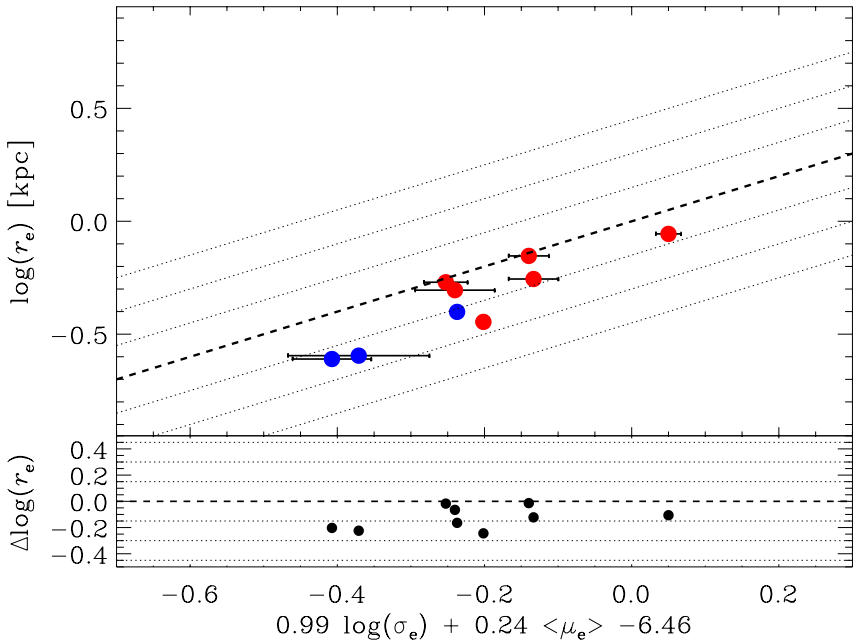

Figure 6.7: Fundamental plane relation for our sample bulges. Red circles stand for our sample bulges with $n > 2$, while blue circles correspond to our sample bulges with $n < 2$. The dashed line corresponds to the best-fit relation derived in Section 4.5.1. The dotted lines show the 1 rms, 2 rms, and 3 rms deviation in $\log(r_e)$ regions, respectively.

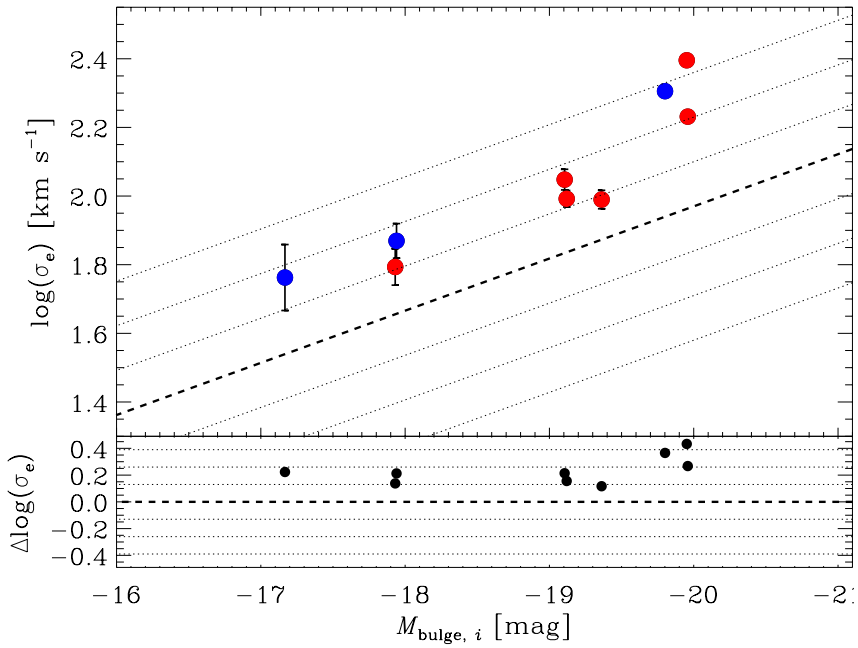

Figure 6.8: As in Fig. 4.9 but for the FJR and with the rms deviation in $\log(\sigma_e)$ from the fit. The dashed line corresponds to the best-fit relation derived in Section 4.5.3.

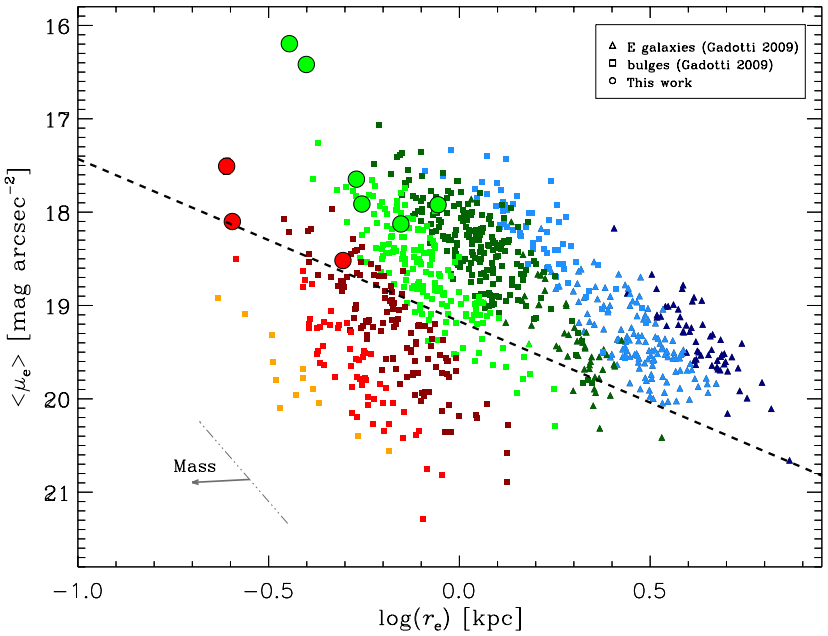

Figure 6.9: Kormendy relation for the bulges of our (larger symbols) and comparison sample (smaller symbols). The elliptical galaxies and bulges of the comparison sample are shown with triangles and squares, respectively. Filled circles correspond to the bulges in our sample. The bulges are divided according to their absolute magnitude in the following bins: $M_i < -22$ mag (dark blue), $M_i = [-22, -21]$ mag (light blue), $M_i = [-21, -20]$ mag (dark green), $M_i = [-20, -19]$ mag (light green), $M_i = [-19, -18]$ mag (dark red), $M_i = [-18, -17]$ mag (light red), and $M_i = [-17, -16]$ mag (orange). The dashed line separates classical bulges from disk-like bulges, according to Gadotti (2009). The dash-dotted line gives the slope of the KR for the magnitude bin $M_i = [-20, -19]$ mag, while the arrow indicates the KR trend for decreasing masses (Nigoche-Netro et al. 2008).

nostics. Indeed, only the bulge of NGC 5687 might be unambiguously classified as classical. Nevertheless, we discussed in detail the results of this classification in the following sections.

6.7.1 Classical vs disk-like bulges: classification criteria

In Table 6.6 we enumerated all the observational criteria that characterize classical bulges, while in Table 6.7 the ones that identify disk-like bulges. As stated before, the bulge of NGC 5687 can be unambiguously classified as classical, since it satisfies all the corresponding criteria and presents no hints for being disk-like. In addition, the bulges of NGC 3245, NGC 3998, and NGC 4578 might be classified as classical but they are missing a criterium, namely the Sérsic index, the line-strength indices, and the central velocity dispersion, respectively. The remaining bulges show a more complex interplay between photometric, kinematic,

Table 6.6: Classification criteria of classical bulges.

Galaxy	Morph. $(\text{I–1})_\text{C}$	n $(\text{I–2})_\text{C}$	Spectral rel. $(\text{I–3})_\text{C}$	γ $(\text{I–4})_\text{C}$	$\sigma_{r_{e/10}}$ $(\text{II–1})_\text{C}$	FPR $(\text{III–1})_\text{C}$	3D shape
(1)	(2)	(3)	(4)	(5)	(6)	(7)	(8)
NGC 3156	•	•		•		•	•
NGC 3245	•		•	•	•	•	•
NGC 3998	•	•	•	•	•	•	•
NGC 4249	n.a.		•			•	•
NGC 4578	•	•	•	•		•	•
NGC 4690	•	•	•			•	•
NGC 5687	n.a.	•	•	•	•	•	•
NGC 6149	n.a.	•	•			•	
PGC 29321	n.a.		•	n.a.		•	•

Notes. Classification criteria of classical bulges. (1) Galaxy name. (2) Morphology. (3) Sérsic index $n > 2$. (4) Consistency with (Mg b – Fe 5015) and (Mg b – σ_0) correlations. (5) Velocity dispersion gradient $\gamma < -0.1$. (6) Central velocity dispersion $\sigma_{r_{e/10}} > 130$ km s^{-1}. (7) Consistency with FPR. (8) Intrinsic shape: either $B/A > 0.85$ & $C/A > 0.4$ or $B/A < 0.85$ & any C/A.

Table 6.7: Classification criteria of disk-like bulges.

Galaxy	Morph. $(\text{I–1})_\text{D}$	n $(\text{I–2})_\text{D}$	Spectral rel. $(\text{I–3})_\text{D}$	Kinematics $(\text{I–4})_\text{D}$		KR $(\text{II–1})_\text{D}$	Line-str. ind. $(\text{II–3})_\text{D}$		FJR $(\text{II–4})_\text{D}$	3D shape
(1)	(2)	(3)	(4)	(5)	(6)	(7)	(8)	(9)	(10)	(11)
NGC 3156			•				•	•		
NGC 3245		•								
NGC 3998								•		
NGC 4249	n.a.	•			•					
NGC 4578										
NGC 4690					•					
NGC 5687	n.a.									
NGC 6149	n.a.			•	•					•
PGC 29321	n.a.	•		n.a.	n.a.			•*		

Notes. Classification criteria of disk-like bulges. (1) Galaxy name. (2) Morphology. (3) Sérsic index $n < 2$. (4) Deviation from (Mg b – Fe 5015) and (Mg b – σ_0) correlations. (5), (6) $\langle v^2 \rangle / \langle \sigma^2 \rangle \geq 0.35$ and velocity dispersion gradient $\gamma \geq -0.1$, respectively. (7) Low surface-brightness outlier from KR. (8), (9) Absorption lines-strength indices (Mg $b < 2.35$ Å Fe 5015 < 3.95 Å). (10) Low-σ outliers from FJR. (11) Intrinsic shape: $B/A > 0.85$ & $C/A < 0.4$.

and stellar populations properties. We considered the previous bulges as classical since the specific criteria they are missing can be controversial.

Firstly, the photometric decomposition reveals that three out of nine of our sample bulges presented a low value of their Sérsic index, namely NGC 3245, NGC4249, and PGC 29321. The Sérsic index is the most extensively adopted criterion to identify distinct bulge types

(e.g., Fisher & Drory 2010; Neumann et al. 2017; Kruk et al. 2018), since the bimodal distribution of n is supposed to separate bulges in classical ($n > 2$) and disk-like ($n < 2$). However, a physical explanation for this bimodality and for the empirical demarcation line $n = 2$ is not well understood yet. Indeed, many authors argued that there is no such bimodality (Graham & Worley 2008; Méndez-Abreu et al. 2018), since the Sérsic index has been shown to be prone to misclassifications. Furthermore, it is now well established that merging events are able to create bulges with $n < 2$ (Eliche-Moral et al. 2011; Querejeta et al. 2015a). Moreover, also low-luminosity elliptical galaxies are well known to present $n < 2$ or even $n \sim 1$ (Davies et al. 1988; Young & Currie 1994). Thus, considering as disk-like a system with low Sérsic index might be confusing and in strong disagreement with the commonly accepted scenario where disk-like bulges are built up from disk material during long-lasting processes.

Secondly, the Mg b and Fe 5015 line-strength indices and their interplay in the (Mg b – Fe 5015) relation are supposed to provide a constraint for the bulge properties. However, the analysis of the spectral properties leads to slightly confused outcomes, mostly inconsistent with other photometric or kinematic parameters. We ascribed this to the heterogeneity of data analysis techniques in measuring the line-strength indices of the comparison sample. Indeed, Fisher & Drory (2016) combined spectral information from both Peletier et al. (2007) and Ganda et al. (2007), even if they measured the strength of the absorption lines within different apertures of fixed size of 1.2- and 1.5-arcsec radius, respectively. Thus, this did not assure a fair comparison of bulge line-strength indices, since the bulge size is not considered. Furthermore, the separation of classical and disk-like bulges in the (Mg b – Fe 5015) and (Mg $b - \sigma_0$) relations was only based on empirical results, once bulges were separated *a priori* due to their morphology and/or Sérsic index in the two different classes. Indeed, we found that the only bulge (i.e., NGC 3156) deviating from the expecting region defined for classical bulges presents $n > 2$, in contrast with the principles under which the relations were built by Fisher & Drory (2016). Moreover, bulges with $n < 2$ are found to be totally compatible with the expected trend of classical bulges.

Finally, since disk-like bulges are supposed to preserve disk properties, their kinematics might be a good indicator of their disky nature. However, we refrained from considering bulges with low velocity dispersion as disk-like bulges. The bulge velocity dispersion

only partially characterizes its dynamical status, being just a good proxy for the mass in dispersion-dominated systems. The fact that only three out of nine bulges in our sample show a central velocity dispersion $\sigma_{r_e/10} > 130$ km s^{-1} did not actually ruled out the possibility of finding more classical bulges. For this reasons, we argued that a combination of the velocity dispersion with the rotational support of the bulge, that is, the $\langle v^2 \rangle / \langle \sigma^2 \rangle$ parameter, defines the bulge dynamical status in a much more reliable way. The bulge in NGC 6149 is the only bulge in our sample that presents $\langle v^2 \rangle / \langle \sigma^2 \rangle > 0.35$.

The position of the sample bulges in the fundamental scaling relations confirmed the interpretation presented in Section 4.6. A single population of galaxy spheroids that follow the same scaling relations seems to populate the FPR and FJR (Fig. 6.7 and 6.8). In this scenario, we argued that the mass seems to be responsible for a smooth transition in the photometric and kinematic properties from less to more massive bulges.

6.7.2 Classical vs disk-like bulges: intrinsic shape and dynamical status

As commented before, the Sérsic index is not a good proxy for separating bulges. Since it is a projected photometric quantity, it is not clear whether it should show a relation with the stellar kinematics (Méndez-Abreu et al. 2018). It is worth noting that the failure of the photometric n and the kinematic $\langle v^2 \rangle / \langle \sigma^2 \rangle$ diagnostics in identifying the same bulge type in our sample is not surprising. Méndez-Abreu et al. (2018) demonstrated that regardless of projection effects, there is no statistically significant relation between either the Sérsic index (or B/T), and the stellar angular momentum (i.e., v/σ) of bulges in their sample of 28 lenticular galaxies. This lack of correlation was previously highlighted by Falcón-Barroso et al. (2003), who studied a sample of 19 early-type disk galaxies arguing that the Sérsic index was not related to the central gradient of the velocity dispersion. Furthermore, Tabor et al. (2017) have recently take advantage of the CALIFA survey to perform a spectro-photometric bulge to disk decomposition of three galaxies, showing that despite the stellar kinematics of these bulges with Sérsic index $n \sim 1$ shows some rotation, they are considered as dispersion-dominated systems due to their high velocity dispersion values. On the contrary, Fabricius et al. (2012) claimed that low Sérsic index bulges have increased rotational support, in favor of an alike dichotomy in both purely kinematic and Sérsic index diagnostics.

Finally, Tables 6.6 and 6.7 demonstrate how the so far proposed criteria can sometimes work on classifying classical bulges, but they fail to classify disk-like bulges, generally producing an overestimation of this bulge type. We studied the bulge three-dimensional shape that, despite its uncertainties, provides an intrinsic property of the bulge. Using the intrinsic shape and considering a disk as a flattened oblate spheroid, we argued that only the bulge of NGC 6149 could lie in this category. This result is completely in agreement with its dynamical status, being the only bulge also exhibiting the disk kinematics. Thus, we considered the intrinsic shape as the most reliable mechanism to separate disk-like bulges from classical bulges. The remaining four bulges (i.e., NGC 3156, NGC 4249, NGC 4690, PGC 29321) result hard to classify, but following the relation between the intrinsic shape and the stellar kinematics we considered them to be probably classical.

We considered the results of our analysis as a benchmark for computing the actual number density of disk-like bulges in the nearby Universe. Indeed, a proper combination of the intrinsic shape and dynamical status information is critical to confirm the disk nature of galactic bulges.

■ 6.8 Conclusions

We fully characterized the photometric and spectroscopic properties of a sample of bulges in nine lenticular galaxies from the ATLAS^{3D} survey to discuss the observational definition of classical and disk-like bulges given by Fisher & Drory (2016).

We obtained the photometric structural parameters applying a two-dimensional photometric decomposition on the SDSS i-band images of the sample galaxies. We argued that the bulge Sérsic index is a poor tool to discriminate the different bulge types, as already highlighted in different works. We derived the three-dimensional shape of each bulge using our statistical approach, calculating also the probability of having an oblate spheroid with $C/A < 0.5$ and $C/A < 0.4$. This allowed us to statistically characterize their intrinsic flattening.

Furthermore, we derived both the kinematic (σ, $\langle v^2 \rangle / \langle \sigma^2 \rangle$, and γ) and spectral (Mg b and Fe 5015) diagnostics of our sample bulges within different apertures. We combined the line-strength indices in the (Mg b – Fe 5015) relation and together with the velocity dispersion

in the (Mg $b - \sigma_0$) relation to study possible deviation of our sample bulges. We found that the kinematic and line-strength indices of the sample bulges provide no clear identification of the bulge type. This remains true also when comparing the results obtained from the line-strength indices with those from the photometric analysis. However, the $\langle v^2 \rangle / \langle \sigma^2 \rangle$ value seems to agree with our definition of disk-like bulges based on their intrinsic shape. It describes the bulge dynamics in a reliable way, whereas we argued that the central velocity dispersion do not characterize the dynamical status of the bulge, being just a good proxy for the mass in dispersion-dominated systems. We found that NGC 6149 hosts the only bulge exhibiting disk kinematics and flattened three-dimensional shape.

We concluded that the common practice of applying the observational criteria for distinguishing bulge types, based on *a priori* classification according to their morphology and/or Sérsic index, has to be carefully reconsidered. We remarked that, even if the different observational characteristics look well motivated in terms of distinct formation paths, their interplay might result in contradictory outcomes. Indeed, we proposed to characterize the disk-like bulges in terms of their intrinsic shape and dynamical status as the most reliable way to separate them from the classical bulges.

7

CONCLUSIONS

This thesis aimed to shed some light on the nature of galactic bulges in nearby galaxies through an extensive study of their observational properties, in order to understand how they form and evolve. The current observational picture of galactic bulges divides these systems into two broad classes, namely classical and disk-like bulges, according to the photometric, kinematic, and stellar population properties which result from their different assembly histories. Indeed, classical bulges can be formed via dissipative collapse of protogalactic gas clouds or by the coalescence of giant clumps in primordial disks. Moreover, they could also grow out of disk material triggered by satellite accretion during minor merging events or by galaxy mergers with different merger histories. Thus, these systems are supposed to be more rounder than their surrounding disks, with their kinematics dominated by the velocity dispersion of the stellar component. On the other hand, disk-like bulges are thought to be the products of secular processes driven by bars. Nevertheless, disk-like bulges might also be created by the secular accretion of low-density satellites into the main galaxy, providing an alternative to their bar-driven growth. Therefore, since these bulges are supposed to preserve disk properties, their intrinsic shape and kinematics might be a good proxy of their disky nature. In this scenario, the proper combination of photometric and kinematic information results crucial to disentangle bulges into classical or disk-like. Indeed, throughout this thesis we had presented a series of new results covering the most important topics of extragalactic astronomy, like the photometry, structure, kinematics, scaling relations, and intrinsic shape of individual bulges.

At the beginning of this thesis, we defined the bulge as the extra component dominating the central galaxy light above the inner surface-brightness profile of the disk. Thus, we applied the GASP2D algorithm to provide a detailed description of the bulge component in nearby galaxies in terms of its photometric properties. Our meticulous multi-component photometric decomposition allowed us to consequently derive the three-dimensional shape of nearby bulges, using the galaXYZ code. At last, we proposed that the intrinsic shape is the most reliable diagnostic of the bulge nature, once combined with its dynamical status.

7.1 Summary of the main results

The conclusions of this thesis can be summarized in four major points:

- *An exhaustive photometric description of the galaxy structures is critical to properly deal with their kinematic, stellar population, and intrinsic shape information.*

Chapter 3. We introduced the multi-component photometric decomposition of 404 galaxies from the CALIFA DR3 survey. We derived the bar fraction (57%) in our volume corrected sample, explored the frequency of different disk types (62% Type I, 28% Type II, and 10% Type III), and analyzed the incidence of pure disks and/or small unresolved bulges, unveiling a clear segregation of the structural composition of galaxies according to stellar mass. We contributed to build up the perfect framework to deal with the IFS information provided by the CALIFA survey, meticulously describing the multiple stellar structures (i.e., bulges, bars, and disks) shaping the CALIFA galaxies. Our photometric analysis allowed to accurately study the mechanisms responsible for generating the spiral structures (Sánchez-Menguiano et al. 2016), investigate the role of stellar radial migration (Ruiz-Lara et al. 2017), present a new galaxy classification system based on the shapes and amplitudes of their CVCs (Kalinova et al. 2017), estimate the current extinction-corrected Hα SFR of the different galaxy components (bulges, bars, and disks), and deeply study the relation between morphology and kinematics of bulges in lenticular galaxies (Méndez-Abreu et al. 2018).

- *All bulges can be described as a single population of galactic spheroids that follow the same scaling relations, where only their mass seems to lead to a smooth transition in the*

photometric and kinematic properties from less to more massive bulges and elliptical galaxies.

Chapter 4. We analyzed the photometric structural parameters and stellar kinematics of a sample of small bulges in late-type spiral galaxies. We investigated whether small bulges follow the same scaling relations traced by elliptical galaxies and large bulges, pushing the limits of scaling relations to the smaller systems and low-σ regime studied so far. We confirmed that the Kormendy relation is a poor indicator of the bulge properties due to the large intrinsic scatter and magnitude bias. Furthermore, our small bulges with resolved velocity dispersion did not follow the expected down-bending of the fundamental plane and Faber-Jackson relations, but trace the same trend as elliptical galaxies and large bulges. We suggested that the bulge properties strongly depend on the mass of the system rather than on the morphology of the host galaxy.

- *Disruptive processes such as merging events and dissipative collapse could be the prevalent responsible for driving the formation and evolution of most massive bulges in our CALIFA sample. Moreover, different pathways can coexist in the same galaxy, noticeably in less massive bulges, where the bar seems to reshape low-mass triaxial bulges.*

Chapter 5. We fully characterized the three-dimensional shape of 83 bulges of nearby galaxies from CALIFA DR3. Using a set of simulated galaxies resulting from merger experiments, we realized that our approach is able to successfully constrain the bulge intrinsic shape when the galaxy inclination is $25^\circ < \theta < 65^\circ$. We unveiled that bulges with a small Sérsic index could be equally axisymmetric or triaxial ellipsoids, while most of the bulges with larger Sérsic index are mostly oblate spheroids. The same trend is also valid when the B/T luminosity ratio is considered. Moreover, less massive bulges and bulges in late-type galaxies are characterized by heterogeneous intrinsic shapes, while more massive bulges and bulges in lenticular galaxies are mostly oblate. Finally, we observed the majority of triaxial bulges in barred galaxies. Our results have imposed further limitations on forthcoming numerical simulations and may help to disentangle different formation pathways for bulges.

- *The three-dimensional shape of the bulge, combined with its dynamical status, is the most suitable diagnostic for unveiling disk-like spheroids as those systems that built-up*

from disk material in long-lasting processes.

Chapter 6. We discussed the observational criteria to classify galactic bulges, which have been recently revised by Fisher & Drory (2016) and are widely adopted in the literature. We derived the photometric, kinematic, and stellar population properties of bulges in nine lenticular galaxies from the ATLAS^{3D} survey. Moreover, we derived the probability distribution of B/A and C/A of our sample bulges. We argued that the Sérsic index is prone to misclassify bulge types, as well as the bulge central velocity dispersion. We stressed that a combination of the velocity dispersion with the rotational support of the bulge identifies its dynamical status in a much more reliable way. Furthermore, we found that the combination of kinematic properties and line-strength indices of the sample bulges provides contradictory identifications in 45% of the cases. We proposed to characterize disk-like bulges in terms of their intrinsic shape and dynamical status as the most reliable way to separate them from classical bulges. We concluded that the common practice of applying the observational criteria for distinguishing bulge types, based on *a priori* classification according to their morphology or Sérsic index, has to be carefully reconsidered.

7.2 Future perspective

Some of the results presented in this thesis have been already considered as starting point for a number of new projects. They will focus on the central regions of spiral galaxies at the end of the Hubble sequence, in order to address open questions regarding (1) the frequency of bulgeless galaxies and (2) formation and evolution of small bulges in nearby galaxies. To date the study of these topics has been affected by the limited spatial and spectral resolution of the available observations. New and forthcoming high-resolution IFSs will allow to overcome the present lack of knowledge in characterizing late-type galaxies combining photometric and spectroscopic information with the analysis of the intrinsic shape of their central regions.

7.2.1 Bulgeless galaxies

The Hubble classification scheme tells us that spiral galaxies go from early to late types according to their B/T luminosity ratio. At the end of the Hubble sequence, we find pure

disk galaxies with a small or no bulge component. Although bulgeless spiral galaxies are the simplest disk galaxies in terms of structure and dynamics, the role of the different physical processes driving their formation and evolution is not fully understood yet. Numerical simulations with a high rate of mergers as expected in the hierarchical scenarios can not completely explain the existence of disk-dominated galaxies with little or no bulge (Kautsch et al. 2006; Weinzirl et al. 2009). Thus, we may wonder if any fundamental information (especially from the observational point of view) is missing when we try to characterize these intriguing systems.

The current definition of bulgeless galaxies is based only on photometric considerations (i.e., the lack of a photometric bulge). Thus, we have to extend our knowledge of these poorly studied systems including kinematics and dynamics. This can be done unveiling the absence of hot dynamical components (e.g., small bulges and kinematically-distinct structures) in the central regions of these pure-disk galaxies. The amount of data already collected with recent integral-field facilities (e.g., MUSE, SAMI, MaNGA, etc.) will be the ideal starting point for developing the analysis of these challenging systems by combining for the first time photometric, kinematic, and dynamical information. Indeed, Schwarzschild dynamical models has been recently applied for the first time on late-type galaxies of the CALIFA survey (Zhu et al. 2018). A comprehensive understanding of photometry, high-resolution kinematics, and dynamics will finally help to bridge the gap between observations and simulations.

7.2.2 Small bulges in late-type galaxies

We have seen that the current paradigm separates galactic bulges into two main categories, namely classical and disk-like bulges. The demarcation line that separates these systems becomes really blurred moving to extremely late-type galaxies, making it challenging to understand the actual frequency of different bulge types. Since both types are thought to be produced by different physical mechanisms, understanding their incidence in local galaxies is crucial to develop a complete picture about galaxy evolution in general. We have to push the limit of scaling relations known so far to the very end of the Hubble sequence, studying the photometric and kinematic properties of small bulges in the low-mass and low-σ regime. Moreover, deriving the intrinsic shape of small bulges in late-type galaxies will be possible

to study correlations with their observed properties.

Recently, I have been awarded telescope time at DOLORES/TNG (proposal ID: TNG011/ 2018A) to follow up the investigation of a larger sample of extremely late-type galaxies. This will allow us to substantially improve the statistical significance of the sample analyzed in this thesis and to provide a more complete view of small bulges properties. This will be done by fully characterizing not only the two-dimensional light distribution of these bulges, but also their kinematics with appropriate spectral and spatial resolution. Improving our knowledge of physical processes ongoing in the central regions of extremely late-type objects is critical for understanding the interplay of galactic structures that coexist in the same galaxy (e.g., composite bulges), discerning the relative importance they have in driving the galaxy evolution.

Finally, we have to characterize for the first time the possible coexistence of different bulge types in late-type galaxies. Indeed, it is already established both theoretically (Athanassoula 2005) and observationally (Méndez-Abreu et al. 2014), that classical and disk-like bulges can coexist in the same galaxy. Late-type galaxies offer an unexplored field for disentangling the coexistence of galactic structures.

In the next few years, these challenging objectives will take advantage of the use of front-line instrumentation mounted at E-ELT and JWST. They will grant outstanding levels of spatial and spectral resolution, allowing to distinguish galactic substructures over a wider redshift range. Indeed, the fair comparison of the observed properties of bulges over time is needed to fully understand how the galaxy potential wells responded to different formation histories. Thus, we will provide the statistical benchmark for understanding the mechanisms of galaxy formation and evolution at the unexplored end of the Hubble sequence.

BIBLIOGRAPHY

Abadi, M. G., Navarro, J. F., Steinmetz, M., & Eke, V. R. 2003, ApJ, 591, 499

Abazajian, K. N., Adelman-McCarthy, J. K., Agüeros, M. A., et al. 2009, ApJS, 182, 543

Abraham, R. G., van den Bergh, S., Glazebrook, K., et al. 1996, ApJS, 107, 1

Abramowitz, M. & Stengun, I. 1964, Handbook of Mathematical Functions (Dover, New York)

Aceves, H., Velázquez, H., & Cruz, F. 2006, MNRAS, 373, 632

Adelman-McCarthy, J. K., Agüeros, M. A., Allam, S. S., et al. 2008, ApJS, 175, 297

Aguerri, J. A. L. 2012, Advances in Astronomy, 2012, 382674

Aguerri, J. A. L., Balcells, M., & Peletier, R. F. 2001, A&A, 367, 428

Aguerri, J. A. L., Elias-Rosa, N., Corsini, E. M., & Muñoz-Tuñón, C. 2005, A&A, 434, 109

Aguerri, J. A. L., Iglesias-Paramo, J., Vilchez, J. M., & Muñoz-Tuñón, C. 2004, AJ, 127, 1344

Aguerri, J. A. L., Méndez-Abreu, J., & Corsini, E. M. 2009, A&A, 495, 491

Ahn, C. P., Alexandroff, R., Allende Prieto, C., et al. 2012, ApJS, 203, 21

Aihara, H., Allende Prieto, C., An, D., et al. 2011, ApJS, 193, 29

Akaike, H. 1974, IEEE Trans Aut Cont, 19, 716

Allen, P. D., Driver, S. P., Graham, A. W., et al. 2006, MNRAS, 371, 2

Amorín, R. O., Muñoz-Tuñón, C., Aguerri, J. A. L., Cairós, L. M., & Caon, N. 2007, A&A, 467, 541

Andredakis, Y. C. 1998, MNRAS, 295, 725

Andredakis, Y. C., Peletier, R. F., & Balcells, M. 1995, MNRAS, 275, 874

Arp, H. 1965, ApJ, 141, 43

Athanassoula, E. 2005, MNRAS, 358, 1477

Athanassoula, E. 2013, in Secular Evolution of Galaxies, ed. J. Falcón-Barroso & J. H. Knapen (Cambridge University Press, Cambridge, UK), 305

Athanassoula, E., Machado, R. E. G., & Rodionov, S. A. 2013, MNRAS, 429, 1949

Athanassoula, E., Morin, S., Wozniak, H., et al. 1990, MNRAS, 245, 130

Aumer, M., Burkert, A., Johansson, P. H., & Genzel, R. 2010, ApJ, 719, 1230

Azzollini, R., Trujillo, I., & Beckman, J. E. 2008, ApJ, 684, 1026

Bacon, R., Copin, Y., Monnet, G., et al. 2001, MNRAS, 326, 23

Balcells, M., Graham, A. W., & Peletier, R. F. 2007, ApJ, 665, 1104

Barazza, F. D., Jogee, S., & Marinova, I. 2008, ApJ, 675, 1194

Barentine, J. C. & Kormendy, J. 2012, ApJ, 754, 140

Barnes, J. E. & Hernquist, L. E. 1991, ApJ, 370, L65

Barway, S., Wadadekar, Y., Vaghmare, K., & Kembhavi, A. K. 2013, MNRAS, 432, 430

Baugh, C. M., Cole, S., Frenk, C. S., & Lacey, C. G. 1998, ApJ, 498, 504

Bender, R., Burstein, D., & Faber, S. M. 1992, ApJ, 399, 462

Bender, R. & Moellenhoff, C. 1987, A&A, 177, 71

Benítez, E., Méndez-Abreu, J., Fuentes-Carrera, I., et al. 2013, ApJ, 763, 136

Bernardi, M., Roche, N., Shankar, F., & Sheth, R. K. 2011a, MNRAS, 412, 684

Bernardi, M., Roche, N., Shankar, F., & Sheth, R. K. 2011b, MNRAS, 412, L6

Bernardi, M., Sheth, R. K., Annis, J., et al. 2003a, AJ, 125, 1817

Bernardi, M., Sheth, R. K., Annis, J., et al. 2003b, AJ, 125, 1866

Bertelli, G., Bressan, A., Chiosi, C., Fagotto, F., & Nasi, E. 1994, A&AS, 106

Bertin, E. & Arnouts, S. 1996, A&AS, 117, 393

Bertola, F., Bettoni, D., Danziger, J., et al. 1991a, ApJ, 373, 369

Bertola, F. & Capaccioli, M. 1975, ApJ, 200, 439

Bertola, F. & Galletta, G. 1979, A&A, 77, 363

Bertola, F., Vietri, M., & Zeilinger, W. W. 1991b, ApJ, 374, L13

Bevington, P. R. & Robinson, D. K. 2003, Data Reduction and Error Analysis for the Physical Sciences (McGraw-Hill, Boston)

Binggeli, B. & Jerjen, H. 1998, A&A, 333, 17

Binney, J. 2005, MNRAS, 363, 937

Blanton, M. R., Hogg, D. W., Bahcall, N. A., et al. 2003, ApJ, 592, 819

Blumenthal, G. R., Faber, S. M., Primack, J. R., & Rees, M. J. 1984, Nature, 311, 517

Böker, T., Laine, S., van der Marel, R. P., et al. 2002, AJ, 123, 1389

Böker, T., Stanek, R., & van der Marel, R. P. 2003, AJ, 125, 1073

Borlaff, A., Eliche-Moral, M. C., Rodríguez-Pérez, C., et al. 2014, A&A, 570, A103

Bournaud, F. 2016, in Galactic Bulges, ed. E. Laurikainen, R. Peletier, & D. Gadotti (Springer, Berlin), 355

Bournaud, F., Combes, F., & Jog, C. J. 2004, A&A, 418, L27

Brooks, A. & Christensen, C. 2016, in Galactic Bulges, ed. E. Laurikainen, R. Peletier, & D. Gadotti (Springer, Berlin), 317

Bruzual, G. & Charlot, S. 2003, MNRAS, 344, 1000

Burbidge, E. M. & Burbidge, G. R. 1959, ApJ, 130, 20

Burbidge, E. M. & Burbidge, G. R. 1962, ApJ, 135, 694

Bureau, M., Aronica, G., Athanassoula, E., et al. 2006, MNRAS, 370, 753

Bureau, M. & Athanassoula, E. 2005, ApJ, 626, 159

Buta, R., Laurikainen, E., Salo, H., & Knapen, J. H. 2010, ApJ, 721, 259

Buta, R. J., Sheth, K., Athanassoula, E., et al. 2015, ApJS, 217, 32

Caon, N., Cairós, L. M., Aguerri, J. A. L., & Muñoz-Tuñón, C. 2005, ApJS, 157, 218

Caon, N., Capaccioli, M., & D'Onofrio, M. 1993, MNRAS, 265, 1013

Capaccioli, M., Held, E. V., & Nieto, J.-L. 1987, AJ, 94, 1519

Cappellari, M. 2002, MNRAS, 333, 400

Cappellari, M. & Copin, Y. 2003, MNRAS, 342, 345

Cappellari, M. & Emsellem, E. 2004, PASP, 116, 138

Cappellari, M., Emsellem, E., Krajnović, D., et al. 2011, MNRAS, 413, 813

Cappellari, M., Scott, N., Alatalo, K., et al. 2013, MNRAS, 432, 1709

Carollo, C. M., Ferguson, H. C., & Wyse, R. F. G. 1999, The Formation of Galactic Bulges (Cambridge University Press, Cambridge)

Carollo, C. M., Stiavelli, M., de Zeeuw, P. T., & Mack, J. 1997, AJ, 114, 2366

Carollo, C. M., Stiavelli, M., & Mack, J. 1998, AJ, 116, 68

Carter, D. 1978, MNRAS, 182, 797

Catalán-Torrecilla, C., Gil de Paz, A., Castillo-Morales, A., et al. 2017, ApJ, 848, 87

Ceverino, D., Dekel, A., Tweed, D., & Primack, J. 2015, MNRAS, 447, 3291

Chabrier, G. 2003, PASP, 115, 763

Chilingarian, I. V., Di Matteo, P., Combes, F., Melchior, A.-L., & Semelin, B. 2010, A&A, 518, A61

Chung, A. & Bureau, M. 2004, AJ, 127, 3192

Coelho, P. & Gadotti, D. A. 2011, ApJ, 743, L13

Cole, S., Lacey, C. G., Baugh, C. M., & Frenk, C. S. 2000, MNRAS, 319, 168

Combes, F. & Sanders, R. H. 1981, A&A, 96, 164

Conselice, C. J. 2003, ApJS, 147, 1

Corsini, E. M., Aguerri, J. A. L., Debattista, V. P., et al. 2007, ApJ, 659, L121

Corsini, E. M., Méndez-Abreu, J., Pastorello, N., et al. 2012, MNRAS, 423, L79

Corsini, E. M., Wegner, G. A., Thomas, J., Saglia, R. P., & Bender, R. 2017, MNRAS, 466, 974

Costantin, L., Méndez-Abreu, J., Corsini, E. M., et al. 2018, A&A, in press (arXiv: 1710.05222)

Costantin, L., Méndez-Abreu, J., Corsini, E. M., et al. 2017, A&A, 601, A84

Cowie, L. L., Songaila, A., Hu, E. M., & Cohen, J. G. 1996, AJ, 112, 839

Cox, T. J., Dutta, S. N., Di Matteo, T., et al. 2006a, ApJ, 650, 791

Cox, T. J., Jonsson, P., Primack, J. R., & Somerville, R. S. 2006b, MNRAS, 373, 1013

Daddi, E., Bournaud, F., Walter, F., et al. 2010, ApJ, 713, 686

Dasyra, K. M., Tacconi, L. J., Davies, R. I., et al. 2007, ApJ, 657, 102

Davies, J. I., Phillipps, S., Cawson, M. G. M., Disney, M. J., & Kibblewhite, E. J. 1988, MNRAS, 232, 239

de Lorenzo-Cáceres, A., Falcón-Barroso, J., & Vazdekis, A. 2013, MNRAS, 431, 2397

de Lorenzo-Cáceres, A., Vazdekis, A., Aguerri, J. A. L., Corsini, E. M., & Debattista, V. P. 2012, MNRAS, 420, 1092

de Souza, R. E., Gadotti, D. A., & dos Anjos, S. 2004, ApJS, 153, 411

de Vaucouleurs, G. 1948, Annales d'Astrophysique, 11, 247

Debattista, V. P., Carollo, C. M., Mayer, L., & Moore, B. 2004, ApJ, 604, L93

Dekel, A., Sari, R., & Ceverino, D. 2009, ApJ, 703, 785

Di Matteo, P., Bournaud, F., Martig, M., et al. 2008, A&A, 492, 31

Di Matteo, P., Combes, F., Melchior, A.-L., & Semelin, B. 2007, A&A, 468, 61

Di Matteo, T., Springel, V., & Hernquist, L. 2005, Nature, 433, 604

Djorgovski, S. & Davis, M. 1987, ApJ, 313, 59

D'Onofrio, M., Fasano, G., Varela, J., et al. 2008, ApJ, 685, 875

Dressler, A., Lynden-Bell, D., Burstein, D., et al. 1987, ApJ, 313, 42

Driver, S. P., Andrews, S. K., da Cunha, E., et al. 2017, MNRAS, in press (arXiv: 1710.06628)

Drory, N. & Fisher, D. B. 2007, ApJ, 664, 640

Dwek, E., Arendt, R. G., Hauser, M. G., et al. 1995, ApJ, 445, 716

Eggen, O. J. 1962, Royal Greenwich Obs Bul, 51, 79

Eggen, O. J., Lynden-Bell, D., & Sandage, A. R. 1962, ApJ, 136, 748

Eliche-Moral, M. C., Balcells, M., Aguerri, J. A. L., & González-García, A. C. 2006, A&A, 457, 91

Eliche-Moral, M. C., González-García, A. C., Balcells, M., et al. 2011, A&A, 533, A104

Eliche-Moral, M. C., Prieto, M., Gallego, J., et al. 2010, A&A, 519, A55

Elmegreen, B. G., Bournaud, F., & Elmegreen, D. M. 2008, ApJ, 688, 67

Elmegreen, D. M. & Elmegreen, B. G. 1982, MNRAS, 201, 1021

Elmegreen, D. M. & Elmegreen, B. G. 1987, ApJ, 314, 3

Elmegreen, D. M., Elmegreen, B. G., Ravindranath, S., & Coe, D. A. 2007, ApJ, 658, 763

Emsellem, E., Cappellari, M., Krajnović, D., et al. 2011, MNRAS, 414, 888

Emsellem, E., Cappellari, M., Krajnović, D., et al. 2007, MNRAS, 379, 401

Emsellem, E., Cappellari, M., Peletier, R. F., et al. 2004, MNRAS, 352, 721

Erwin, P. 2004, A&A, 415, 941

Erwin, P. 2015, ApJ, 799, 226

Erwin, P., Beckman, J. E., & Pohlen, M. 2005, ApJ, 626, L81

Erwin, P., Beltrán, J. C. V., Graham, A. W., & Beckman, J. E. 2003, ApJ, 597, 929

Erwin, P. & Debattista, V. P. 2013, MNRAS, 431, 3060

Erwin, P., Pohlen, M., & Beckman, J. E. 2008, AJ, 135, 20

Erwin, P., Saglia, R. P., Fabricius, M., et al. 2015, MNRAS, 446, 4039

Erwin, P. & Sparke, L. S. 2002, AJ, 124, 65

Eskridge, P. B., Frogel, J. A., Pogge, R. W., et al. 2000, AJ, 119, 536

Faber, S. M. & Jackson, R. E. 1976, ApJ, 204, 668

Fabricius, M. H., Saglia, R. P., Fisher, D. B., et al. 2012, ApJ, 754, 67

Falcón-Barroso, J., Balcells, M., Peletier, R. F., & Vazdekis, A. 2003, A&A, 405, 455

Falcón-Barroso, J., Lyubenova, M., van de Ven, G., et al. 2017, A&A, 597, A48

Falcón-Barroso, J., Peletier, R. F., & Balcells, M. 2002, MNRAS, 335, 741

Falcón-Barroso, J., van de Ven, G., Peletier, R. F., et al. 2011, MNRAS, 417, 1787

Fall, S. M. & Efstathiou, G. 1980, MNRAS, 193, 189

Fathi, K. & Peletier, R. F. 2003, A&A, 407, 61

Ferrers, N. M. 1877, Quart. J. Pure Appl. Math, 14, 1

Fisher, D. B. & Drory, N. 2008, AJ, 136, 773

Fisher, D. B. & Drory, N. 2010, ApJ, 716, 942

Fisher, D. B. & Drory, N. 2016, in Galactic Bulges, ed. E. Laurikainen, R. Peletier, & D. Gadotti (Springer, Berlin), 41

Förster Schreiber, N. M., Shapley, A. E., Genzel, R., et al. 2011, ApJ, 739, 45

Foster, C., van de Sande, J., D'Eugenio, F., et al. 2017, MNRAS, 472, 966

Freeman, K. C. 1966, MNRAS, 133, 47

Freeman, K. C. 1970, ApJ, 160, 811

Friedli, D. & Benz, W. 1995, A&A, 301, 649

Fu, Y. N., Huang, J. H., & Deng, Z. G. 2003, MNRAS, 339, 442

Fukugita, M., Hogan, C. J., & Peebles, P. J. E. 1998, ApJ, 503, 518

Gadotti, D. A. 2008, MNRAS, 384, 420

Gadotti, D. A. 2009, MNRAS, 393, 1531

Ganda, K., Peletier, R. F., McDermid, R. M., et al. 2007, MNRAS, 380, 506

García-Benito, R., Zibetti, S., Sánchez, S. F., et al. 2015, A&A, 576, A135

Genel, S., Naab, T., Genzel, R., et al. 2012, ApJ, 745, 11

Genzel, R., Burkert, A., Bouché, N., et al. 2008, ApJ, 687, 59

Gerhard, O. E. 1993, MNRAS, 265, 213

Gomes, J. M., Papaderos, P., Vílchez, J. M., et al. 2016, A&A, 585, A92

Governato, F., Mayer, L., Wadsley, J., et al. 2004, ApJ, 607, 688

Governato, F., Willman, B., Mayer, L., et al. 2007, MNRAS, 374, 1479

Graham, A. W., Driver, S. P., Petrosian, V., et al. 2005, AJ, 130, 1535

Graham, A. W. & Guzmán, R. 2003, AJ, 125, 2936

Graham, A. W. & Worley, C. C. 2008, MNRAS, 388, 1708

Gratton, R. G. & Ortolani, S. 1988, A&AS, 73, 137

Green, E. M. & Norris, J. E. 1990, ApJ, 353, L17

Guérou, A., Emsellem, E., McDermid, R. M., et al. 2015, ApJ, 804, 70

Gutiérrez, L., Erwin, P., Aladro, R., & Beckman, J. E. 2011, AJ, 142, 145

Hamabe, M. & Kormendy, J. 1987, in IAU Symposium, Vol. 127, Structure and Dynamics of Elliptical Galaxies, ed. P. T. de Zeeuw (D. Reidel Pub, Dordrecht), 379

Hasan, H., Pfenniger, D., & Norman, C. 1993, ApJ, 409, 91

Häußler, B., Bamford, S. P., Vika, M., et al. 2013, MNRAS, 430, 330

Head, J. T. C. G., Lucey, J. R., Hudson, M. J., & Smith, R. J. 2014, MNRAS, 440, 1690

Hernquist, L. & Barnes, J. E. 1991, Nature, 354, 210

Hinojosa-Goñi, R., Muñoz-Tuñón, C., & Méndez-Abreu, J. 2016, A&A, 592, A122

Hopkins, P. F., Cox, T. J., Younger, J. D., & Hernquist, L. 2009, ApJ, 691, 1168

Hopkins, P. F., Kereš, D., Murray, N., Quataert, E., & Hernquist, L. 2012, MNRAS, 427, 968

Hubble, E. 1943, ApJ, 97, 112

Hubble, E. P. 1926, ApJ, 64

Huertas-Company, M., Aguerri, J. A. L., Bernardi, M., Mei, S., & Sánchez Almeida, J. 2011, A&A, 525, A157

Husemann, B., Jahnke, K., Sánchez, S. F., et al. 2013, A&A, 549, A87

Hyde, J. B. & Bernardi, M. 2009, MNRAS, 394, 1978

Illingworth, G. 1977, ApJ, 218, L43

Immeli, A., Samland, M., Gerhard, O., & Westera, P. 2004a, A&A, 413, 547

Immeli, A., Samland, M., Westera, P., & Gerhard, O. 2004b, ApJ, 611, 20

Inoue, S. & Saitoh, T. R. 2012, MNRAS, 422, 1902

Jablonka, P., Gorgas, J., & Goudfrooij, P. 2007, A&A, 474, 763

Jarvis, B. J. 1986, AJ, 91, 65

Jedrzejewski, R. I. 1987, MNRAS, 226, 747

Jesseit, R., Naab, T., Peletier, R. F., & Burkert, A. 2007, MNRAS, 376, 997

Jorgensen, I., Franx, M., & Kjaergaard, P. 1996, MNRAS, 280, 167

Kalinova, V., Colombo, D., Rosolowsky, E., et al. 2017, MNRAS, 469, 2539

Kauffmann, G., White, S. D. M., & Guiderdoni, B. 1993, MNRAS, 264, 201

Kautsch, S. J. 2009, PASP, 121, 1297

Kautsch, S. J., Grebel, E. K., Barazza, F. D., & Gallagher, III, J. S. 2006, A&A, 445, 765

Kaviraj, S., Tan, K.-M., Ellis, R. S., & Silk, J. 2011, MNRAS, 411, 2148

Kent, S. M. 1986, AJ, 91, 1301

Khochfar, S., Emsellem, E., Serra, P., et al. 2011, MNRAS, 417, 845

Kim, K., Oh, S., Jeong, H., et al. 2016, ApJS, 225, 6

Kim, T., Gadotti, D. A., Sheth, K., et al. 2014, ApJ, 782, 64

Kormendy, J. 1977, ApJ, 217, 406

Kormendy, J. 1979, ApJ, 227, 714

Kormendy, J. 1985, ApJ, 295, 73

Kormendy, J. 1993, in IAU Symposium, Vol. 153, Galactic Bulges, ed. H. Dejonghe & H. J. Habing (Kluwer Acad Pub, Dordrecht), 209

Kormendy, J. 2016, in Galactic Bulges, ed. E. Laurikainen, R. Peletier, & D. Gadotti (Springer, Berlin), 431

Kormendy, J. & Barentine, J. C. 2010, ApJ, 715, L176

Kormendy, J., Bender, R., & Bower, G. 2002, in ASP Conf Ser, Vol. 273, The Dynamics, Structure & History of Galaxies: A Workshop in Honour of Professor Ken Freeman, ed. G. S. Da Costa, E. M. Sadler, & H. Jerjen (ASP, San Francisco, CA), 29

Kormendy, J. & Bruzual, A. G. 1978, ApJ, 223, L63

Kormendy, J. & Cornell, M. E. 2004, in Astrophysics and Space Science Library, Vol. 319, Penetrating Bars Through Masks of Cosmic Dust, ed. D. L. Block, I. Puerari, K. C. Freeman, R. Groess, & E. K. Block (Kluwer Acad Pub, Dordrecht), 261

Kormendy, J., Drory, N., Bender, R., & Cornell, M. E. 2010, ApJ, 723, 54

Kormendy, J., Fisher, D. B., Cornell, M. E., & Bender, R. 2009, ApJS, 182, 216

Kormendy, J. & Illingworth, G. 1982, ApJ, 256, 460

Kormendy, J. & Kennicutt, Jr., R. C. 2004, ARAA, 42, 603

Krajnović, D., Bacon, R., Cappellari, M., et al. 2008, MNRAS, 390, 93

Krajnović, D., Emsellem, E., Cappellari, M., et al. 2011, MNRAS, 414, 2923

Kruk, S. J., Lintott, C. J., Bamford, S. P., et al. 2018, MNRAS, 473, 4731

Kuijken, K. & Merrifield, M. R. 1995, ApJ, 443, L13

Kuntschner, H., Emsellem, E., Bacon, R., et al. 2010, MNRAS, 408, 97

La Barbera, F., Busarello, G., Merluzzi, P., Massarotti, M., & Capaccioli, M. 2003, ApJ, 595, 127

La Barbera, F., de Carvalho, R. R., de La Rosa, I. G., & Lopes, P. A. A. 2010, MNRAS, 408, 1335

Lackner, C. N. & Gunn, J. E. 2012, MNRAS, 421, 2277

Laine, J., Laurikainen, E., Salo, H., et al. 2014, MNRAS, 441, 1992

Laine, S., Shlosman, I., Knapen, J. H., & Peletier, R. F. 2002, ApJ, 567, 97

Lake, G. & Dressler, A. 1986, ApJ, 310, 605

Lauer, T. R., Faber, S. M., Gebhardt, K., et al. 2005, AJ, 129, 2138

Laurikainen, E. & Salo, H. 2016, in Galactic Bulges, ed. E. Laurikainen, R. Peletier, & D. Gadotti (Springer, Berlin), 77

Laurikainen, E., Salo, H., & Buta, R. 2005, MNRAS, 362, 1319

Laurikainen, E., Salo, H., Buta, R., & Knapen, J. H. 2007, MNRAS, 381, 401

Laurikainen, E., Salo, H., Buta, R., & Knapen, J. H. 2009, ApJ, 692, L34

Laurikainen, E., Salo, H., Buta, R., Knapen, J. H., & Comerón, S. 2010, MNRAS, 405, 1089

Lee, G.-H., Park, C., Lee, M. G., & Choi, Y.-Y. 2012, ApJ, 745, 125

Leja, J., van Dokkum, P. G., Franx, M., & Whitaker, K. E. 2015, ApJ, 798, 115

L'Huillier, B., Combes, F., & Semelin, B. 2012, A&A, 544, A68

Lindblad, B. 1951, PASP, 63, 133

Lindblad, B. 1956, StAn, 19

López-Sanjuan, C., Cenarro, A. J., Varela, J., et al. 2015, A&A, 576, A53

Lotz, J. M., Jonsson, P., Cox, T. J., & Primack, J. R. 2008, MNRAS, 391, 1137

Lütticke, R., Dettmar, R.-J., & Pohlen, M. 2000a, A&AS, 145, 405

Lütticke, R., Dettmar, R.-J., & Pohlen, M. 2000b, A&A, 362, 435

MacArthur, L. A., Courteau, S., & Holtzman, J. A. 2003, ApJ, 582, 689

Mackay, D. J. C. 2003, in Information Theory, Inference and Learning Algorithms (Cambridge University Press, Cambridge, UK), 640

Madore, B. F. 2016, Galactic Bulges, 418, 1

Makarov, D., Prugniel, P., Terekhova, N., Courtois, H., & Vauglin, I. 2014, A&A, 570, A13

Malin, D. F. & Carter, D. 1980, Nature, 285, 643

Mandelker, N., Dekel, A., Ceverino, D., et al. 2014, MNRAS, 443, 3675

Marino, A., Bianchi, L., Rampazzo, R., et al. 2011, ApJ, 736, 154

Marino, R. A., Gil de Paz, A., Sánchez, S. F., et al. 2016, A&A, 585, A47

Markwardt, C. B. 2009, in ASP Conf Ser, Vol. 411, Astronomical Data Analysis Software and Systems XVIII, ed. D. A. Bohlender, D. Durand, & P. Dowler (ASP, San Francisco, CA), 251

Martinez-Valpuesta, I., Shlosman, I., & Heller, C. 2006, ApJ, 637, 214

Masters, K. L., Nichol, R. C., Haynes, M. P., et al. 2012, MNRAS, 424, 2180

Masters, K. L., Nichol, R. C., Hoyle, B., et al. 2011, MNRAS, 411, 2026

McDermid, R. M., Alatalo, K., Blitz, L., et al. 2015, MNRAS, 448, 3484

Méndez-Abreu, J. 2016, in Galactic Bulges, ed. E. Laurikainen, R. Peletier, & D. Gadotti (Springer, Berlin), 15

Méndez-Abreu, J., Aguerri, J. A. L., Barrena, R., et al. 2012, A&A, 537, A25

Méndez-Abreu, J., Aguerri, J. A. L., Corsini, E. M., & Simonneau, E. 2008a, A&A, 478, 353

Méndez-Abreu, J., Aguerri, J. A. L., Falcón-Barroso, J., et al. 2018, MNRAS, 474, 1307

Méndez-Abreu, J., Corsini, E. M., Debattista, V. P., et al. 2008b, ApJ, 679, L73

Méndez-Abreu, J., Debattista, V. P., Corsini, E. M., & Aguerri, J. A. L. 2014, A&A, 572, A25

Méndez-Abreu, J., Ruiz-Lara, T., Sánchez-Menguiano, L., et al. 2017, A&A, 598, A32

Méndez-Abreu, J., Simonneau, E., Aguerri, J. A. L., & Corsini, E. M. 2010, A&A, 521, A71

Merlin, E. & Chiosi, C. 2006, A&A, 457, 437

Mihos, J. C. & Hernquist, L. 1994a, ApJ, 437, 611

Mihos, J. C. & Hernquist, L. 1994b, ApJ, 431, L9

Mihos, J. C. & Hernquist, L. 1996, ApJ, 464, 641

Mihos, J. C., Walker, I. R., Hernquist, L., Mendes de Oliveira, C., & Bolte, M. 1995, ApJ, 447, L87

Mishra, P. K., Wadadekar, Y., & Barway, S. 2017, MNRAS, 467, 2384

Moffat, A. F. J. 1969, A&A, 3, 455

Möllenhoff, C. & Heidt, J. 2001, A&A, 368, 16

Moré, J. J., Garbow, B. S., & E., H. K. 1980, Argonne Nat Lab Report ANL-80-74

Morelli, L., Cesetti, M., Corsini, E. M., et al. 2010, A&A, 518, A32

Morelli, L., Halliday, C., Corsini, E. M., et al. 2004, MNRAS, 354, 753

Morelli, L., Parmiggiani, M., Corsini, E. M., et al. 2016, MNRAS, 463, 4396

Morelli, L., Pompei, E., Pizzella, A., et al. 2008, MNRAS, 389, 341

Muñoz-Mateos, J. C., Sheth, K., Gil de Paz, A., et al. 2013, ApJ, 771, 59

Naab, T. & Burkert, A. 2003, ApJ, 597, 893

Naab, T., Oser, L., Emsellem, E., et al. 2014, MNRAS, 444, 3357

Nair, P. B. & Abraham, R. G. 2010, ApJS, 186, 427

Neistein, E., van den Bosch, F. C., & Dekel, A. 2006, MNRAS, 372, 933

Neumann, J., Wisotzki, L., Choudhury, O. S., et al. 2017, A&A, 604, A30

Nigoche-Netro, A., Aguerri, J. A. L., Lagos, P., et al. 2010, A&A, 516, A96

Nigoche-Netro, A., Moles, M., Ruelas-Mayorga, A., Franco-Balderas, A., & Kjørgaard, P. 2007, A&A, 472, 773

Nigoche-Netro, A., Ruelas-Mayorga, A., & Franco-Balderas, A. 2008, A&A, 491, 731

Noguchi, M. 1999, ApJ, 514, 77

Norman, C. A., Sellwood, J. A., & Hasan, H. 1996, ApJ, 462, 114

Ocvirk, P., Pichon, C., Lançon, A., & Thiébaut, E. 2006a, MNRAS, 365, 74

Ocvirk, P., Pichon, C., Lançon, A., & Thiébaut, E. 2006b, MNRAS, 365, 46

Oh, K., Sarzi, M., Schawinski, K., & Yi, S. K. 2011, ApJS, 195, 13

Pagotto, I., Corsini, E. M., Dalla Bontà, E., et al. 2017, AN, 338, 841

Papaderos, P., Loose, H.-H., Thuan, T. X., & Fricke, K. J. 1996, A&AS, 120, 207

Peebles, P. J. E. & Nusser, A. 2010, Nature, 465, 565

Peletier, R. F. & Balcells, M. 1996, AJ, 111, 2238

Peletier, R. F., Falcón-Barroso, J., Bacon, R., et al. 2007, MNRAS, 379, 445

Peng, C. Y., Ho, L. C., Impey, C. D., & Rix, H.-W. 2002, AJ, 124, 266

Peng, C. Y., Ho, L. C., Impey, C. D., & Rix, H.-W. 2010, AJ, 139, 2097

Pérez, I. 2004, A&A, 427, L17

Persic, M. & Salucci, P. 1992, MNRAS, 258, 14P

Pfenniger, D. & Norman, C. 1990, ApJ, 363, 391

Pignatelli, E., Fasano, G., & Cassata, P. 2006, A&A, 446, 373

Pohlen, M. & Trujillo, I. 2006, A&A, 454, 759

Press, W. H., Flannery, B. P., & Teukolsky, S. A. 1986, Numerical Recipes. The Art of Scientific Computing (Cambridge University Press, Cambridge)

Prieto, M., Aguerri, J. A. L., Varela, A. M., & Muñoz-Tuñón, C. 2001, A&A, 367, 405

Prieto, M. & Eliche-Moral, M. C. 2015, MNRAS, 451, 1158

Prieto, M., Eliche-Moral, M. C., Balcells, M., et al. 2013, MNRAS, 428, 999

Prieto, M., Gottesman, S. T., Aguerri, J.-A. L., & Varela, A.-M. 1997, AJ, 114, 1413

Prugniel, P. & Soubiran, C. 2001, A&A, 369, 1048

Querejeta, M., Eliche-Moral, M. C., Tapia, T., et al. 2015a, A&A, 573, A78

Querejeta, M., Eliche-Moral, M. C., Tapia, T., et al. 2015b, A&A, 573, A78

Querejeta, M., Eliche-Moral, M. C., Tapia, T., et al. 2015c, A&A, 579, L2

Raha, N., Sellwood, J. A., James, R. A., & Kahn, F. D. 1991, Nature, 352, 411

Ravikumar, C. D., Barway, S., Kembhavi, A., Mobasher, B., & Kuriakose, V. C. 2006, A&A, 446, 827

Renzini, A. 1999, in The Formation of Galactic Bulges, ed. C. M. Carollo, H. C. Ferguson, & R. F. G. Wyse (Cambridge University Press, Cambridge), 9

Robotham, A. S. G., Taranu, D. S., Tobar, R., Moffett, A., & Driver, S. P. 2017, MNRAS, 466, 1513

Rodríguez, S. & Padilla, N. D. 2013, MNRAS, 434, 2153

Rudick, C. S., Mihos, J. C., Frey, L. H., & McBride, C. K. 2009, ApJ, 699, 1518

Ruiz-Lara, T., Pérez, I., Florido, E., et al. 2017, A&A, 604, A4

Ryden, B. S. 2004, ApJ, 601, 214

Ryden, B. S. 2006, ApJ, 641, 773

Salo, H., Laurikainen, E., Laine, J., et al. 2015, ApJS, 219, 4

Samland, M. & Gerhard, O. E. 2003, A&A, 399, 961

Sánchez, S. F., García-Benito, R., Zibetti, S., et al. 2016, A&A, 594, A36

Sánchez, S. F., Kennicutt, R. C., Gil de Paz, A., et al. 2012, A&A, 538, A8

Sánchez Almeida, J., Elmegreen, B. G., Muñoz-Tuñón, C., & Elmegreen, D. M. 2014, A&ARv, 22, 71

Sánchez-Blázquez, P., Peletier, R. F., Jiménez-Vicente, J., et al. 2006, MNRAS, 371, 703

Sánchez-Blázquez, P., Rosales-Ortega, F. F., Méndez-Abreu, J., et al. 2014, A&A, 570, A6

Sánchez-Janssen, R., Méndez-Abreu, J., & Aguerri, J. A. L. 2010, MNRAS, 406, L65

Sánchez-Menguiano, L., Sánchez, S. F., Pérez, I., et al. 2016, A&A, 587, A70

Sandage, A. 1961, The Hubble Atlas of Galaxies (Carnegie Institution, Washington)

Sandage, A. 1990, JRASC, 84, 70

Sandage, A., Freeman, K. C., & Stokes, N. R. 1970, ApJ, 160, 831

Sarzi, M., Alatalo, K., Blitz, L., et al. 2013, MNRAS, 432, 1845

Sarzi, M., Falcón-Barroso, J., Davies, R. L., et al. 2006, MNRAS, 366, 1151

Scannapieco, C. & Tissera, P. B. 2003, MNRAS, 338, 880

Schwarz, G. 1978, Ann Stat, 6, 461

Schwarzschild, M. 1979, ApJ, 232, 236

Schweizer, F. 1982, ApJ, 252, 455

Scott, N., Cappellari, M., Davies, R. L., et al. 2013, MNRAS, 432, 1894

Sellwood, J. A. 2014, Rev Mod Phys, 86, 1

Semelin, B. & Combes, F. 2002, A&A, 388, 826

Serra, P., Oser, L., Krajnović, D., et al. 2014, MNRAS, 444, 3388

Sérsic, J. L. 1968, Atlas de Galaxias Australes (Observatorio Astronomico de Cordoba, Cordoba)

Seth, A. C., Dalcanton, J. J., Hodge, P. W., & Debattista, V. P. 2006, AJ, 132, 2539

Shaw, M. 1993, A&A, 280, 33

Shen, J., Rich, R. M., Kormendy, J., et al. 2010, ApJ, 720, L72

Sheth, K., Regan, M., Hinz, J. L., et al. 2010, PASP, 122, 1397

Sil'chenko, O. K. 2013, AN, 334, 781

Sil'chenko, O. K., Proshina, I. S., Shulga, A. P., & Koposov, S. E. 2012, MNRAS, 427, 790

Simard, L. 1998, in ASP Conf Ser, Vol. 145, Astronomical Data Analysis Software and Systems VII, ed. R. Albrecht, R. N. Hook, & H. A. Bushouse (ASP, San Francisco, CA), 108

Simard, L., Mendel, J. T., Patton, D. R., Ellison, S. L., & McConnachie, A. W. 2011, ApJS, 196, 11

Simonneau, E., Varela, A. M., & Munoz-Tunon, C. 1998, Nuovo Cimento B, 113, 927

Somerville, R. S. & Primack, J. R. 1999, MNRAS, 310, 1087

Sommer-Larsen, J., Götz, M., & Portinari, L. 2003, ApJ, 596, 47

Springel, V., Di Matteo, T., & Hernquist, L. 2005, ApJ, 620, L79

Springel, V. & Hernquist, L. 2005, ApJ, 622, L9

Statler, T. S., Lambright, H., & Bak, J. 2001, ApJ, 549, 871

Stebbins, J. & Whitford, A. E. 1947, ApJ, 106, 235

Steinmetz, M. & Muller, E. 1995, MNRAS, 276, 549

Tabor, M., Merrifield, M., Aragón-Salamanca, A., et al. 2017, MNRAS, 466, 2024

Tacconi, L. J., Neri, R., Genzel, R., et al. 2013, ApJ, 768, 74

Tapia, T., Eliche-Moral, M. C., Aceves, H., et al. 2017, A&A, 604, A105

Tapia, T., Eliche-Moral, M. C., Querejeta, M., et al. 2014, A&A, 565, A31

Taylor, M. A., Puzia, T. H., Gomez, M., & Woodley, K. A. 2015, ApJ, 805, 65

Tempel, E., Saar, E., Liivamägi, L. J., et al. 2011, A&A, 529, A53

Thomas, D. & Davies, R. L. 2006, MNRAS, 366, 510

Thomas, D., Maraston, C., Schawinski, K., Sarzi, M., & Silk, J. 2010, MNRAS, 404, 1775

Tissera, P. B., Smith Castelli, A. V., & Scannapieco, C. 2006, A&A, 455, 135

Toomre, A. 1964, ApJ, 139, 1217

Toomre, A. 1977, in Evolution of Galaxies and Stellar Populations, ed. B. M. Tinsley & R. B. G. Larson, D. Campbell (Yale University Press, New Haven), 401

Toomre, A. & Toomre, J. 1972, ApJ, 178, 623

Torres-Papaqui, J. P., Coziol, R., Andernach, H., et al. 2012, RMxAA, 48, 275

Tremblay, B. & Merritt, D. 1996, AJ, 111, 2243

Trujillo, I., Aguerri, J. A. L., Cepa, J., & Gutiérrez, C. M. 2001a, MNRAS, 328, 977

Trujillo, I., Aguerri, J. A. L., Gutiérrez, C. M., & Cepa, J. 2001b, AJ, 122, 38

Trujillo, I. & Pohlen, M. 2005, ApJ, 630, L17

Vaghmare, K., Barway, S., & Kembhavi, A. 2013, ApJ, 767, L33

van den Bergh, S., Abraham, R. G., Ellis, R. S., et al. 1996, AJ, 112, 359

van den Bosch, R. C. E., van de Ven, G., Verolme, E. K., Cappellari, M., & de Zeeuw, P. T. 2008, MNRAS, 385, 647

van der Marel, R. P. & Franx, M. 1993, ApJ, 407, 525

van Dokkum, P. G. 2001, PASP, 113, 1420

Vega Beltrán, J. C., Corsini, E. M., Pizzella, A., & Bertola, F. 1997, A&A, 324, 485

Wadadekar, Y., Robbason, B., & Kembhavi, A. 1999, AJ, 117, 1219

Walcher, C. J., Wisotzki, L., Bekeraité, S., et al. 2014, A&A, 569, A1

Walker, I. R., Mihos, J. C., & Hernquist, L. 1996, ApJ, 460, 121

Wallerstein, G. 1962, AJ, 67, 329

Wegg, C. & Gerhard, O. 2013, MNRAS, 435, 1874

Weijmans, A.-M., de Zeeuw, P. T., Emsellem, E., et al. 2014, MNRAS, 444, 3340

Weinzirl, T., Jogee, S., & Barazza, F. D. 2008, in ASP Conf Ser, Vol. 393, New Horizons in Astronomy, ed. A. Frebel, J. R. Maund, J. Shen, & M. H. Siegel (ASP, San Francisco, CA), 279

Weinzirl, T., Jogee, S., Khochfar, S., Burkert, A., & Kormendy, J. 2009, ApJ, 696, 411

White, S. D. M. & Rees, M. J. 1978, MNRAS, 183, 341

Williams, M. J., Zamojski, M. A., Bureau, M., et al. 2011, MNRAS, 414, 2163

Williams, T. B. & Schwarzschild, M. 1979, ApJ, 227, 56

Worthey, G., Faber, S. M., Gonzalez, J. J., & Burstein, D. 1994, ApJS, 94, 687

Wuyts, S., Förster Schreiber, N. M., Genzel, R., et al. 2012, ApJ, 753, 114

Wyse, R. F. G., Gilmore, G., & Franx, M. 1997, ARAA, 35, 637

Young, C. K. & Currie, M. J. 1994, MNRAS, 268, L11

Young, L. M., Scott, N., Serra, P., et al. 2014, MNRAS, 444, 3408

Zavala, J., Avila-Reese, V., Firmani, C., & Boylan-Kolchin, M. 2012, MNRAS, 427, 1503

Zhao, Y. 2012, A&AS, 337, 719

Zhu, L., van den Bosch, R., van de Ven, G., et al. 2018, MNRAS, 473, 3000

Zwicky, F. 1957, Morphological Astronomy (Springer, Berlin)